



Defense Threat Reduction Agency
8725 John J. Kingman Road, MS
6201 Fort Belvoir, VA 22060-6201



DTRA-TR-15-88

TECHNICAL REPORT

Modeling Turbulent Mixing/Combustion of Bio-Agents Behind Detonations: Effect of Instabilities, Dense Clustering, and Trace Survivability

Distribution Statement A. Approved for public release; distribution is unlimited.

June 2017

HDTRA1-10-1-0008

K. Gottiparthi et al.

Prepared by:
Georgia Institute of
Technology
270 Ferst Drive
Atlanta, GA 30332

DESTRUCTION NOTICE:

Destroy this report when it is no longer needed.
Do not return to sender.

PLEASE NOTIFY THE DEFENSE THREAT REDUCTION
AGENCY, ATTN: DTRIAC/ J9STT, 8725 JOHN J. KINGMAN ROAD,
MS-6201, FT BELVOIR, VA 22060-6201, IF YOUR ADDRESS
IS INCORRECT, IF YOU WISH IT DELETED FROM THE
DISTRIBUTION LIST, OR IF THE ADDRESSEE IS NO
LONGER EMPLOYED BY YOUR ORGANIZATION.

REPORT DOCUMENTATION PAGE

Form Approved
OMB No. 0704-0188

Public reporting burden for this collection of information is estimated to average 1 hour per response, including the time for reviewing instructions, searching existing data sources, gathering and maintaining the data needed, and completing and reviewing this collection of information. Send comments regarding this burden estimate or any other aspect of this collection of information, including suggestions for reducing this burden to Department of Defense, Washington Headquarters Services, Directorate for Information Operations and Reports (0704-0188), 1215 Jefferson Davis Highway, Suite 1204, Arlington, VA 22202-4302. Respondents should be aware that notwithstanding any other provision of law, no person shall be subject to any penalty for failing to comply with a collection of information if it does not display a currently valid OMB control number. **PLEASE DO NOT RETURN YOUR FORM TO THE ABOVE ADDRESS.**

1. REPORT DATE (DD-MM-YYYY)		2. REPORT TYPE		3. DATES COVERED (From - To)	
4. TITLE AND SUBTITLE				5a. CONTRACT NUMBER	
				5b. GRANT NUMBER	
				5c. PROGRAM ELEMENT NUMBER	
6. AUTHOR(S)				5d. PROJECT NUMBER	
				5e. TASK NUMBER	
				5f. WORK UNIT NUMBER	
7. PERFORMING ORGANIZATION NAME(S) AND ADDRESS(ES)				8. PERFORMING ORGANIZATION REPORT NUMBER	
9. SPONSORING / MONITORING AGENCY NAME(S) AND ADDRESS(ES)				10. SPONSOR/MONITOR'S ACRONYM(S)	
				11. SPONSOR/MONITOR'S REPORT NUMBER(S)	
12. DISTRIBUTION / AVAILABILITY STATEMENT					
13. SUPPLEMENTARY NOTES					
14. ABSTRACT					
15. SUBJECT TERMS					
16. SECURITY CLASSIFICATION OF:		17. LIMITATION OF ABSTRACT	18. NUMBER OF PAGES	19a. NAME OF RESPONSIBLE PERSON	
a. REPORT	b. ABSTRACT			c. THIS PAGE	19b. TELEPHONE NUMBER (include area code)

UNIT CONVERSION TABLE
U.S. customary units to and from international units of measurement*

U.S. Customary Units	Multiply by ← Divide by [†]	International Units
Length/Area/Volume		
inch (in)	2.54 $\times 10^{-2}$	meter (m)
foot (ft)	3.048 $\times 10^{-1}$	meter (m)
yard (yd)	9.144 $\times 10^{-1}$	meter (m)
mile (mi, international)	1.609 344 $\times 10^3$	meter (m)
mile (nmi, nautical, U.S.)	1.852 $\times 10^3$	meter (m)
barn (b)	1 $\times 10^{-28}$	square meter (m^2)
gallon (gal, U.S. liquid)	3.785 412 $\times 10^{-3}$	cubic meter (m^3)
cubic foot (ft^3)	2.831 685 $\times 10^{-2}$	cubic meter (m^3)
Mass/Density		
pound (lb)	4.535 924 $\times 10^{-1}$	kilogram (kg)
unified atomic mass unit (amu)	1.660 539 $\times 10^{-27}$	kilogram (kg)
pound-mass per cubic foot ($lb\ ft^{-3}$)	1.601 846 $\times 10^1$	kilogram per cubic meter ($kg\ m^{-3}$)
pound-force (lbf avoirdupois)	4.448 222	newton (N)
Energy/Work/Power		
electron volt (eV)	1.602 177 $\times 10^{-19}$	joule (J)
erg	1 $\times 10^{-7}$	joule (J)
kiloton (kt) (TNT equivalent)	4.184 $\times 10^{12}$	joule (J)
British thermal unit (Btu) (thermochemical)	1.054 350 $\times 10^3$	joule (J)
foot-pound-force (ft lbf)	1.355 818	joule (J)
calorie (cal) (thermochemical)	4.184	joule (J)
Pressure		
atmosphere (atm)	1.013 250 $\times 10^5$	pascal (Pa)
pound force per square inch (psi)	6.984 757 $\times 10^3$	pascal (Pa)
Temperature		
degree Fahrenheit ($^{\circ}$ F)	$[T(^{\circ}F) - 32]/1.8$	degree Celsius ($^{\circ}$ C)
degree Fahrenheit ($^{\circ}$ F)	$[T(^{\circ}F) + 459.67]/1.8$	kelvin (K)
Radiation		
curie (Ci) [activity of radionuclides]	3.7 $\times 10^{10}$	per second (s^{-1}) [becquerel (Bq)]
roentgen (R) [air exposure]	2.579 760 $\times 10^{-4}$	coulomb per kilogram ($C\ kg^{-1}$)
rad [absorbed dose]	1 $\times 10^{-2}$	joule per kilogram ($J\ kg^{-1}$) [gray (Gy)]
rem [equivalent and effective dose]	1 $\times 10^{-2}$	joule per kilogram ($J\ kg^{-1}$) [sievert (Sv)]

* Specific details regarding the implementation of SI units may be viewed at <http://www.bipm.org/en/si/>.

[†]Multiply the U.S. customary unit by the factor to get the international unit. Divide the international unit by the factor to get the U.S. customary unit.

TABLE OF CONTENTS

LIST OF TABLES	ii
LIST OF FIGURES	ii
I GOALS OF THE PROJECT	1
1.1 Objectives	2
1.2 Summary of Accomplishments	2
II FORMULATION	4
2.1 Gas Phase	4
2.2 Particle Phase	6
2.3 Collision/contact Model	7
2.4 Coupling particle and gas phases	8
2.5 Lagrangian tracking	9
III ACCOMPLISHMENTS	11
3.1 Detonation in gas-particle mixtures	11
3.2 DDT in gas-particle mixtures	11
3.3 Influence of particles on RMI	12
3.4 Neutralization of bacterial endospores by explosives	12
3.5 Quantification of Uncertainties in Modeling and Numerical Approach	12
3.5.1 Model Form Uncertainty	14
3.5.2 Model Input Uncertainty	14
IV OPPORTUNITIES FOR TRAINING AND PROFESSIONAL DEVELOPMENT	17
V DISSEMINATION OF RESULTS TO COMMUNITIES OF INTEREST	18
APPENDIX A — LIST OF PAPERS	20

LIST OF FIGURES

2.1 Schematic of (a) gather-scatter and (b) point-to-point communication strategies for Lagrangian particle tracking. The boxes with P1 to P8 indicate the grid of processors performing computation for particles. A small box corresponding to each processor is shown to indicate the two-way coupling between the gas-phase and the dispersed-phase. The double sided arrow indicates two-way communication between the processors. The gathering operation is indicated with single arrow and scattering operation is indicated using single dashed arrow. P0 performs all the book-keeping operations and updates the full particle data array at each time step in Gather-Scatter approach. Note that there can be communication between corner neighbors (P4-P0, P4-P2, P4-P6 and P4-P8) in point-to-point method which is not illustrated. . .	10
3.1 Variation of mean value of intact spore percentages for different post-shock temperatures. The vertical error bars indicate the error extremes with 95% confidence and horizontal error bars indicate variation of post-shock temperature. Experimental results are indicated by black squares.	16
3.2 Number of occurrences of each intact spore percentage for different shock Mach numbers.	16

CHAPTER I

GOALS OF THE PROJECT

Neutralization of Chemical/Biological (CB) agents via entrainment into flames/hot spots, ignition/combustion by blast waves, dispersion of particles/droplets, and venting and plume formation from the damaged structure are all highly transient phenomena with a wide range of characteristic time and length scales. Geometry of the target structure can also introduce unsteady flow complexities, such as re-circulating flow behind obstacles and in corners that can affect mixing and combustion processes. The dynamics of the Agent Defeat (AD) scenario encompasses a wide range of scales: the molecular scale (at which species mix and react), the nano-scale (at which nucleation, surface growth and chemistry, and Brownian aggregation occurs), the micron scale (at which shear-induced aggregation, unsteady shear flows, shock or detonation structure, coagulation, breakup, vaporization, and small-scale mixing occurs), the meso-scale (at which large-scale turbulent mixing and transport occurs), and macro scale (at which geometrical constraints of the problem manifest). It is estimated that an over seven order of range of scales interact in both space and time in a highly non-linear manner for these types of problems [1].

Clearly, full resolution of all these scales in a computational framework is beyond the current and perhaps, the future hardware capability. Besides, many of the physics in the AD problem are simply unknown at present. However, some significant progress has been made recently towards developing and validating a generalized simulation capability that accounts for particle-turbulence-shock/detonation-chemistry interactions in complex three-dimensional flows [2, 3, 4, 5]. This simulation strategy has the spatial and the temporal accuracy to carry out either direct numerical simulation (DNS) or Large-Eddy Simulation (LES) of multi-phase (gas, liquid and/or solid), turbulent reacting flows (e.g., [6]). For LES, localized dynamic subgrid models for turbulence and reaction-diffusion processes provide a unique strategy that contains no ad hoc parameters [7, 8].

Application and validation in complex turbulent reacting flows without and with high compressibility have also been demonstrated in the past. Its highly optimized parallel multi-block approach allows modeling of complex geometries, and has recently been employed to simulate AD related flows by independent researchers. The research performed has enhanced the capability of this code (called LESLIE3D, hereafter) by using an efficient massively-parallel approach to account for the presence of large number (“dense cloud”) of particles (in the nano-to-micron scale) in the domain.

This report summarizes the accomplishments under the current project towards achieving a simulation capability to handle the complex physics of detonations and blast waves and also the interaction of detonations/blast waves with distribution of particles. Further, simulations performed, which quantify the endospore survival in post-shock and post-detonation environments, are reported. In the following chapters

the accomplishments under this research effort are summarized and the details of each task are provided in the articles provided in the appendix. Further, the modeling uncertainties are quantified and analyzed for spore neutralization in the post-shock regions and are reported here.

1.1 Objectives

The key technical objectives of this project are:

1. To simulate turbulent instabilities with and without particles in detonation and post detonation flow fields to understand the fundamental interactions between shock, shear instability, turbulent mixing/combustion and particle motion
2. To simulate, validate and extend the current dense-dilute modeling capability [9] to account for dispersion/neutralization of CB agents in flows with shear instability and turbulence
3. To quantify the impact of detonation on bio-agent destruction, including trace survivability
4. To develop an envelop of operating conditions, including sensitivity to parametric changes using Uncertainty Quantification (UQ) strategy

1.2 Summary of Accomplishments

The research effort has been focused on simulation of dense post-detonation flows, neutralization of spore-laden aerosol by explosive charges and quantification of uncertainty in the predictions. The results obtained under the current project are provided in this report. The accomplishments (published in the citations provided) are arranged in the following order:

1. Detonation in gas-particle mixtures [2]

Propagation of a gaseous detonation through a dense inert particle cloud is investigated. The effect of the particle cloud on the detonation is analyzed by quantifying the strength of the detonation front and studying the formation or suppression of transverse waves. The regimes of propagation, suppression and quenching are examined based on the initial particle cloud volume fraction and the initial particle cloud length. Three-dimensional gaseous detonation propagation is also investigated.

2. Deflagration-to-Detonation Transition (DDT) in gas-particle mixtures [10, 11, 12, 13]

The formation of a detonation from a deflagration is a channel with reactive gas-particle mixtures are investigated. The effect of the particles on flame acceleration and flame-shock coupling is investigated by varying the initial volume

fraction the particles in the flow. Both inert and reactive particles are considered. The time and the distance to DDT are quantified and the mechanisms for transition to a detonation are analyzed.

3. Richtmyer-Meshkov Instability (RMI) in gas-particle mixtures [5]

The process of RMI generation and growth in the presence of particles is investigated. The growth rate of the mixing zone is evaluated for different particle volume fractions and the effects on the shock wave and the RMI are studied. In particular, vorticity generation is quantified to analyze the role of the particles in enhancing or suppression the instability generation.

4. Simulation of post-detonation flow with inert and reactive particles [14]

Post-detonation flows ensuing the detonation of explosive charges are investigated. The particle dispersion and combustion in the high temperature mixing zone formed after the detonation of the charge is studied. The change in the degree of mixedness due to the particle is quantified.

5. Endospore dispersion and neutralization in post-detonation flow of an explosive charge [15]

Quantification of endospore neutralization by explosive charges is very challenging and is addressed here. Endospore-laden aerosol is modeled and the interaction of the aerosol with blast waves is investigated. Based on the results from experiments on shock-spore interaction, sensitivity analysis of the modeling is performed. Aerosol dispersion, vaporization and endospore neutralization in post-detonation flows is studied under this task.

6. Uncertainty Quantification (UQ) of endospore neutralization studies

In order to provide confidence in the overall simulation strategy, it is essential to quantify the uncertainties in the modeling. Dempster-Shafer theory and polynomial chaos expansion are used to quantify the uncertainties in the endospore neutralization by shock waves. Both the confidence in the prediction and the uncertainty in the modeling, for a given set of input parameters, are evaluated in this task.

CHAPTER II

FORMULATION

In this chapter, we summarize the key equations of the numerical formulation used in these studies. Both the gas phase and particle phase models are discussed along with relevant closure issues.

2.1 Gas Phase

In this section, we describe the governing equations and the numerical methodology used in the current solver. We use a Large Eddy Simulation (LES) approach in which a filter of the kind $f = \tilde{f} + f''$ is applied to the conventional Navier-Stokes equations, where \sim denotes the resolved scale and $''$ the unresolved sub-grid scale. The Favre filtered variable is defined as $\tilde{f} = \bar{\rho}f/\bar{\rho}$; the overbar represents a spatial filtering. The filtered gas phase Navier-Stokes equations, applicable in dense two-phase flow scenarios in the absence of body forces are

$$\begin{aligned} \frac{\partial}{\partial t} \begin{bmatrix} \alpha_g \bar{\rho}_g \\ \alpha_g \bar{\rho}_g \tilde{u}_{g,i} \\ \alpha_g \bar{\rho}_g E_g \\ \alpha_g \bar{\rho}_g \tilde{Y}_{g,k} \end{bmatrix} + \frac{\partial}{\partial x_j} \begin{bmatrix} \alpha_g \bar{\rho}_g \tilde{u}_{g,j} \\ \alpha_g \bar{\rho}_g \tilde{u}_{g,i} \tilde{u}_{g,j} + \alpha_g \bar{\rho}_g \delta_{ij} - \alpha_g \bar{\tau}_{g,ij} \\ \alpha_g \left(\bar{\rho}_g \tilde{E}_g + \bar{p}_g \right) \tilde{u}_{g,j} - \alpha_g \tilde{u}_{g,i} \bar{\tau}_{g,ji} + \alpha_g \bar{q}_{g,j} \\ \alpha_g \bar{\rho}_g \tilde{Y}_{g,k} \left(\tilde{u}_{g,j} + \tilde{V}_{g,j} \right) \end{bmatrix} + \\ \frac{\partial}{\partial x_j} \begin{bmatrix} 0 \\ \tau_{g,ij}^{sgs} \\ H_{g,j}^{sgs} + \sigma_{g,j}^{sgs} \\ Y_{g,k}^{sgs} + \theta_{g,k}^{sgs} \end{bmatrix} = \begin{bmatrix} 0 \\ p^* \frac{\partial \alpha_g}{\partial x_j} \delta_{ij} - \tau_{ij}^* \frac{\partial \alpha_g}{\partial x_j} \\ p^* u_j^* \frac{\partial \alpha_g}{\partial x_j} - u_i^* \tau_{ij}^* \frac{\partial \alpha_g}{\partial x_j} \\ 0 \end{bmatrix} + \begin{bmatrix} 0 \\ 0 \\ 0 \\ \dot{\omega}_k \end{bmatrix} + \begin{bmatrix} \dot{\rho}_p \\ \dot{F}_{p,i} \\ \dot{Q}_p + \dot{W}_p \\ \dot{S}_{p,k} \end{bmatrix} \quad (2.1) \end{aligned}$$

Here, the matrices on the left side denote respectively, the conservative variables, the conservative resolved fluxes and the conservative sub-grid fluxes. The terms on the right side denote respectively, the multi-phase “nozzling” terms, the chemical source term and the inter-phase coupling terms. α_g denotes the gas phase volume fraction, ρ_g the density, $u_{g,i}$ the i -th component of velocity, E_g the total energy given by the sum of the internal (e_g) and kinetic energies, $e_g + \frac{1}{2}u_{g,i}u_{g,i}$, and $Y_{g,k}$ the mass fraction of the k -th species. The stress tensor is denoted by $\tau_{g,ij}$, the j -direction heat flux by $q_{g,j}$, the j -component diffusion velocity by $V_{g,j}$, and the chemical production of the k -th species by $\dot{\omega}_k$. Also, p^* , u_i^* and τ_{ij}^* denote respectively, the pressure, i -th component of velocity and stress tensor at the interface between the two phases. The filtered viscous stress tensor, $\bar{\tau}_{g,ij}$ is obtained from the filtered quantities. The filtered heat flux vector $\bar{q}_{g,j}$ is obtained as

$$\bar{q}_{g,j} = -\bar{\kappa} \frac{\partial \tilde{T}}{\partial x_j} + \bar{\rho} \sum_1^{N_s} \tilde{h}_k \tilde{Y}_{g,k} \tilde{V}_{g,j} + \sum_1^{N_s} q_{g,j}^{sgs} \quad (2.2)$$

where N_s denotes the total number of species under consideration.

All the terms with superscript sgs are the sub-grid terms that require closure. These terms are defined as:

$$\tau_{g,ij}^{sgs} = \bar{\rho} (\widetilde{u_{g,i} u_{g,j}} - \widetilde{u_{g,i}} \widetilde{u_{g,j}}) \quad (2.3)$$

$$H_{g,i}^{sgs} = \bar{\rho} (\widetilde{E_g u_{g,i}} - \widetilde{E_g} \widetilde{u_{g,i}}) + (\widetilde{u_{g,i} P_g} - \widetilde{u_{g,i}} \widetilde{P_g}) \quad (2.4)$$

$$\sigma_{g,i}^{sgs} = (\widetilde{u_{g,j} \tau_{g,ij}} - \widetilde{u_{g,j}} \widetilde{\tau_{g,ij}}) \quad (2.5)$$

$$Y_{i,k}^{sgs} = \bar{\rho} (\widetilde{u_i Y_k} - \widetilde{u_i} \widetilde{Y_k}) \quad (2.6)$$

The closure of these terms employ a subgrid eddy viscosity ν_t approach. This term requires definition of a characteristic length and velocity scale. The characteristic length scale is chosen to be the grid scale Δ while the velocity scale is determined by solving a transport model for the subgrid kinetic energy k^{sgs} . This equation is

$$\frac{\partial \bar{\rho}_g k^{sgs}}{\partial t} + \frac{\partial}{\partial x_j} (\bar{\rho}_g \tilde{u}_{g,j} k^{sgs}) = -\tau_{g,ij}^{sgs} \frac{\partial \tilde{u}_{g,j}}{\partial x_i} - C_\epsilon \bar{\rho}_g \frac{(k^{sgs})^{3/2}}{\bar{\Delta}} + \frac{\partial (\bar{\rho}_g \frac{\nu_t}{C_t} \frac{\partial k^{sgs}}{\partial x_j})}{\partial x_j} + F_p \quad (2.7)$$

In the above equation, F_p is a term appearing due to the particle phase interactions, and the sub-grid eddy viscosity is modeled as $\nu_t = C_\nu \bar{\Delta} \sqrt{k^{sgs}}$, where $\bar{\Delta} = (\Delta x \Delta y \Delta z)^{1/3}$ is based on the local grid size $(\Delta x, \Delta y, \Delta z)$. The coefficients, C_ν , C_ϵ and C_t have nominal values 0.067, 0.916 and 1.0, respectively. However, future studies will employ the localized dynamic approach (LDKM) whereby all these model parameters are computed as part of the simulation [7].

The sub-grid stress tensor requires closure and is obtained as

$$\tau_{g,ij}^{sgs} = -2\bar{\rho}_g \nu_t \left[\tilde{S}_{ij} - \frac{1}{3} \tilde{S}_{kk} \delta_{ij} \right] + \frac{2}{3} \bar{\rho}_g k^{sgs} \delta_{ij} \quad (2.8)$$

where \tilde{S}_{ij} denotes the strain rate. The sub-grid total enthalpy flux, $H_{g,j}^{sgs}$ is obtained as

$$H_{g,j}^{sgs} = -\bar{\rho}_g \frac{\nu_t}{Pr} \frac{\partial \tilde{H}_g}{\partial x_j} \quad (2.9)$$

where \tilde{H}_g denotes the filtered total enthalpy of the gas, and Pr , the Prandtl number. The sub-grid species flux is modeled as

$$Y_{g,k}^{sgs} = -\frac{\bar{\rho}_g \nu_t}{Sc} \frac{\partial \tilde{Y}_{g,k}}{\partial x_j} \quad (2.10)$$

where Sc denotes the Schmidt number.

The other sub-grid terms, namely $\sigma_{g,j}^{sgs}$, $q_{g,j}^{sgs}$ and $\theta_{g,k}^{sgs}$ are neglected for the time being.

The last term on the right side identifies the inter-phase coupling terms: mass transfer $\dot{\rho}_p$, i-th component momentum transfer $\dot{F}_{p,i}$, heat transfer \dot{Q}_p , work transfer \dot{W}_p , and chemical production of k-th species $\dot{S}_{p,k}$. These terms are evaluated using Lagrangian tracking of solid particles, and are discussed later.

For a perfect gas, the equation of state is given by $p_g = \rho_g RT_g$, where R represents the gas constant. The speed of sound (a_g) for a perfect gas is given as $a_g^2 = \gamma RT_g$, where γ represents the ratio of the specific heats. For a calorically perfect gas, γ is a constant, while for a thermally perfect gas, γ is expressed as a function of temperature.

In the case of detonation, it is necessary to use real gas equation of state. To account for real gas behavior, the JWL Equation of state is solved for the detonation products using the constant specific heat at constant volume (C_v) approach [16] to obtain a thermal form of the equation of state.

$$p_g = A \exp\left(\frac{-R_1 \rho_o}{\rho_g}\right) + B \exp\left(\frac{-R_2 \rho_o}{\rho_g}\right) + \omega \rho_g C_v T_g, \quad (2.11)$$

where T_g denotes the gas temperature; A , B , R_1 , R_2 and ω denote JWL constants, and ρ_o , the explosive density [17].

2.2 Particle Phase

For the solid and/or liquid phase, Lagrangian tracking is used to compute the particle velocity vector ($u_{p,i}$) from the forces acting on a particle. Since the number of particles to be tracked can be very large under some scenarios, the concept of parcel is employed. Here, a parcel represents a group of particles, each corresponding to the same position and velocity vectors, and temperature. The number of parcels is chosen based on various factors such as computational cost, and available memory, and the number of particles to be assigned to a parcel is chosen based on the desired volume fraction/mass loading. The particle position vector ($x_{p,i}$) is obtained from the velocity vector. These equations are summarized below

$$\frac{dm_p}{dt} = -\dot{m}_p \quad (2.12)$$

$$\frac{dx_{p,i}}{dt} = u_{p,i}, \quad (2.13)$$

$$m_p \frac{du_{p,i}}{dt} = \frac{\pi}{2} r_p^2 C_D \rho_g |u_{g,i} - u_{p,i}| (\tilde{u}_{g,i} - u_{p,i}) - \frac{m_p}{\rho_p} \nabla(\bar{p}_g) + m_p A_{c,i}, \quad (2.14)$$

where m_p is the particle mass, \dot{m}_p is the mass transfer rate, r_p is the particle radius, and $A_{c,i}$ is the i-component of net acceleration/deceleration on a particle due to inter-particle collisions [18, 19]. The particle mass m_p is obtained as $4/3\pi r_p^3 \rho_p$, where ρ_p is the solid particle material density. In the above equation, C_D represents the drag coefficient and is usually expressed as empirical functions of Reynolds number, Mach

number and solid volume fraction. Several different drag laws have been proposed in literature, each being unique to a specific multi-phase problem. To the best of our knowledge, no universally accepted drag law is available in literature, applicable for all kinds of multi-phase problems, i.e., dilute and dense, low and high speed. Thus, we will use different drag laws for different problems depending on the regime of application.

The heat transfer between the two phases is estimated assuming only convection and neglecting radiation, and is used to obtain the particle temperature (T_p)

$$m_p C_p \frac{dT_p}{dt} = 2\pi r_p \kappa_g Nu (\bar{T}_g - T_p) - \dot{m}_p L_{vap} + 4\pi r_p^2 \epsilon \sigma (\bar{T}_g^4 - T_p^4), \quad (2.15)$$

where C_p is the specific heat of the solid particle, κ_g is the thermal conductivity of the gas phase, ϵ is the emissivity and σ is the Stefan-Boltzman constant. The Nusselt number (Nu) is typically expressed as empirical functions of Reynolds number and Prandtl number in the literature. The term L_{vap} represents the heat of vaporization.

In the above equations, the gas phase properties $u_{g,i}$ represents the interpolated value of the resolved velocity and subgrid velocity (which is obtained using k^{sgs}). Thus, in LES, the effect of subgrid turbulence is introduced into the particle phase. Given the parcel locations within the Eulerian finite-volume cell, the volume fraction $\alpha_g = 1 - \alpha_g$ can be directly computed.

The mass transfer, \dot{m}_p , for aluminum particles is given as

$$\dot{m}_p = \left(\frac{1}{\dot{m}_k} + \frac{1}{\dot{m}_d} \right)^{-1} \quad (2.16)$$

$$\dot{m}_d = \pi r_p^2 \rho_p r_p \chi_{ox} (1 + 0.276 Re^{1/2} Pr^{1/3}) / [K r_{p0}^2] \quad (2.17)$$

$$\dot{m}_k = 4\pi r_p^2 k_0 C_{ox} \exp(-Ea/RT_p) \quad (2.18)$$

where C_{ox} is the oxidizer concentration, χ_{ox} is the oxidizer mole fraction and the values of Ea , k_0 and K are obtained from [20].

2.3 Collision/contact Model

To account for the dense nature of the problem, Snider's collision model [18, 19] is used to compute the inter-particle collision force. This inter-particle collision force is as a result of the constant collision/contact between particles. The dynamic compaction involved in granular explosives results in these terms, and thus a collision/contact model, like the one used here, is essential to model dense two-phase explosives. In the collision/contact model used in this study [18, 19], the inter-particle collision force is obtained as an empirical function of the solid volume fraction. This inter-particle force is obtained from the inter-particle stress (τ) given by

$$\tau = \frac{P_s \alpha_p^\beta}{\alpha_{cs} - \alpha_p}, \quad (2.19)$$

where P_s (units of pressure) and β are model coefficients, and α_{cs} is the solid volume fraction at close packing. The particle acceleration/deceleration due to inter-particle collision is obtained as a gradient of the inter-particle stress using the equation

$$A_{c,i} = -\frac{1}{\alpha_p \rho_p} \frac{\partial \tau}{\partial x_i}. \quad (2.20)$$

In addition to changes to the particle Lagrangian equations by the new term $A_{c,i}$, the Euler (gas-phase) fluxes in each of the cells have to be changed to account for the dense loading. This is described in a later section.

2.4 Coupling particle and gas phases

The system of governing equations for the solid-phase are solved using a 4th order Runge-Kutta scheme to obtain the solid particle position vector, velocity vector and temperature. The coupling terms that appear on the right side of the gas phase governing equations (Eqn. 1) are obtained by applying a filtering operation on all the particles in the filter domain. For the finite-volume approach we employ a top-hat filter and for the first approximation, a volume averaging over all the particles in a finite volume (Vol) is sufficient, and is given by:

$$\dot{\rho}_p = \frac{1}{Vol} \sum_1^N n_p \dot{m}_p, \quad (2.21)$$

$$\dot{F}_{p,i} = \frac{1}{Vol} \sum_1^N n_p \left[\dot{m}_p u_{p,i} + \frac{4}{3} \pi r_p^3 \frac{\partial p_g}{\partial x_i} + \frac{\pi}{2} r_p^2 C_D \rho_g |u_{p,i} - u_{g,i}| (u_{p,i} - u_{g,i}) \right], \quad (2.22)$$

where N is the total number of parcels in a finite volume cell and n_p is the number of particles per parcel.

$$\dot{Q}_p = \frac{1}{Vol} \sum_1^N n_p \left[\dot{m}_p h_{vap} + 2\pi r_p \kappa_g N u (T_p - T_g) + 4\pi r_p^2 \epsilon \sigma (T_p^4 - T_g^4) \right], \quad (2.23)$$

where h_{vap} is the enthalpy associated with the mass transfer.

$$\dot{W}_p = \frac{1}{Vol} \sum_1^N n_p \left[\frac{4}{3} \pi r_p^3 \frac{\partial p_g}{\partial x_i} u_{p,i} + \frac{\pi}{2} r_p^2 C_D \rho_g |u_{p,i} - u_{g,i}| (u_{p,i} - u_{g,i}) u_{p,i} \right]. \quad (2.24)$$

Thus, the system of equations are closed and can be solved to obtain the gas and particle phase flow-fields.

2.5 Lagrangian tracking

Compared to the strategy of treating dispersed phase using Eulerian approach, several researchers prefer Lagrangian particle tracking. Lagrangian approach, especially in complex flows ubiquitous in spray combustion, offers unique advantages such as the ability to model accurate particle dispersion, mixing, breakup and range of particle sizes. From an implementation perspective, Lagrangian particle tracking can be achieved mainly by two MPI communication strategies, i.e., point-to-point and gather-scatter. In the gather-scatter strategy, the communication is based on a master-slave approach. The dispersed phase data is gathered in the master at each time step to facilitate the master in performing the majority of the book-keeping operations. In order to hold this data, a global array of size equal to the number of parcels/particles is allocated in each processor and the updated information is communicated to all the processors at each time step. Since the book-keeping and communication are not dependent on the number of processors used, this strategy provides only marginal increase in speedup of about 20% with increase in number of cores. However, time to compute particle/parcel parameters can still scale linearly as it is dependent on particles/parcels per each processor. The main advantage of the gather-scatter strategy is the ease of book-keeping which strictly ensures the presence of all the required particles (mass conservation) at each time step. However, since the data is allocated for all particles in each processor, the total number of particles handled is severely restricted based on the memory limitations of a given processor cluster. Although, this limitation can be relaxed in the point-to-point approach, in most spray calculations, the number of particles (droplets) present from injection to evaporation/combustion is limited. Thus, gather-scatter approach can provide reliable results with minimum implementation effort in these cases.

The point-to-point strategy involves communication of only the particles in the ghost cells to the adjacent neighbor. The particle data is allocated per each processor and so the total number of particles handled can scale linearly with the number of processors used. This is very advantageous in cases that have inevitably large number of particles. However, the implementation of the book-keeping is not trivial and is time consuming. At each time step, declaration of the intent to communicate, evaluation of the size of message to be communicated and actual communication of the message are to be performed which add extra latency. However, the communication cost is relatively small in comparison to the gather-scatter approach. The over-all performance and the memory management in the point-to-point strategy is expected to be superior. Both the gather-scatter and the point-to-point strategies suffer from load-balancing issues. If the particles are concentrated in a particular group of processors the computational time may not scale favorably. This problem can be over come by adapting the processor distribution based on the particle concentration. However, care is needed as the gas-phase properties are needed to update the particle properties and adapting the processors should be accompanied by appropriate interpolation techniques necessary for two-way coupling.

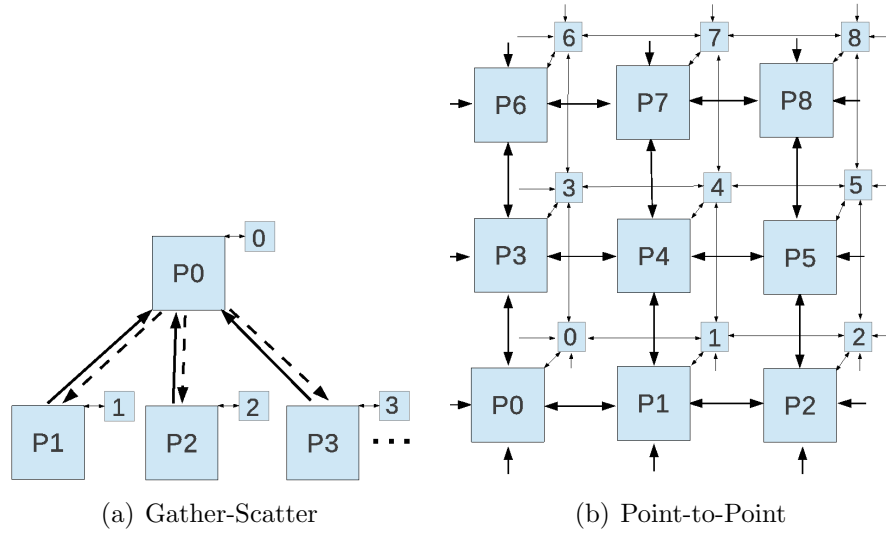


Figure 2.1: Schematic of (a) gather-scatter and (b) point-to-point communication strategies for Lagrangian particle tracking. The boxes with P1 to P8 indicate the grid of processors performing computation for particles. A small box corresponding to each processor is shown to indicate the two-way coupling between the gas-phase and the dispersed-phase. The double sided arrow indicates two-way communication between the processors. The gathering operation is indicated with single arrow and scattering operation is indicated using single dashed arrow. P0 performs all the book-keeping operations and updates the full particle data array at each time step in Gather-Scatter approach. Note that there can be communication between corner neighbors (P4-P0, P4-P2, P4-P6 and P4-P8) in point-to-point method which is not illustrated.

CHAPTER III

ACCOMPLISHMENTS

The results from the research performed under the current project have been presented in several conferences and have also been published in archived journals. In this chapter, these published results are summarized. The full results and the analysis are available in articles attached to this report.

3.1 Detonation in gas-particle mixtures

Propagation of detonations in reactive gaseous mixtures is self-sustained by the formation of the transverse waves and the triple points due to the interaction of the shock waves (Mach stem and Incident shock) at the detonation front. The effect of inert particles in this self-sustained propagation is examined and different regime of propagation are described. The detonation interacts with a particle cloud based on the initial particle cloud volume fraction (α_{p_0}) and the initial particle cloud length ($L_0/L_{1/2}$). Three regimes of detonation propagation are identified which correspond to sustained propagation, detonation suppression and detonation quenching, respectively. The details of each regime and the analysis are provided in the paper [2] provided in the appendix.

3.2 DDT in gas-particle mixtures

Acceleration of a flame ignited at the closed end of a channel and the subsequent transition to a detonation is investigated in channels of different lengths and widths. Also, the channels filled with obstacles placed at regular intervals are considered. The effect of particles on the flame acceleration and the detonation formation is investigated by allowing the flame to propagate through particle clouds. In pure gaseous mixtures, the transition to detonation occurs mostly due to the shock reflections from the channel wall and the obstacles. In gas-particle mixtures, the shock wave attenuation and the flame acceleration due to the mixing induced by the particles results in the flame-shock coupling and the generation of the detonation. The time and the distance to DDT along with the flame position are quantified for different cases and compared with experimental results, if available. The detailed analysis of the effect of inert particles [10, 13], channel dimensions [11], and the reactive particles [12] are provided in the papers listed and attached in Appendix A.

3.3 Influence of particles on RMI

The mixing in the post-detonation flow is characterized by the generation of hydrodynamic instabilities. The earlier stages of mixing are dominated by the Rayleigh-Taylor instability. After the implosion, due to the secondary shock wave, the mixing and the dispersion are characterized by the RMI. To investigate the effects of particles on the RMI, cases with the classical planar shock tube configuration are considered. The simulations are initially performed in pure gaseous mixtures and compared with the experimental observations. The role of particles on the vorticity generation is quantified and the variations in the mixing zone length for different initial particle volume fractions is analyzed. The details of this analysis are provided in Appendix A in the attached paper [5]

3.4 Neutralization of bacterial endospores by explosives

Bacterial spore neutralization is very challenging due to the resistance of the spores to extreme temperatures, pressures and toxic environments. Using explosives is a viable strategy for spore neutralization and is used in several threat reduction scenarios. Here, the spore neutralization by explosives is investigated by considering the interaction of spore clouds with the post-detonation flow. The spore clouds is formed from an atomized aqueous spore aerosol and is modeled based on the available experimental results [21]. The spore neutralization in post-shock and post-detonation flow is quantified by the critical spore temperature required for neutralization. The analysis of the initial distance from the charge required for optimal mixing and neutralization is provided in the attached paper (listed in the appendix) [15].

3.5 Quantification of Uncertainties in Modeling and Numerical Approach

The intention of using explosive charges for spore neutralization is to leverage the extreme thermal and mechanical stresses resulting from the blast wave and post-detonation flow for effective kill. However, given the complexity of the problem and the large number of unknowns, determining the effectiveness of such a method in any given situation is difficult. To mitigate this risk, an assessment of the probability for endospore survival is critical. For computational studies, this requirement translates into the necessity of using uncertainty quantification (UQ) strategies to determine the range of conditions required for endospore neutralization within a given confidence level. Thus, the goal of the work discussed below is to propose a UQ strategy for two-phase flows and use it to quantify the accuracy of numerical simulations of recent experiments on endospore neutralization.

Generally speaking the motivation for quantifying predictive error is essential to all engineering design since a large degree of variability is inherent in the uncertainties of various modeling assumptions, initial conditions, boundary conditions, etc., all of

which can never be fully characterized mathematically by the numerical scheme. As a result methods of uncertainty quantification (UQ) attempt to formalize the understanding of how errors propagate and affect the model's accuracy using classical statistical theory. This approach adopts a Bayesian view of probability by differentiating the various types and sources of uncertainty in the model and then assessing the uncertainty of the numerical prediction using a probability bounds analysis. Therefore, the starting point for this methodology begins with the identification of all sources of uncertainty and the characterization of those uncertainties as either aleatory or epistemic. Aleatory uncertainty is statistical uncertainty meaning that the uncertainty is inherent in the randomness of the system such that it can be described by a probability distribution function (PDF). This type of uncertainty is irreducible. Epistemic uncertainty is uncertainty resulting from a lack of knowledge of the system, sometimes referred to as systematic or bias uncertainty. Values with epistemic uncertainty are represented by interval-valued quantities with no associated likelihood of occurrence. This type of uncertainty can in theory be eliminated with sufficient knowledge, however, this is typically not feasible for all values in consideration.

Furthermore, uncertainties stem from three main sources: numerical approximations, model formulation and model inputs. The first two sources of uncertainty are typically characterized through a verification and validation (V&V) process, while the uncertainties in model inputs are evaluated using one of the many available UQ procedures. For a comprehensive measure of uncertainty on the system response, all three sources need to be quantified. Each pose their own difficulties and have their own constraints given the system in consideration. In the current work, the focus is on ascertaining the uncertainties resulting from model input and model form. Numerical approximation uncertainty occurs because of errors in discretization, numerical convergence, precision and algorithmic implementation and is characterized through code verification which has been discussed in previous section.

Model form uncertainties are those incurred from the approximations, abstractions and mathematical formulas used in the model and are characterized through a code *validation* process. The purpose of which is to assess how well the numerical results compare to experimental measurements of a relevant system. This statistically quantifiable disagreement must, in many situations, be extrapolated from the regions where the experimental data is available to a region where no data is available, but where the region of interest exists using linear regression. Treated in this way, model form error is an epistemic uncertainty. Typically this is one of the more difficult types of uncertainties to quantify and often requires the tailoring of experiments to the numerical validation process. In the lack of available experimental data, model form uncertainty can be characterized through comparison to other simulations or to theoretical predictions. Once the model input uncertainties are known and quantified as epistemic or aleatory, they are propagated through the model. There are many UQ methods for propagating uncertainty through a deterministic system. The simplest approach is to use Monte Carlo (MC) sampling, however, this approach suffers from requiring a large number of samples for statistical convergence. While this constraint can be alleviated using Latin hypercube sampling (LHS) or Markov Chain Monte Carlo (MCMC) sampling, any sampling method is typically limited since the

computational expense is often too prohibitive for conducting many large-scale, complex simulations. However, this approach still remains the easiest to implement since it is independent of the mathematical description of the system. Moreover, when combined with response surface techniques to develop a surrogate model, the computational expense can be significantly reduced.

In the current work, model form and model input uncertainties in two-phase flows are discussed. The available experimental data offers insight into the parameters of importance in spore neutralization and provides a point of references for model validation. With this knowledge identification of the model input uncertainties is possible. The mathematical definition of these input uncertainties are then propagated through the model using LHS. This is possible, since the computational cost is not large for the simulation in question.

3.5.1 Model Form Uncertainty

In this work, the primary focus is on the validation and quantification of uncertainty associated with the multi-phase coupling terms and the aerosol neutralization model. Three main sources of uncertainty are identified: the neglected higher order terms in the dispersion equations, the dispersed-phase closure models and the simplifications made in the spore neutralization model.

First, several terms in the dispersed phase equation have been neglected in order to simplify the formulation. From a simple sensitivity analysis, however, these terms, are negligible for the range of conditions considered in applications of bacterial endospore neutralization. This is inherent in the relatively small size and mass of all bacterial endospores. As a result any model form incurred from this assumption is neglected. More importantly, the dispersed phase governing equations are closed using expressions for the drag coefficient and theoretical justifications for the heat and mass transfer rates. The uncertainties in the drag model used in this study are quantified by simulating the experiment [21], already described, used to derive the empirical relationship.

3.5.2 Model Input Uncertainty

Model input uncertainty includes values such as those used to describe the initial/boundary conditions, external source terms or any other parameter used in the various physical models comprising the numerical simulation. These uncertainties can be aleatory, epistemic or mixed. From previous experimental and theoretical studies as well as numerical sensitivity studies conducted in this work several unknowns are identified. These include but not limited to the following parameters:

1. aerosol droplet size distribution, $r_p(\chi)$
2. aerosol specific heat capacity, c_p
3. critical temperature, T_c
4. radius of the endospore, r_s

5. initial concentration χ_s^0
6. location and volume concentration of the aerosol in the simulation domain,
7. evaporation mass transfer rate, \dot{m}_p ,
8. post-shock temperature, T_5
9. residence time, t_r , at which the aerosol is exposed to the elevated temperatures

Based on sensitivity analysis, the parameters specifying the droplet size distribution (μ_χ, σ_χ) are initially shown to impact the intact endospore percentage the most. If these two parameters are treated as epistemic uncertainties, they can be defined as having an equal probability of occurrence between the ranges [4.5, 5.5] and [0.4, 0.6]. By performing a LHS with a sample size of 250, the 95% confidence levels are computed on the mean intact spore percentage for each post-shock temperature considered in the experiment of Gates et al. These calculations are performed by coupling the hydrocode, LESLIE, with large-scale engineering optimization and uncertainty analysis code, DAKOTA, provided by Sandia National Laboratories. The coupled UQ analysis routines enable numerous simulations to be performed simultaneously. The statistics from the output are also efficiently computed by the combined solver, reducing the time and effort needed to perform UQ over large input parametric space.

In Fig. 3.1, the mean values of the intact spore percentages obtained for each T_5 over the entire set of 250 simulations with error bars are shown. The horizontal error bar indicates the variation in T_5 and the vertical error bar the variation in the intact spore percentages. To understand the disagreement between the experimental results and the mean values predicted by the UQ analysis, the number of events of occurrences of a specific intact spore percentage is shown in Fig. 3.2. In case of $T_5 \approx 1100.0K$, i.e. $M = 2.1$, intact spore percentage is nearly zero in 120 samples out of 250 simulations. Rest of the samples skew the result to higher ($\approx 20\%$) mean value. To avoid this skewness the sample space should be increased. This will be addressed in future reports and the analysis with sample space sizes greater than 250 (≈ 1000) are currently underway. However, the capabilities presented here provide sufficient proof of novel ability to assess UQ in AD problems of interest.

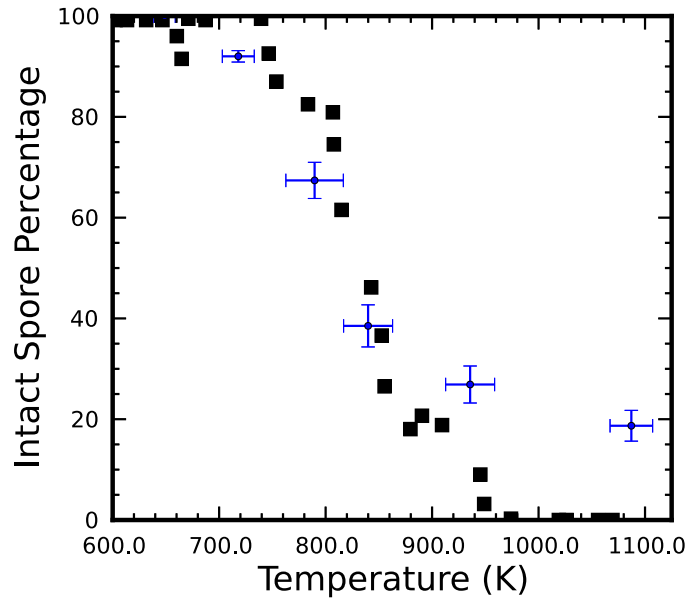


Figure 3.1: Variation of mean value of intact spore percentages for different post-shock temperatures. The vertical error bars indicate the error extremes with 95% confidence and horizontal error bars indicate variation of post-shock temperature. Experimental results are indicated by black squares.

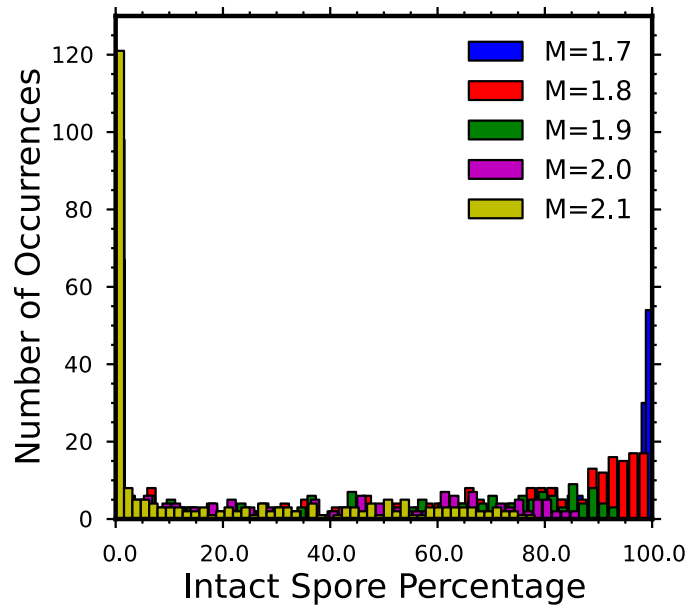


Figure 3.2: Number of occurrences of each intact spore percentage for different shock Mach numbers.

CHAPTER IV

OPPORTUNITIES FOR TRAINING AND PROFESSIONAL DEVELOPMENT

This research project has supported two doctoral candidates. The work performed as a part of this effort has been presented at several conferences and has been published in several peer reviewed articles.

CHAPTER V

DISSEMINATION OF RESULTS TO COMMUNITIES OF INTEREST

Interaction with multiple research organizations, working on AD problem, has been made possible by the current work. The following have been major collaborations and transitions

1. Source codes developed and/or validated are already being used in Eglin AFB for 6.3 type related classified research.
2. The code has been delivered (July, 2011) to LLNL (Dr. Salari and Dr. Najjar) for blast wave impact studies.
3. Post-detonation flow in a full scale room problem has been validated and spore neutralization studies in this configuration are being carried out in collaboration with CRAFT tech.

Further, the results obtained under this effort have been published in archived journals. These articles are

- K. C. Gottiparthi and S. Menon, “Study of deflagration-to-detonation transition in gas-particle mixtures,” AIAA-2011-0801, 2011.
- K. C. Gottiparthi and S. Menon, “Simulations of heterogeneous detonations and post-detonation turbulent mixing and afterburning,” AIP Conference Proceedings, 1426, 1639-1642, 2012.
- K. C. Gottiparthi, K. C. and S. Menon, “A study of interaction of clouds of inert particles with detonation in gases,” Combustion Science and Technology, 184(3), 406-433, 2012.
- K. C. Gottiparthi and S. Menon, “Multi-scale simulation of deflagration-to-detonation transition in turbulent dense two-phase reactive mixtures,” 2012 High Performance Computer Modernization Program Contributions to DoD Mission Success, 209-218, 2012.
- J. C. Schulz, K. C. Gottiparthi and S. Menon, “Richtmyer-Meshkov instability in dilute gas-particle mixtures with re-shock,” Physics of Fluids, 25, 114105, 2013.
- K. C. Gottiparthi, J. C. Schulz and S. Menon, “Multi-scale simulation of deflagration-to-detonation transition in turbulent dense two-phase reactive mixtures,” 2013 High Performance Computer Modernization Program Contributions to DoD Mission Success, 2013.

- K. C. Gottiparthi and S. Menon, “Flame acceleration and transition to detonation in gas-particle mixtures,” Proceedings of the European Combustion Meeting, 2013.
- K. C. Gottiparthi and S. Menon, “Multi-scale simulation of deflagration-to-detonation transition in turbulent dense two-phase reactive mixtures,” 2014 High Performance Computer Modernization Program Contributions to DoD Mission Success, 2014.
- K. C. Gottiparthi, J. C. Schulz and S. Menon, “On the neutralization of bacterial spores in post-detonation flows,” Shock Waves, 24, 455-466, 2014.
- E. Fedina, K. C. Gottiparthi, C. Fureby and S. Menon, “Combustion in after-burning behind explosive blasts,” 6th European Conference on Computational Fluid Dynamics, 2014.
- K. C. Gottiparthi and S. Menon, “Turbulent Mixing and Afterburn in Post-Detonation Flow with Dense Particle Clouds” 19th Biennial Conference of the APS Topical Group on Shock Compression of Condensed Matter, 60, 8, 2015.

APPENDIX A

LIST OF PAPERS

The following is the list of papers (in the order they are attached) appended to this report which contain the detailed analysis of the results obtained from the current work:

1. K. C. Gottiparthi, K. C. and S. Menon, "A study of interaction of clouds of inert particles with detonation in gases," *Combustion Science and Technology*, 184(3), 406-433, 2012.
2. K. C. Gottiparthi and S. Menon, "Study of deflagration-to-detonation transition in gas-particle mixtures," *AIAA-2011-0801*, 2011.
3. K. C. Gottiparthi and S. Menon, "Flame acceleration and transition to detonation in gas-particle mixtures," *Proceedings of the European Combustion Meeting*, 2013.
4. K. C. Gottiparthi, J. C. Schulz and S. Menon, "Multi-scale simulation of deflagration-to-detonation transition in turbulent dense two-phase reactive mixtures," *2013 High Performance Computer Modernization Program Contributions to DoD Mission Success*, 2013.
5. K. C. Gottiparthi and S. Menon, "Multi-scale simulation of deflagration-to-detonation transition in turbulent dense two-phase reactive mixtures," *2014 High Performance Computer Modernization Program Contributions to DoD Mission Success*, 2014.
6. J. C. Schulz, K. C. Gottiparthi and S. Menon, "Richtmyer-Meshkov instability in dilute gas-particle mixtures with re-shock," *Physics of Fluids*, 25, 114105, 2013.
7. K. C. Gottiparthi and S. Menon, "Simulations of heterogeneous detonations and post-detonation turbulent mixing and afterburning," *AIP Conference Proceedings*, 1426, 1639-1642, 2012.
8. K. C. Gottiparthi, J. C. Schulz and S. Menon, "On the neutralization of bacterial spores in post-detonation flows," *Shock Waves*, 24, 455-466, 2014.

This article was downloaded by: [Suresh Menon]

On: 19 February 2012, At: 19:44

Publisher: Taylor & Francis

Informa Ltd Registered in England and Wales Registered Number: 1072954 Registered

office: Mortimer House, 37-41 Mortimer Street, London W1T 3JH, UK



Combustion Science and Technology

Publication details, including instructions for authors and subscription information:

<http://www.tandfonline.com/loi/gcst20>

A Study of Interaction of Clouds of Inert Particles with Detonation in Gases

K. C. Gottiparthi ^a & S. Menon ^a

^a School of Aerospace Engineering, Georgia Institute of Technology, Atlanta, Georgia, USA

Available online: 17 Feb 2012

To cite this article: K. C. Gottiparthi & S. Menon (2012): A Study of Interaction of Clouds of Inert Particles with Detonation in Gases, Combustion Science and Technology, 184:3, 406-433

To link to this article: <http://dx.doi.org/10.1080/00102202.2011.641627>

PLEASE SCROLL DOWN FOR ARTICLE

Full terms and conditions of use: <http://www.tandfonline.com/page/terms-and-conditions>

This article may be used for research, teaching, and private study purposes. Any substantial or systematic reproduction, redistribution, reselling, loan, sub-licensing, systematic supply, or distribution in any form to anyone is expressly forbidden.

The publisher does not give any warranty express or implied or make any representation that the contents will be complete or accurate or up to date. The accuracy of any instructions, formulae, and drug doses should be independently verified with primary sources. The publisher shall not be liable for any loss, actions, claims, proceedings, demand, or costs or damages whatsoever or howsoever caused arising directly or indirectly in connection with or arising out of the use of this material.

A STUDY OF INTERACTION OF CLOUDS OF INERT PARTICLES WITH DETONATION IN GASES

K. C. Gottiparthi and S. Menon

School of Aerospace Engineering, Georgia Institute of Technology, Atlanta, Georgia, USA

Interaction of a cloud of inert particles with a detonation in gaseous mixture is simulated and studied. The structure of both two- and three-dimensional detonations are modeled using a simplified chemical model with Arrhenius kinetics. Particle clouds are characterized based on the initial solid phase volume fraction (α_{p_0}) of the particle cloud and the initial cloud length (L_0). The results show that the minimum average detonation speed decreases with increase in α_{p_0} at fixed L_0 , and with an increase in L_0 at fixed α_{p_0} . The detonation propagation through inert particle clouds is observed to fall into three regimes based on α_{p_0} and L_0 . In the first regime, the detonation speed is suppressed, but the reaction zone and leading shock remain coupled, and the triple points are nearly unaffected. In the second regime, the detonation is temporarily quenched but restored as the particle cloud moves away from the detonation front. In the third regime, the detonation is quenched permanently or at least does not get restored within the time available for the detonation propagation. It is also shown that the effects of inert particle clouds on the detonation front in three-dimensional studies are qualitatively similar to the results from two dimensional simulations. However, in post-detonation flow where transverse velocity components are important, simulations in three dimensions are necessary, especially to estimate particle dispersion.

Keywords: Dense flow; Detonation; Inert particles; Quenching; Solid phase

1. INTRODUCTION

Many investigations over the past years have studied detonations to understand and address safety issues, as well as to explore possible applications for propulsion systems such as pulse detonation engines. Most of these earlier investigations focused on detonations in pure gaseous phase reactant mixtures (Shepherd, 2009), and provided an improved understanding of several important phenomena that effect the propagation and the stability of these detonations (Hanana et al., 2001; Lee and Stewart, 1990; Williams et al., 1996). In contrast, very few investigations have focused on the effect of presence of particles, either solid or liquid, on detonations (Carvel et al., 2003; Chen et al., 2006; Ju and Law, 2002). Detonations in two-phase mixtures involve additional phenomena due to the interaction between the two phases, and are important because past results have suggested that the

Received 23 February 2011; revised 25 October 2011; accepted 14 November 2011.

Address correspondence to S. Menon, School of Aerospace Engineering, Georgia Institute of Technology, Atlanta, GA 30332-0150, USA. E-mail: suresh.menon@aerospace.gatech.edu

addition of inert particles to a gas can prevent the propagation of detonations through it (Laffitte and Bouchet, 1959). This phenomenon has several potential applications, such as the enhancement of safety in industrial systems and mines, and the development of effective weapon systems. However, in order to control or quench detonations by adding inert additives, understanding the effect of parameters such as the mass of inert particles in the gas-particle mixture is vital, as they impact the detonation characteristics (Papalexandris, 2004).

Based on the physical nature of different phases, their distribution in the mixture, and their chemical properties, the heterogeneous media can be categorized into different categories. Detonations in mixtures containing fine solid particles with an oxidizer in gaseous phase are classified into three types (Veyssiére, 2006). Detonations involving inert particles with the fuel entirely in gaseous phase are dusty detonations, and those involving gaseous fuel with reactive particles are denoted hybrid detonations. If the fuel is contained entirely in the solid particles, then the detonation is considered a heterogeneous detonation. In this article, the effect of inert particles on detonation propagation in a gaseous fuel-oxidizer mixture is investigated, i.e., only dusty detonations are considered.

Several experimental studies on dusty detonations are available in the literature. In some experiments, suppression or quenching of detonations with inert particle addition was observed (Chen et al., 2006). In fact, many industrial systems exist where deflagrations are suppressed using powdered inhibitors (Nettleton, 1987). However, there are differences in the suppression process of deflagrations and detonations. In a deflagration, the gas velocity is subsonic with respect to the wave front. Hence, the particles would effect the reaction-zone propagation velocity, even if they were injected behind the leading front of the wave. However, detonation suppression occurs when the particles are injected before the leading wave front. Deflagrations can also be suppressed by a priori introduction of inert particles from the channel walls, through which the deflagration wave propagates. In this approach, the dust cloud formed by entrainment of the particles by the gas facilitates the suppression. On the other hand, it is not possible to suppress detonations using this approach, as the mixture moves between the leading wave front and the Chapman-Jouguet (CJ) surface in a substantially shorter time than the time required for particle entrainment and mixing (Krasnyansky, 2006).

Past experiments demonstrated detonation suppression by injecting and mixing particles with the gas before initiating the detonation (Chen and Fan, 2005). However, in real applications, premixing the reactant mixture and inert particles perfectly before the detonation wave reaches the mixture is not possible. Variation in local concentration of particles ahead of the detonation wave can have a multidimensional effect, and this particular issue is of considerable interest, although not much has been done so far (Fomin and Chen, 2009). In this article, we address this particular situation and carry out both two dimensional (2D) and three dimensional (3D) studies by injecting a cloud of solid particles before the detonation front.

The experimental studies on the detonations with inert particles have investigated the effects of varying number of particles, volume density of the dust cloud, particle size, and particle material density on detonation suppression (Chen et al., 2006; Laffitte and Bouchet, 1959), and on the changes in the detonation velocity (Kauffmann et al., 1984). These investigations showed that the suppression of

detonation is effective with increase in concentration of solid phase and decrease in the particle size and density. However, detailed measurements of minimum spatial size of the dust cloud and total mass loading of the particles needed for effective suppression of the detonations are still not available.

Numerical investigations have been even fewer for detonations in gases with chemically inert particles. Some studies have addressed the influence of particle size and concentration on suppression and detonation parameters (Chen et al., 2006; Ju and Law, 2002). The effect of the particle material density on the quenching of the detonation was also considered earlier (Chen et al., 2006). Fomin and Chen (2009) calculated the minimum mass of particles and the characteristic size of the particle cloud necessary for suppression of dusty detonations involving Al_2O_3 , SiO_2 and W particles. Suppression of detonation in a $\text{H}_2 - \text{O}_2$ mixture by sand particles was reported by Fedorov et al. (2010). Their study shows that the detonation velocity decreases by 60% with increase in mass fraction of particles to nearly 90%, leading to detonation failure. However, the modeling was one dimensional (1D) in these cases. Some 2D studies have been reported earlier as well (Kutushev and Pichugin, 1993; Loth et al., 1997; Papalexandris, 2004, 2005). In the study by Loth et al. (1997), a two-step induction mechanism to model the chemical reactions in a dilute stoichiometric $\text{H}_2 - \text{O}_2$ system was employed. But this study neglected the volume occupied by the particles, and hence is valid only for very dilute mixtures. Papalexandris (2004, 2005) investigated the effect on volume fraction and particle size on the detonation velocity and detonation quenching. He used a Eulerian–Eulerian formulation to model the two – phase flow and studied the detonation structure as it propagates through a continuous stream of uniformly distributed solid particles. Here, both inert and reactive particles were considered. These studies indicate that the efficiency of wave quenching by chemically inert particles is enhanced by the increase in condensed phase volume fraction (α_p) and decrease in particle size. Again, only dilute mixtures were considered.

To the authors' knowledge, there are no reported studies of detonations in gases with chemically inert particles in 3D. Several past studies showed that the detonation propagation involves formation and interaction of triple-point lines along the detonation front, which generate complex flow field downstream of the front with interacting vortices (Dou et al., 2008; Williams et al., 1996). However, earlier investigations suggest that the primary direction of momentum exchange between particles and gas is along the direction of detonation propagation, and thus the 1D or the 2D calculations provided resonable estimation of detonation propagation through gas-particle mixtures (Papalexandris, 2005). But the particle dispersion can vary significantly in 3D and is discussed in this article. Also, the effect of volume fraction (dilute to dense) has not been systematically studied or reported in open literature. The present article therefore addresses these particular issues and compares both 2D and 3D results.

Studies of detonations in pure gaseous mixtures suggest that the occurrence of the transverse waves and triple points along the detonation front is vital to sustain detonation along the whole front (Dou et al., 2008; Sharpe, 2001). Thus, one of the mechanisms of detonation suppression by inert particles would be to suppress transverse waves, resulting in reduction of detonation velocity as reported (Papalexandris, 2004). None of the past studies, however, studied the influence of the initial particle

cloud length necessary, considering both dilute and dense gas-particle mixtures, to achieve the detonation suppression, and we also address this in the current article. Finally, previous results (Papalexandris, 2005) indicate that a zone of compaction is formed after the particles cross the detonation front. Thus, there exists a maximum initial condensed phase volume fraction for which the flow remains dilute everywhere, even after the compaction occurs. Therefore, we study both dilute and dense gas-particle flows in this paper. Lagrangian tracking can accurately evaluate the particle trajectories in dilute and marginally dense flows, especially when particles are not distributed throughout the flow. Hence, an Eulerian–Lagrangian formulation (Balakrishnan et al., 2010b) is used in to solve for the gas and the solid phase.

This paper is organized as follows. First, the two-phase model and the assumptions employed are described in Section 2. Next in Section 3, the effect of varying the initial length of the inert particle clouds and initial solid phase volume fraction on the structure and the suppression of the detonation are analyzed and discussed. This section also includes comparisons with available past numerical studies. This is followed by 3D results in Section 4, which are compared with the corresponding 2D results. Finally, conclusions and future directions are discussed in the last section.

2. FORMULATION AND NUMERICAL SETUP

The compressible unsteady Euler equations for reacting gas flow used here, following past studies (Balakrishnan et al., 2010b; Papalexandris, 2004), are as follows:

$$\begin{aligned} \frac{\partial}{\partial t} \begin{bmatrix} \alpha_g \rho_g \\ \alpha_g \rho_g u_{g,i} \\ \alpha_g \rho_g E_g \\ \alpha_g \rho_g Y_g \end{bmatrix} + \frac{\partial}{\partial x_j} \begin{bmatrix} \alpha_g \rho_g u_{g,j} \\ \alpha_g \rho_g u_{g,i} u_{g,j} + \alpha_g p_g \delta_{ij} \\ \alpha_g (\rho_g E_g + p_g) u_{g,j} \\ \alpha_g \rho_g Y_g u_{g,j} \end{bmatrix} \\ = \begin{bmatrix} 0 \\ p^* \frac{\partial \alpha_g}{\partial x_j} \delta_{ij} \\ p^* u_j^* \frac{\partial \alpha_g}{\partial x_j} \\ 0 \end{bmatrix} + \begin{bmatrix} 0 \\ 0 \\ 0 \\ \dot{\omega} \end{bmatrix} + \begin{bmatrix} 0 \\ \dot{F}_{p,i} \\ \dot{Q}_p + \dot{W}_p \\ 0 \end{bmatrix} \end{aligned} \quad (1)$$

Here, α_g is the gas phase volume fraction, ρ_g is the density, p_g is the pressure, $u_{g,i}$ is the i -th component of velocity, E_g is the total energy given by the sum of the internal (e_g) and kinetic energies, $(e_g + \frac{1}{2} u_{g,i} u_{g,i})$, and Y_g is the mass fraction of the reactant. Also, p^* and u_i^* denote, respectively, the pressure and the i -th component of velocity at the interface between the two phases. The expressions for p^* and u_i^* and discussion regarding the interface closure are presented elsewhere (Balakrishnan et al., 2010b). Note that the subscripts g and p refer to gas phase and solid phase, respectively. A first-order Arrhenius kinetics in ethylene–oxygen mixtures used in earlier studies (Khokhlov et al., 2004) is also used here and is given as

$$\dot{\omega} = -A \rho_g Y_g \exp\left(-\frac{Ea}{RT_g}\right) \quad (2)$$

where Ea , T_g , and R are, respectively, the activation energy, the gas temperature, and the gas constant, and A is the pre-exponential factor adjusted to $44.325/t_0$ to match the cell size observed in experiments and previous numerical results (Gottiparthi et al., 2009) for ethylene-oxygen mixtures. In this article, $L_{1/2}$ is used to nondimensionalize length scales, where $L_{1/2}$ is the distance between the detonation front and the location downstream of the detonation front, in the direction perpendicular to the detonation front, where half of the unburned mixture has reacted. Also, $t_0 = L_{1/2}/\sqrt{RT_0}$ is used to nondimensionalize time scales. Here, T_0 is the initial temperature of the unburned mixture.

Lagrangian tracking is used to compute the particle position vector ($x_{p,i}$) and velocity vector ($u_{p,i}$). Since there could be a very large number of particles to track, the concept of parcel, which is a group of particles, is employed (Snider, 2001). All particles present in a parcel are considered to have the same position, velocity vectors, and temperature. The number of particles assigned to each parcel and the number of parcels chosen is determined based primarily on the desired volume fraction/mass loading and numerical accuracy. Considering no interphase mass transfer, which is valid for inert particles, the equations for the solid phase are (Balakrishnan and Menon, 2010; Maxey and Riley, 1983) as follows:

$$\frac{dx_{p,i}}{dt} = u_{p,i} \quad (3)$$

$$m_p \frac{du_{p,i}}{dt} = \frac{\pi}{2} r_p^2 C_D \rho_g |u_{g,i} - u_{p,i}| (u_{g,i} - u_{p,i}) - \frac{4}{3} \pi r_p^3 \frac{\partial p_g}{\partial x_i} + m_p A_{c,i} \quad (4)$$

$$m_p C_p \frac{dT_p}{dt} = 2\pi r_p \kappa_g N u (T_g - T_p) \quad (5)$$

where m_p is the particle mass, r_p is the particle radius, $A_{c,i}$ is the i-component of net acceleration/deceleration on a particle due to interparticle collisions (Patankar and Joseph, 2001; Snider, 2001), T_p is the particle temperature, C_p is the specific heat of solid particle, and κ_g is the thermal conductivity of gas phase. In dense gas-particle flows, the collisions between particles are significant, and the force on a particle due to the collisions with other particles, called the interparticle collision force, cannot be neglected (Zhang, 2009). Also, strong pressure gradients in the flow, primarily due to shocks, influence the particle acceleration. Hence, along with the drag, the pressure gradient and the interparticle collision forces are considered in this article. The lift, inertial force of virtual mass, Basset force, and buoyancy for the cases considered in the current study are small in comparison to the other terms, and hence are not considered here (Papalexandris, 2004). Also, note that, due to the shear in interparticle collision/contact, energy dissipation can occur due to inelastic collisions (Crowe et al., 1998). However, following past studies (Balakrishnan et al., 2010b), in the current article, the dominant heat transfer mechanism between the two phases is assumed to be convection. The particle mass m_p is obtained as $4/3\pi r_p^3 \rho_p$, where ρ_p is the solid particle material density. Based on the number of parcels in each Eulerian finite-volume cell, the solid phase volume fraction is

$$\alpha_p = \frac{1}{Vol} \sum_{n=1}^N n_{p,n} \frac{4}{3} \pi r_{p,n}^3 \quad (6)$$

and $\alpha_g = 1 - \alpha_p$. Here, Vol is the volume of the computational cell, N is the total number of parcels in a finite volume cell, and n_p is the number of particles per parcel. In the above equations, C_D represents the drag coefficient. The expression for C_D , validated by comparisons with experiments for shock-particle and detonation-particle interactions (Balakrishnan et al., 2010b; Boiko et al., 1997; Fedorov et al., 2010), is

$$C_D = \left[0.38 + \frac{24}{Re} + \frac{4}{Re^{0.5}} \right] \left[1 + \exp\left(\frac{-0.43}{M_{pg}^{4.67}}\right) \right] \quad (7)$$

where $Re = 2\rho_g r_p |u_{g,i} - u_{p,i}| / \mu$ and $M_{pg} = |u_{g,i} - u_{p,i}| \sqrt{\rho_g} / \sqrt{\gamma p_g}$ denote Reynolds number and Mach number based on the relative velocity between gas and the particle, respectively. γ is the ratio of the specific heats of the gas. As the gas mixture ($C_2H_4 + 3O_2 + 11.2Ar$) consists mostly of argon, for the purpose of the present study, the viscosity of the mixture is assumed to be same as viscosity of argon. The viscosity is computed based on Sutherland's law as

$$\mu = \mu_{ref} \left(\frac{T_g}{T_{ref}} \right)^{3/2} \frac{T_{ref} + S}{T_g + S} \quad (8)$$

Here, for argon, μ_{ref} , T_{ref} , and S are taken to be $1.025P_0 t_0 L_{1/2}$, $0.93T_0$, and $0.49T_0$, respectively (White, 2006). Here, P_0 is the initial pressure of the unburned mixture. The Nusselt number as a function of Re and Prandtl number (Pr) is expressed as $Nu = 2.0 + 0.459Pr^{0.33}Re^{0.55}$ (Drake, 1961).

The inter-particle collision force, which is a result of constant collision/contact between particles, is computed based on Snider's collision model that has been used in other studies as well and validated (Snider, 2001). The particle acceleration/deceleration due to the inter-particle collision is obtained as a gradient of interparticle stress (τ) and is given by

$$A_{c,i} = -\frac{1}{\alpha_p \rho_p} \frac{\partial \tau}{\partial x_i} \quad (9)$$

where $\tau = P_s \alpha_p^\beta / (\alpha_{cs} - \alpha_p)$. Here, P_s (units of pressure) and β are model coefficients, and α_{cs} is the solid volume fraction at close packing. In the current study, P_s , β , and α_{cs} are taken to be $49.35P_0$, 3.0, and 0.9, respectively, based on past studies (Balakrishnan et al., 2010b). Finally, the interphase coupling terms [in Equation (1)] obtained by averaging overall particles/parcels in a computational cell are

$$\begin{aligned} \dot{F}_{p,i} = & \frac{1}{Vol} \sum_{n=1}^N n_{p,n} \left[\frac{4}{3} \pi r_{p,n}^3 \frac{\partial p_{g,n}}{\partial x_i} \right. \\ & \left. + \frac{\pi}{2} r_{p,n}^2 C_{D,n} \rho_{g,n} |u_{p,i,n} - u_{g,i,n}| (u_{p,i,n} - u_{g,i,n}) \right] \end{aligned} \quad (10)$$

$$\dot{Q}_p = \frac{1}{Vol} \sum_{n=1}^N n_{p,n} [2\pi r_{p,n} \kappa_g Nu_n (T_{p,n} - T_{g,n})] \quad (11)$$

$$\begin{aligned} \dot{W}_p = \frac{1}{Vol} \sum_{n=1}^N n_{p,n} & \left[\frac{4}{3} \pi r_{p,n}^3 \frac{\partial p_{g,n}}{\partial x_i} u_{p,i,n} \right. \\ & \left. + \frac{\pi}{2} r_{p,n}^2 C_{D,n} \rho_{g,n} |u_{p,i,n} - u_{g,i,n}| (u_{p,i,n} - u_{g,i,n}) u_{p,i,n} \right] \end{aligned} \quad (12)$$

Note that in the above equations, as the interparticle collision force is the force due to collisions between the particles, the effects of interparticle stress on the gas phase are neglected.

The governing equations for the gas phase are solved using approximate Riemann solver with Monotone Upstream-centered Schemes for Conservative Laws (MUSCL) reconstruction and monotonized-central limiter. The Riemann solver used is a hybrid solver (Einfeldt, 1988), which employs the HLLC flux solver everywhere except in the shock capturing region, where, in the direction transverse to the shock, the HLLE Riemann solver is used. The scheme is second-order accurate in both time and space, although its spatial accuracy decreases in the region where the discontinuity is present. Detailed validation of this approach for shock-turbulence interaction (Génin and Menon, 2010) and detonations (Balakrishnan et al., 2010a) has been reported elsewhere. The governing equations for solid phase are integrated in time using a fourth-order Runge–Kutta scheme. In order to account for dense loading effects, Euler gas-phase fluxes in each cell are modified using the discrete equations method (DEM) (Abgrall and Saurel, 2003). DEM allows for the treatment of volume fraction of gas phase as a piecewise continuous variable, and the intercell interfaces are evaluated using distinctive Riemann problems. Details of the DEM approach for Eulerian–Lagrangian formulation, used in the current study, are presented elsewhere (Balakrishnan et al., 2010b).

The computational domain is a rectangular box discretized using a uniform structured grid. The grid resolution is chosen based on earlier resolution studies (Gottiparthi et al., 2009). The domain size and cell spacing (Δ) in each case are summarized in Table 1. Number of grid points used per half reaction zone length ($L_{1/2}$) is also shown. For three-dimensional simulations, the domain height and width are taken to be equal. In all cases, the radius of each particle is $3.85 \times 10^{-3} L_{1/2}$ ($2 \mu\text{m}$). We presented cases with $r_p = 5.77 \times 10^{-3} L_{1/2}$ earlier (Gottiparthi and Menon, 2010), and the results are qualitatively similar to the results presented in this article. The effects of variation of particle size are not discussed here, and we will try to address them in future.

The particles are considered to have properties (i.e., C_p and ρ_p) of steel. Table 2 lists the various cases, the number of parcels, the number of particles per parcel, initial cloud length (L_0), and the initial volume fraction of the solid phase for each case. Flows with $\alpha_p \leq 0.01$ are considered to be dilute flows (Zhang et al., 2001). An inlet velocity equal to the detonation speed (D) is imposed. At the outflow boundary, all the parameters are extrapolated from the upstream conditions. Periodic boundary conditions are imposed on all other boundaries. These boundary conditions are similar and consistent with the conditions employed in many previous studies (Dou et al., 2008; Papalexandris, 2004; Sharpe and Falle, 2000).

Table 1 Test cases for pure gaseous phase simulations

Case	Domain dimensions	Grid size	Cell spacing ($\times 10^{-3}$)	Points per $L_{1/2}$
1D1	623.0	9000	69.20	8
1D2	311.5	9000	34.60	16
1D3	155.75	9000	17.30	32
1D4	77.875	9000	8.65	64
2D1	103.85×34.62	1800×600	57.70	17
2D2	103.85×23.08	2457×546	42.30	24
2D3	103.85×34.62	3600×1200	28.85	34
2D4	103.85×34.62	7200×2400	14.425	69
3D1	34.62×11.54^2	400×150^2	86.54	12
3D2	34.62×11.54^2	750×250^2	46.15	22
3D3	34.62×11.54^2	800×300^2	43.27	24

Domain dimensions and cell spacing are normalized by $L_{1/2}$

Table 2 Parameters for cases with particle clouds

Case	Dimension	Initial volume fraction of solid phase (α_{p_0})	Initial cloud length ($L_0/L_{1/2}$)	Number of parcels	Number of particles per parcel
$L_{1/8}V_{1/4}$	2D	0.0025	0.125	1286	1
$L_{1/8}V_{1/2}$	2D	0.0050	0.125	2561	1
$L_{1/8}V_1$	2D	0.0100	0.125	5121	1
$L_{1/8}V_2$	2D	0.0200	0.125	10242	1
$L_{1/8}V_4$	2D	0.0400	0.125	20484	1
$L_{1/4}V_1$	2D	0.0100	0.250	10242	1
$L_{1/2}V_1$	2D	0.0100	0.500	20484	1
L_2V_1	2D	0.0100	2.000	81936	1
L_4V_1	2D	0.0100	4.000	163872	1
L_4V_{10}	2D	0.1000	4.000	409680	4
$L_1V_{1/4}$	2D	0.0025	1.000	10242	1
$L_1V_{1/2}$	2D	0.0050	1.000	20484	1
L_1V_1	2D	0.0100	1.000	40968	1
L_1V_2	2D	0.0200	1.000	81936	1
L_1V_4	2D	0.0400	1.000	163872	1
L_1V_8	2D	0.0800	1.000	327744	1
L_1V_{10}	2D	0.1000	1.000	409680	1
$L_8V_{1/4}$	2D	0.0025	8.000	81936	1
$L_8V_{1/2}$	2D	0.0050	8.000	163872	1
L_8V_1	2D	0.0100	8.000	327744	1
L_8V_2	2D	0.0200	8.000	163872	4
L_8V_4	2D	0.0400	8.000	163872	8
$L_{16}V_1$	2D	0.0100	16.00	327744	2
$L_{32}V_1$	2D	0.0100	32.00	327744	4
$L_{64}V_1$	2D	0.0100	64.00	327744	8
$3DL_{1/8}V_{1/4}$	3D	0.0025	0.125	174580	1
$3DL_{1/8}V_{1/2}$	3D	0.0050	0.125	349160	1
$3DL_{1/8}V_1$	3D	0.0100	0.125	698320	1

3. DETONATION-PARTICLE CLOUD INTERACTION

3.1. Pure Gas-Phase Studies

Pure gaseous detonations are first investigated by choosing the controlling parameters, the overdrive factor $f = (D/D_{CJ})^2$, the activation energy Ea/RT_0 , the heat release Q/RT_0 , and the ratio of specific heats γ . Here, D_{CJ} is the Chapman–Jouget detonation speed. These parameters determine the stability of the detonation and the regularity of cellular structures produced (Bourlioux and Majda, 1992), and are set based on the properties of the gaseous mixture used in a particular case.

Previous studies, both experimental and numerical, showed that the leading shock at the detonation front is wrinkled and comprises alternate strong Mach stems and weak incident shocks (Sharpe, 2001). These strong and weak shocks are connected at triple points by transverse waves that extend back into the reaction zone. As the detonation propagates, the triple points move back and forth along the detonation front. This movement of triple point is traced to form a soot foil, which is shown in Figure 1. The current study uses maximum pressure recording to trace the triple point location, consistent with past studies. Figure 1 also shows the movement of incident shock and Mach stem shock as the detonation propagates. The cellular structures obtained for ethylene/oxygen mixtures diluted with argon are characterized to be marginally irregular (Khokhlov et al., 2004). For the current 2D study, the parameter set 2 used in 1D studies (see the Appendix) is used. The resolution and domain used for each case with this parameter set correspond to Cases 2D1, 2D2, 2D3, and 2D4 shown in Table 1.

Numerical soot foils for marginally irregular case obtained at two different resolutions are presented (see Figure 2). From Figure 2, the cell width and cell length for this case are observed to be nearly $11.54L_{1/2}$ and $19.23L_{1/2}$, respectively, which are in agreement with past studies (Khokhlov et al., 2004; Strehlow and Engel, 1968).

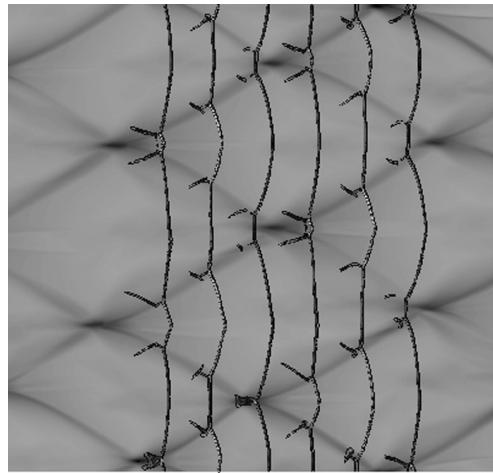


Figure 1 Formation of soot foil over one complete cell length. The detonation fronts are shown here plotting pressure gradient. The cell is observed to contain Mach stem shock in the first half of the cell and incident shock in the second half of the cell. The thick lines forming the cellular pattern in the soot foil are at the triple points.

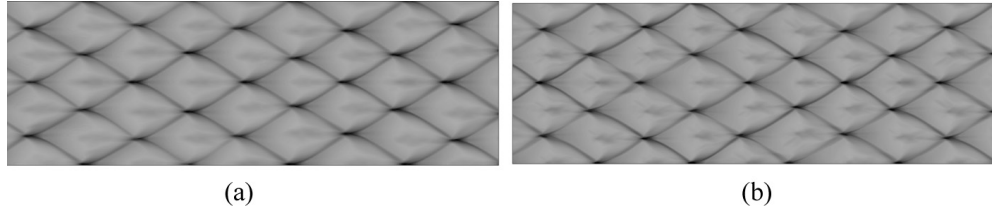


Figure 2 Numerical soot foil showing cellular structures obtained for ethylene-oxygen detonation diluted with argon. The cases presented here correspond to (a) Case 2D1 (b) Case 2D3 (Table 1).

The soot foils obtained for different resolutions, two of which are mentioned in Table 1 and shown in Figure 2, are almost identical.

3.2. Influence of Particle Clouds

When inert particles are placed in the path of a detonation, they affect the characteristic features of the detonation, such as the detonation velocity and the structure of the detonation front, due to the energy and momentum transfer (Fomin and Chen, 2009; Papalexandris, 2005). In the present study, the inert particles are arranged as a cloud and are injected into the detonation. Here, a cloud is a group of particles that spans over the entire width of the domain (and also the entire height in 3D cases) and has a specific initial length (L_0) and initial solid phase volume fraction (α_{p0}). The effects of the inert particle cloud over the detonation are studied by varying the initial parameters α_{p0} and L_0 .

3.2.1. Effect of initial solid-phase volume fraction. Clouds of fixed initial length, $L_0/L_{1/2}$, and varying α_{p0} are simulated to investigate the characteristics of particle cloud propagation and its effects on the detonation. Although we conducted several studies, as shown in Table 2, we discuss representative cases with $L_0/L_{1/2} = 1.0$ to first study the effect of α_{p0} . As the detonation front hits the particle cloud, the particle cloud gets compact due to the variation in the momentum of the particles within the cloud. This leads to an increase in the solid-phase volume fraction. We define the maximum average solid-phase volume fraction ($\alpha_{p\max}$) as the maximum of the mean values computed by averaging α_p over the width of the domain along the direction of propagation of the detonation at a given instant. Figure 3 shows the variation of $\alpha_{p\max}$ with time as the detonation passes through the particle clouds of different α_{p0} . A cloud that has a lower α_{p0} gets compacted greater than a cloud with relatively higher α_{p0} . This is due to the increase in the interparticle stress with increase in α_p . Thus, as α_{p0} increases from 0.0025 to 0.02, the maximum value of $\alpha_{p\max}/\alpha_{p0}$ decreases from 2.4 to 1.7. As the detonation propagates, the particle cloud moves away from the detonation front and is dispersed by the flow behind the front. Thus, the particle cloud propagation is characterized by initial compaction near the detonation front followed by the dispersion after the detonation has passed. Also, note that the particle cloud with $\alpha_{p0} = 0.005$ gets compacted to α_p nearly 0.01. Hence, even though the cloud is initially dilute, as a result of compaction it is necessary to consider the dense loading effects.

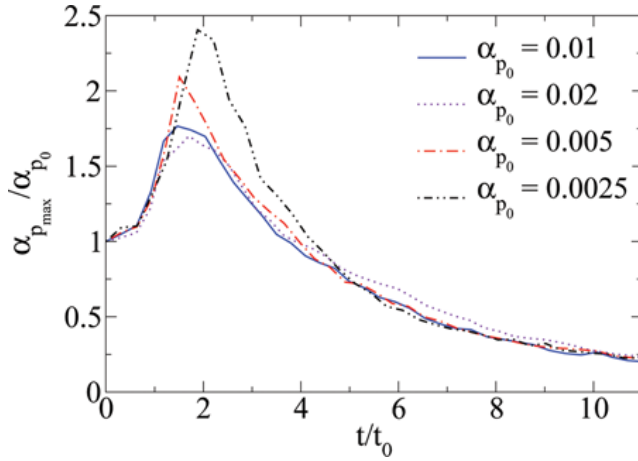


Figure 3 Variation of maximum average solid phase volume fraction ($\alpha_{p_{\max}}$) with time. Here, $L_0/L_{1/2}$ is 1.0. (Figure is provided in color online.)

The particle cloud absorbs energy and momentum from the flow as the detonation passes through it. This results in reduction in the detonation speed. The variation of average detonation speed deficit (η) with time is shown in Figure 4. Here, $\eta = D_{av}/D_{av_0}$, where D_{av} is the average detonation speed and D_{av_0} is the average detonation speed for a pure gaseous detonation. Initially, as the detonation passes through the particle cloud, the energy and the momentum absorbed by the particles from the flow result in reduction of the reaction rate. With increase in α_{p_0} , the mass of fuel available for the reaction decreases. Also, with increase in α_{p_0} , the energy and the momentum loss increase due to the availability of greater number of particles. All these effects result in sharp decrease in η , and the minimum

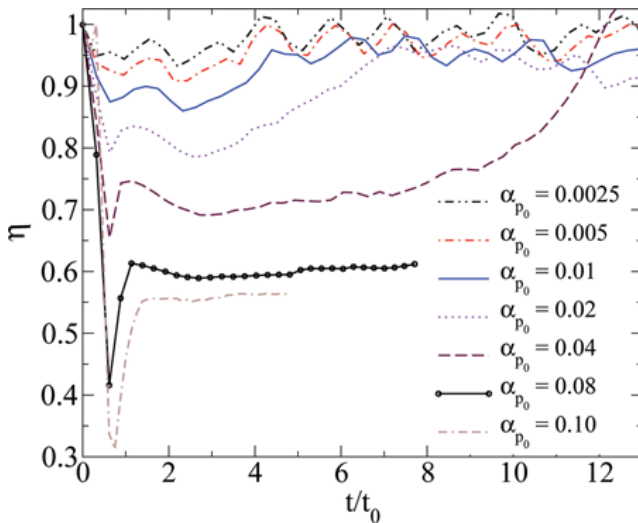


Figure 4 Variation of detonation velocity deficit (η) with time as the detonation passes through the particle cloud. The initial volume fraction (α_{p_0}) for each case is indicated. For all cases, the initial length of the cloud ($L_0/L_{1/2}$) is 1.0. (Figure is provided in color online.)

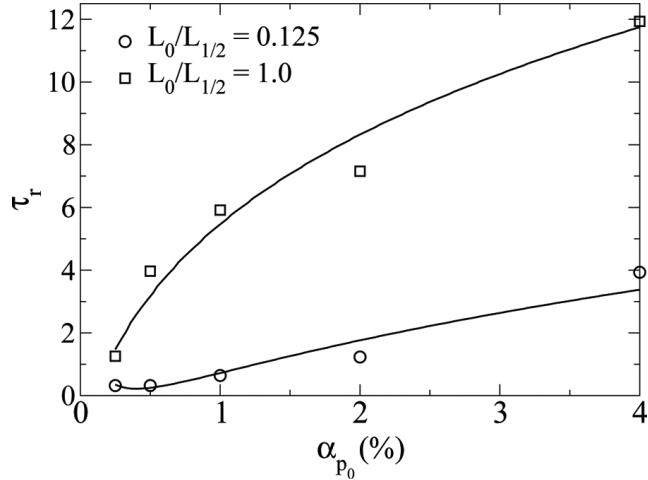


Figure 5 Variation of τ_r with the initial solid phase volume fraction (α_{p_0}). The initial length of the cloud ($L_0/L_{1/2}$) is indicated. Solid lines are from Equation (13).

value of η (η_{min}) decreases from 0.93 to 0.65 with increase in α_{p_0} from 0.0025 to 0.04 (see Figure 4). As the detonation further propagates, the particle cloud moves away from the reaction zone. This facilitates the rise in the reaction rate due to the increase in temperature. Also, as the particles in the cloud increase their velocity and temperature, they come to an equilibrium with the flow, which reduces the energy and momentum loss. Thus, η increases to a value nearly 1.0, i.e., the detonation is restored. As α_{p_0} increases from 0.0025 to 0.04, the time taken for the detonation restoration, $\tau_r = (t/t_0)_{\eta=1.0}$, increases from 1.3 to 11.9 and 0.3 to 3.9 for $L_0/L_{1/2} = 1.0$ and 0.125, respectively (see Figure 5).

The particle cloud affects the characteristics of the detonation based on α_{p_0} . To understand this, we discuss two representative cases, Cases L_1V_1 and L_1V_4 given in Table 2. In Case L_1V_1 , the particle cloud does not disrupt the formation of the transverse waves and triple points. Figures 6 and 7 show that at $t/t_0 = 2.3$, when the detonation is recovering, and $\eta = 0.86$, the difference in the characteristics of the detonation front is negligible in comparison to the case of pure gaseous detonation. However, the unburned mixture behind the front has increased after the interaction of the particle cloud with the detonation front due to the decrease in reaction rate. The reduction in the reaction rate is due to the energy and momentum absorption by the particle cloud. As already discussed, this momentum and energy exchange between the two phases results in particle cloud compaction. Thus the particle cloud has regions with maximum volume fraction of nearly 0.06 as shown in Figure 7b. In this case, even though the particle cloud reduces the detonation speed, the losses are not sufficient to quench the detonation. For the case with $\alpha_{p_0} = 0.04$, i.e., Case L_1V_4 , the detonation is quenched. Here, we consider the detonation to be quenched if the reaction zone is uncoupled from the leading shock wave. However, this quenching is not permanent. As the particle cloud moves away from the leading shock and the reaction zone, the unburned mixture away from the leading shock gradually burns to reach the shock and restore the detonation. Figure 8 shows this process. At $t/t_0 = 5.2$, the reaction zone is uncoupled from the leading shock wave, and the

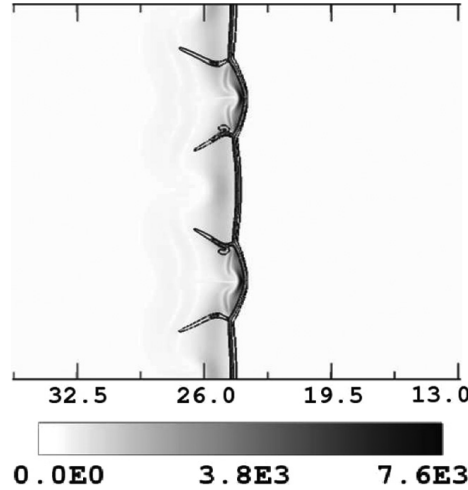


Figure 6 Gradient of the mass fraction of the unburned mixture ($|\nabla Y_g|$) at $t/t_0 = 0.0$. Gradient of pressure ($|\nabla(P_g/P_0)|$) (black lines) is plotted to show the detonation front. The length $X/L_{1/2}$ is also indicated.

distance between the shock and the reaction zone (D_{SR}) is nearly $5.0L_{1/2}$. Also, at $t/t_0 = 5.2$, the distance between the particle cloud and the shock front (D_{SP}) is $22.75L_{1/2}$. As the particle cloud propagates further downstream, at $t/t_0 = 8.9$, D_{SP} increases to $42.25L_{1/2}$ and D_{SR} increases to $10L_{1/2}$. Due to the interaction with the post-detonation flow structures, the particles disperse to form “finger-like” projections (see Figures 8e and 8f). With further propagation of the particle cloud, the effects induced by the particle cloud are reduced, and the reaction zone couples with the shock front as shown in Figure 8c. Also, note that the triple points and the transverse waves, which are very weak at $t/t_0 = 5.2$ and 8.9, are regenerated.

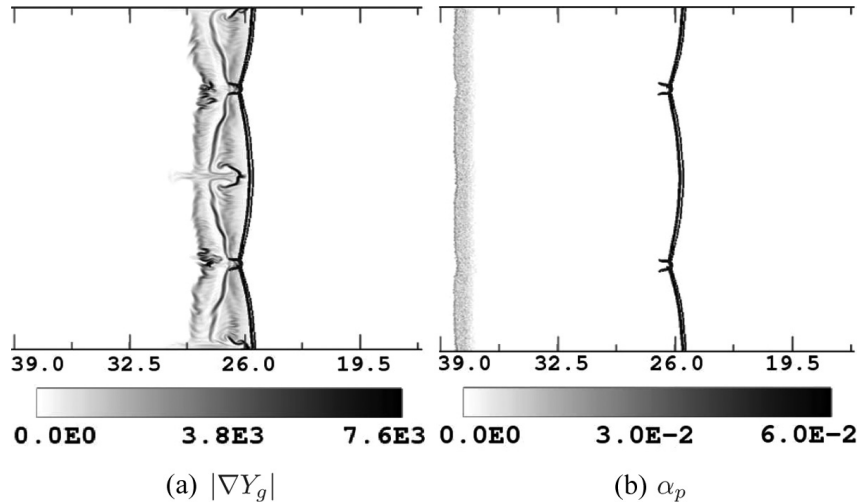


Figure 7 Gradient of the mass fraction of the unburned mixture ($|\nabla Y_g|$) and solid phase volume fraction (α_p) for $L_0/L_{1/2} = 1.0$ and $\alpha_{p0} = 0.01$ at $t/t_0 = 2.3$. Gradient of pressure ($|\nabla(P_g/P_0)|$) (black lines) is plotted to show the detonation front. The length $X/L_{1/2}$ is also indicated.

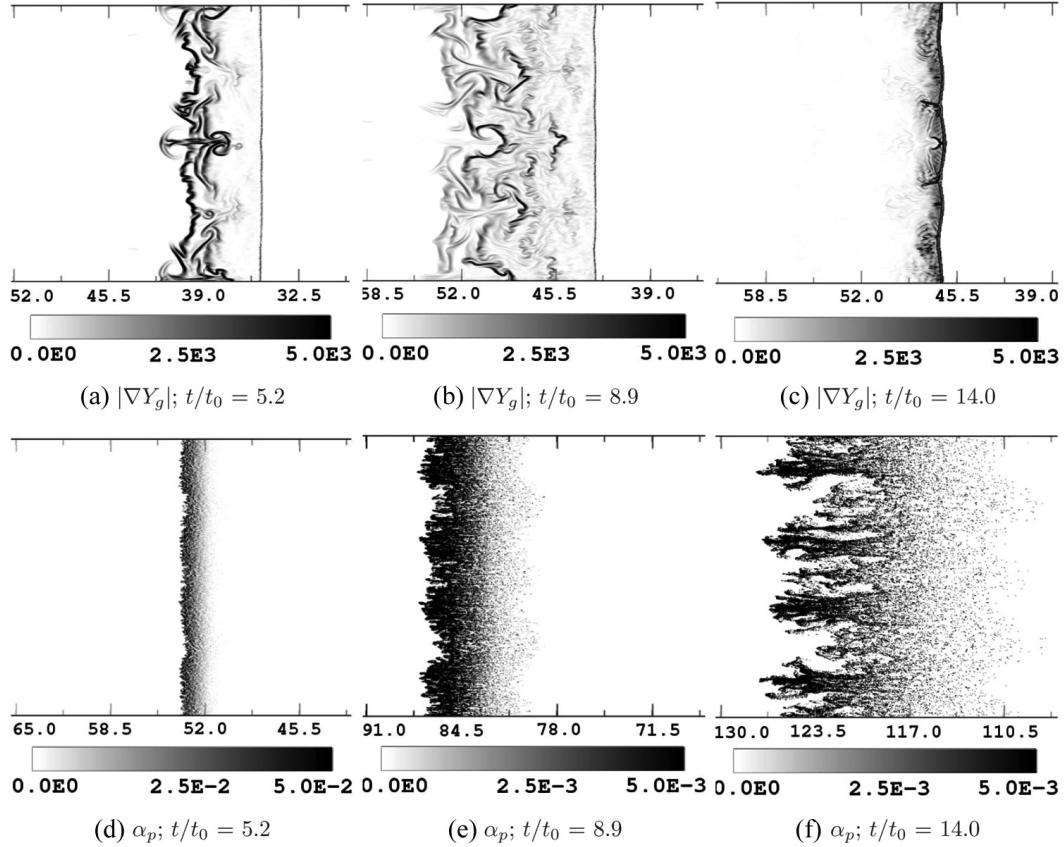


Figure 8 $|\nabla Y_g|$ and α_p for $L_0/L_{1/2}=1.0$ and $\alpha_{p_0}=0.04$ at t/t_0 (indicated). Gradient of pressure ($|\nabla(P_g/P_0)|$) (black lines) is plotted to show the detonation front. The length $X/L_{1/2}$ is also indicated.

In order to analyze the contribution of each particle acceleration term to the total particle acceleration, shown in Equation (4), the variations in the average acceleration due to viscous drag (A_{VD}), gas pressure gradient (A_{PG}), and interparticle collision/contact (A_{PC}) with time for Case L_1V_4 are presented in Figure 9. The contributions of A_{PC} and A_{PG} to the total particle acceleration are nearly 100 times smaller than the contribution of A_{VD} for $t > 7.5t_0$. However, as the particle cloud interacts with the detonation front, i.e., for $t < 7.5t_0$, A_{VD} is about 10 times A_{PG} and A_{PC} . Thus, due to the particle cloud compaction and the flow pressure gradients associated with the detonation front, A_{PG} and A_{PC} provide significant contribution to the total particle acceleration during the detonation-particle cloud interaction phase.

3.2.2. Effect of initial cloud length. The effect of increasing L_0 on the detonation-particle cloud interaction is systematically studied by varying L_0 for a fixed α_{p_0} . Here, for brevity, we discuss cases with $\alpha_{p_0}=0.01$. As already discussed, as the detonation propagates through the particle cloud, the particle cloud gets compact. A longer cloud has a greater number of particles in comparison to a shorter cloud for the same α_{p_0} . Also, a longer cloud interacts with the detonation front for longer time. Thus, when the longer cloud gets compact, the increase in α_p is greater.

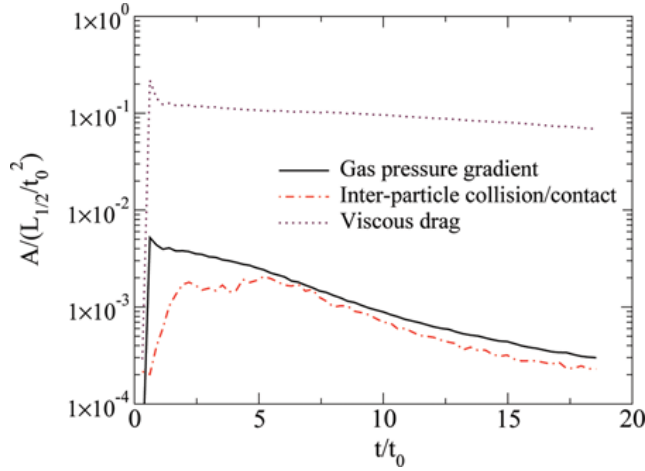


Figure 9 Variation of the average acceleration (A) due to viscous drag, gas pressure gradient, and interparticle collisions/contact with time for Case $L_1 V_4$. (Figure is provided in color online.)

This is shown in Figure 10, where with increase in $L_0/L_{1/2}$ from 0.125 to 2.0, the maximum value of $\alpha_{p_{\max}}/\alpha_{p_0}$ increases from 1.3 to 1.8. Also, the time taken to reach maximum compaction increases from $1.27t_0$ to $1.74t_0$ with increase in $L_0/L_{1/2}$ from 0.125 to 2.0. Here again, the particle cloud disperses in the downstream, and the α_p decreases as the particle cloud moves away from the detonation front. Due to the initial compaction of the particle cloud, the particle cloud length (L) decreases, and as the particle cloud disperses, L increases (see Figure 11). The minimum value of $L/L_{1/2}$ decreases from 0.99 to 0.94 with increase in $L_0/L_{1/2}$ from 1.0 to 4.0. This is again due to longer interaction time of the longer cloud with the detonation front in comparison to the shorter cloud.

The variation of η with time for clouds of different L_0 , shown in Figure 12, shows a sharp decrease in η followed by gradual increase as the particle cloud moves

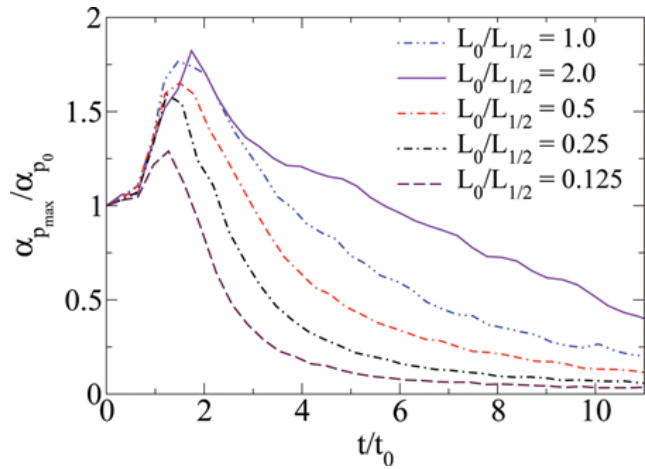


Figure 10 Variation of maximum average solid phase volume fraction ($\alpha_{p_{\max}}$) with time. Here, α_{p_0} is 0.01. (Figure is provided in color online.)

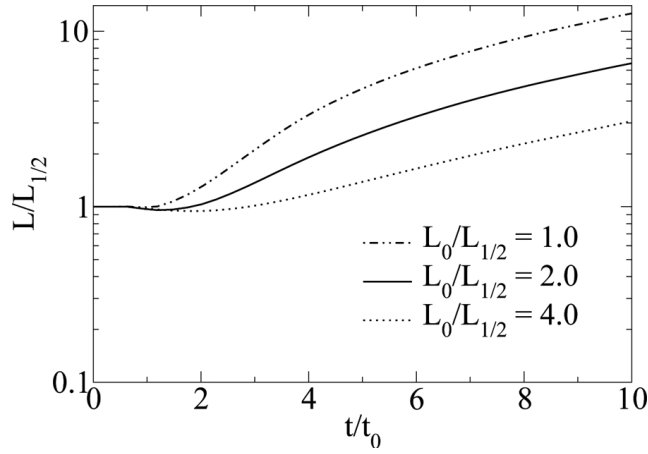


Figure 11 Variation of particle cloud length ($L/L_{1/2}$) with time as the particle cloud passes through the detonation for $\alpha_{p_0} = 0.01$.

away from the detonation front, as observed in cases with different α_{p_0} . However, unlike the cases where, with varying α_{p_0} and fixed L_0 , where the particle cloud interaction time with the detonation front is almost constant, here the longer clouds interact for a greater time with the detonation front. Thus, the time taken to achieve η_{min} increases from $0.3t_0$ to $2.0t_0$ as $L_0/L_{1/2}$ increases from 0.125 to 8.0. Also, as the cloud length increases, because of the increased interaction time and increased number of particles, the capacity of the cloud to suppress the detonation increases. Figure 12 shows that η_{min} decreases with increase in L_0 . Also, τ_r increases from 0.6 to 13.5 with increase in $L_0/L_{1/2}$ from 0.125 to 4.0, as shown in Figure 13.

In order to discuss the effect of the particle cloud length on the detonation propagation, we consider an additional case, Case L_4V_1 (see Table 2), and compare

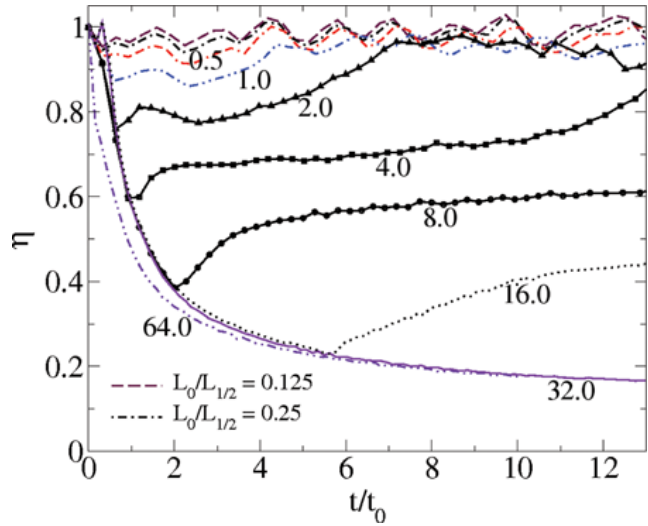


Figure 12 Variation of detonation velocity deficit (η) with time for various initial cloud lengths ($L_0/L_{1/2}$). For all cases, α_{p_0} is 0.01, and $L_0/L_{1/2}$ for each case is shown. (Figure is provided in color online.)

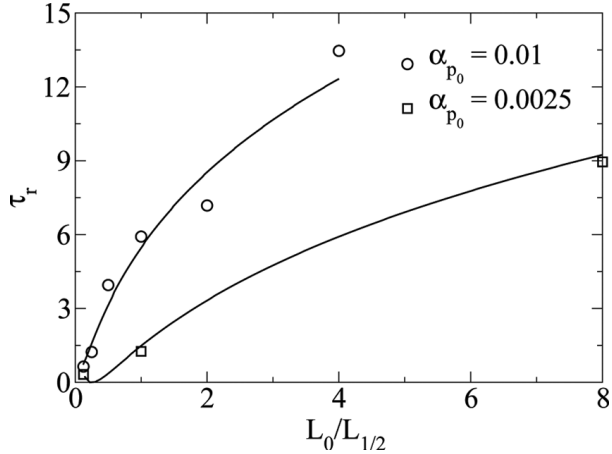


Figure 13 Variation of τ_r with the initial particle cloud length ($L_0/L_{1/2}$). The initial solid phase volume fraction (α_{p_0}) is indicated. Solid lines are from Equation (13).

with Case $L_1 V_1$ already discussed. Here again, as observed in Case $L_1 V_4$, the detonation is quenched by the cloud of length $4.0L_{1/2}$, and this quenching is temporary. Figure 14 shows the formation of quenched front with very weak transverse waves at $t/t_0 = 6.7$ and the restoration of the detonation front at $t/t_0 = 19.6$. Thus, with increase in $L_0/L_{1/2}$ from 1.0 to 4.0, the effect on the detonation changes from suppression to temporary quenching. However, with further increase in $L_0/L_{1/2}$, i.e., for Case $L_8 V_1$, the detonation is not restored by $t/t_0 = 14.0$. In this case, at time $t/t_0 = 13.2$, η is 0.62 and the reaction zone and the leading shock are still uncoupled with distance between them increasing in time. It is possible that even in this case the detonation is restored at a later time. But past results (Fomin and Chen, 2009; Papalexandris, 2005) indicate that the propagation of a detonation into a gas-particle mixture of sufficient α_{p_0} would cause permanent quenching. Thus, for a very

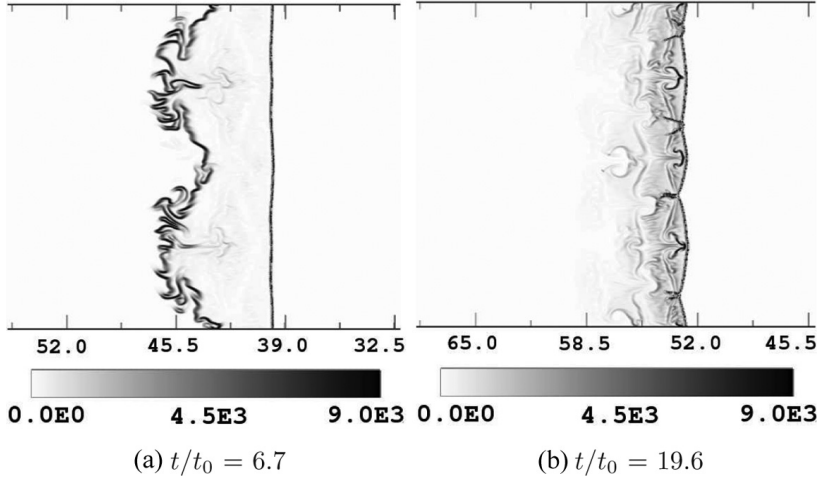


Figure 14 $|\nabla Y_g|$ for $L_0/L_{1/2} = 4.0$ and $\alpha_{p_0} = 0.01$ at $t/t_0 =$ (a) 6.7 and (b) 19.6. Gradient of pressure ($|\nabla(P_g/P_0)|$) (black lines) is plotted to show the detonation front. The length $X/L_{1/2}$ is also indicated.

long cloud, i.e., for $L_0/L_{1/2} \geq 8.0$, it is possible to have permanent detonation quenching. In order to describe permanent quenching, we consider Case $L_{32}V_1$. The variation of average temperature (averaged over the entire width of the domain at each location in the direction of the detonation propagation), T_{av} , at different times for Cases $L_{32}V_1$ and L_4V_1 , is shown in Figure 15. For Case L_4V_1 , after the reaction zone and the shock front decouple, the shock wave transmitted through the particle cloud results in post-shock temperature nearly $3.5T_0$ (see Figure 15a at $t = 4.19t_0$). This post-shock temperature generates reaction rates sufficient enough to enable the reaction zone to reach the shock front and restore the detonation (at $t = 18.29t_0$ in Figures 15a). However, for Case $L_{32}V_1$, the transmitted shock is very weak. η in this case reduces to 0.17 at $t/t_0 = 13.0$, as shown in Figure 12. The weak transmitted shock generates a post-shock temperature of at most $1.1T_0$ (see Figure 15b). Thus, due to the post-shock temperature, which cannot induce the necessary reaction rates, the detonation is not restored in this case. This scenario is also observed in Case $L_{64}V_1$. Thus, among the cases presented in this article, only Cases $L_{32}V_1$ and $L_{64}V_1$ show permanent detonation quenching due to the reduction in temperature across the shock front and the contact between the unburned and the burned gases. However, if a maximum time is set for restoration of the detonation ($\tau_{r_{\max}}$), which is practical, even temporary quenching transforms into permanent quenching based on the maximum time available for detonation propagation. This happens because the leading shock and the reaction zone cannot couple in the specified time. Thus, in this case, Cases L_1V_4 , L_4V_1 , and L_8V_1 would result in permanent quenching based on the time limit specified, i.e., if $\tau_r < \tau_{r_{\max}}$.

In summary, based on τ_r , $L_0/L_{1/2}$, and α_{p_0} , the propagation of detonation through inert particle clouds can be divided into three regimes. In the first regime, as in Case L_1V_1 , the detonation is suppressed and restored to the state similar to pure gaseous detonation propagation while the reaction zone remains coupled with the detonation front. In regime I, the transverse waves or triple-point formation resemble that of pure gaseous detonation. In regime II, as in Cases L_1V_4 and L_4V_1 , the detonation is temporarily quenched. The reaction zone and the leading shock uncouple, and the distance between the leading shock and the reaction zone

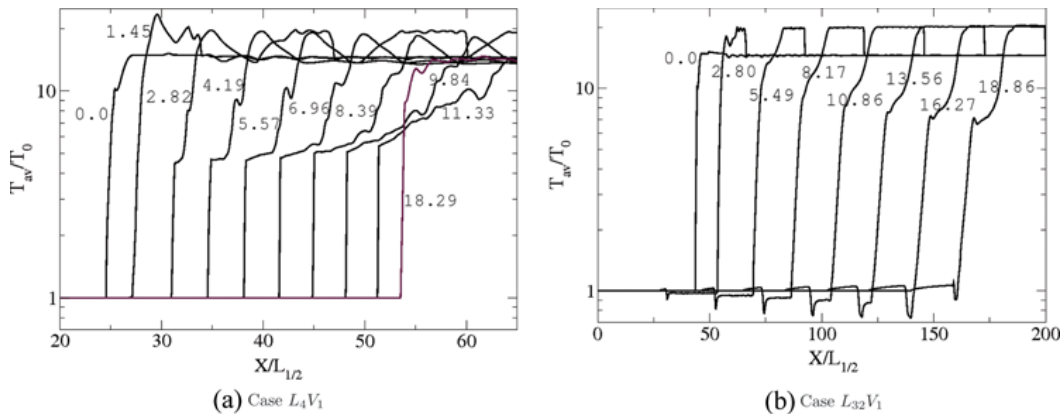


Figure 15 Average temperature (T_{av}) variation at different time (t/t_0 indicated) as the particle cloud interacts with the detonation front for Cases (a) L_4V_1 and (b) $L_{32}V_1$. (Figure is provided in color online.)

increases with time, initially. At a later time, as the particle cloud moves away from the detonation front, the distance between the leading shock and the reaction zone decreases, and the detonation is restored at $t/t_0 = \tau_r$. In this regime, the transverse waves or the triple-point formation are temporarily suppressed or weak. Finally, in regime III, the detonation is permanently quenched. The leading shock and the reaction zone remain uncoupled, and the distance between them increases with time. In the current study, the detonation propagates in regime I for $L_0/L_{1/2} < 4.0$ and $\alpha_{p_0} < 0.01$ or $L_0/L_{1/2} < 1.0$ and $\alpha_{p_0} < 0.04$ with $\tau_{r_{\max}} = 13.0$. For $L_0/L_{1/2} \geq 4.0$ and $\alpha_{p_0} \geq 0.01$ or $L_0/L_{1/2} \geq 1.0$ and $\alpha_{p_0} \geq 0.04$ with $\tau_{r_{\max}} = 13.0$, the detonation propagates in regime II, and for $L_0/L_{1/2} \geq 32.0$ and $\alpha_{p_0} \geq 0.01$, the detonation propagates in regime III. Figure 16 shows the variation from regime I to regime II with increase in α_{p_0} and $L_0/L_{1/2}$. Since only two of the current cases fall under Regime III, it is not indicated in Figure 16. Based on the current study, in order to facilitate the prediction of the detonation behavior, an empirical fit relating τ_r , $L_0/L_{1/2}$ and α_{p_0} (%) is

$$\begin{aligned} \tau_r = & 5.6 + 2.6 \log_2(\alpha_{p_0}) + 2.7 \log_2(L_0/L_{1/2}) \\ & + 0.3[\log_2(\alpha_{p_0})]^2 + 0.6 \log_2(\alpha_{p_0}) \log_2(L_0/L_{1/2}) + 0.4[\log_2(L_0/L_{1/2})]^2 \end{aligned} \quad (13)$$

From Equation (13), $\partial\tau_r/\partial\alpha_{p_0}$ and $\partial\tau_r/\partial(L_0/L_{1/2})$ are

$$\frac{\partial\tau_r}{\partial\alpha_{p_0}} = \frac{1}{\alpha_{p_0}} [2.6 + 0.6 \log_2(\alpha_{p_0}) + 0.6 \log_2(L_0/L_{1/2})] \quad (14)$$

$$\frac{\partial\tau_r}{\partial(L_0/L_{1/2})} = \frac{1}{(L_0/L_{1/2})} [2.7 + 0.6 \log_2(\alpha_{p_0}) + 0.8 \log_2(L_0/L_{1/2})] \quad (15)$$

Further, Equations (14) and (15) indicate that for $\alpha_{p_0} \approx 0.01$, $\partial\tau_r/\partial\alpha_{p_0} \propto 1/\alpha_{p_0}$, and for $L_0 \approx L_{1/2}$, $\partial\tau_r/\partial(L_0/L_{1/2}) \propto (L_{1/2}/L_0)$. It should be noted that Equation (13) is valid for $L_0/L_{1/2} \leq 8.0$ and $\alpha_{p_0} < 0.08$.

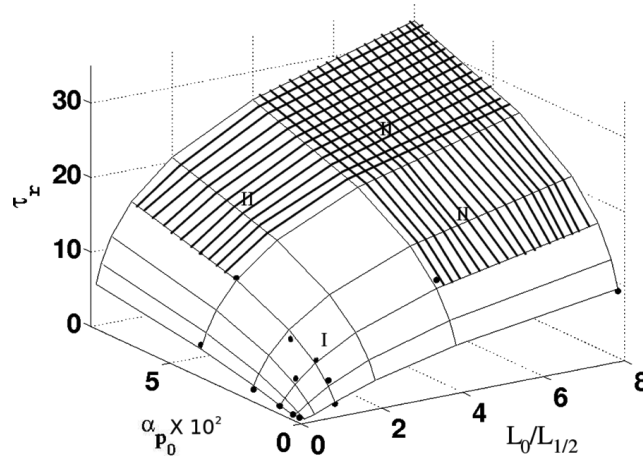


Figure 16 Variation of τ_r with the initial particle cloud length ($L_0/L_{1/2}$) and the initial solid phase volume fraction (α_{p_0}).

4. THREE-DIMENSIONAL EFFECTS

One of the focuses of this study is the full 3D simulation for both gaseous and two-phase detonations. Past researchers have shown that detonations involve complex 3D features, such as formation and interaction of triple-point lines (Dou et al., 2008; Eto et al., 2005; Williams et al., 1996). Here, we conduct simulations in 3D using the parameter set 2 used earlier in the 2D study for cases summarized in Table 1 (cases 3D1, 3D2, and 3D3). However, for brevity, all the results presented here correspond to a representative, Case 3D2. In the current study, the domain is taken to contain at least one cellular structure based on the 2D results. The propagation of the front indicates that here the detonation has rectangular structure. Similar rectangular fronts have been reported earlier (Hanana et al., 2001; Williams et al., 1996). Detailed discussion regarding the 3D detonation front structure can be found elsewhere (Deledicque and Papalexandris, 2006; Dou et al., 2008).

Figure 17 shows the detonation front, which has the horizontal (H) and the vertical (V) triple-point lines. The movement of the triple point lines on the front is observed from Figures 17a–17f shown at equally spaced time intervals of nearly $0.457t_0$. Figure 18 shows the schematic diagram of the motion of the triple point lines shown in Figure 17. The vertical triple-point lines move from the edge toward the center as shown in Figures 17a–17d and 18a–18d. During this time, the horizontal triple point lines reach the edge and form “slapping waves” (Hanana et al., 2001; Williams et al., 1996, see Figures 17b and 18b) on top and bottom surfaces. Thus, the soot foil obtained from the 3D simulation (shown in Figure 19) shows the slapping wave on the bottom wall, the location of which corresponds to the location where the soot foil trace on the side wall meets the edge. Similarly, the horizontal triple point lines move from the edges to the center (Figures 17b–17e and 18b–18e) while the vertical triple-point lines move back to the edges. This forms the slapping waves on the side walls, which correspond to the location where the soot foil trace meets the edges on the bottom and the top walls (see Figure 19). The soot foil also shows cell width to be same as that observed in the 2D case, i.e., nearly $11.54L_{1/2}$, and the cell length to be nearly $19.23L_{1/2}$.

The cell size can also be estimated based on the motion of the triple-point lines. Past studies indicate that the soot foil is formed as a combination of movement of triple point lines on the detonation front and the propagation of the front. The cell length in this case can be estimated based on the time taken for the triple line to complete one cycle starting from the center of the front to the edges and back to the center again. Here, it is found that the time for this movement is nearly $2.756t_0$. Thus, the cell length, which is the distance traveled by the front in this time period, is nearly $19.23L_{1/2}$, which is the cell length observed in the 2D and 3D cases described above.

Some of the studies discussed above in 2D are also performed in 3D to study the variations in effect of detonation on the particle clouds in 3D. As a particle cloud passes through the detonation front, as already discussed above, the particle cloud length (L) decreases initially and then increases. In order to study the 3D effects, the variation of L in 2D and 3D are compared (see Figure 20). Even though the parameters used for both the 2D and 3D cases are identical, the cloud length in each 3D case increases to a greater extent in comparison to the corresponding 2D case. For instance, at $t/t_0 = 2.9$, for Case 3D $L_{1/8}V_1$, $L/L_{1/2}$ is 10.2, whereas for Case $L_{1/8}V_1$,

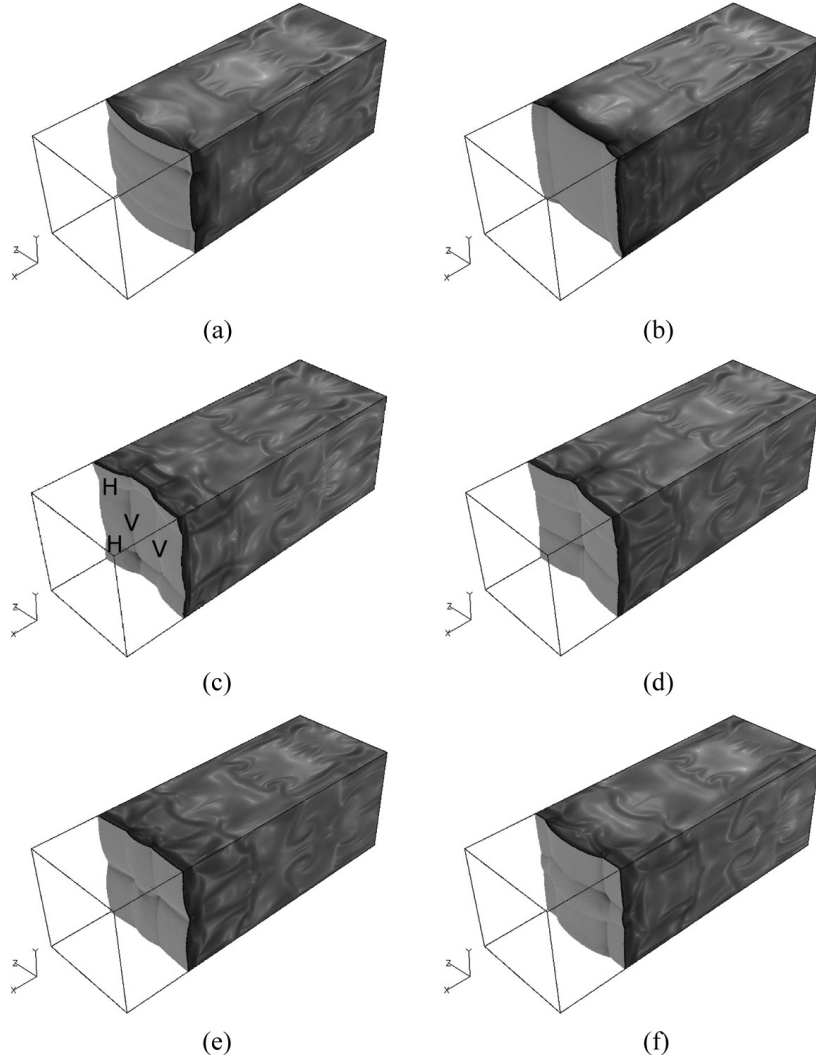


Figure 17 The movement of the triple-point lines and the occurrence of the slapping waves. Figures show one complete cycle, i.e., the movement of the triple lines from the center to the edges and back to the center. The figures also show the roll up of the edges from the triple-point lines and the formation of vorticity. Density gradient plotted on the top and the side to log scale show these features. The detonation front is visualized by iso surface of pressure. The pictures are taken at equal time intervals of $0.457t_0$.

$L/L_{1/2}$ is 8.5. This difference is due to the additional dimension provided in 3D, which allows for an additional transverse velocity component and enhances the particle dispersion in the post-detonation flow. Apart from this variation, the general trend in the variation of L , η , and α_p in 2D and 3D studies is the same. Figure 21 shows that the reaction zone and the leading shock remain coupled in Case $3DL_{1/8}V_{1/4}$. The detonation front is similar to the one observed in pure gaseous study in 3D. In fact, all the 3D cases presented here belong to regime I discussed earlier, and the propagation characteristics are the same as discussed in the 2D study for this regime. Past studies of detonation in gas, particle mixtures in 1D and 2D show similarities in results because the primary momentum exchange direction is the direction

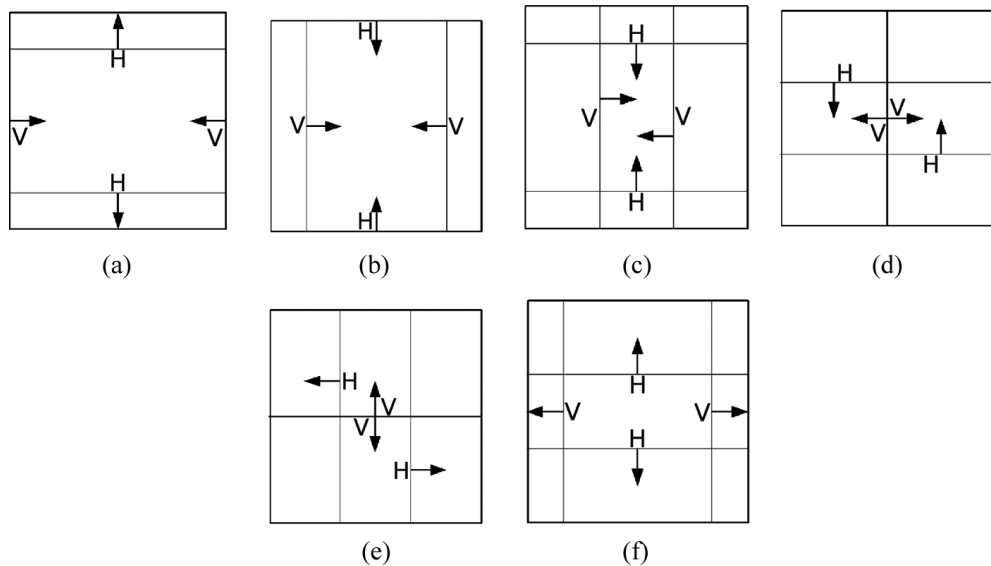


Figure 18 Schematic of movement of the triple point lines (H and V) and the occurrence of the slapping waves. Here, the parts (a)–(f) correspond to Figures 17a–17f, respectively. The arrows indicate the direction of motion of the triple-point lines.

of propagation of the detonation [34]. Hence the effects of particle clouds near the detonation front are similar in 1D, 2D, and 3D. However, in regions where transverse velocity components play a role, multidimensional calculations are necessary. Thus, although the results and the justifications provided in Section 4 are accurate qualitatively, for more exact quantitative estimates, especially for particle dispersion studies in post-detonation flow, performing 3D calculations is important.

5. CONCLUSIONS

The effect of inert particle clouds on detonations is studied using a simplified chemical model with Arrhenius kinetics. The two-phase equations are modeled using Eulerian–Lagrangian formulation, and DEM is used to account for volume fraction of the particle clouds. Pure gas phase simulations have been performed in 1D, 2D, and 3D and are used to study the two-phase cases. These simulations show the differences in 2D and 3D detonation propagation. In 3D, the motion of triple-point

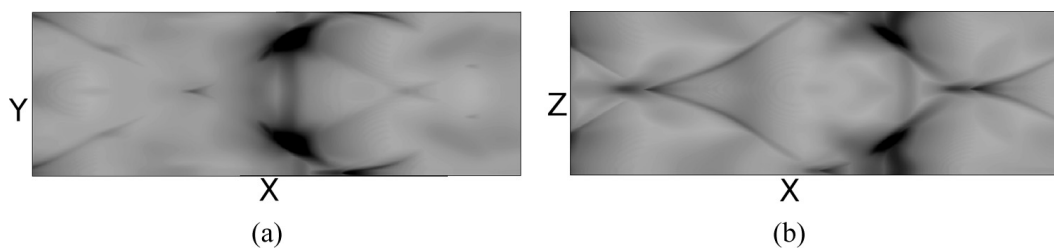


Figure 19 Numerical soot foil track recording maximum pressure obtained from the 3D simulation: (a) side wall at $z=0$ and (b) bottom wall at $y=0$.

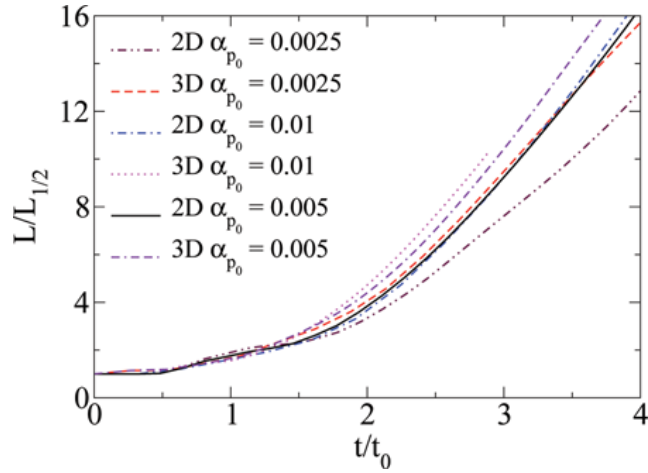


Figure 20 Variation of particle cloud lengths ($L/L_{1/2}$) with time as the particle cloud passes through the detonation. Here $L_0/L_{1/2} = 0.125$. (Figure is provided in color online.)

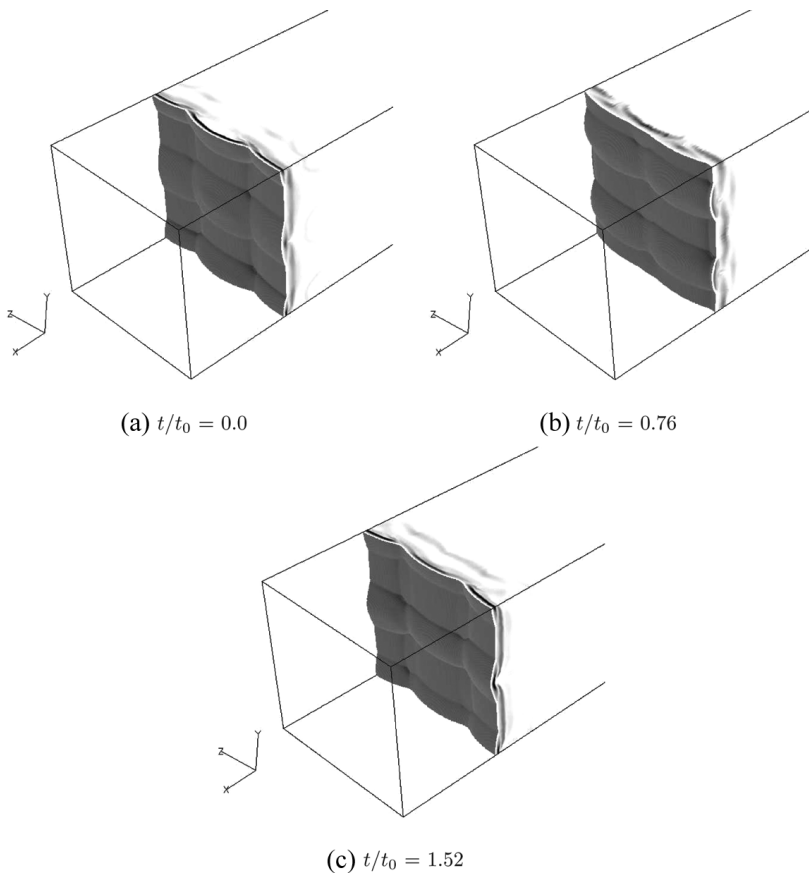


Figure 21 $|\nabla Y_g|$ behind the detonation front (a) before, and (b) and (c) after the particle cloud passes the detonation front in Case $3DL_{1/8}V_{1/4}$.

lines generates the slappingwaves absent in 2D cases, as observed by other researchers (Hanana et al., 2001; Williams et al., 1996).

The effect of the inert particle clouds on detonation is studied by varying particle cloud length (L_0) and initial particle cloud volume fraction (α_{p_0}). The 2D studies conducted show that the particle clouds interact with the detonation in two stages. The first stage involves the compaction of the particle cloud due to the momentum exchange behind the detonation front, and the second stage involves dispersion as it interacts with the flow downstream. The compaction of the particle cloud with $\alpha_{p_0} = 0.005$ and $L_0/L_{1/2} = 1.0$ results in maximum $\alpha_{p_{\max}}$ nearly 0.01, which indicates that considering the dense loading effects is important even if the $\alpha_{p_0} < 0.01$. In particular, the studies performed indicate that for cases with $L_0/L_{1/2} \geq 1.0$ and $\alpha_{p_0} \geq 0.005$, dense loading effects are important.

The effects of the particle clouds on the detonation propagation are observed to fall into three regimes, which are as follows:

- I. The detonation is suppressed and restored to the state similar to pure gaseous detonation propagation. The reaction zone remains coupled with the detonation front, and the transverse waves or triple-point formation resemble that of pure gaseous detonation.
- II. The detonation is temporarily quenched. Initially, the reaction zone uncouples from the leading shock, and the distance between the leading shock and the reaction zone increases. Later, as the particle cloud moves away from the front, the distance between the leading shock and the reaction zone decreases, and the detonation is restored. The transverse waves or triple-point formation are temporarily suppressed or weak.
- III. The detonation is permanently quenched. The reaction zone uncouples from the leading shock, and the distance between the leading shock and the reaction zone increases, monotonically. The transverse waves or triple-point formation are suppressed.

Among the cases presented in this article, particle clouds with $L_0/L_{1/2} \geq 4.0$ with $\alpha_{p_0} \geq 0.01$ or with $L_0/L_{1/2} \geq 1.0$ and $\alpha_{p_0} \geq 0.04$ are shown to cause temporary detonation quenching. Further, detonation interaction with particle clouds with $L_0/L_{1/2} \geq 32.0$ and $\alpha_{p_0} \geq 0.01$ resulted in permanent quenching, i.e., regime III.

The simulations performed in 3D showed similar trends with variation in L_0 and α_{p_0} , as observed in 2D. But the values of the cloud length (L) at any given time, obtained from 2D and 3D simulations, differed for the same initial parameters. This variation is due to additional dispersion allowed in 3D due to the additional dimension, and hence for exact quantitative results in post-detonation flow, the simulations should be performed in 3D.

The simulations performed here can also be done with reacting particles to investigate additional features or regimes of detonation propagation. Recent studies (Balakrishnan et al., 2010c) suggest that the dispersion of reactive particles by blast waves results in preferential ignition of the particles. Thus, the study of reactive particle dispersion downstream of detonation can be vital for proper understanding of ignition process in hybrid detonations. These studies will be interesting, and can be compared with results presented in this paper. We leave them for future analysis.

ACKNOWLEDGMENTS

This work is supported by the Defense Threat Reduction Agency (Dr. S. Peiris, Program Manager). The computational resources were provided by DoD HPC Centers at the U.S. Army Research Laboratory DoD Supercomputing Resource Center, Engineer Research and Development Center, and the Maui High Performance Computing Center. We are grateful for the constructive comments provided by the two anonymous reviewers, and acknowledge that the suggestions made by them have enhanced the quality of this article.

REFERENCES

Abgrall, R., and Saurel, R. 2003. Discrete equations for physical and numerical compressible multiphase mixtures. *J. Comput. Phys.*, **186**(2), 361.

Balakrishnan, K., and Menon, S. 2010. On the role of ambient reactive particles in the mixing and afterburn behind explosive blast waves. *Combust. Sci. Technol.*, **182**, 186.

Balakrishnan, K., Nance, D.V., and Menon, S. 2010a. Numerical study of blast characteristics from detonation of homogeneous explosives. *Shock Waves*, **20**, 147.

Balakrishnan, K., Nance, D.V., and Menon, S. 2010b. Simulation of impulse effects from explosive charges containing metal particles. *Shock Waves*, **20**, 217.

Balakrishnan, K., Ukai, S., and Menon, S. 2010c. Clustering and combustion of dilute aluminum particle clouds in a post-detonation flow field. *Proc. Combust. Inst.*, **33**, 2255.

Boiko, V.M., Kiselev, V.P., Keselev, S.P., Papyrin, A.P., Poplavsky, S.V., and Fomin, V.M. 1997. Shock wave interaction with a cloud of particles. *Shock Waves*, **7**, 275.

Bourlioux, A., and Majda, A.J. 1992. Theoretical and numerical structure for unstable two-dimensional detonations. *Combust. Flame*, **90**, 211.

Carvel, R.O., Thomas, G.O., and Brown, C.J. 2003. Some observations of detonation propagation through a gas containing dust particles in suspension. *Shock Waves*, **13**, 83.

Chen, Z., and Fan, B. 2005. Flame propagation through aluminum particle cloud in a combustion tube. *J. Loss Prev. Process Ind.*, **18**, 13.

Chen, Z., Fan, B., and Jiang, X. 2006. Suppression effects of powder suppressants on the explosions of oxyhydrogen gas. *J. Loss Prev. Process Ind.*, **19**, 648.

Crowe, C., Sommerfeld, M., and Tsuji, Y. 1998. *Multiphase Flows with Droplets and Particles*, CRC Press, Boca Raton, FL.

Deledicque, V., and Papalexandris, M.V. 2006. Computational study of three-dimensional gaseous detonation structures. *Combust. Flame*, **144**, 821.

Dou, H-S., Tsai, H.M., Khoo, B.C., and Qiu, J. 2008. Simulations of detonation wave propagation in rectangular ducts using a three-dimensional WENO scheme. *Combust. Flame*, **154**, 644.

Drake, R.M. 1961. Discussion on the paper entitled “Forced convection heat transfer from an isothermal sphere to water,” by G. C. Violet and G. Leppert. *ASME J. Heat Transfer*, **83**(2), 170.

Einfeldt, B. 1988. On Godunov-type methods for gas dynamics. *SIAM J. Numer. Anal.*, **25**(2), 294.

Eto, E., Tsuboi, N., and Hayashi, A.K. 2005. Numerical study on three-dimensional detonation waves: Detailed propagating mechanism and existence of the OH radical. *Proc. Combust. Inst.*, **30**, 1907.

Fedorov, A.V., Tropin, D.A., and Bedarev, I.A. 2010. Mathematical modeling of detonation suppression in a hydrogen-oxygen mixture by inert particles. *Combust., Expl. Shock Waves*, **46**(3), 332.

Fomin, P.A., and Chen, J.R. 2009. Effect of chemically inert particles on parameters and suppression of detonation in gases. *Combust., Expl. Shock Waves*, **45**, 303.

Génin, F., and Menon, S. 2010. Studies of shock/turbulent shear layer interaction using large-eddy simulation. *Comput. Fluids*, **39**, 800.

Gottiparthi, K.C., Génin, F., Srinivasan, S., and Menon, S. 2009. Simulation of cellular detonation structures in ethylene-oxygen mixtures. AIAA Paper 2009-0437.

Gottiparthi, K.C., and Menon, S. 2010. Study of interaction of dense or dilute cloud of inert and/or reactive particles with cellular detonation structures. AIAA Paper 2010-0770.

Hanana, M., Lefebvre, M.H., and Van Tiggelen, P.J. 2001. Pressure profiles in detonation cells with rectangular and diagonal structures. *Shock Waves*, **11**, 77.

Ju, Y., and Law, C.K. 2002. Propagation and quenching of detonation waves in particle laden mixtures. *Combust. Flame*, **129**, 356.

Kauffmann, C.W., Wolanski, P., Arisoy, A., Adams, P.R., Maker, B.N., and Nicholls, J.A. 1984. Dust, hybrid and dusty detonations. *Prog. Astronaut. Aeronaut.*, **94**, 221.

Khokhlov, A.M., Austin, J.M., Pintgen, F., and Shepherd, J.E. 2004. Numerical study of the detonation wave structure in ethylene-oxygen mixtures. AIAA Paper 2004-0792.

Krasnyansky, M. 2006. Prevention and suppression of explosions in gas-air and dust-air mixtures using powder aerosol-inhibitor. *J. Loss Prev. Process Ind.*, **19**, 729.

Kutushev, A.G., and Pichugin, O.N. 1993. Numerical investigation of the process of interrupting the detonation wave propagation in monofuel gas suspensions using an inert particle layer. *Combust., Expl. Shock Waves*, **29**(2), 215.

Laffitte, P., and Bouchet, R. 1959. Suppression of explosion waves in gaseous mixtures by means of fine powders. *Proc. Combust. Inst.*, **7**, 504.

Lee, H.I., and Stewart, D.S. 1990. Calculation of linear detonation instability: One-dimensional instability of plane detonation. *J. Fluid Mech.*, **216**, 103.

Loth, E., Silver, S., and Baum, J. 1997. Dusty detonation simulations with adaptive unstructured finite elements. *AIAA J.*, **35**, 1018.

Maxey, M.R., and Riley, J.J. 1983. Equation of motion for a small rigid sphere in a nonuniform flow. *Phys. Fluids*, **26**, 883.

Nettleton, M.A. 1987. *Gaseous Detonations, Their Nature, Effects and Control*, Chapman and Hall, London, Chap. 8.

Papalexandris, M.V. 2004. Numerical simulation of detonations in mixtures of gases and solid particles. *J. Fluid Mech.*, **507**, 95.

Papalexandris, M.V. 2005. Influence of inert particles on the propagation of multidimensional detonation waves. *Combust. Flame*, **141**, 216.

Patankar, N.A., and Joseph, D.D. 2001. Modeling and numerical simulation of particulate flows by the Eulerian–Lagrangian approach. *Int. J. Multiphase Flow*, **27**, 1659.

Sharpe, G.J. 2001. Transverse waves in numerical simulations of cellular detonations. *J. Fluid Mech.*, **447**, 31.

Sharpe, G.J., and Falle, S.A. 2000. Two-dimensional numerical simulations of idealized detonations. *Proc. Soc. London, Ser. A*, **456**, 2081.

Shepherd, J.E. 2009. Detonation in gases. *Proc. Combust. Inst.*, **32**, 83.

Snider, D.M. 2001. An incompressible three-dimensional multiphase particle-in-cell model for dense particle flows. *J. Comput. Phys.*, **170**, 523.

Strehlow, R.A., and Engel, C.D. 1968. Transverse waves in detonations: II. Structure and spacing in $H_2 - O_2$, $C_2H_2 - O_2$, $C_2H_4 - O_2$ and $CH_4 - O_2$ systems. *AIAA J.*, **7**, 492.

Veyssiére, B. 2006. Detonations in gas-particle mixtures. *J. Propul. Power*, **22**(6), 1269.

White, F.M. 2006. *Viscous Fluid Flow*, 3rd ed., McGraw-Hill, Boston.

Williams, D.N., Bauwens, L., and Oran, E.S. 1996. Detailed structure and propagation of three-dimensional detonations. *Proc. Combust. Inst.*, **26**, 2991.

Zhang, F. 2009. *Shock Wave Science and Technology Reference Library, Volume 4: Heterogeneous Detonation*, Springer-Verlag, Berlin.

Zhang, F., Frost, F.D., Thibault, P.A., and Murray, S.B. 2001. Explosive dispersal of solid particles. *Shock Waves*, **10**, 431.

APPENDIX

The capability of the code to simulate detonations of various characteristics is established by using different sets of controlling parameters for initialization. Although many cases were evaluated earlier (Gottiparthi et al., 2009), we focus here on two specific sets, given in Table A1, following past similar studies (Papalexandris, 2004), to discuss the key representative features. Initially, using parameter set 1, 1D steady detonation is simulated. The resulting pressure profiles are shown in Figure A1a and Figure A1b for two different grid resolutions. The profiles indicate that the detonation becomes a steady detonation as time progresses. This is in excellent agreement with the results in literature (Dou et al., 2008; Lee and Stewart, 1990). Also, the peak value of the pressure approaches the ZND pressure value ($P/P_0 = 42.1$) with increase in the resolution. To confirm numerical accuracy, the error in the peak pressure is evaluated for different mesh sizes, $\Delta/L_{1/2}$. Figure A2 shows that the peak pressure value converges to the ZND pressure value with increase in resolution as expected.

Table A1 Parameter sets to describe the gaseous phase detonation

Parameter set	f	Ea/RT_0	Q/RT_0	γ	P_0 (atm)	T_0 (K)
1	1.0	20.0	50.0	1.2	1.0	300.0
2	1.6	38.2	26.89	1.313	0.2	293.0

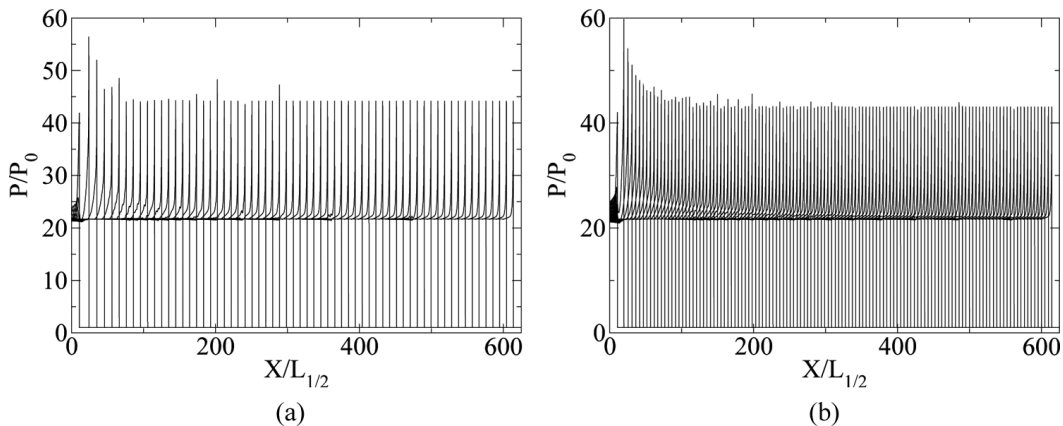


Figure A1 Pressure profiles from one-dimensional detonation simulation using (a) 16 points per half reaction zone length ($L_{1/2}$) and (b) 32 points per half reaction zone length. Here, parameter set 1 given in Table A1 is used.

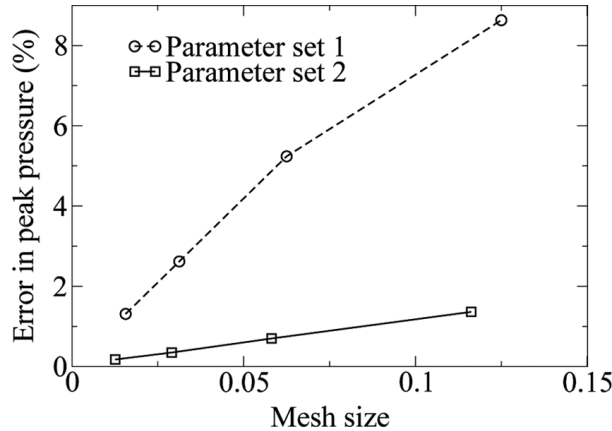


Figure A2 Variation of percentage error in peak pressure with mesh size.

Another 1D study is performed using parameter set 2, which is chosen so that the detonation resembles a detonation in stoichiometric ethylene/oxygen mixture diluted with argon. The parameters are obtained from previous experimental and numerical studies (Gottiparthi et al., 2009; Khokhlov et al., 2004; Strehlow and Engel, 1968), and the heat release is adjusted to obtain D_{CJ} of nearly 1700 m/s. The error in the peak value of pressure, after obtaining a stable detonation, is again evaluated, and shown in Figure A2 to converge to the ZND pressure value with decrease in mesh size. Along with the above mentioned verification, the 1D detonation studies performed specify the resolution requirement, i.e., minimum of 16 points per $L_{1/2}$, for the 2D and 3D studies discussed in this article. Also, the 1D flow field is used to initialize the domain in 2D and 3D simulations.

Study of Deflagration-to-Detonation Transition in Gas-Particle Mixtures

Kalyana C. Gottiparthi,* and Suresh Menon†

School of Aerospace Engineering, Georgia Institute of Technology, Atlanta, GA, 30332, USA

Effect of presence of inert particles on the process of deflagration to detonation transition (DDT) in stoichiometric H_2 -Air mixture in channels with obstacles has been simulated and studied. The numerical simulations in pure gaseous mixture are conducted in channels with widths 2, 4, 8 and 16 cm with a constant blockage ratio 0.5 to simulate the quasi-detonation and the detonation regimes observed in experiments and earlier computational results. The effect of variation of volume fraction (α_{p0}) and the radius (r_p) of the inert particles on DDT in channels is analyzed by introducing steel particles into the accelerating flame in a channel of width 16 cm and blockage ratio 0.5. The energy and the momentum absorbed by the particles results in the deceleration of the leading shock wave and the flame, and the interaction of the particles with the flame enhanced the instabilities, thereby increasing the flame speed. These two conflicting effects in combination results in detonation initiation at the wall due to direct coupling of flame and leading shock unlike DDT in gaseous mixture where detonation is initiated at the corner formed by the wall and the obstacle. In the current study, the time and distance to DDT increases linearly with α_{p0} for $\alpha_{p0} = 10^{-4}$ to 10^{-3} . Finally, the time to DDT decreases by 0.9 % with increase in r_p from $2\mu m$ to $8\mu m$ for a fixed $\alpha_{p0} = 10^{-5}$. The results indicate that the change in particle size for a fixed α_{p0} produces a change of about 0.1 ms in the time to DDT in comparison to DDT in pure gaseous mixture.

I. Introduction

Detonations in explosive systems can be generated in two ways, either by direct initiation or by deflagration to detonation transition. Direct initiation occurs when an ignition source of sufficient strength, which can couple the reaction and the shock wave and cause detonation immediately, is used. However, if a weak ignition source is used a deflagration is formed and under suitable initial and boundary conditions the deflagration accelerates to form a detonation. This process of transition of a deflagration to a detonation involves several complicated multiscale phenomena. The study of these phenomena is essential to understand DDT which has several applications ranging from ensuring safe fuel and explosive storage to addressing fundamental issues of some of the most basic problems in astrophysics and cosmology.

Due to several numerical and experimental investigations, over past several years significant advances have been made in understanding the basic mechanisms involved in flame acceleration and DDT in gaseous mixtures.¹ The studies involving DDT in channels with and without obstacles provide insights into the processes involved in DDT and enable to estimate the duct length and time required for detonation initiation.^{2,3} Especially, channels with obstacles provide a suitable environment to study the three consecutive stages of DDT which are (1) creation of conditions for detonation initiation due to flame and flow evolution, (2) detonation formation and (3) the survival of the detonation ensured by the spread of the detonation into unburned fluid.⁴ The detonation initiation in the channels with obstacles is caused by the collision of Mach stem, generated by the reflection of the leading shock from the bottom wall, with an obstacle or by the direct collision of the leading shock with an obstacle.⁵ Depending on the channel width, the generated detonation would either spread past the leading shock or get extinguished due to the diffraction from the obstacle. The flame acceleration in these cases is attributed to the Kelvin-Helmholtz, Rayleigh-Taylor and Richtmyer-Meshkov instabilities which are generated due to the shock flame interactions and the density

*Graduate Research Assistant and Student Member AIAA.

†Professor and AIAA Associate Fellow.

gradients in the flow. These instabilities enhance the flame surface area which supports the flame acceleration.⁶ Also, the flame acceleration is enhanced by the generation of jet flow in the unobstructed part of the channel due to the combustion of the fuel present between the obstacles.⁷

In comparison to pure gaseous phase DDT studies, very few investigations have been conducted on DDT in multiphase mixtures.⁸⁻¹² A two phase theory for DDT in reactive granular materials was described by Baer and Nunziato.⁸ Using the theory they were able to predict the distance for the transition to detonation. Zhang et al¹¹ have investigated DDT in an end multiphase slug using experiments and numerical analysis. Their results suggest that the presence of dense cloud of particles ahead of an accelerating flame would lead to the formation of reflected shocks which facilitate rapid transition to detonation. Also, the reflected detonations, from the end wall, are observed to be achieve peak pressures which are twice than that achieved in pure gaseous phase cases. Experimental investigation of effect of sand particles of radius of the order of 0.1-1.0 mm on DDT in stoichiometric $H_2 - Air$ mixture in channels without obstacles showed that the increase in particle volume fraction results in decrease in the time and distance to DDT.⁹ The particles in the experiment, which are much larger than the micron size particles considered in the present study, enhance the flame acceleration by generating small scale turbulence and bow shocks. However, in all these investigations, the processes involved in DDT in gas-particle mixtures, where particle size is in orders of microns, are not explored and to the authors' knowledge there are no results available in literature on the influence of inert particles on DDT in channels with obstacles.

In this paper, the influence of inert particle on DDT in dilute gas-particle mixtures is studied to address the processes which explain the flame acceleration and transition to detonation. An Eulerian-Lagrangian formulation is used to solve for gas and solid phase. Lagrangian tracking can accurately evaluate the particle dispersion in dilute and turbulent flows and hence it is used in the current study. Transition to detonation in pure gaseous stoichiometric $H_2 - Air$ mixture in channels with blockage ratio 0.5 and diameters (d) = 2, 4, 8 and 16 cm is considered to simulate different regimes of DDT in channels with obstacles observed in experiments. The influence of inert particles on DDT is studied by varying initial solid phase volume fraction (α_{p_0}) and particle radius (r_p). The time and distance to DDT in each case is evaluated and the processes affecting DDT are explained.

II. Governing Equations and Numerical Method

The compressible Navier-Stokes equations for reacting gas flow used to model the gas phase are:¹³

$$\frac{\partial}{\partial t}(\rho_g) + \frac{\partial}{\partial x_j}(\rho_g u_{g,j}) = 0, \quad (1)$$

$$\frac{\partial}{\partial t}(\rho_g u_{g,i}) + \frac{\partial}{\partial x_j}(\rho_g u_{g,i} u_{g,j} + p_g \delta_{ij} - \tau_{g,ij}) = \dot{F}_{p,i}, \quad (2)$$

$$\frac{\partial}{\partial t}(\rho_g E_g) + \frac{\partial}{\partial x_j}((\rho_g E_g + p_g) u_{g,j} - u_{g,i} \tau_{g,ji} + q_{g,j}) = \dot{Q}_p + \dot{W}_p, \quad (3)$$

$$\frac{\partial}{\partial t}(\rho_g Y_{g,k}) + \frac{\partial}{\partial x_j}(\rho_g Y_{g,k} (u_{g,j} + V_{g,j,k})) = \dot{\omega}_k. \quad (4)$$

Here, ρ_g is the density, p_g is the pressure, $u_{g,i}$ is the i -th component of velocity, E_g is the total energy given by the sum of the internal (e_g) and kinetic energies, ($e_g + \frac{1}{2} u_{g,i} u_{g,i}$), and $Y_{g,k}$ is the mass fraction of the k^{th} species. Note that the α_g , which is the volume fraction of the gas phase, has been approximated to 1.0 in the above equations as the current study deals with dilute gas-particle flows, i.e. $(1 - \alpha_g) = \alpha_p \sim \mathcal{O}(10^{-3} - 10^{-4})$. The stress tensor, $\tau_{g,ij}$, the heat flux vector, $q_{g,j}$, and the species diffusion velocities, $V_{g,i,k}$, are

$$\tau_{g,ij} = \mu_g \left[\left(\frac{\partial u_{g,i}}{\partial x_j} + \frac{\partial u_{g,j}}{\partial x_i} \right) - \frac{2}{3} \frac{\partial u_{g,k}}{\partial x_k} \delta_{ij} \right], \quad (5)$$

$$q_{g,j} = -\kappa_g \frac{\partial T_g}{\partial x_j} + \rho_g \sum_1^{N_s} Y_{g,k} h_{g,k} V_{g,j,k}, \quad (6)$$

$$V_{g,j,k} = -\frac{D_{g,k}}{Y_{g,k}} \frac{\partial Y_{g,k}}{\partial x_j}, \quad (7)$$

where T_g is the gas temperature and $h_{g,k}$ is the enthalpy of the k -th species. The thermal conductivity of the gas, κ_g , and the diffusion coefficient, $D_{g,k}$, are obtained from Lewis number (Le) and Prandtl number (Pr) as

$$\kappa_g = \frac{C_{p,g}\mu_g}{Pr}, \quad (8)$$

$$D_{g,k} = \frac{\kappa_g}{\rho_g C_{p,g} Le}, \quad (9)$$

where $C_{p,g}$ is the specific heat of the gas at constant pressure. The viscosity is computed based on the power law⁴

$$\mu_g = \mu_0 T_g^{0.7}. \quad (10)$$

A first-order Arrhenius kinetics for DDT in stoichiometric $H_2 - Air$ mixture used in earlier studies^{4,5} is used here and is given as

$$\dot{\omega}_k = (-1.0)^k A \rho_g Y_{g,1} \exp\left(-\frac{Ea}{RT_g}\right), \quad (11)$$

where Ea , A and R are, respectively, the activation energy, the pre-exponential factor and the gas constant. In the current study, the reaction is assumed to proceed as $X \rightarrow Y$, where X is the unburnt mixture and Y is the burnt mixture. Thus k takes value 1 for the reactant mixture and 2 for the product mixture. All the modeling parameters used in this study are given in Table 1.

Lagrangian tracking is used to compute the particle position vector ($x_{p,i}$) and velocity vector ($u_{p,i}$). Based on the case being considered, there could be very large number of particles to track. Hence, the concept of parcel, which is a group of particles, is employed.¹⁴ All particles present in a parcel are considered to have same position, velocity vectors and temperature. The number of particles assigned to each parcel and the number of parcels chosen is determined based primarily on the desired volume fraction/mass loading and numerical accuracy. Considering no inter-phase mass transfer for inert particles, the equations for solid phase are:^{15,16}

$$\frac{dx_{p,i}}{dt} = u_{p,i}, \quad (12)$$

$$m_p \frac{du_{p,i}}{dt} = \frac{\pi}{2} r_p^2 C_D \rho_g |u_{g,i} - u_{p,i}| (u_{g,i} - u_{p,i}), \quad (13)$$

$$m_p C_p \frac{dT_p}{dt} = 2\pi r_p \kappa_g Nu (T_g - T_p), \quad (14)$$

where m_p is the particle mass and T_p is the particle temperature. The lift, inertial force of virtual mass, Basset force, inter-particle collisions and buoyancy for the cases considered in the current study are small in comparison to the drag and hence are not considered here.¹⁷ C_p represents specific heat of the solid particle. The particle mass m_p is obtained as $4/3\pi r_p^3 \rho_p$, where ρ_p is the solid particle material density. Based on the number of parcels in each Eulerian finite-volume cell α_p is evaluated. In the above equations, C_D represents the drag coefficient. The expression for C_D , validated by comparisons with experiments,^{13,18} is

$$C_D = \left[0.38 + \frac{24}{Re} + \frac{4}{Re^{0.5}} \right] \left[1 + \exp\left(\frac{-0.43}{M_{pg}^{4.67}}\right) \right], \quad (15)$$

where $Re = 2\rho_g r_p |u_{g,i} - u_{p,i}| / \mu$ and $M_{pg} = |u_{g,i} - u_{p,i}| \sqrt{\rho_g} / \sqrt{\gamma p_g}$ denote Reynolds number and Mach number based on the relative velocity between gas and the particle, respectively. γ is the ratio of the specific heats of the gas. The Nusselt number as a function of Re and Pr is expressed as $Nu = 2.0 + 0.459 Pr^{0.33} Re^{0.55}$.¹⁹ Finally, the inter-phase coupling terms (in equations (2)-(4)) are obtained by averaging over all particles/parcels in a computational cell of a finite volume (Vol).

$$\dot{F}_{p,i} = \frac{1}{Vol} \sum_{n=1}^N n_{p,n} \frac{\pi}{2} r_{p,n}^2 C_{D,n} \rho_{g,n} |u_{p,i,n} - u_{g,i,n}| (u_{p,i,n} - u_{g,i,n}), \quad (16)$$

$$\dot{Q}_p = \frac{1}{Vol} \sum_{n=1}^N n_{p,n} [2\pi r_{p,n} \kappa_g Nu_n (T_{p,n} - T_{g,n})], \quad (17)$$

$$\dot{W}_p = \frac{1}{Vol} \sum_{n=1}^N n_{p,n} \frac{\pi}{2} r_{p,n}^2 C_{D,n} \rho_{g,n} |u_{p,i,n} - u_{g,i,n}| (u_{p,i,n} - u_{g,i,n}) u_{p,i,n}, \quad (18)$$

where N is the total number of parcels in a finite volume cell, n_p is the number of particles per parcel.

The governing equations for gas phase are solved using an approximate Riemann solver with Monotone Upstream-centered Schemes for Conservative Laws (MUSCL) reconstruction and monotonized-central limiter. The Riemann solver used is a hybrid solver (HLLC/E)²⁰ which employs the contact preserving HLLC flux solver every where except in the shock capturing region, where in the direction transverse to the shock HLLE Riemann solver is used. The scheme is second order accurate in both time and space, although its spatial accuracy decreases in the region where the discontinuity is present. Detailed validation of this approach for shock-turbulence interaction²¹ and detonations^{22–24} has been reported elsewhere. The governing equations for solid phase are integrated in time using 4th order Runge-Kutta scheme.

The computational domain used is shown in Figure 1 and is discretized using a structured grid. The grid is uniformly fine in the regions (of length L_f given in Table 2), where the flame and shock exits and is coarsened in the regions where the fuel is completely burnt or completely unburnt with no flow property gradients. The total channel length, L , and the number of obstacles considered in each case are shown in Table 2. The minimum grid resolution $\Delta_{min} = 1/144$ cm is used which corresponds to 5 points per flame thickness ($x_l = 0.035$ cm) and 3 points per half reaction zone thickness ($L_{1/2} = 0.02$ cm) of the detonation in stoichiometric $H_2 - Air$ mixture. The grid resolution is chosen based on resolution studies available in literature⁵ and resolution studies performed in the current study.

The particles are considered to have properties of steel (i.e. C_P and ρ_p). Tables 1 and 3 list the initial solid phase conditions, the various cases, the number of parcels, the number of particles per parcel, and the initial volume fraction of the solid phase for each case. The flame is ignited by placing a hot region of burnt mixture where the temperature is $2.0T_b$, where $T_b = 7.289T_0$ is the post-flame temperature. This mode of ignition is ‘soft’ mode, i.e., the energy provided for the flame ignition is of the order of the energy release due to the flame. The boundary conditions used are also shown in Fig. 1. The surfaces of the walls and obstacles are adiabatic no-slip reflecting surfaces. At the outlet of the channel the properties are extrapolated as the flow becomes supersonic. The simulation is performed in half channel by employing symmetry condition at the half channel width. These boundary conditions are similar to the conditions used in previous studies.^{4,5}

Gas Phase		
$P_{g,0}$	1.0 atm	Initial gas pressure
$T_{g,0}$	293 K	Initial gas temperature
R	385.93 J/(mol K)	Gas constant
γ	1.17	Ratio of specific heats
MW	21 g/mol	Molecular weight
A	$6.85 \times 10^{12} cm^3/(gs)$	Pre-exponential factor
Ea	$46.37RT_0$	Activation energy
Q	$43.28RT_0$	Chemical energy release
μ_0	$2.9 \times 10^{-5} g/(scmK^{0.7})$	Transport constant
Le	1.0	Lewis number
Pr	0.72	Prandtl number
Solid Phase		
ρ_p	7874 kg/m^3	Particle density
$T_{p,0}$	293 K	Initial particle temperature
$u_{p,i}$	0.0 m/s	Initial particle velocity

Table 1. Input parameters for deflagrations and detonations in stoichiometric $H_2 - Air$ mixture and inert particles used in the current study.^{4,5}

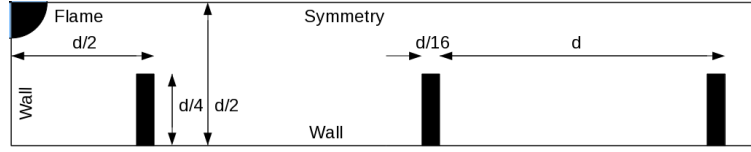


Figure 1. Computational domain used for simulation of DDT in a channel with obstacles. The obstacles and the initial flame location are shown along with the boundary conditions used. The simulation domain is same as that used by Gamezo et al.⁵ Here, the blockage ratio is 0.5 and the initial flame radius is $d/8$. The length of the channel in each case is long enough to initiate detonation and the obstacles are equally spaced.

$d/2$ (cm)	L (cm)	Number of obstacles	L_f (cm)	Grid size for $L_f \times d/2$
1.0	60.0	30	23.0	3312×144
2.0	72.0	18	34.0	4896×288
2.0	72.0	18	32.0	9216×576
4.0	96.0	12	44.0	6336×576
8.0	176.0	11	56.5	8136×1152

Table 2. Grid and domain lengths for channels of different widths used in the current study.

r_p (μm)	α_{p_0}	Number of parcels	Particles per parcel	Number of particles
2.0	1.0×10^{-5}	185024	8	1480192
4.0	1.0×10^{-5}	23128	8	185024
8.0	1.0×10^{-5}	23128	1	23128
8.0	1.0×10^{-4}	23128	10	231280
8.0	5.0×10^{-4}	115586	10	1155860
8.0	1.0×10^{-3}	231280	10	2312800

Table 3. Number of parcels tracked in each case (i.e. for a particular r_p and α_{p_0}) in the current study. The particles are distributed over length = 80.0 cm and over the entire half width (8 cm), and are located at 80.0 cm from the closed end of the channel.

III. Results and Discussion

In order to investigate the effect of inert particles on DDT in channels with obstacles, initially, DDT in pure gaseous mixture is simulated. Channels of half widths 1, 2, 4, and 8 cm are considered to simulate the quasi-detonation and the detonation regimes of DDT in channels with obstacles. The results obtained from pure gaseous simulations are validated by comparing with the results available in the literature. The accelerated flame obtained from the gaseous simulation is used to study the effect of the inert particles on flame acceleration and DDT.

III.A. DDT in pure gaseous mixtures

DDT involves acceleration of flame and flow, initiation of detonation and sustaining the initiated detonation. This process is shown in Fig. 2. Initially, the flame introduced at the closed end of the channel propagates slowly. As the flame propagates the flame surface starts to wrinkle which increases the surface area of the flame. This increase in the flame surface generates greater energy release and the flame accelerates. The accelerating flame propagates into the reactant mixture which is almost stationary. The shear between reactants and products results in Kelvin-Helmholtz (KH) instability. Rayleigh-Taylor (RT) and Richtmyer-Meshkov (RM) instabilities are generated due to the acceleration of the low density products into relatively high density reactants. These instabilities further increase the overall flame surface and the flame accelerates further. Once the flow accelerates to supersonic speed, a leading shock wave is generated in front of the flame. Figure 2 (a) shows the highly wrinkled flame and the leading shock wave in a channel with $d/2 = 8$ cm. The leading shock collides with the bottom wall to forms a Mach stem and when this Mach stem,

after gaining sufficient strength, hits the corner formed by the obstacle and the bottom wall, a detonation is ignited. This detonation ignition is shown in Fig. 2 (b) where the detonation is ignited at obstacle 8. The ignited detonation spreads around the obstacle and overtakes the leading shock (see Figs. 2 (c) and (d)). The detonation diffracts as it passes over the obstacle and produces cellular structures. This detonation which now occupies the entire channel width survives the collision and diffraction with the next series of obstacles and continues to propagate. This regime of DDT where the detonation initiated continuously propagates has been observed in experiments and previous numerical simulations.⁵

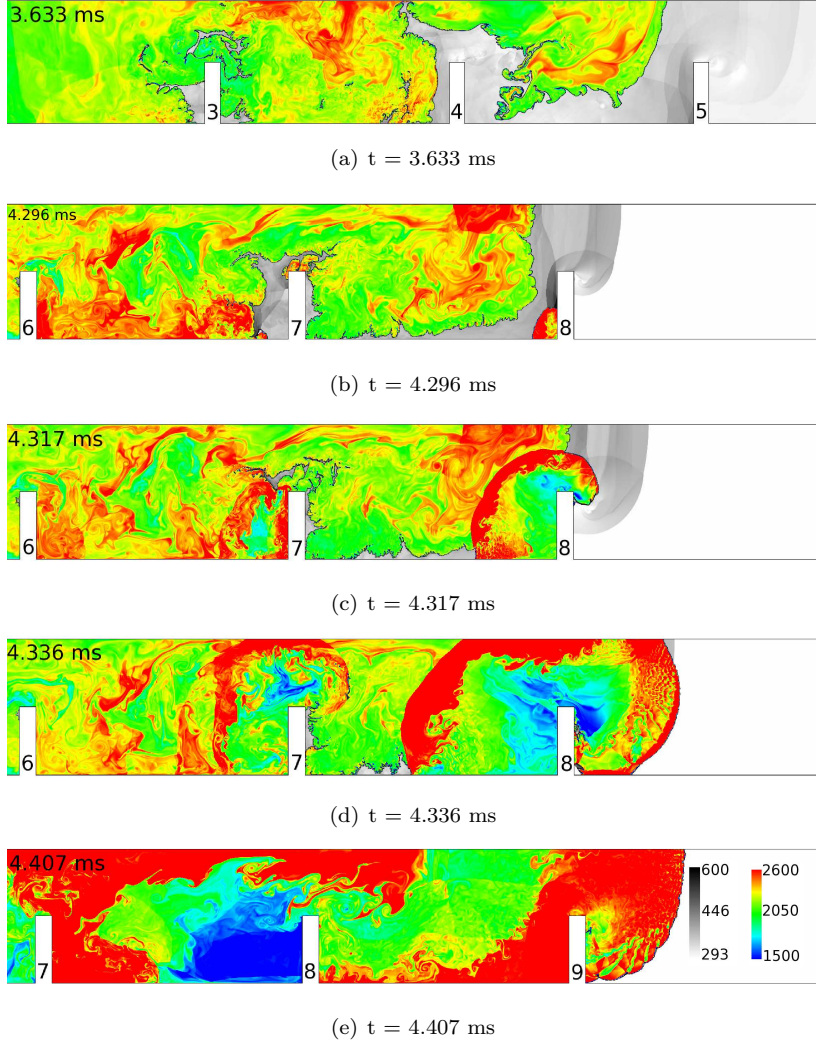


Figure 2. Flame acceleration and detonation initiation. The half channel width is 8 cm and the blockage ratio is 0.5. The temperature range of the unburnt mixture is shown in gray scale and the burnt mixture is shown in color spectrum.

III.A.1. Effect of channel width and resolution

In order to simulate the main regimes of DDT in channels with obstacles, channels of different widths are considered. For the channel with $d/2 = 1$ cm, the ignited flame accelerated and produced detonations starting from obstacle 16. But these detonations did not spread past the leading shock and failed after single diffraction from the obstacle. In channel with $d/2 = 2$ cm, the detonation is produced initially at obstacle 10. But this detonation fails to overtake the leading shock. Similarly failed detonation appears at obstacle 11. However, at obstacle 12, the detonation produced overtakes the leading shock and propagates surviving the diffraction at obstacle 13. But after diffraction from obstacle 14, the leading shock decouples from the reaction zone and the detonation is quenched. The process of this detonation formation and quenching is

again observed from obstacle 16 to 18. This mode of propagation is called quasi-detonation regime and is observed in earlier numerical and experimental investigations. Similar quasi-detonation mode is observed for the case of channel with $d/2 = 4$ cm.

The flame position variation with time in channels of different d is shown in Fig. 3. Here, the flame position is the maximum position along the length of the channel where mass fraction of the reactant mixture is less than 0.5. The flame position increases rapidly as the flame accelerates and in the cases where the transition to detonation occurs the flame position varies almost linearly with the time as the detonation propagates with velocity nearly equal to Chapman-Jouget detonation velocity, D_{CJ} . Past numerical results suggest that the time and distance to DDT increase linearly with $(d/2)^2$.⁵ From the current simulations, the time and distance to DDT are not exactly linearly varying with $(d/2)^2$ (see Fig. 4). Although the qualitative behavior of DDT in these channels is same as that observed by Gamezo et al,^{4,5} the distance and time to DDT does not match exactly. The variations in the values are due to the difference in the ignition mode chosen and the stochastic nature of DDT.

In order to perform resolution tests, the simulations are conducted considering channel with $d/2 = 2$ cm and $\Delta_{min} = 1/144$ cm and $1/288$ cm. $\Delta_{min} = 1/288$ cm corresponds to 10 points per x_l and 6 points per $L_{1/2}$. The flame position variation with time for these two resolutions is shown in Fig. 5. Initially, the flame acceleration is same for both the resolutions. But as the flame interacts with obstacles and in the high vorticity areas the higher resolution case produces small flamelets which enhance the flame acceleration slightly. However, the qualitative behavior in both the cases is same. Also, in channels with obstacles the position of detonation initiation is controlled by the location of the obstacle⁵ and thus the resolution has only minor effect on the distance and time to DDT. For the cases with gas-particle mixtures discussed in this paper, $\Delta_{min} = 1/144$ cm is used.

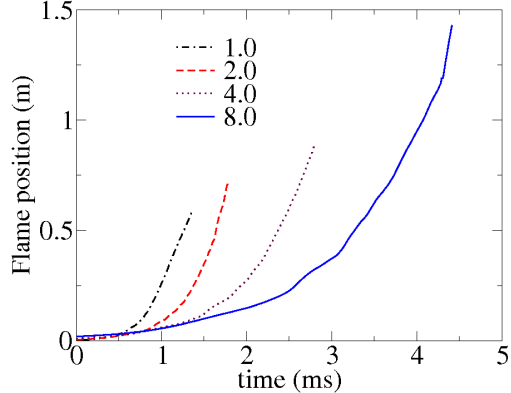


Figure 3. Variation of the position of the flame tip with time for channel with for different half channel widths.

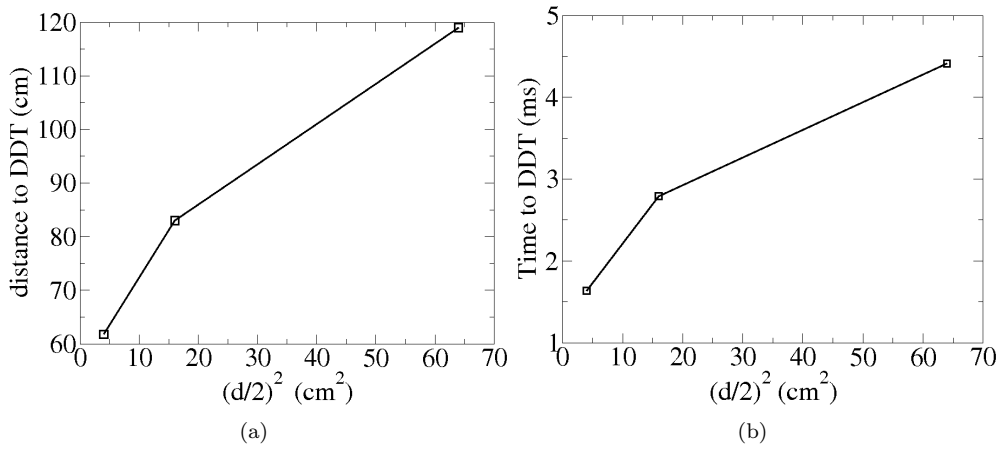


Figure 4. (a) Distance and (b) time required for DDT for channels of different widths (d).

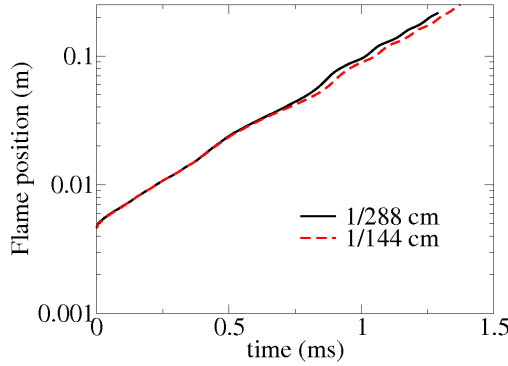


Figure 5. Variation of the position of the flame tip with time for channel with $d = 4.0$ cm for $\Delta_{min} = 1/144$ and $1/288$ cm.

III.B. DDT in gas-particle mixtures

In the current paper, the process of DDT in gas-particle mixture is studied by introducing inert particles, which are uniformly distributed over the length and the width of the channel, into the accelerating flame developed in the channel with obstacles and $d/2 = 8$ cm. The flame accelerates in the pure gaseous mixtures and encounters gas-particle mixture at nearly $t_0 = 3.7$ ms from the time of flame ignition. The flame at t_0 is shown in Fig. 6 (a). The particles are located 80 cm from the closed end of the channel (see Fig. 7 (a)). The propagation characteristics of the accelerating flame and the subsequent transition to detonation in the gas-particle mixture is studied by varying α_{p0} and r_p .

III.B.1. Effect of initial volume fraction of solid phase

The effect of particle volume fraction on DDT is studied by varying α_{p0} from 10^{-5} to 10^{-3} for a fixed particle radius $8\mu\text{m}$. When inert particles interact with the accelerating flame, due to the instabilities generated by the particles fine flamelets are generated along the flame front as shown in Fig. 6 (b). These flamelets enhance the reaction and increase the flame speed. Also, the flame spreads evenly, in comparison to pure gaseous case, along the width of the channel due to the spreading of the flamelets. This causes the flame to accelerate further. However, the particles also absorb momentum and energy from the flow and can lead to deceleration of the flame and the leading shock wave. These two effects are counteracting and, as discussed below, would reduce or increase the distance and time to DDT based on the volume fraction of the particles in the flow.

When the accelerating flame interacts with the gas-particle mixture of $\alpha_{p0} = 10^{-5}$, the flame accelerates marginally in comparison to pure gaseous case (See Fig. 8) because of the flamelet generation. The energy and momentum absorbed by the particles causes the leading shock to decelerate. However, in this case the deceleration is marginal, as shown in Fig. 9, and the flame does not reach the leading shock to initiate the detonation. Thus in this case the detonation is initiated at distance 1.19 m by the collision of the Mach stem with the obstacle 8, shown in Fig. 10 (a), as observed in pure gaseous case. In the case of $\alpha_{p0} = 10^{-4}$, the flamelets enhance the flame speed and the flame accelerates to reach the marginally decelerated leading shock wave (see Figs. 8 and 9). The leading shock wave reflects from the bottom wall producing a strong Mach stem which couples with the accelerated flame to initiate the detonation at distance 1.11 m. Thus in this case the detonation initiation does not occur at the corner of obstacle 8. The process of flame and leading shock wave coupling at the bottom wall for the case with $\alpha_{p0} = 5.0 \times 10^{-4}$ is shown in Fig. 10 (b). In this case, although flamelets are generated, the energy and momentum absorption from the flow leads to net flame deceleration. However the leading shock also decelerates such that the flame reaches the leading shock and couples to initiate the detonation. For this case, the detonation is initiated at a distance of 1.16 m from the closed end of the channel. The detonation produced at the bottom wall diffracts from the obstacle 8 and survives as shown in Fig. 6 (e). The particle dispersion, for $\alpha_{p0} = 5 \times 10^{-4}$, in the channel at different times is shown in Fig. 7. The flame and flow interact with the particles and generate particle clusters, especially near obstacles. However, α_p even in these regions does not exceed 1.0 % in all the cases considered here. The characteristics of particle dispersion are not discussed in this paper and are left to be

addressed in future. Finally, in the case of $\alpha_{p0} = 10^{-3}$, the loss of energy and momentum to the particles results in net flame and leading shock deceleration and the flame does not reach the leading shock wave. Thus in this case, as observed in pure gaseous mixture and the mixture with $\alpha_{p0} = 10^{-5}$, the detonation is initiated at obstacle 8, i.e., at a distance of 1.19 m from the closed end of the channel.

In summary, detonation initiation in gas-particle mixtures in channels with obstacles can occur either at the corner of an obstacle as observed in pure gaseous mixtures or at the wall due to coupling of flame and leading shock wave. The process is governed by the accelerating effect of particles through flamelet generation and decelerating effect through energy and momentum absorption. Further, both the distance and time to DDT estimated in the current study (shown in Fig. 11) vary linearly with α_{p0} for $\alpha_{p0} = 10^{-4}$ to 10^{-3} .

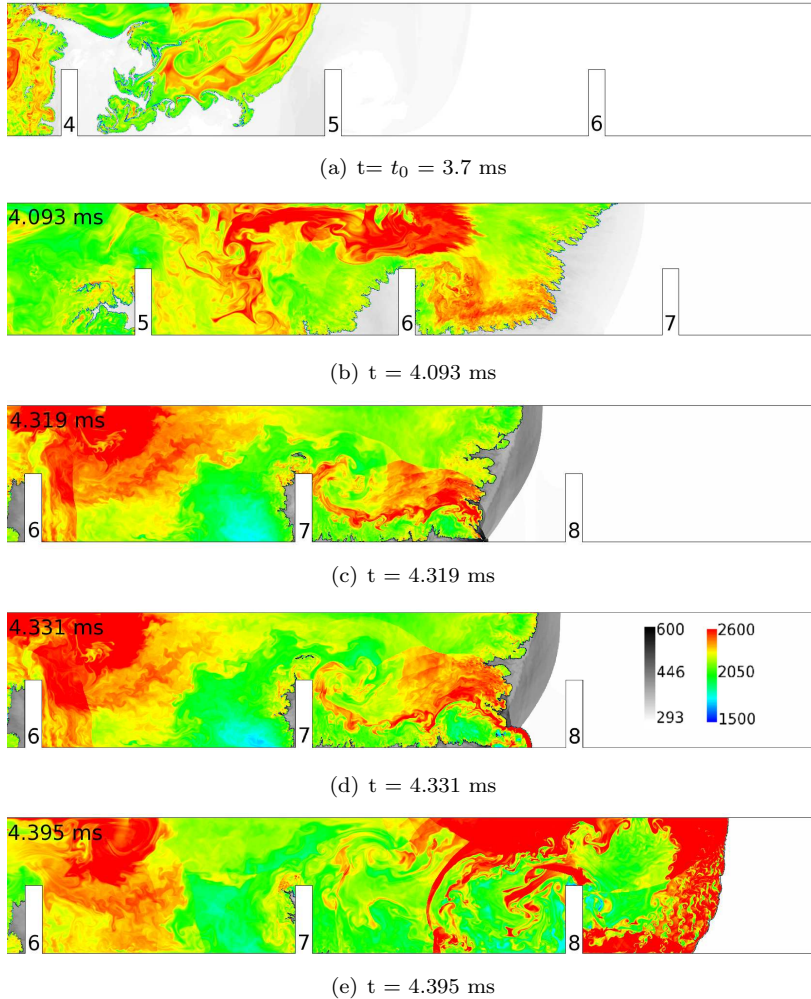


Figure 6. Flame acceleration and detonation initiation in a channel with inert particles. The half channel width is 8 cm, the blockage ratio is 0.5, $\alpha_{p0} = 5.0 \times 10^{-4}$ and $r_p = 8 \mu\text{m}$. The temperature range of the unburnt mixture is shown in gray scale and the burnt mixture is shown in color spectrum.

III.B.2. Effect of particle radius

The effect of particle size on DDT in gas-particle mixture is studied by considering inert particles of radius 2, 4 and $8 \mu\text{m}$. The particles are uniformly distributed in the channel starting from the location 80 cm from the closed end so as to obtain $\alpha_{p0} = 10^{-5}$. In all cases, the detonation initiation is observed at the corner of the obstacle 8 as observed for pure gaseous case and thus the distance to DDT evaluated by varying particle size is constant and is equal to 1.19 m. The time to DDT for different r_p shown in Fig. 12 varies slightly, about 0.1 ms, from the time to DDT for pure gaseous case. Decrease in r_p for fixed α_{p0} results in increase

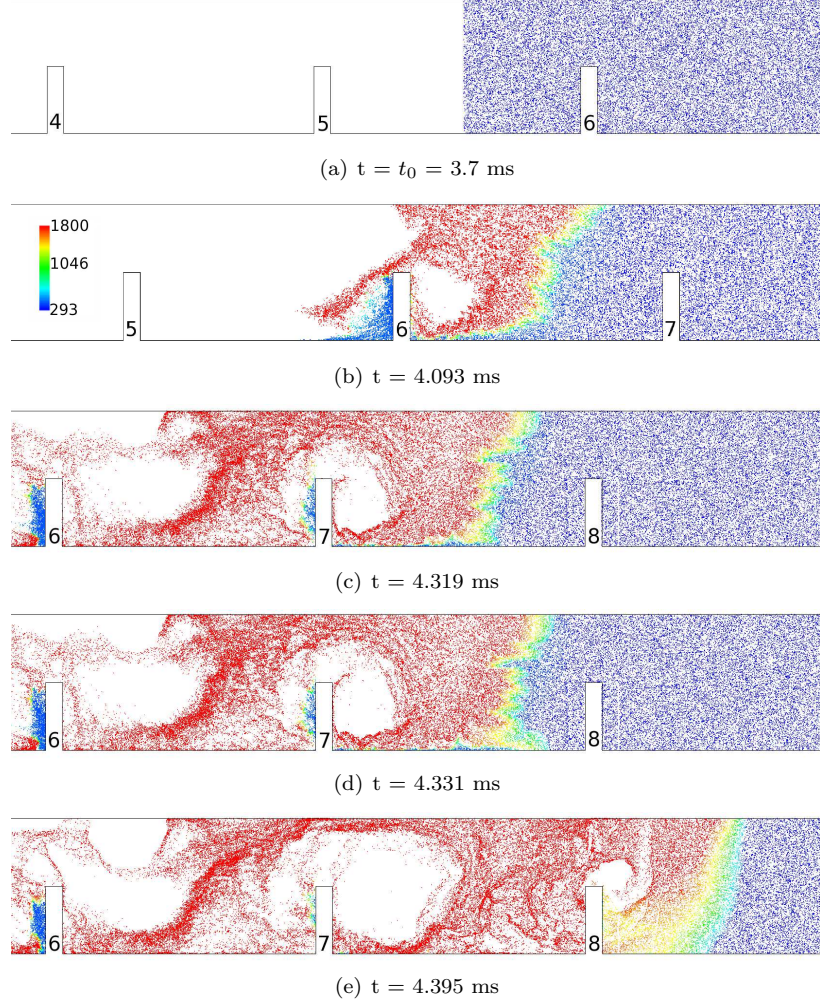


Figure 7. Particle dispersion in the channel as the flame accelerates and the detonation is initiated. The half channel width is 8 cm and the blockage ratio is 0.5. $\alpha_{p0} = 5.0 \times 10^{-4}$ and $r_p = 8 \mu\text{m}$. The temperature of the particles is shown in color spectrum.

in number of particles and thus a possibility of increase in energy and momentum absorption and flamelet generation. However, in the current study, $\alpha_{p0} = 10^{-5}$ is so dilute that the effects of particle size variation observed are negligible. This is shown in Fig. 13, where the overall flame surface is almost identical in each case. Also, Fig 8 shows that the flame acceleration in each case is almost identical. Thus, for α_{p0} considered, the effects of varying particle size are minor and the propagation of the flame and detonation initiation resemble the DDT in pure gaseous mixture.

IV. Conclusions

The process of deflagration-to-detonation transition in gas-particle mixtures is studied using inert (steel) particles and $H_2 - Air$ mixture. The reaction is modeled using single step Arrhenius kinetics and Lagrangian tracking is used to solve for the particle phase. Simulations in channels of half width 1, 2, 4, and 8 cm are performed to simulate the quasi-detonation and detonation regimes of DDT in channels with obstacles and to compare with the numerical and experimental results from literature. The results from the pure gaseous simulations are in agreement, qualitatively, with the past results.^{4,5} The process of DDT in gas-particle mixtures in channels with obstacles is studied by varying initial volume fraction of solid phase, α_{p0} , for fixed particle radius, r_p . The studies indicate that the inert particles control DDT in gas-particle mixtures by absorbing energy and momentum and generating flamelets. The particles, for $\alpha_{p0} = 10^{-4}$ and 5.0×10^{-4} ,

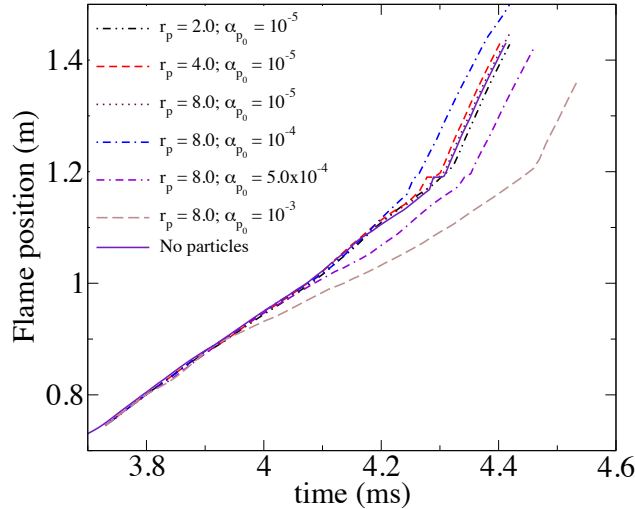


Figure 8. Variation of the position of the flame tip with time as the flame interacts with the inert particles. α_{p0} and r_p in each case is indicated. The half channel width is 8 cm and the blockage ratio is 0.5.

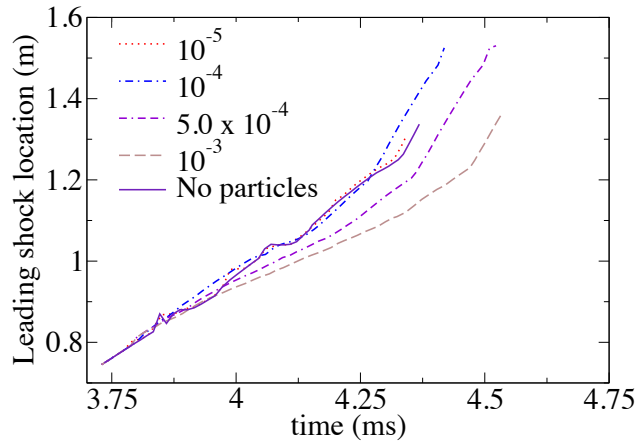


Figure 9. Variation of the position of the leading shock with time as the flame interacts with the inert particles. α_{p0} in each case is indicated and $r_p = 8 \mu\text{m}$. The half channel width is 8 cm and the blockage ratio is 0.5.

facilitated the flame acceleration and leading shock deceleration and the detonation was initiated at the wall unlike pure gaseous cases where the detonation is initiated at a corner connecting the wall and the obstacle. For $\alpha_{p0} = 10^{-5}$ and 10^{-3} , the flame could not couple with the leading shock wave and detonation initiation resembled DDT in pure gaseous mixture. The time and distance to DDT increased linearly with α_{p0} for $\alpha_{p0} = 10^{-4}$ to 10^{-3} . The effect of varying particle size for fixed $\alpha_{p0} = 10^{-5}$ is minor and the detonation initiation occurred at the corner formed by the wall and the obstacle 8 as observed in pure gaseous mixtures.

Acknowledgments

This work is supported by the Defense Threat Reduction Agency. The computational resources were provided by DOD HPC Centers at ERDC, ARL and NAVO.

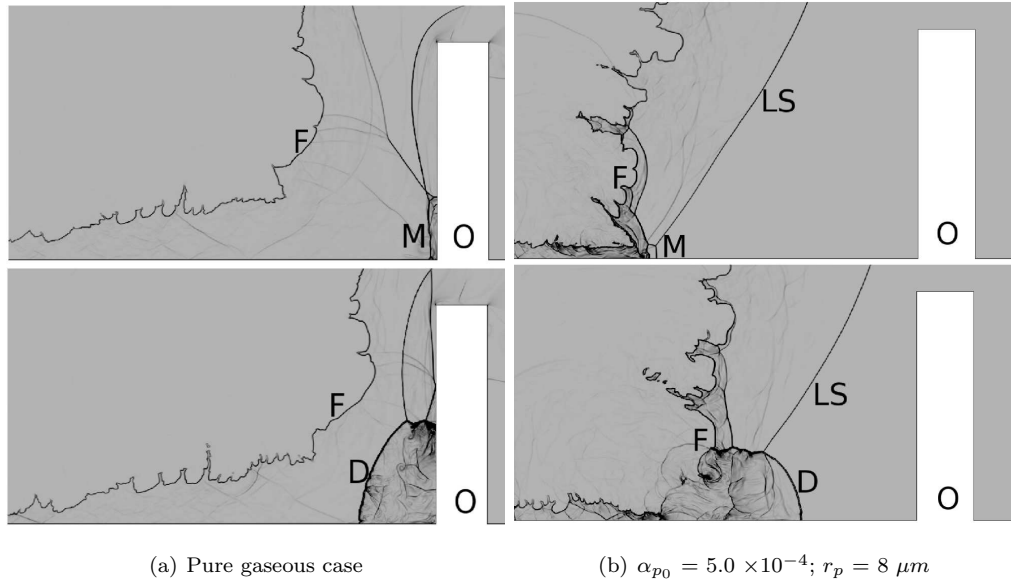


Figure 10. The detonation initiation at the bottom wall and at the obstacle. Here, density gradient is plotted. O - Obstacle; F - Flame; LS - Leading Shock; M - Mach stem; D - Detonation.

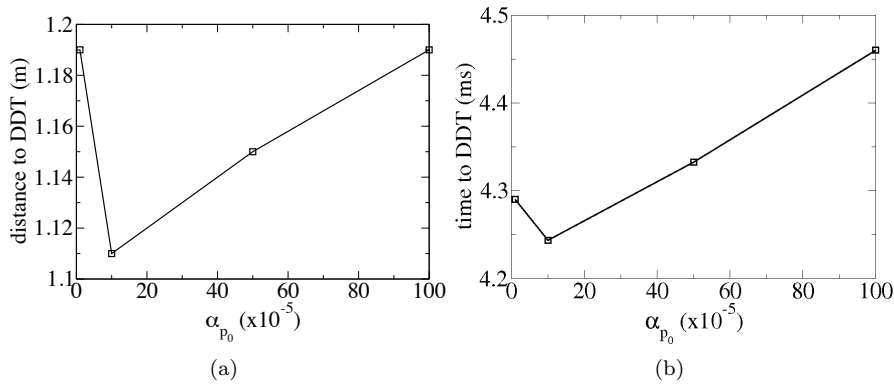


Figure 11. Distance and time to DDT for different initial solid phase volume fraction (α_{p_0}) for fixed particle radius, $r_p = 8 \mu\text{m}$. The half channel width is 8 cm and the blockage ratio is 0.5.

References

- ¹Ciccarelli, G. and Dorofeev, S., "Flame Acceleration and Transition to Detonation in Ducts," *Progress in Energy and Combustion Science*, Vol. 34, 2008, pp. 499–550.
- ²Bradley, D., Lawes, M., and Liu, K., "Turbulent Flame Speeds in Ducts and the Deflagration/Detonation Transition," *Combustion and Flame*, Vol. 154, 2008, pp. 96–108.
- ³Silvestrini, M., Genova, B., Parisi, G., and Trujillo, F. J. L., "Flame Acceleration and DDT Run-Up Distance for Smooth and Obstacles Filled Tubes," *Journal of Loss Prevention in the Process Industries*, Vol. 21, 2008, pp. 555–562.
- ⁴Gamezo, V. N., Ogawa, T., and Oran, E. S., "Flame Acceleration and DDT in Channels with Obstacles: Effect of Obstacle Spacing," *Combustion and Flames*, Vol. 155, 2008, pp. 302–315.
- ⁵Gamezo, V. N., Ogawa, T., and Oran, E. S., "Numerical Simulation of Flame Propagation and DDT in Obstructed Channels Filled with Hydrogen-Air Mixture," *Proceedings of the Combustion Institute*, Vol. 31, 2007, pp. 2463–2471.
- ⁶Oran, E. S. and Gamezo, V. N., "Origins of the Deflagration-to-Detonation Transition in Gas-Phase Combustion," *Combustion and Flame*, Vol. 148, 2007, pp. 4–47.
- ⁷Valiev, D., Bychkov, V., Akkerman, V., Law, C. K., and Eriksson, L.-E., "Flame Acceleration in Channels with Obstacles in the Deflagration-to-Detonation Transition," *Combustion and Flame*, Vol. 157, 2010, pp. 1012–1021.
- ⁸Baer, M. R. and Nunziato, J. W., "A Two-Phase Mixture Theory for the Deflagration-To-Detonation Transition (DDT) in Reactive Granular Materials," *International Journal of Multiphase Flow*, Vol. 12, No. 6, 1986, pp. 861–889.
- ⁹Borissov, A. A., *Dynamic Structure of Detonation in Gaseous and Dispersed Media*, Kluwer academic publishers, 1991.

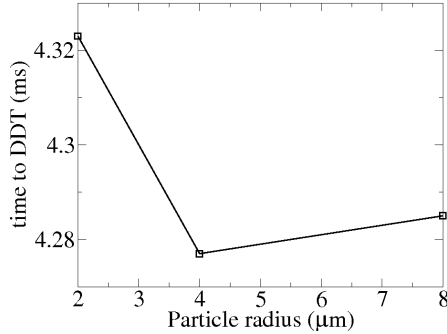


Figure 12. Time to DDT for particle radius (r_p) = 2, 4 and 8 μm for a fixed initial solid phase volume fraction, $\alpha_{p0} = 10^{-5}$. The half channel width is 8 cm and the blockage ratio is 0.5.

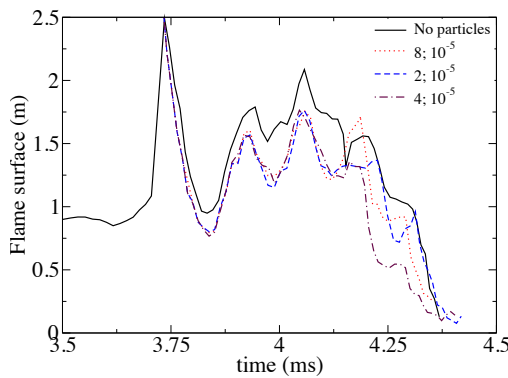


Figure 13. Flame surface variation with time for different r_p for a fixed initial solid phase volume fraction, $\alpha_{p0} = 10^{-5}$. The half channel width is 8 cm and the blockage ratio is 0.5.

¹⁰Kapila, A. K., Son, S. F., Bdzil, J. B., Menikoff, R., and Stewart, D. S., “Two-Phase Modeling of DDT: Structure of the Velocity-Relaxation Zone,” *Physics of Fluids*, Vol. 9, No. 12, 1997, pp. 3885–3897.

¹¹Zhang, F., Thibault, P. A., and Murray, S. B., “Transition from Deflagration to Detonation in an End Multiphase Slug,” *Combustion and Flame*, Vol. 114, 1998, pp. 13–25.

¹²Kapila, A. K., Menikoff, R., Bdzil, J. B., Son, S. F., and Stewart, D. S., “Two-Phase Modeling of Deflagration-to-Detonation Transition in Granular Materials: Reduced Equations,” *Physics of Fluids*, Vol. 13, No. 10, 2001, pp. 3002–3024.

¹³Balakrishnan, K., Nance, D. V., and Menon, S., “Simulation of Impulse Effects from Explosive Charges Containing Metal Particles,” *Shock Waves*, Vol. 20, 2010, pp. 217–239.

¹⁴Snider, D. M., “An incompressible three-dimensional multiphase particle-in-cell model for dense particle flows,” *Journal of Computational Physics*, Vol. 170, 2001, pp. 523–549.

¹⁵Balakrishnan, K. and Menon, S., “On the Role of Ambient Reactive Particles in the Mixing and Afterburn Behind Explosive Blast Waves,” *Combustion Science and Technology*, Vol. 182, 2010, pp. 186–214.

¹⁶Maxey, M. R. and Riley, J. J., “Equation of Motion for a Small Rigid Sphere in a Nonuniform Flow,” *Physics of Fluids*, Vol. 26, 1983, pp. 883.

¹⁷Papalexandris, M. V., “Numerical Simulation of Detonations in Mixtures of Gases and Solid Particles,” *Journal of Fluid Mechanics*, Vol. 507, 2004, pp. 95–142.

¹⁸Boiko, V. M., Kiselev, V. P., Keselev, S. P., Papyrin, A. P., Poplavsky, S. V., and Fomin, V. M., “Shock Wave Interaction With a Cloud of Particles,” *Shock Waves*, Vol. 7, 1997, pp. 275–285.

¹⁹Drake, R. M., “Discussion on the paper entitled ‘Forced convection heat transfer from an isothermal sphere to water’ by G. C. Violet and G. Leppert,” *ASME Journal of Heat Transfer*, Vol. 83, No. 2, 1961, pp. 170–179.

²⁰Einfeldt, B., “On Godunov-Type Methods for Gas Dynamics,” *SIAM J. Numer. Anal.*, Vol. 25, No. 2, 1988, pp. 294–318.

²¹Génin, F. and Menon, S., “Studies of Shock / Turbulent Shear Layer Interaction Using Large-Eddy Simulation,” *Computers & Fluids*, Vol. 39, 2010, pp. 800–819.

²²Balakrishnan, K., Nance, D. V., and Menon, S., “Numerical Study of Blast Characteristics from Detonation of Homogeneous Explosives,” *Shock Waves*, Vol. 20, 2010, pp. 147–162.

²³Gottiparthi, K. C., Génin, F., Srinivasan, S., and Menon, S., “Simulation of Cellular Detonation Structures in Ethylene-Oxygen Mixtures,” *AIAA Paper 2009-0437*, 2009.

²⁴Gottiparthi, K. C. and Menon, S., “Study of Interaction of Dense or Dilute Cloud of Inert and/or Reactive Particles with Cellular Detonation Structures,” *AIAA Paper 2010-0770*, 2010.

Flame Acceleration and Transition to Detonation in Gas-Particle Mixtures

K. C. Gottiparthi, S. Menon*

School of Aerospace Engineering, Georgia Institute of Technology, Atlanta, GA.

Abstract

Simulations of accelerating flames and deflagration-to-detonation transition (DDT) in gas-particle mixtures are presented in this article. Flame acceleration and subsequent detonation initiation are initially investigated in stoichiometric methane-air mixture or hydrogen-air mixture in channels with obstacles. These studies show good agreement with available experimental results. Detonation initiation in pure gaseous mixtures, in the current work, occurred due to hot spot generation by the leading shock wave - obstacle interaction. DDT in gas-particle mixtures is studied by allowing the accelerating flame to propagate through steel particle cloud of fixed initial volume fraction (α_{p0}). When α_{p0} is about 10^{-4} or above, the relative velocity of the leading shock and the flame is reduced allowing for the detonation initiation by leading shock-flame coupling. For α_{p0} nearly 10^{-5} or less, the detonation initiation was similar to that in the case of pure gaseous mixtures. These mechanisms are discussed in detail and the differences with pure gas cases are highlighted.

Introduction

When an ignition source is placed at the closed end of a channel filled with a combustible mixture a deflagration is generated. This deflagration accelerates and, with proper initial and boundary conditions, would transition to a detonation. This process of flame acceleration and DDT has attracted attention of several investigations over years with an intention to improve safety in industrial systems and provide novel propulsion devices. In many practical scenarios, such as in mining tunnels with coal dust and marsh gas, accelerating flames and DDT occur in two-phase mixtures. Due to several past studies [1-3] DDT in channels in gaseous mixtures has been investigated but the processes in gas-particle mixtures have been largely unexplored. In this paper we present both flame acceleration and DDT in channels with obstacles in gas-particle mixtures.

Numerical [1-2] and experimental [3] investigations of DDT in channels indicate the series of events leading to detonation initiation to be (1) flame acceleration due to flow evolution and instability generation, (2) leading shock wave formation and (3) transition to detonation and propagation of the detonation over the obstacles. Experimental studies of effect of sand particles of radius nearly 0.1-1.0 mm in stoichiometric hydrogen-air mixtures show that with increase in particle volume fraction the distance and time to DDT decrease [4]. Studies on DDT in dust mixtures suggest that the transition to detonation occurs based on reactivity and concentration of the dust particles [5]. However, there are no results available in the literature on the effect of inert particles on DDT in channels with obstacles. The role of particles on the propagation of an accelerating flame and shock wave and subsequent transition to a detonation is yet to be explored. We endeavor to investigate this in the current study.

In this paper, the process of flame acceleration and DDT in stoichiometric methane-air and hydrogen-air

mixtures in channels with obstacles is discussed. Blockage ratios, the ratio of obstacle height to half channel width, 0.3, 0.5 and 0.6 are considered. For two-phase cases, steel particles are distributed in the channel based on α_{p0} . Here, α_{p0} is evaluated as the initial ratio of the volume occupied by the particles to the volume of the domain over which particles are distributed. In this article α_{p0} in range of 10^{-5} to 10^{-3} are considered. In all cases, the flame and shock speeds are evaluated and the process of transition to detonation is analyzed.

Formulation and Numerical Setup

In order to conduct numerical investigation of DDT in gas-particle mixtures, the unsteady, compressible, multi-phase Navier-Stokes equations for reacting gas flows are used to solve for the gas phase, and Lagrangian tracking approach is used to solve for the position, the mass, the velocity and the temperature of the solid particles [6-7]. Single-step Arrhenius kinetics based on the parameters described in previous numerical studies of DDT in hydrogen-air [1] and methane-air [2] mixtures are employed here. The momentum and the energy transfer between the two phases are evaluated based on the empirical expressions for the drag coefficient (C_d) and the Nusselt number (Nu) [6]. The complete set of governing equations used in the current study can be found elsewhere [1].

An approximate Riemann solver with Monotone Upstream-centered Schemes for Conservative Laws (MUSCL) reconstruction and monotonized-central limiter is used to solve the governing equations for the gas phase. The Riemann solver used is a hybrid solver, which employs the Harten-Lax-van Leer (HLL) flux solver with contact wave (HLLC) everywhere except in the shock-capturing region, where in the direction transverse to the shock the HLLE (HLL by Einfeldt [8]) Riemann solver is used. The scheme is second order accurate in both space and time. Detailed validation of this approach to simulate shock-turbulence interaction

* Corresponding author: suresh.menon@ae.gatech.edu

Proceedings of the European Combustion Meeting 2013

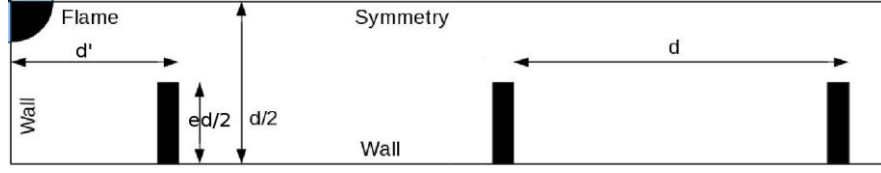


Fig. 1. Computational domain used for simulation of DDT in channel with obstacles. Here, e is the blockage ratio. $d' = d$ for Cases G1 and G2 and $d' = d/2$ for Cases G3, P1, P2 and P3 (see Table 1). The location of equally spaced obstacles and the boundary conditions employed are indicated.

Case	d (cm)	e	Premixed mixture	a_{p0}	Number of particles
G1	17.4	0.3	Methane-air	-	-
G2	17.4	0.6	Methane-air	-	-
G3	16.0	0.5	Hydrogen-air	-	-
P1	16.0	0.5	Hydrogen-air	1.0×10^{-5}	23128
P2	16.0	0.5	Hydrogen-air	1.0×10^{-4}	231280
P3	16.0	0.5	Hydrogen-air	5.0×10^{-4}	1155860

Table 1. Cases considered in this article to study DDT in gas-particle mixtures. Δx_{\min} for Cases G1 and G2 is 167 μm and in all other cases $\Delta x_{\min} = 69.5 \mu\text{m}$. Here, Cases G1, G2 and G3 are pure gas-phase cases and Cases P1, P2 and P3 are two-phase cases.

[9] and detonations/ explosions in multi-phase flows [6-7] has already been reported. The governing equations for solid phase are integrated in time using 4th-order Runge-Kutta scheme.

The domain shown in Fig. 1 is discretized using a structured grid. The grid is configured to be fine in the regions where flame, shocks and flow structures exist and is coarsened ($\Delta x_{\max} = 0.2 \text{ cm}$) elsewhere i.e. in the regions where the gaseous mixture completely comprises of products or reactants away from the flame/shock structures. The minimum computational cell width, Δx_{\min} is chosen to resolve the laminar flame thickness and half -reaction zone thickness of the detonation [1-2] in each case. Here, Δx_{\min} corresponds to 3 points per flame thickness in Cases G1 and G2, and 5 points per flame thickness in all other cases. The channel dimensions and the blockage ratios used in each case are shown in Table 1. Also, the obstacle width in Cases G1 and G2 is 2 cm and 1 cm in Cases G3, P1, P2 and P3. In all cases the initial pressure and the initial temperature of the gas phase is 1 atm and 298K, respectively. For gas-particle cases (P1 to P3) presented here, the particle radius, $r_p = 8 \mu\text{m}$ is considered. Studies with $r_p = 2$ and 4 μm have been reported earlier [1], albeit for $a_{p0} = 1.0 \times 10^{-5}$. The flame is ignited in the channel by means of a hot zone of product gases where the temperature is set to be $2.0T_b$, where T_b is the adiabatic flame temperature of the mixture considered.

The boundary conditions employed in the current studies are indicated in Fig. 1. Here all the walls, including the surfaces of the obstacles, are set to be adiabatic no-slip reflecting surfaces. Also, the flow properties and derivatives at the out flow of the channel are evaluated by extrapolation. As the flame propagates in the channel, the deflagration front and shock front are tracked and the flame/shock speed in each case are evaluated. The mechanism for detonation transition in each case is identified and presented along with experimental comparisons, where available, in the next section.

Results and Discussion

Before investigating flame acceleration and transition to detonation in gas-particle mixtures, studies of DDT in pure gaseous methane-air and hydrogen-air mixtures are performed. The channel configurations in these cases are chosen based on available experimental [3] and numerical investigations [2]. The results obtained under the current work are compared with past results and are further used to study the interaction of particles with accelerating flames.

Transition to detonation in stoichiometric methane-air mixture is studied by considering two blockage ratios, $e = 0.3$ and 0.6, i.e. Cases G1 and G2. The flame initially ignited at the closed end of the channel propagates into the premixed fuel-air mixture and the expanding product gases generate flow over the obstacles in the channel. This flow produces Rayleigh-Taylor and Richtmyer-Meshkov instabilities [1-2], which accelerates the flame further by increasing the

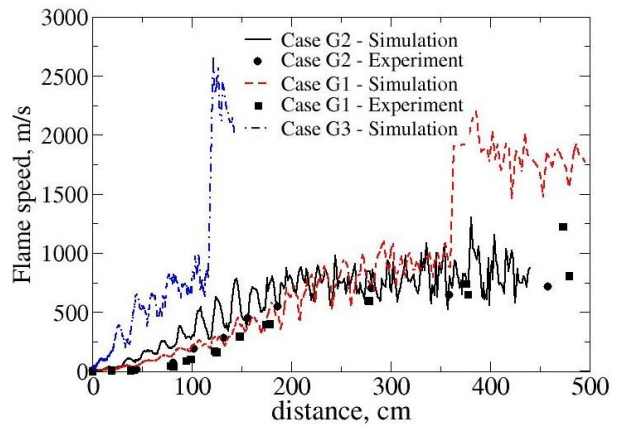


Fig. 2. Speed of the flame at different locations in the channel as the flame accelerates. Here, flame speeds for Cases G1, G2 and G3 (see Table 1) are plotted along with corresponding experimental results [3].

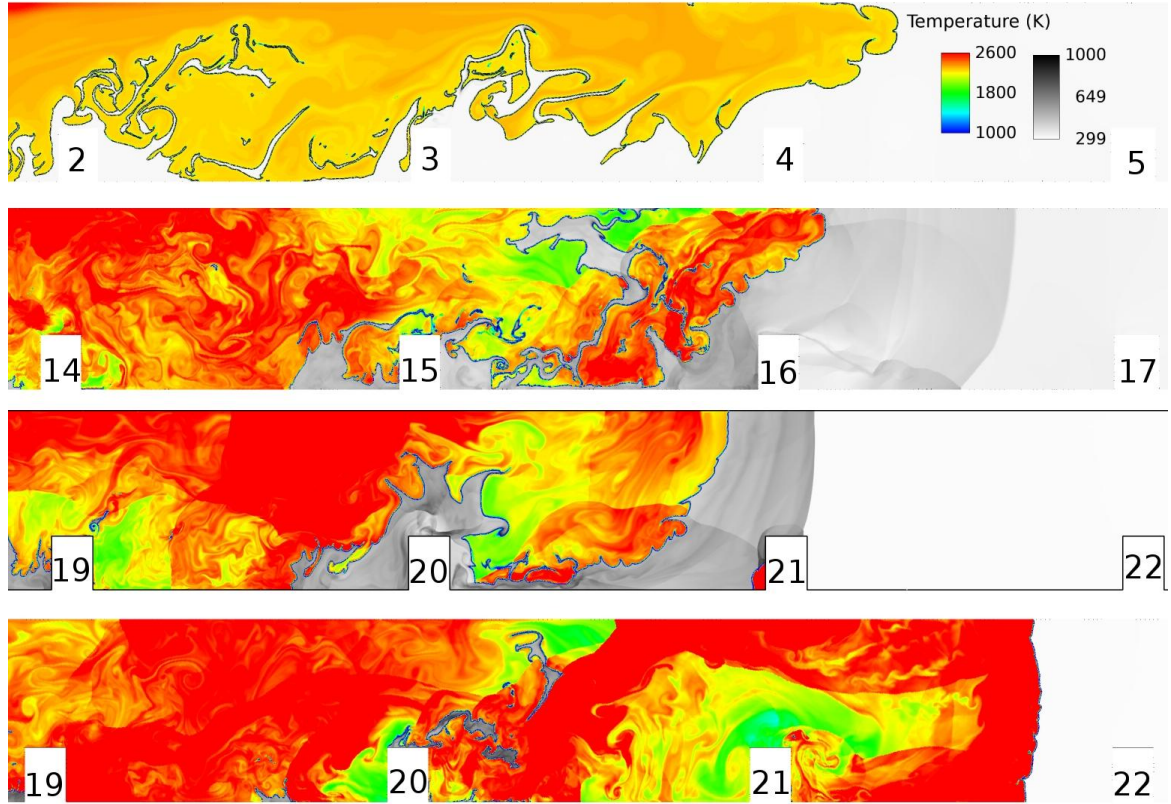


Fig. 3. Flame acceleration and detonation initiation in Case G1. The obstacle number is indicated in each figure. Color scale is used to indicate the post-combustion flow and grey scale is used to show the post-shock features.

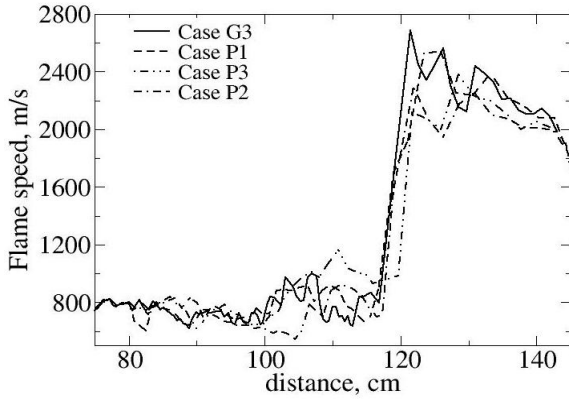
flame surface area. The flame speed evaluated as the flame propagates in the channel (shown in Fig. 2) indicates that the flame accelerates to a speed nearly 700 m/s before a leading shock wave is formed ahead of the flame. As leading shock (LS) wave and the flame couple propagate in the channel, the shock acquires sufficient strength to generate a hot spot due to shock-obstacle interaction. In case G1, at Obstacle 21, the hot spot produced initiates a detonation, which overtakes LS and propagates into the ambient fuel-air mixture.

The chronology of acceleration of flame and detonation initiation in Case G1 is shown in Fig. 3. Note that, in this case (see Fig. 3), the detonation initiation occurs away from the primary flame at the obstacle. Also, in Case G1, the constricted channel width, i.e. the width of the channel at the obstacle locations, is sufficient for self-propagation of the detonation [2-3, 10]. The detonation diffracts over the obstacle and survives to propagate into the ambient gas. However, in Case G2, the channel is constricted enough to allow only the propagation of accelerating flame and even though local hot spots generate detonations these do not survive to propagate and overtake LS. Thus, the flame speed in this case reaches nearly 700 m/s and the deflagration propagates in a choked regime. This is shown in Fig. 2, where the flame speed comparison with experimental results [3] indicates good agreement with the current work. However, in Case G1, the model employed here predicts transition distance to be 365 cm unlike the experimental result (nearly 550 cm).

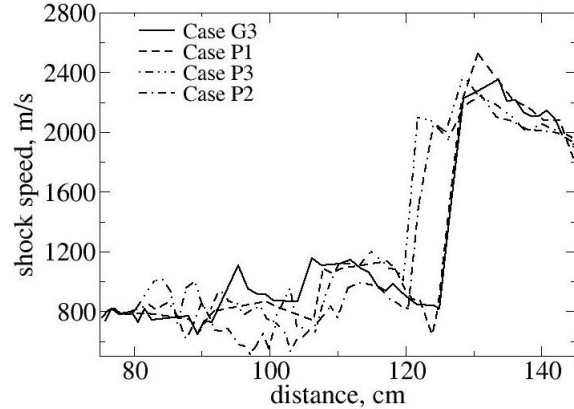
Numerical results [2] reported earlier using the modeling employed here are consistent with the current results.

The process of flame acceleration in Case G3 is similar to that presented for Case G1. Here, the transition to detonation occurs at 119 cm at Obstacle 8. In Fig. 2, the transition to detonation in Cases G1 and G2 can be observed at the location of sudden jump in flame speed. After transition to detonation in these cases, the speed approaches the detonation speed of the mixture considered. Note that Case G3 has been simulated to ascertain the propagation of the detonation over the next two successive obstacles. Thus Fig. 2 shows the flame speed variation in this case till distance = 150 cm. Also, in comparison to Cases G1 and G2, the length of the channel in which the accelerated flame propagates with almost constant average speed is relatively small owing to the properties of the fuel used.

When the flame propagates through gas-particle mixture, the interaction between the two phases changes the flame speed and the shock strength. Inert particles which are initially in ambient conditions absorb energy and momentum from the flow. The amount of energy and momentum transfer is based on α_{p0} . Here, we present three cases which show the effect of α_{p0} on transition to detonation. In case P1, despite the energy and momentum transfer to particles, only negligible change in the flame speed and the shock strength occur in comparison to Case G3 (see Fig. 4). Thus, in this case, the process of flame acceleration and detonation



(a)



(b)

Fig. 4. (a) Flame and (b) shock speed variation in the channel for Cases G3, P1-P3.

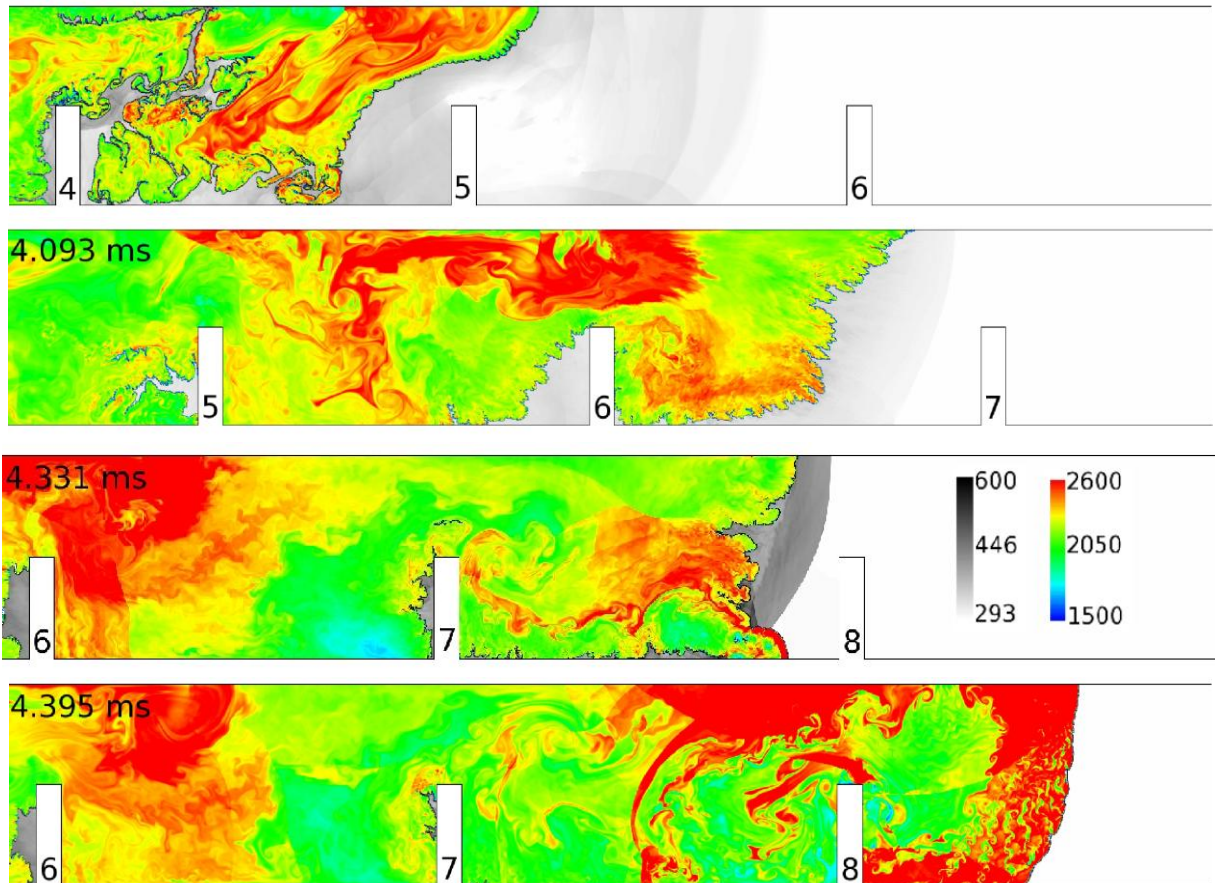


Fig. 5. Flame acceleration and detonation initiation in Case P3. Here, post-flame temperature is shown in color and pre-flame conditions are plotted in grey scale.

initiation is same as described in Case G3.

In Case P2, LS strength reduces enough such that the flame accelerating through the gas-particle mixture reaches the shock wave. This is shown in Fig. 4 where the shock propagation, in comparison to Cases P1 and G3, is slow. The shock wave generates a strong Mach stem at the wall of the channel which couples with the flame and initiates a detonation. This detonation spreads through the ambient flow propagating past the next obstacle. Thus, in this case unlike Case G3, the transition to detonation occurs away from the obstacle. This same process of detonation initiation (as in Case

P2) occurs in Case P3 and is shown in Fig. 5. The difference in the chronology of events between pure gaseous and gas-particle cases is evident from Figs. 3 and 5. Also, in Fig. 4, the shock speed and the flame speed coincide indicating detonation initiation at distance 116 cm.

The particles are also affected and dispersed or clustered by the flame and the flow in the channel. Due to the shock-particle interaction the particles are concentrated at the corners of the obstacles creating regions of particle clusters. However, the regions where vortices are generated, like top of obstacles, the particles

are dispersed away forming relatively particle free zones. These regions can be observed in Fig. 6. Here, the sequence of figures corresponds to the sequence of figures shown in Fig. 5. Although particle clusters are formed in the cases considered here, in all cases, the volume fraction of solid phase in the dense regions does not exceed 10^{-3} . So the dilute gas-particle flow assumption made is not violated.

In summary, inert particles influence the flame acceleration and transition to detonation through energy and momentum transfer. In cases where the particle concentration is small, as in Case P1, the flame behavior is identical to that observed in pure gaseous cases. However, when particles form concentrations large enough to reduce leading shock strength, the flame couples with the shock wave and a detonation is initiated as a result of the LS-flame couple (as in Cases P2 and P3). This difference in detonation initiation between Cases G3 and P3 is clearly illustrated in Fig. 7.

Note that the Mach stem, in Case G3 (or P1), reaches the obstacle before flame can reach LS forming a detonation at the obstacle. In Cases P2 and P3, the shock wave is slowed down sufficiently by the particles, which enables the flame-shock couple formation.

Conclusions

Numerical investigations of flame acceleration and transition to detonation in gas-particle flows have been presented. The flame speeds and the process of DDT in pure gaseous mixtures obtained in the current study agree well with the available experimental and numerical results. In gas-particle mixtures, based on the initial particle volume fraction, leading shock strength changed such that the flame-shock couple is formed and detonation is initiated. Thus, unlike gaseous cases, gas-particle cases provide an alternative mechanism for detonation initiation for the same fuel-air mixture and geometric configuration of the channel.

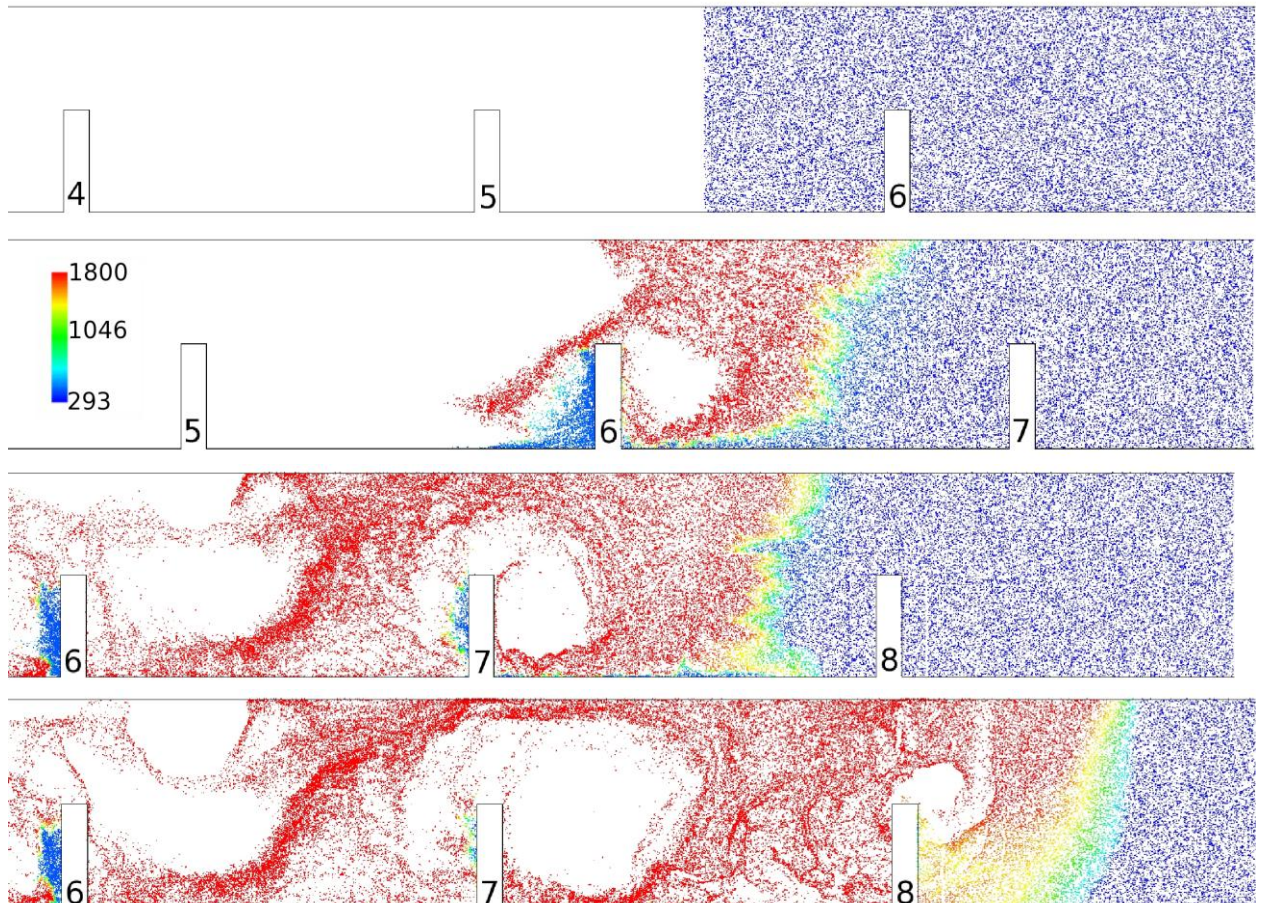


Fig. 6. Dispersion of particles by accelerating flame and shock waves in Case P3. The temperature of particles is indicated in color scale. The relatively cold particle clusters on the left side of obstacles can be noticed. Also, large regions devoid of particles are observed emanating from the top of the obstacles. Note that the first figure shows the initial particle distribution in the channel starting from distance = 80 cm.

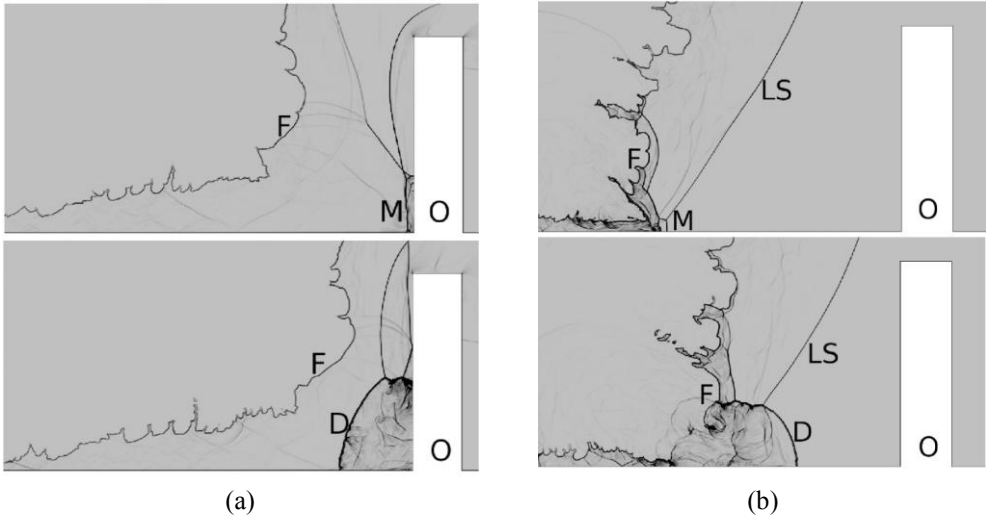


Fig. 7. Detonation initiation (a) at the obstacle (Case G3) and (b) at the wall (Case P3). The labels F, M, D, O and LS indicate the flame, Mach stem, detonation, obstacle and the leading shock.

Acknowledgements

This work is supported by the Defense Threat Reduction Agency (Dr. Suhithi Peiris, Program Manager). The computational resources were provided under DoD HPCMP challenge project by DoD Supercomputing Resource Centers at U. S. Air Force Research Laboratory and U. S. Army Engineer Research and Development Center.

References

- [1] K. C. Gottiparthi, S. Menon, Study of deflagration-to-detonation transition in gas-particle mixtures, in: 49th AIAA Aerospace Sciences Meeting and Exhibit, Orlando, Florida, AIAA Paper 2011-0801, 2011.
- [2] D. A. Kessler, V. N. Gamezo, E. S. Oran, Combust. Flame 157 (2010) 2063-2077.
- [3] M. Kuznetsov, G. Ciccarelli, S. Dorofeev, V. Alekseev, Yu. Yankin, T. H. Kim, Shock Waves 12 (2002) 215-220.
- [4] A. A. Borisov (Ed.), Dynamic Structure of Detonation in Gaseous and Dispersed Media, Kluwer academic publishers, Dordrecht, 1991, p. 267-311.
- [5] P. Wolanski, Prog. Astronaut. Aeronaut. 132 (1990) 3-31.
- [6] K. C. Gottiparthi, S. Menon, Combust. Sci. Technol. 184 (2012) 406-433.
- [7] K. Balakrishnan, S. Menon, Combust. Sci. Technol. 182 (2010) 186-214.
- [8] B. Einfeldt, SIAM J. Numer. Anal. 25 (1988) 294-318.
- [9] F. Genin, S. Menon, Comput. Fluids 39 (2010) 800-819.
- [10] J. H. S. Lee, The Detonation Phenomenon, Cambridge University Press, New York, 2008.

Title: Multi-Scale Simulation of Deflagration-to-Detonation Transition in Turbulent Dense Two-Phase Reactive Mixtures

HPCMP Computation project number: C5J

Project Lead: Prof. Suresh Menon

suresh.menon@ae.gatech.edu

Keywords: Detonation, Reactive particles, Two-phase flow

Sponsor Contact: Dr. Suhithi Peiris

suhithi.peiris@dtra.mil

DTRA, 8725, Kingman Road, Fort Belvoir, VA 22060.

User Contact: Prof. Suresh Menon

suresh.menon@ae.gatech.edu

School of Aerospace Engineering,
270, Ferst dr., Atlanta, GA 30332.

Multi-Scale Simulation of Deflagration-to-Detonation Transition in Turbulent Dense Two-Phase Reactive Mixtures

Kalyana C. Gottiparthi, Joseph C. Schulz and Suresh Menon

School of Aerospace Engineering, Georgia Institute of Technology, Atlanta, GA, 30332-0150, USA
{kalyan.gottiparthi, jschulz, suresh.menon} @ gatech.edu

Abstract

The deflagration-to-detonation transition (DDT) of stoichiometric methane-air mixtures in a channel with obstacles is simulated. The goal of the investigation is to determine how DDT varies in two-phase gas-particle mixtures. Investigations are initially performed in pure gaseous stoichiometric methane-air mixtures and show good agreement to available experiment data. From this data, an initial reference condition for an accelerated flame is chosen and then set such that it can propagate through a gas-particle mixture of different initial volume fractions (α_{p0}) where the particles are either inert and reactive. The time and distance to DDT are quantified for each case and compared to the pure gaseous results. In single-phase simulations, the DDT occurs from a leading shock wave interacting at an obstacle wall. In gas-particle mixtures, however, the leading shock strength is reduced due to momentum and energy transfer between the gas and the particles, which results in an increase in the time and distance to DDT.

1 Introduction

Chemical/biological (CB) agent neutralization in post-detonation turbulent flows is a highly transient phenomena occurring over a wide range of characteristic length and time scales. The geometry of the target structure adds additional complexities, such as re-circulating flow regions behind obstacles that alter the mixing and combustion physics. The knowledge of these processes is vital for development of effective Agent Defeat (AD) strategies. A fundamental problem occurring in many AD scenarios is deflagration-to-detonation transition (DDT) since in any reactive mixture, a confined flame can easily transition to detonation and alter the survival of CB agents. With a primary focus being on the role solid particles play on DDT, the process of flame acceleration and transition to detonation in gas-particle mixtures is investigated.

Detonations in reactive gaseous mixtures are initiated either by direct initiation or through DDT (Lee, 2008). Direct initiation occurs when an ignition source of sufficient strength results in the fast coupling of a shock wave and reaction front to form a detonation. This is in contrast to the DDT process, which occurs when a comparatively weak ignition source results in a propagating deflagration. With suitable initial and boundary conditions, the deflagration eventually accelerates to form a detonation. Many investigations, both experimental and numerical, have been performed to understand the multi-scale phenomena that result in DDT (Kuznetsov et al., 2002; Silvestrini et al., 2008). Most of these studies are based on pure gaseous reactive mixtures. Only a few studies have investigated DDT in multi-phase mixtures (Wolanski, 1990; Kapila et al., 2001). A two-phase theory for DDT in reactive granular materials is provided by Baer and Nunziato (1986) to estimate the transition distance. Studies of DDT in dust mixtures (Wolanski, 1990) were reported, which suggest that DDT in grain dust mixtures occurs based on the reactivity and the concentration of the particles. However, in all these investigations, the processes involved in DDT in gas-particle mixtures, are not explored and to the authors' knowledge there are no results available in the literature reporting the influence of particles, either inert or reactive, on DDT in channels with or without obstacles.

Due to the unique nature of the threat posed by CB agents, there is a critical need to develop a first principle simulation methodology that can be used a priori to evaluate the threat and aid in defining optimum threat countermeasures. As a part of a multi-year research, sponsored by Defense Threat Reduction Agency, novel approaches to simulate destruction

of CB agents using fuel mixtures that can mix and burn with aerosolized materials behind strong blast waves created by targeted detonation, are being developed. These simulation strategies aim to provide accurate and reliable predictions of AD scenarios when implemented on actual targets as well as to develop new strategies to handle unforeseen scenarios. DDT modeling covers the entire gamut of the problem areas of direct interest and is a challenge because of the physical complexity of the many processes occurring in the flow and interacting across a wide-range of scales. The results obtained during this phase of the challenge project are presented here with focus on the DDT in two-phase mixtures with reactive particles.

This paper is organized as follows. The second section of this paper summarizes the numerical method used and the performance of the code (LESLIE3D). In the third section, simulations in the pure gas phase mixtures, which form the base for the two-phase simulations, and the effect of volume loading on DDT are discussed. Conclusions from the current work are summarized in Section four. Finally, Sections five and six provide the significance of the current work to DoD and the impact of the HPCMP resources, respectively.

2 Formulation and Performance of the Code

2.1 Numerical method and setup

The unsteady, compressible, multi-phase Navier-Stokes equations for reacting gas flows are used to simulate the gas-phase flow. The position, mass, velocity and temperature of each solid particle is deterministically tracked using a Lagrangian approach (Balakrishnan et al., 2010). Numerically, the gas-phase governing equations are solved using an upwind scheme based on a hybrid approximate HLLC/E Riemann solver with Monotone Upstream-centered Schemes for Conservative Laws (MUSCL) reconstruction and a monotonized-central limiter. The Riemann solver dynamically switches from the HLLC Riemann solver to a HLLE Riemann solver in directions transverse to the propagating shock (Einfeldt, 1988). The scheme is second order accurate in both time and space, although its spatial accuracy decreases in the region where the discontinuity is present. The solid-phase governing equations are solved using a 4th order Runge-Kutta scheme. More details of the current modeling approach and its application to studies of shock-turbulence interaction (Génin and Menon, 2010) and two-phase detonation (Gottiparthi and Menon, 2012) can be found in the cited references.

The parameter set used to model DDT in CH_4 -air mixtures is presented elsewhere (Kessler et al., 2010). In cases with reactive particles, the heat release due to combustion of the particle, Q_p , and the activation energy for particle reaction rate, Ea_p are set as indicated in Table 1. Expressions for the drag coefficient (C_D), the Nusselt number (Nu) and the solid-phase mass transfer rate are discussed in previous work (Gottiparthi and Menon, 2012; Balakrishnan et al., 2010).

The computational domain and boundary conditions used in this study are shown in Figure 1. The surfaces of the walls and obstacles are adiabatic no-slip reflecting boundaries. At the outlet of the channel the properties are extrapolated and a symmetry condition is set at the half channel width. These boundary conditions are similar to the conditions used in previous studies (Gottiparthi and Menon, 2012b). The computational grid is refined only in the regions where the flame and shock exist and then coarsened in the regions where the fuel is either completely burnt or unburnt and no flow gradients exist. The minimum grid resolution is $\Delta_{min} = 166 \mu\text{m}$, which corresponds to resolution of 4 points in the flame thickness ($x_l = 0.044 \text{ cm}$). This grid resolution is chosen based on previous grid-independent studies (Kessler et al., 2010; Gottiparthi and Menon, 2011).

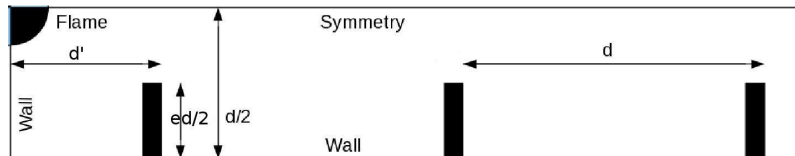


Figure 1. Computational domain used for simulation of DDT in channel with obstacles. Here, e is the blockage ratio and $d' = d$ is the distance of the first obstacle from the closed end of the channel. The location of equally spaced obstacles and the boundary conditions employed are indicated.

The particles are defined as having the properties of aluminum (i.e. C_p and ρ_p). Table 1 lists the initial solid phase

conditions, the various cases, the number of particles, and the initial volume fraction of the solid phase for each case. Only results with particle radii (r_p) of $16 \mu\text{m}$ are present here. Additional cases with different particle radii can be found elsewhere (Gottiparthi and Menon, 2011). The flame is ignited by a hot region of burnt mixture in the upper left corner of the domain. The temperature in this region is set to be $2.0T_b$, where $T_b = 2210\text{K}$ is the post-flame temperature of a stoichiometric CH₄-air mixture. This is ‘soft’ mode ignition, i.e., the energy provided for the flame ignition is of the order of the energy release due to the flame.

Table 1. Number of particles tracked in each case (i.e. for a particular α_{p0}) in the current study. The diameter of the channel (d) is 17.4 cm in all cases presented here. The radius of particles $r_p = 16.0 \mu\text{m}$ and are distributed over length = 165.0 cm and over the entire half width (8.7 cm), and are located at 235.0 cm from the closed end of the channel. The gas phase setup for all two-phase cases is same as Case G1. Also, $q_r = Q_p/Q$ and $e_r = Eap/Ea$ are provided. Here, Q and Ea are the heat release and activation energy for the gas-phase, respectively.

Case	e	α_{p0}	Number of particles	q_r	e_r
Without particles					
G1	0.3	-	-	-	-
G2	0.6	-	-	-	-
With particles					
I1	0.3	1.0×10^{-5}	13470	0.0	0.0
I2	0.3	5.0×10^{-5}	67350	0.0	0.0
R1	0.3	1.0×10^{-5}	13470	1.0	1.0
R2	0.3	5.0×10^{-5}	67350	1.0	1.0
R3	0.3	1.0×10^{-4}	134700	1.0	1.0
R4	0.3	1.0×10^{-5}	13470	1.0	0.5
R5	0.3	1.0×10^{-5}	13470	0.5	1.0

2.2 Code scaling

The speed-up and efficiency Gottiparthi and Menon (2012b) of the code for the representative case, Case G1, on Spirit (SGI Ice X) is shown in Fig. 2. The scaling of the code is very good and the efficiency remained above 90 % over the wide range of processors used, i.e. from 128 to 4000. Most of the cases presented in this paper have been run using 1000 processors where the efficiency is nearly 90 %. Eventhough each particle is deterministically tracked in the case of two-phase flow, Case R1, the speed up and efficiency are good in comparison to other cases.

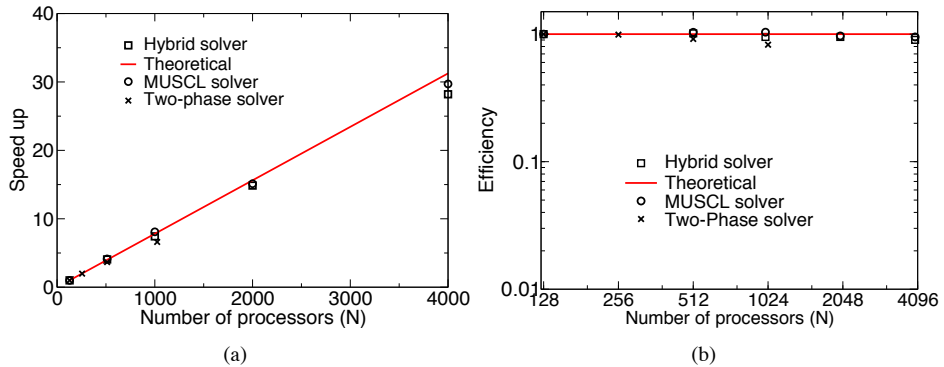


Figure 2. (a) Speed up and (b) efficiency with MUSCL, hybrid (2nd-order centered/3rd-order MUSCL scheme) and two-phase solvers (Case R1) on Spirit (SGI Ice X). N_{ref} is 128.

3 Results and Discussion

The pure gaseous simulations are validated based on comparisons to experimental data available in the literature. These results are discussed in this section. Following that is a discussion of the gas-particle simulations where the accelerated flame obtained from pure gaseous simulations is used to study the effect solid particles have on DDT.

3.1 DDT in pure gaseous mixtures

Beginning with an ignited flame kernel, the surface of the flame slowly increases as it propagates through the mixture. Eventually, flow instabilities such as Kelvin-Helmholtz (KH), Rayleigh-Taylor (RT) and Richtmyer-Meshkov (RM) instabilities (Kessler et al., 2010; Gottiparthi and Menon, 2011), trigger a non-linear growth in the flame surface thereby increasing the flame velocity, as shown in Fig. 3 (a). Once the flow ahead of the accelerating flame is compressed enough to form a leading shock, hot-spot is formed due to the reflection of the leading shock wave at the obstacle wall. The detonation, thus initiated by the hot spot, propagates into the flow across the successive obstacles. This process of flame acceleration and detonation initiation for Case G1 is shown in Fig. 4. In this case, the distance to DDT is about 365 cm (at Obstacle 21) and time to DDT is 37.7 msec.

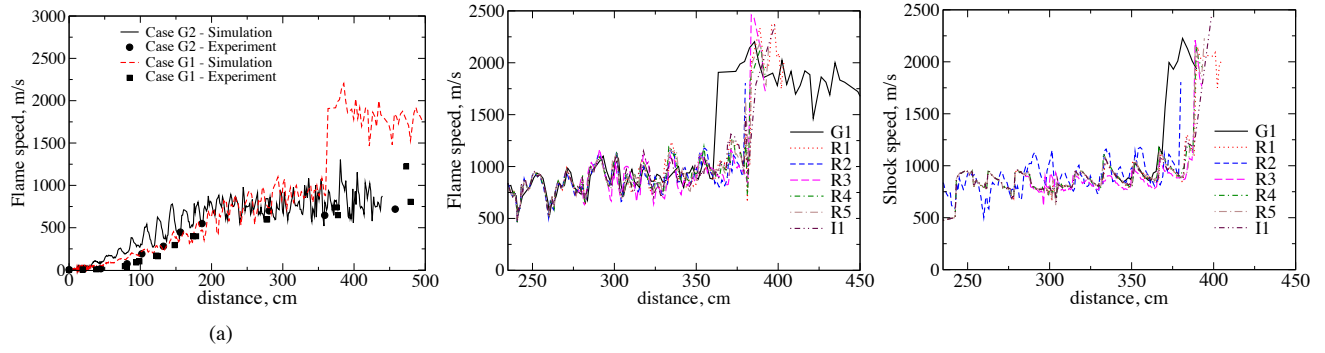


Figure 3. (a) and (b) Flame speed, and (c) shock speed at different locations in the channel for Cases G1,G2,I1 and R1-R5. Corresponding experimental results (Kuznetsov et al., 2002) are also shown.

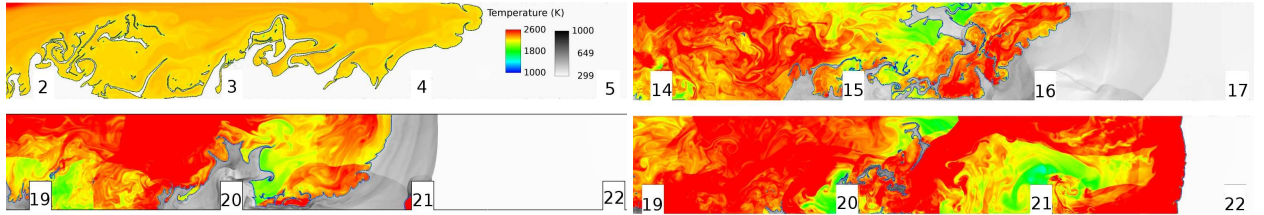


Figure 4. Flame acceleration, and initiation and propagation of detonation in channel with obstacles. The half channel width is 8.7 cm and the blockage ratio is 0.3 (Case G1). Notice that the detonation is initiated due to the shock-obstacle interaction. The temperature range of the unburnt mixture is shown in gray scale and the burnt mixture is shown in color spectrum.

Varying the blockage ratio in the channel affects the flame acceleration and subsequent detonation initiation. For instance if blockage ratio is too high, the flow is constricted such that only the flame can propagate through the channel. While local hot spots generate detonations, these never survive to overtake the leading shock. Thus in this chocked regime, case G2, the flame speed does not increase past 700 m/s (see Fig. 3 (a)) matching the experimental measurements of this configuration

rather well. In more ideal situations, case G1, the blockage ratio is low enough that DDT occurs at 365 cm, which is similar to prior numerical simulations (Kessler et al., 2010), but occurring earlier than the experimental data (nearly 550 cm).

3.2 DDT in gas-particle mixtures

When the flame propagates through a gas-particle mixture, the interaction between the two phases changes the flame speed and the shock strength. Inert particles absorb energy and momentum, the amount of which is based on the initial volume fraction of the flow. In the current work, the initial volume fraction is varied from α_{p0} from 10^{-5} to 10^{-4} for a fixed particle radius $16\mu\text{m}$. In all cases with particles, the leading shock strength was reduced in comparison to Case G1 as shown in Fig. 3 (c). Thus, the detonation initiation was delayed in Cases R1-R5 and I1 by 17.4 cm and 0.2 msec. Here again, irrespective of Q_p , Ea_p and α_{p0} , detonation is initiated at Obstacle 22 due to the reflection of the leading shock at the obstacle. Figure 3 (b) and (c) negligible difference in flame speed and shock speed among gas-particle cases considered here. However, differences between pure gaseous and gas-particle cases suggest that with further increase in α_{p0} , the distance and time to DDT would change and this will be investigated in reactive particle mixtures in future.

4 Conclusions

Flame acceleration and transition to detonation in CH_4 -air mixtures is investigated in channels with obstacles of different height. In case where the obstacle height choked the flow (Case G2), initiated detonation is not sustained which is consistent with experimental observations. Detonation initiation, in Case G1, is also in agreement with the past work. In gas-particle cases, the reduced shock strength resulted in delay in onset of the detonation by 17.4 cm in comparison to Case G1. However, the difference in shock and flame propagation among gas-particle cases is negligible as all cases considered represent low volume fraction cases. Future investigations will consider cases with higher α_{p0} than the values considered here to study the effect of particle reactivity on DDT and possible further increase in time and distance to DDT.

5 Significance to DoD

A mission of the Defense Threat Reduction Agency (DTRA) is to develop strategies for the defeat of chemical and biological agents released in either combat or urban environments. The successful development of such strategies relies on accurate and robust predictive tools, which requires a detailed understanding of physics involved such that all possible scenarios can be effectively mitigated. One of the fundamental scenarios encountered in multiple agent defeat strategies is DDT. In the current work, flame acceleration and detonation initiation in multiphase mixtures is investigated using a computational approach developed and applied for this work. The goal here is to understand the effects of particle reactivity and particle interaction with detonation and flow instabilities so as to aid the DTRA funded basic research on bio-agent neutralization in post-blast wave environments.

6 Value and Impact of HPCMP Resources

It is very challenging and vital to resolve all the relevant length and time scales to simulate accurate flame acceleration and detonation initiation. Addition of particles to the flow further adds to the challenge. Thus, numerical simulation of DDT in gas-particle mixtures, a basic research problem of interest, is not possible without dedicated access to computational resources at state-of-the art facilities. By providing answers to fundamental questions about flame propagation and detonation formation, these investigations not only aid the interests of DTRA (and DoD) but also the research community at large. From this perspective, the resources provided by HPCMP are valuable and would provide long lasting impact on the research in the fields of combustion and multi-phase flows.

Acknowledgments

This work is supported by the Defense Threat Reduction Agency (Dr. Suhithi Peiris, Program Manager). The computational resources were provided under DoD HPC Challenge project by Navy DoD Supercomputing Resource Center and U. S. Air Force Research Laboratory DoD Supercomputing Resource Center.

References

Baer, M. R., and J. W. Nunziato, "A two-phase mixture theory for the deflagration-to-detonation transition (DDT) in reactive granular materials." *Int. J. of Multiphase Flow*, 12(6), pp. 861–889, 1986.

Balakrishnan, K., and S. Menon, "On the role of ambient reactive particles in the mixing and afterburn behind explosive blast waves" *Combust. Sci. Technol.*, 182, pp. 186–214, 2010.

Einfeldt, B., "On godunov-type methods for gas dynamics." *SIAM J. Numer. Anal.*, 25(2), pp. 294–318, 1988.

Génin, F., and S. Menon, "Studies of shock / turbulent shear layer interaction using large-eddy simulation." *Comput. Fluids*, 39, pp. 800–819, 2010.

Gottiparthi, K. C., and S. Menon, "Study of deflagration-to-detonation transition in gas-particle mixtures." *AIAA Paper 2010-0801*, 2011.

Gottiparthi, K. C., and S. Menon, "A study of interaction of clouds of inert particles with detonation in gases." *Combust. Sci. Technol.*, 184, pp. 406–433, 2012.

Gottiparthi, K. C., and S. Menon, "Multi-scale simulation of deflagration-to-detonation transition in turbulent dense two-phase reactive mixtures." *2012 High Performance Computer Modernization Program Contributions to DoD Mission Success.*, pp. 209–217, 2012b.

Kapila, A. K., R. Menikoff, J. B. Bdzil, S. F. Son, and D. S. Stewart, "Two-phase modeling of deflagration-to-detonation transition in granular materials: Reduced equations." *Phys. Fluids*, 13(10), pp. 3002–3024, 2001.

Kessler, D. A., Gamezo, V. N., and E. S. Oran, "Simulations of flame acceleration and deflagration-to-detonation transitions in methane-air systems." *Combust. Flame*, 157, pp. 2063–2077, 2010.

Kuznetsov, M., Ciccarelli, G., Dorofeev, S., Alekseev, V., Yankin, Yu., and T. H. Kim, "DDT in methane-air mixtures." *Shock Waves*, 12, pp. 215–220, 2002.

Lee, J. H. S., *The Detonation Phenomenon*. Cambridge University Press, New York, 2008.

Silvestrini, M., B. Genova, G. Parisi, and F. J. L. Trujillo, "Flame acceleration and DDT run-up distance for smooth and obstacles filled tubes." *J. Loss Prev. Process Ind.*, 21, pp. 555–562, 2008.

Wolanski, P., "Deflagration and detonation combustion of dust mixtures." *Prog. in Astronautics and Aeronautics*, 132, pp. 3–31, 1990.

Title: Multi-Scale Simulation of Deflagration-to-Detonation Transition in Turbulent Dense Two-Phase Reactive Mixtures

HPCMP Computation project number: C5J

Project Lead: Prof. Suresh Menon

suresh.menon@ae.gatech.edu

Keywords: Detonation, Deflagration, Chemically inert particles, Two-phase flow

Sponsor Contact: Dr. Suhithi Peiris

suhithi.peiris@dtra.mil

DTRA, 8725, Kingman Road, Fort Belvoir, VA 22060.

Phone: (703) 767-4732

User Contact: Prof. Suresh Menon

suresh.menon@ae.gatech.edu

School of Aerospace Engineering,

270, Ferst dr., Atlanta, GA 30332.

Phone: (404)-894-9126

Multi-Scale Simulation of Deflagration-to-Detonation Transition in Turbulent Dense Two-Phase Reactive Mixtures

Kalyana C. Gottiparthi and Suresh Menon

School of Aerospace Engineering, Georgia Institute of Technology, Atlanta, GA, 30332-0150, USA
{kalyan.gottiparthi, suresh.menon} @ gatech.edu

Abstract

Flame acceleration and deflagration-to-detonation transition (DDT) in gas-particle mixtures are simulated using detailed chemical kinetic mechanism. Chemically inert steel particles are added to stoichiometric hydrogen-oxygen mixture to investigate the effect of particles on the flame propagation and transition to detonation. The initial volume fraction of the particles and the radius of the particles is varied and the change in the time and distance to DDT is quantified. Additionally, the process of transition in gas-particle mixtures is compared with DDT in pure gaseous mixture. Both the time and the distance to DDT is marginally increased by inert particles for the initial volume fraction $\leq 5.0 \times 10^{-6}$. The particles inhibited both the flame propagation and the DDT when the initial volume fraction $\geq 5.0 \times 10^{-5}$.

1 Introduction

Complete and reliable neutralization of chemical/biological (CB) agents in post-detonation flows is challenging due to the complex transient phenomena occurring over a wide range of characteristic length and time scales. In many cases the flow physics is altered by the particulate matter ejected by the detonation or entrained by the ensuing turbulent flow. Thus, it is vital to understand the interaction of the flow with particles to develop effective Agent Defeat (AD) strategies. Most AD scenarios use reactive mixtures and these mixtures are susceptible to detonation. Therefore, estimation of the criteria for transition to detonation is necessary for both safety and effective CB agent neutralization.

Transition to detonation can occur either by direct initiation or through DDT (Lee, 2008). Fast coupling of a shock wave and a reaction front by an ignition source of sufficient strength results in direct detonation initiation. In contrast, when a weak ignition source is used, a deflagration is formed and with proper boundary conditions the deflagration accelerates to initiate a detonation. Past several investigations focused on the deflagration-to-detonation (DDT) process in pure gaseous mixtures using both experimental and numerical methods (Kuznetsov et al., 2002; Kessler et al., 2010; Silvestrini et al., 2008). However, only few studies investigated DDT in two-phase mixtures (Baer and Nunziato, 1986; Kapila et al., 2001; Wolanski, 1990). These studies focused on estimation of distance and time to DDT. Also, DDT is observed to be based on the reactivity and the concentration of the particles (Wolanski, 1990). In all these investigations, the processes involved in DDT in gas-particle mixtures are not explored. To the authors' knowledge there are no results available in the literature reporting the influence of particles, inert or reactive, on DDT. Here, we aim to address the process of transition to detonation in mixtures of reactive gases and chemically inert particles with focus on the mechanism of transition.

A priori evaluation of threats and defining optimal countermeasures, based on first principle simulation methodology, is critical to neutralize threats by CB agents. Novel approaches to simulate destruction of CB agents using fuel mixtures that can mix and burn with aerosolized materials behind strong blast waves created by targeted detonation are being developed as a part of a multi-year research sponsored by Defense Threat Reduction Agency (Gottiparthi et al., 2014). Simulation of DDT covers the entire gamut of the problem areas of direct interest. Additionally, it is a challenge because of the physical complexity of the many processes occurring in the flow and interacting across a wide-range of scales. Here, we present the results obtained during this phase of the challenge project with focus on the DDT in two-phase mixtures in channels with

square cross-sections. The simulations are carried out with a detailed chemical kinetic mechanism (Schulz et al., 2012). The particle properties are updated using a massively parallel Lagrangian tracking solver and different initial volume fraction of the particles are considered.

This paper is organized as follows. The numerical method, the problem setup and the performance of the code are discussed in the second section. In the third section, DDT in pure gaseous stoichiometric hydrogen-oxygen mixtures is analyzed followed by the analysis of the role of particles on the transition process. Summary of the conclusions from the current work are provided in the fourth section. Finally, the fifth and the sixth sections provide the value of the current work to DoD and the impact of the HPCMP resources on the current research, respectively.

2 Formulation and Performance of the Code

2.1 Numerical method and setup

The gas-phase flow is solved using the unsteady, compressible, multi-phase Navier-Stokes equations for reacting gas flows. A Lagrangian approach is used to compute the position, the velocity and the temperature of the solid particles (Gottiparthi et al., 2014). The gas-phase governing equations are solved using an upwind scheme based on a hybrid approximate Harten-Lax-Van Leer (with contact and Einfeldt approach) (Einfeldt, 1988) Riemann solver with Monotone Upstream-centered Schemes for Conservative Laws (MUSCL) reconstruction and a monotonized-central limiter. The scheme is second order accurate in both time and space.

The solid-phase governing equations are solved using a 4th order Runge-Kutta scheme. The deflagration and subsequent detonation are modeled using 18 step mechanism and 8 species (H_2 , O_2 , H_2O , O , H , OH , HO_2 and H_2O_2) (Schulz et al., 2012). Expressions for the drag coefficient (C_D), the Nusselt number (Nu) and the solid-phase mass transfer rate are discussed in previous work (Gottiparthi and Menon, 2012; Gottiparthi et al., 2014). More details of the current modeling approach and its application to studies of shock-turbulence interaction (Génin and Menon, 2010), two-phase detonations (Gottiparthi and Menon, 2012) and explosions Gottiparthi et al. (2014) can be found in the cited references.

The computational domain is a rectangular channel of length 75.0 cm and width 1.0 cm. The domain is discretized using a uniform Cartesian mesh. The surfaces of the walls and obstacles are adiabatic, no-slip and reflecting boundaries. At the outlet of the channel the properties are extrapolated. These boundary conditions are similar to the conditions used in previous studies (Gottiparthi and Menon, 2011, 2012,b). The grid resolution is 50.0 μm , which corresponds to resolution of 6 points in the flame thickness ($\delta_f = 0.275$ mm). This grid resolution is chosen based on previous grid-independent studies (Ivanov et al., 2013; Schulz et al., 2012).

The particles are defined to have the properties of steel (i.e. C_P and ρ_p). Table 1 lists the initial solid phase conditions, the various cases, the number of particles, and the initial volume fraction of the solid phase for each case. Particles of radius (r_p) of 1.0 μm and 2.0 μm are considered here. Additional cases with different particle radii, albeit in different gaseous mixture, are found elsewhere (Gottiparthi and Menon, 2011). The flame is initialized by a hot region of burnt mixture at the closed end of the channel. The temperature in this region is set to be $1.3T_b$, where $T_b = 3100$ K is the post-flame temperature of a stoichiometric H_2 - O_2 mixture. Note that the energy provided for the flame ignition is of the order of the energy release due to the flame.

2.2 Code scaling

Homogeneous isotropic turbulence with 5.2 million particles is used to compute the speed-up of the code. Here, the domain is a cube of length 1.6 mm and is discretized using 256^3 grid points. The turbulence is set based on the past results from literature (Ferrante and Elghobashi, 2003). The speed-up of the code on Spirit (SGI Ice X) and Garnet (Cray XE6) is shown in Fig. 1. The scaling of the code is good and compares well with the theoretical prediction over the wide range of processors considered, i.e. from 64 to 2048. Most of the cases presented here have been run using 1000 processors, where the code has excellent performance. Note that all the particles in the studies presented are deterministically tracked without any approximation. The scaling of the code gives the confidence to run these large scale computations with minimum effect on the computational cost.

Table 1. Number of particles tracked in each case (i.e. for a particular α_{p_0}) in the current study. The diameter of the channel (d) is 1.0 cm in all cases presented here. The particles of radius, r_p , are distributed over the entire length and the width of the channel. The gas phase setup for all two-phase cases is same as Case G.

Case	α_{p_0}	Number of particles	r_p (μm)
G1	-	-	-
P1	1.0×10^{-4}	1086880	2.0
P2	5.0×10^{-5}	543440	2.0
P3	1.0×10^{-5}	108688	2.0
P4	5.0×10^{-6}	54344	2.0
P5	1.0×10^{-4}	8700568	1.0
P6	5.0×10^{-5}	4350284	1.0
P7	1.0×10^{-5}	870056	1.0
P8	5.0×10^{-6}	435028	1.0

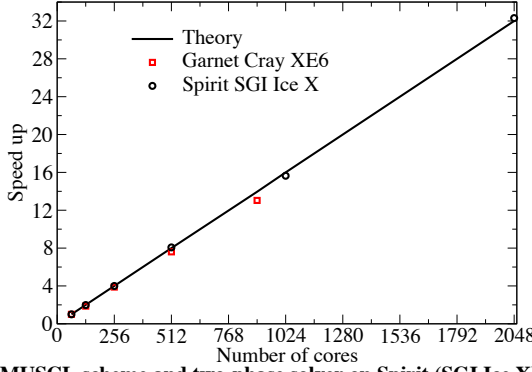


Figure 1. Speed up with MUSCL scheme and two-phase solver on Spirit (SGI Ice X) and Garnet (Cray XE6).

3 Results and Discussion

The process of transition to DDT in gaseous and two-phase mixtures is discussed in this section. DDT in pure gaseous stoichiometric H_2-O_2 mixture is simulated, initially. Since detailed reaction kinetics are used, the possibility of unwanted hot spots (with temperature less than 800 K) initiating a detonation in the unburnt mixture is prohibited (Ivanov et al., 2013).

3.1 DDT in pure gaseous mixtures

After the ignition at the closed end of the channel, the flame slowly propagates and the flame surface increases. The expansion of the burnt gases generates an outward flow and the effect of flame moving in a non-stationary flow results in exponential increase in the flame speed (shown in Fig. 2 (a)). The flow ahead of the flame is also compressed and a shock wave is formed at directly the flame front (Ivanov et al., 2013). The pressure at the flame front increases gradually and eventually effects the reactions at the front. This results in transition to the detonation. This increase in pressure is shown and transition to detonation is shown for Case G in Fig. 2 (b). The distance to DDT is nearly 0.15 m and the the time to DDT is nearly 0.4 ms. These results are consistent with the results available from the past studies (Ivanov et al., 2013).

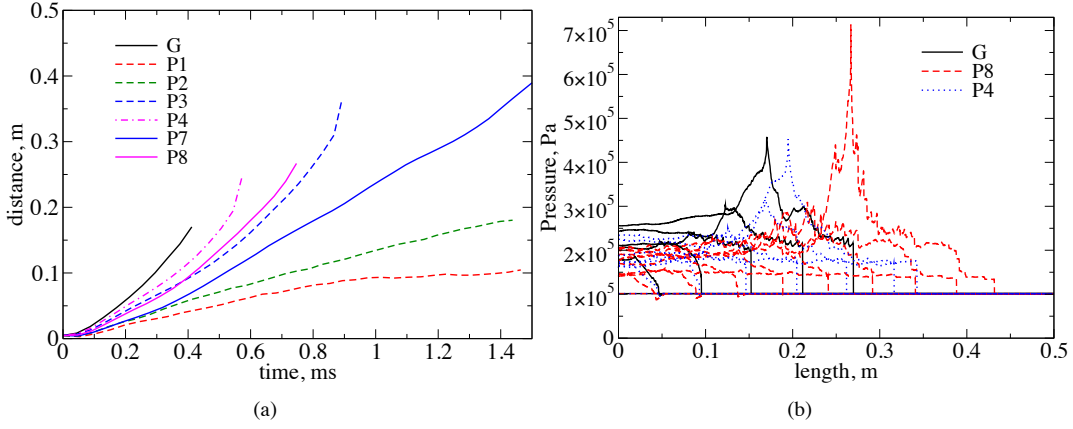


Figure 2. (a) Position of the flame front with time for different cases shown in Table 1. and (b) Pressure profiles for cases G, P4 and P8.

3.2 DDT in gas-particle mixtures

The process of DDT in gas-particle mixture is affected by the initial volume fraction of the particles (α_{p0}) in the flow. The flame ignited at the closed end of the channel accelerates as in the Case G. However, the particles absorb the momentum and energy from the flow resulting in a lower flame speed in comparision. With increase in α_{p0} the flame speed is reduced further, as shown in Fig. 2 (a), independent of particle size. Thus, the flow velocity and the compression of the flow ahead of the flame is delayed in all gas-particle cases. However, for $\alpha_{p0} \leq 5.0 \times 10^{-6}$, a shock of sufficient strength is formed at the flame front leading to formation of a detonation. This process of flame acceleration and detonation formation for Case P8 are shown in Fig. 3.

For $\alpha_{p0} \geq 5.0 \times 10^{-5}$, the flame suppression by particles does not allow for any pressure increase sufficient to effect the reaction front. Thus, in these cases, the transition to a detonation does not occur. Hence, with change in α_{p0} from 5.0×10^{-6} to 1.0×10^{-4} , the flame speed gradually reduces from the value in the pure gaseous cases to a value which inhibits DDT.

4 Conclusions

The process of transition of a deflagration to a detonation in gas-particle mixtures is investigated in stoichiometric hydrogen-oxygen mixtures using detailed reaction kinetics. The formation of the flame front and the flame acceleration simulated in pure gaseous mixture is in agreement with past results (Ivanov et al., 2013). The detonation in gaseous mixture is initiated by formation of shock wave directly at the flame front. The particles added to the reactive gaseous mixture interacted with the flow through momentum and energy transfer. Due to the loss of the flame speed and the flow speed ahead of the flame, the transition process is marginally delayed in cases with $\alpha_{p0} \leq 5.0 \times 10^{-6}$. However, for cases with $\alpha_{p0} \geq 5.0 \times 10^{-5}$, the suppression by particles is sufficient to inhibit DDT. The results show that the particles would alter the time and distance to DDT and can also prohibit detonation formation. Thus, proper control and addition of particles can be used to develop safety in systems with reactive mixtures. Further work in future would investigate role of reactive particles DDT.

5 Significance to DoD

Development of strategies for the defeat of chemical and biological agents released in either combat or urban environments is a vital mission of the Defense Threat Reduction Agency (DTRA). To formulate such strategies, reliable and accurate tools are needed. The development of predictive tools requires a detailed understanding of the physics involved such that all possible scenarios can be effectively mitigated. DDT is one of the fundamental scenarios encountered in multiple agent

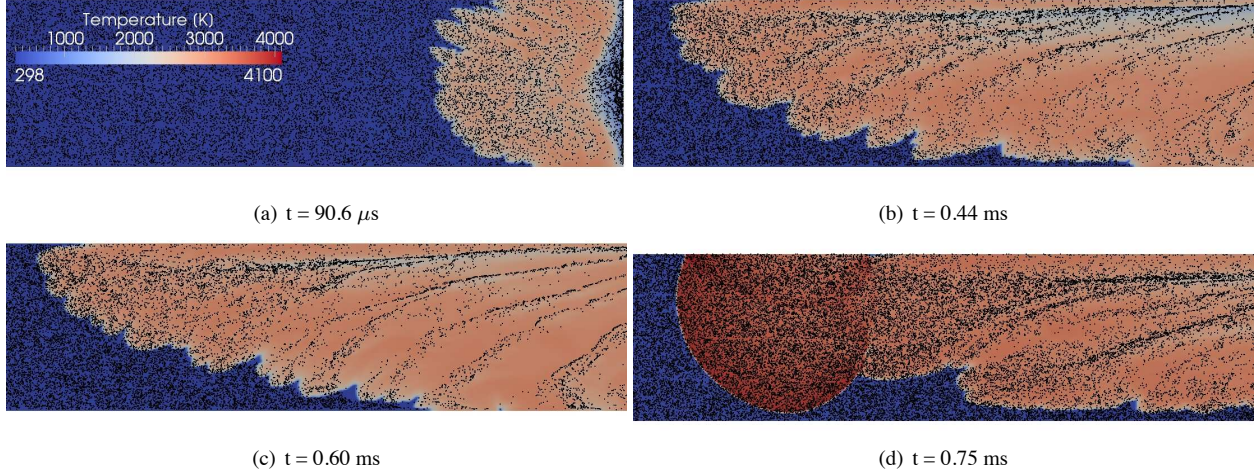


Figure 3. Flame acceleration, and initiation and propagation of detonation in the channel (Case P8). The channel width is 1.0 cm. The particles are shown in black.

defeat strategies. Using massively parallel two-phase computational approach developed as a part of DTRA funded research, flame acceleration and detonation initiation in multi-phase mixtures is investigated in the current work. The results from this work aid in understanding the role of particles in reactive explosive mixtures which is vital for the DTRA funded basic research on bio-agent neutralization in post-blast wave environments.

6 Value and Impact of HPCMP Resources

It is very challenging and vital to resolve all the relevant length and time scales to simulate accurate flame acceleration and detonation initiation. Addition of particles to the flow further adds to the challenge. Thus, numerical simulation of DDT in gas-particle mixtures, a basic research problem of interest, is not possible without dedicated access to computational resources at state-of-the art facilities. By providing answers to fundamental questions about flame propagation and detonation formation, these investigations not only aid the interests of DTRA (and DoD) but also the research community at large. From this perspective, the resources provided by HPCMP are valuable and would provide long lasting impact on the research in the fields of combustion and multi-phase flows.

Acknowledgments

This work is supported by the Defense Threat Reduction Agency (Dr. Suhithi Peiris, Program Manager). The computational resources were provided under DoD HPC Challenge project by DoD Supercomputing Resource Centers at U. S. Army Engineer Research and Development Center and U. S. Air Force Research Laboratory.

References

Baer, M. R., and J. W. Nunziato, “A two-phase mixture theory for the deflagration-to-detonation transition (DDT) in reactive granular materials.” *Int. J. of Multiphase Flow*, 12(6), pp. 861–889, 1986.

Einfeldt, B., “On godunov-type methods for gas dynamics.” *SIAM J. Numer. Anal.*, 25(2), pp. 294–318, 1988.

Ferrante, A., and S. Elghobashi, "On the physical mechanisms of two-way coupling in particle-laden isotropic turbulence." *Phys. Fluids*, 15, pp. 315–329, 2003.

Génin, F., and S. Menon, "Studies of shock / turbulent shear layer interaction using large-eddy simulation." *Comput. Fluids*, 39, pp. 800–819, 2010.

Gottiparthi, K. C., and S. Menon, "Study of deflagration-to-detonation transition in gas-particle mixtures." *AIAA Paper 2010-0801*, 2011.

Gottiparthi, K. C., and S. Menon, "A study of interaction of clouds of inert particles with detonation in gases." *Combust. Sci. Technol.*, 184, pp. 406–433, 2012.

Gottiparthi, K. C., and S. Menon, "Multi-scale simulation of deflagration-to-detonation transition in turbulent dense two-phase reactive mixtures." *2012 High Performance Computer Modernization Program Contributions to DoD Mission Success.*, pp. 209–217, 2012b.

Gottiparthi, K. C., Schulz, J. C. and S. Menon, "On the neutralization of bacterial spores in post-detonation flows." *Shock Waves*, 2014.

Ivanov, M. F., Kiverin, A. D., Yakovenko, I. S., and M. A. Liberman, "Hydrogen-oxygen flame acceleration and deflagration-to-detonation transition in three-dimensional rectangular channels with no-slip walls." *Int. J. Hydrogen Energ.*, 38, pp. 16427–16440, 2013.

Kapila, A. K., R. Menikoff, J. B. Bdil, S. F. Son, and D. S. Stewart, "Two-phase modeling of deflagration-to-detonation transition in granular materials: Reduced equations." *Phys. Fluids*, 13(10), pp. 3002–3024, 2001.

Kessler, D. A., Gamezo, V. N., and E. S. Oran, "Simulations of flame acceleration and deflagration-to-detonation transitions in methane-air systems." *Combust. Flame*, 157, pp. 2063–2077, 2010.

Kuznetsov, M., Ciccarelli, G., Dorofeev, S., Alekseev, V., Yankin, Yu., and T. H. Kim, "DDT in methane-air mixtures." *Shock Waves*, 12, pp. 215–220, 2002.

Lee, J. H. S., *The Detonation Phenomenon*. Cambridge University Press, New York, 2008.

Schulz, J. C., Gottiparthi, K. C., and S. Menon, "Ionization in gaseous detonation waves." *Shock Waves*, 22, pp. 579–590, 2012.

Silvestrini, M., B. Genova, G. Parisi, and F. J. L. Trujillo, "Flame acceleration and DDT run-up distance for smooth and obstacles filled tubes." *J. Loss Prev. Process Ind.*, 21, pp. 555–562, 2008.

Wolanski, P., "Deflagration and detonation combustion of dust mixtures." *Prog. in Astronautics and Aeronautics*, 132, pp. 3–31, 1990.



Richtmyer-Meshkov instability in dilute gas-particle mixtures with re-shock

J. C. Schulz, K. C. Gottiparthi, and S. Menon

Citation: *Physics of Fluids* **25**, 114105 (2013); doi: 10.1063/1.4829761

View online: <http://dx.doi.org/10.1063/1.4829761>

View Table of Contents: <http://scitation.aip.org/content/aip/journal/pof2/25/11?ver=pdfcov>

Published by the AIP Publishing

Articles you may be interested in

Reshocked Richtmyer-Meshkov instability: Numerical study and modeling of random multi-mode experiments
Phys. Fluids **26**, 084107 (2014); 10.1063/1.4893678

On the Kolmogorov inertial subrange developing from Richtmyer-Meshkov instability
Phys. Fluids **25**, 071701 (2013); 10.1063/1.4813608

On Richtmyer-Meshkov instability in dilute gas-particle mixtures
Phys. Fluids **22**, 104103 (2010); 10.1063/1.3507318

Richtmyer-Meshkov instability induced by shock-bubble interaction: Numerical and analytical studies with experimental validation
Phys. Fluids **18**, 036102 (2006); 10.1063/1.2185685

Nonlinear regime of a multimode Richtmyer-Meshkov instability: A simplified perturbation theory
Phys. Fluids **14**, 1111 (2002); 10.1063/1.1447914

Did your publisher get
18 MILLION DOWNLOADS in 2014?
AIP Publishing did.



THERE'S POWER IN NUMBERS. Reach the world with AIP Publishing.



Richtmyer-Meshkov instability in dilute gas-particle mixtures with re-shock

J. C. Schulz, K. C. Gottiparthi, and S. Menon

School of Aerospace Engineering, Georgia Institute of Technology, Atlanta, Georgia 30332, USA

(Received 17 August 2013; accepted 28 October 2013; published online 13 November 2013)

The Richtmyer-Meshkov instability (RMI) is investigated in a dilute gas-particle mixture using three-dimensional numerical simulations. This work extends an earlier two-dimensional study [S. Ukai, K. Balakrishnan, and S. Menon, “On Richtmyer-Meshkov instability in dilute gas-particle mixtures,” *Phys. Fluids* **22**, 104103 (2010)] to a larger parameter space consisting of variations in the mass loading and the particle size as well as considering both single-mode and multi-mode interface initializations. In addition, the effect of the presence of particles on re-shock RMI is also investigated. Single-phase numerical predictions of the mixing layer growth-rate are shown to compare well to both experimental and theoretical results. In a dilute gas-particle mixture, the initial growth-rate of RMI shows similar trends compared to previous work; however, the current numerical predictions show that there is an observable increase, not previously predicted, in the growth of the mixing layer at higher mass loadings. For the range of cases considered, an increase as much as 56% is observed. This increase is attributed to additional vorticity production in the mixing layer resulting from inter-phase momentum coupling. Moreover, the presence of particles introduces a continuous drag on the gas-phase resulting in a delay in the time at which re-shock occurs. This delay, which is observed to be as much as 6%, is largest for higher initial mass loadings and smaller particle radii and has a corresponding effect on both the growth-rate of the mixing-layer after re-shock and the final width of the mixing layer. A new semi-analytical correlation is developed and verified against the numerical data to predict the re-shocked RMI growth-rate in dilute gas-particle flows. The correlation shows that the re-shock RMI growth-rate is linearly proportional to the velocity jump at re-shock, the molecular mixing fraction, and the multi-phase Atwood number. Depending on the initial mass loading and particle radii, the re-shock RMI growth-rates were observed to be reduced by as much as 48% in some cases with variations of around 26% in the width of the mixing layer after re-shock.

© 2013 AIP Publishing LLC. [<http://dx.doi.org/10.1063/1.4829761>]

I. INTRODUCTION

The Richtmyer-Meshkov instability (RMI) develops when a shock wave accelerates an initially perturbed interface between two fluids of different properties. During shock refraction, a misalignment between the density and pressure gradients causes vorticity generation by baroclinic torque along the interface. This unstable vortex sheet drives the amplification of the initial perturbations which can be characterized either by a sinusoidal function of a given wavelength and amplitude (i.e., single-mode RMI) or a superposition of these perturbations (i.e., multi-mode RMI).¹ Additional instabilities, such as the Kelvin-Helmholtz instability, result in vortex roll-up and an increase in the growth of the mixing layer. Furthermore, possible secondary shocks impacting the evolving mixing layer can substantially amplify the mixing processes² and quicken the transition of the layer to a fully turbulent mixing zone.

RMI is a fundamental fluid instability ubiquitous in both nature and engineering. Thus it is the topic of much experimental, analytical, and computational study.¹ The first of such analysis

was by Richtmyer,³ who treated the RMI as the impulsive limit of the Rayleigh-Taylor instability and was able to show that the interface amplitude grows linearly in time. Experiments^{4–6} show good agreement with the impulsive formulation; however, as the interface amplitude increases to roughly a tenth of the perturbation wavelength,¹ the RMI transitions to nonlinear growth, and the linear theory is no longer valid. This phase of the instability is often described as having “bubbles” rising into the heavier fluid and “spikes” falling into the lighter fluid. Several nonlinear models have been developed to predict the bubble/spike velocities and the subsequent reduction in growth of the interface width from mode saturation.^{7–9} Such models show good agreement to two- and three-dimensional numerical simulations.²

In realistic applications, however, the initial interface is more accurately quantified as a superposition of perturbations spanning a large range of amplitudes and wavelengths. In this case, the RMI quickly transitions to nonlinear growth following a self-similar power-law dependence with time, $h \approx t^\theta$, where h is the peak-to-valley amplitude with values of θ ranging from 0.2 to 1.0. The exact value of θ is an on-going topic of discussion.^{1,10,11} Assuming that the just-saturated mode dominates the mixing dynamics, Dimonte *et al.*¹² determine the overall growth of the mixing layer to have a growth exponential of $\theta \approx 0.5$. Modifications to include the effects of initial conditions, however, show that the growth from mode-coupling alone results in $\theta = 0.24$, concluding that any measured growth-rate larger than that must be dependent on the initial conditions.¹³ Recent experiments^{14–16} and other analytical models^{17–19} show similar discrepancies complicating the understanding of the driving factors in the RMI growth-rate. In addition, several computational studies have attempted to better understand how the RMI growth-rate depends on a number of factors including the initial multi-mode perturbations,¹³ the impulse strength,^{5,20,21} and the fluid composition.²²

Re-shock RMI occurs when a second shock perturbs the already evolving interface. All experiments indicate that this second impulse results in a significant increase in the mixing layer growth-rate.^{11,23–25} Yet, once again there is some discrepancy in determining functional relationship of the re-shocked RMI growth-rate. In the experiments by Leinov *et al.*²⁴ and Vetter and Sturtevant,²⁵ the re-shock growth is observed to be linear in time ($\theta = 1$) and is proportional to the velocity jump at the re-shock interface. This is consistent with theoretical predictions,^{11,26,27} numerical parametric studies,² and several computational studies^{28–30} of the experiments by Vetter and Sturtevant,²⁵ all of which show a linear growth-rate after re-shock. Only at very late times is there an indication of mode saturation and nonlinear growth. Yet, experiments by Houas and Chemouni³¹ show a growth exponential somewhere between $\theta = 2/3$ and $\theta = 1.0$, and in the gas-curtain experiments of Balakumar *et al.*²³ and the corresponding computational simulations of Gowardhan and Grinstein,³² the re-shock growth is much more nonlinear. Thornber *et al.*³³ have proposed to reconcile these differences by modifying the linear model of Mikaelian³⁴ to depend on the molecular mixing fraction. An extension of this model to two-phase flows is discussed in this work.

As summarized above, much of the focus on RMI has been on the development of the instability in single-phase media within the parameter space encompassing three parameters: the scales and type of initial perturbations, the impulse strength, and the fluid composition. In many applications, such as in chemical explosions with burning metal particles³⁵ or in astrophysical dusty plasmas,³⁶ the instability develops in a highly complex multi-phase environment. Earlier studies^{37,38} have addressed some of these aspects using numerical simulations. For example, Balakrishnan and Menon³⁸ have proposed a multi-phase buoyancy-drag model for both the RMI and the Rayleigh-Taylor instability by extending the work of Srebro³⁹ to dilute gas-particle mixtures. Using this model, the authors calculate the RMI growth-rate for both single-mode (SM) and multi-mode (MM) initial perturbations and show a reduction in the RMI growth for increases in the mass loading. The model has certain limitations, however, such as the assumption that the particles are always in equilibrium with the gas. Thus, the momentum and energy coupling between the two phases is neglected. This assumption is relaxed in this study.

Also in a previous study, Ukai *et al.*³⁷ derive a linear impulsive model for the growth-rate of the single-mode RMI in a dilute gas under the assumption of small Stokes number, St , which is defined as the ratio of the time scale of the flow (τ) to that of the particle field (τ_p). In the range of the model’s validity, the model compares reasonably well to two-dimensional numerical simulations showing a similar dependence on mass loading as predicted by the buoyancy-drag model of Balakrishnan

and Menon.³⁸ For $St > 0.01$, however, the model is less accurate in comparison with the numerical simulations where the simulation results seem to indicate a reversal in trend, i.e., high mass loadings resulting in larger growth-rates. A possible reason for this reversal in trend is explained in this work. Moreover, since impulsive models are only valid within the linear growth regime of the RMI and thus only applicable to small amplitude single-mode perturbations during early times, prior work leaves it unclear how the presence of particles might affect the nonlinear processes of the RMI, particularly since after re-shock such processes accelerate mixing. More importantly, both the linear impulsive model and the buoyancy-drag model implicitly assume that the gas-particle mixture is in equilibrium, and thus they cannot account for any coupling between the phases. The three-dimensional numerical simulations discussed in the current work seek to explain in a more rigorous manner how the RMI evolves in a two-phase flow before and after re-shock. To do this, studies based on prior single-phase re-shock RMI simulations^{2,28–30} are used to extend the previous analysis of two-dimensional single-mode RMI in dilute-gas mixtures.^{37,38} By analyzing a wide range of initial Stokes numbers and particle number densities, a previously unobserved increase in the initial two-phase RMI growth-rate is explained. Additionally, a new model for the re-shock RMI growth-rate in a dilute gas-particle mixture is introduced that correlates well with the numerical predictions.

This paper is organized as follows. Section II presents an overview of the numerical formulation for the gas and particle phases. Section III introduces the simulation methodology, presents a brief validation of gas-phase re-shock simulations, and introduces the multi-phase setup and initialization. The results of the multi-phase numerical simulations are discussed in Sec. IV. Finally, this study concludes with a summary of the key observations and a discussion of future work.

II. NUMERICAL FORMULATION

A. Gas phase

The compressible Navier-Stokes equations for multi-species and multi-phase flow in the limit of negligible volume fraction (i.e., a dilute gas-particle mixture) are

$$\frac{\partial \rho}{\partial t} + \frac{\partial \rho u_i}{\partial x_i} = 0, \quad (1)$$

$$\frac{\partial \rho u_i}{\partial t} + \frac{\partial}{\partial x_j} \left(\rho u_i u_j + p \delta_{ij} - \tau_{ij} \right) = \dot{F}_{p,i}, \quad (2)$$

$$\frac{\partial \rho E}{\partial t} + \frac{\partial}{\partial x_i} \left[(\rho E + p) u_i + q_i - u_j \tau_{ij} \right] = \dot{Q}_p + \dot{W}_p, \quad (3)$$

$$\frac{\partial \rho Y_k}{\partial t} + \frac{\partial}{\partial x_i} \left[\rho Y_k (u_i + V_{i,k}) \right] = 0. \quad (4)$$

In the above equations, ρ is the gas density, u_i is the velocity vector, E is the total specific energy, and Y_k is the k th species mass fractions. In the current RMI simulations, only two species are considered, one with a small molecular weight, W_1 , referred to as the light species, and one with a larger molecular weight, W_2 , referred to as the heavy species. The thermodynamic pressure, p , is computed using the perfect gas equation of state, $p = \rho RT$, where T is the temperature of the gas phase and R is the mixture-averaged gas constant. The viscous terms, τ_{ij} , q_i , and $V_{i,k}$, are the shear-stress tensor, the rate of heat transfer, and the k th species diffusion flux, respectively. They are given as

$$\tau_{ij} = \mu \left(\frac{\partial u_i}{\partial x_j} + \frac{\partial u_j}{\partial x_i} \right) + \delta_{ij} \lambda \frac{\partial u_m}{\partial x_m}, \quad (5)$$

$$q_i = -\kappa \frac{\partial T}{\partial x_i} + \rho \sum_{k=1}^2 h_k Y_k V_{i,k}, \quad (6)$$

$$V_{i,k} = -\frac{D_k}{Y_k} \frac{W_k}{\bar{W}} \left(\frac{\partial X_k}{\partial x_i} \right), \quad (7)$$

where μ is the mixture-averaged viscosity, δ_{ij} is the Kronecker delta function, λ ($= -2/3\mu$) is the bulk viscosity, κ is the mixture-averaged thermal conductivity of the gas phase, \bar{W} is the mixture-average molecular weight, and h_k , X_k , and D_k are, respectively, the specific enthalpy, the mole fraction, and the mixture-averaged diffusion coefficient of the k th species. The transport properties for each species are computed using curve-fits as a function of the gas temperature.^{40,41} The interphase coupling terms, $\dot{F}_{p,i}$, \dot{W}_p , and \dot{Q}_p , in the conservation equations are the rates of momentum, work, and heat transfers resulting from the presence of particles in the two-phase mixture. These terms are discussed further in Sec. II B.

The governing equations are solved numerically using a second-order predictor-corrector finite-volume scheme where the cell-surface fluxes are computed using a hybrid upwind-central scheme. In the vicinity of flow discontinuities, shocks or density gradients, the fluxes are computed using a Harten-Lax-Van Leer (HLL) type approximate Riemann solver with Monotone Upstream-Center Schemes for Conservation Laws (MUSCL) reconstruction. A second-order central scheme is used elsewhere. The hybrid switch is based on a sensor that detects the curvature of the pressure and density fields. More information about the numerical scheme can be found in previous work.^{40,41}

B. Particle phase

Lagrangian tracking is used to compute the particle position, $x_{p,i}$, the particle velocity, $u_{p,i}$, and the particle temperature, T_p . In scenarios where the number of particles is too large for Lagrangian tracking to be computationally feasible, the parcel method^{42,43} can be used. A parcel is a group of one or more particles that all have the same position, velocity, and temperature. The approach reduces the computational cost since only the parcel is tracked. The number of particles per parcel needs to be judiciously chosen to ensure accuracy.⁴⁴ If there is no inter-phase mass transfer (inert particles), the solid-phase governing equations are given as

$$\frac{dx_{p,i}}{dt} = u_{p,i}, \quad (8)$$

$$m \frac{du_{p,i}}{dt} = \frac{\pi}{2} r_p^2 C_D \rho |\bar{u}_i - u_{p,i}| (\bar{u}_i - u_{p,i}), \quad (9)$$

$$m C_p \frac{dT_p}{dt} = 2\pi r_p \kappa_g \text{Nu}(T - T_p), \quad (10)$$

where \bar{u}_i is the local velocity of the gas, Nu is the gas-phase Nusselt number, r_p is the particle radius, and m is the particle mass, which is obtained as $(4/3)\pi r_p^3 \rho_p$ where ρ_p is the particle density. For this study, the model assumes that the pressure gradient term, the Basset term, the Saffman lift, the Magnus lift, and the inter-particle interaction term are all second-order effects.^{37,43} They are neglected in this study. The drag coefficient, C_D , is based on the following empirical relationship validated for shock-particle interactions:⁴⁵

$$C_D = \left[0.38 + \frac{24}{\text{Re}_p} + \frac{4}{\text{Re}_p^{0.5}} \right] \left[1 + \exp \left(-\frac{0.43}{M_p^{4.467}} \right) \right]. \quad (11)$$

In this expression, the drag is a function of the particle Reynolds number, $\text{Re}_p = 2r_p |u_{p,i} - \bar{u}_i| \rho / \mu$, and the particle Mach number, $M_p = |u_{p,i} - \bar{u}_i| / a_s$, where a_s is the speed of sound in the gas. Following previous studies,⁴³ convection is assumed to be the dominant heat transfer mechanism between the two phases. The Nusselt number, Nu , used in Eq. (10), is computed as a function of Re_p and the Prandtl number, Pr , from the following relationship:⁴⁶ $\text{Nu} = 2.0 + 0.459 \text{Pr}^{0.33} \text{Re}_p^{0.55}$.

The governing equations for the solid-phase are integrated in time using a fourth-order Runge-Kutta scheme, and the inter-phase coupling terms in Eqs. (2) and (3) are the volumetrically averaged

quantities given as

$$\dot{F}_{p,i} = \frac{1}{\mathcal{V}} \sum_{n=1}^{N_p} \left[\frac{\pi}{2} r_{p,n}^2 C_{D,n} \rho_n |u_{p,i,n} - u_{i,n}| (u_{p,i,n} - u_{i,n}) \right], \quad (12)$$

$$\dot{Q}_p = \frac{1}{\mathcal{V}} \sum_{n=1}^{N_p} [2\pi r_{p,n} \kappa_g \text{Nu}_n (T_n - T_{p,n})], \quad (13)$$

$$\dot{W}_p = \frac{1}{\mathcal{V}} \sum_{n=1}^{N_p} \left[\frac{\pi}{2} r_{p,n}^2 C_{D,n} \rho_n |u_{p,i,n} - \bar{u}_{i,n}| (u_{p,i,n} - \bar{u}_{i,n}) u_{p,i,n} \right], \quad (14)$$

where \mathcal{V} is the volume of the computational cell, and the subscript n indicates a quantity of the n th parcel in the summation over the total number of particles in \mathcal{V} . More information regarding the implementation, validation, and application of the current multi-phase solver can be found in previous work.^{35,37,43}

III. SIMULATION METHODOLOGY

A. Single-phase simulations

Since many past numerical simulations^{28–30} show a reasonably good comparison to data measured in the air/SF₆ (single-phase) re-shock RMI experiments of Vetter and Sturtevant,²⁵ a similar configuration is adopted here to act as a reference point for the two-phase studies. Yet, it is important to note that recent experiments²³ have used particle image velocimetry (PIV) and planar laser-induced fluorescence (PLIF) techniques to obtain more detailed measurements of the RMI before and after re-shock. Particularly, these experiments have avoided introducing errors through the use of a cellulose membrane to initially separate the light and heavy gas mixtures. For computational studies, however, the correct initialization of such experimental configurations, while not impossible,³² is more difficult to obtain. Thus, in the current work, previous computational studies of the Vetter and Sturtevant²⁵ are leveraged as a basis for the two-phase studies.

The Vetter and Sturtevant²⁵ experiments were conducted in a shock-tube with cross-sectional dimensions of $L_y \times L_z$, and a variable longitudinal length of L_x . The air/SF₆ mixture is initially separated by a thin membrane supported by a wire mesh of 1 cm spacing. As the initial shock speed is varied from Mach 1.18 to 1.98, the length of the test section is adjusted from 61 cm to 122 cm to ensure that the re-shocked mixing zone is within the observational test-section. High resolution spark-Schlieren images and high-speed cameras were used to obtain data about the mixing zone flow features and growth-rates. For the validation study, two experimental configurations are simulated, denoted as VS0-VI and VS0-VII, which correspond to case VI^b and case VII^b of Vetter and Sturtevant.²⁵ Only the gas-phase initialization of case VS0-VI is used for the multi-phase studies presented later. The reference conditions for these cases are summarized in Table I, and a schematic of the simulation domain is given in Fig. 1.

TABLE I. Test conditions and measurements of the re-shocked RMI experiments of Vetter and Sturtevant²⁵ where VS0-VI and VS0-VII correspond to experiments VI^b and VII^b.

	VS0-VI	VS0-VII
Incident Mach number	1.5	1.98
Pressure (kPa)	23.0	8.0
Distance from interface to wall, L_x (m)	0.62	0.49
Instantaneous velocity, ΔV (m/s)	150.0	287.0
Shocked growth-rate (m/s)	4.2	7.5
Re-shocked observation time (m/s)	37.2	74.4
Shocked observation time (ms)	2.2–3.2	1.7–2.5
Re-shocked observation time (ms)	4.0–5.5	1.7–2.5

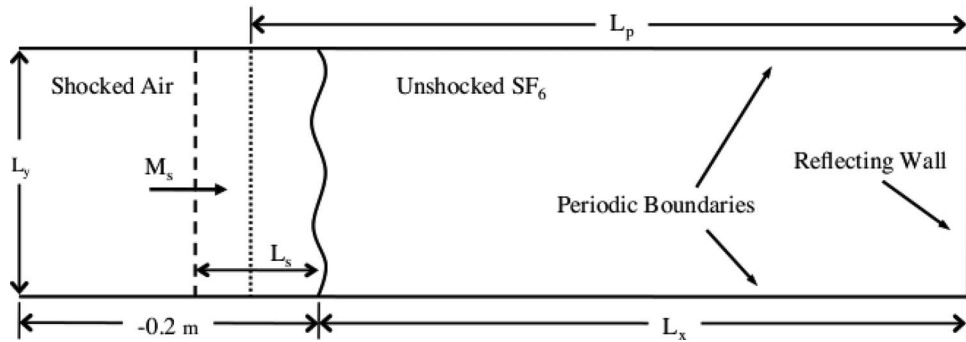


FIG. 1. Schematic of the simulation domain where M_s is the Mach number of the shock, L_x is the distance from the end wall to the contact, and L_s is the distance from the contact to the initial shock position. For the multi-phase simulations, L_p is the length of the initial particle cloud.

The experiments were designed to avoid boundary layer interaction with the mixing layer. Thus, the side-walls of the shock tube (in y - and z -directions) can safely be treated numerically as periodic boundaries, an assumption also made in prior numerical studies.^{28–30} The end wall ($x = L_x$) is modeled as a no-slip boundary, and the inflow boundary at $x = -0.2$ m is initially modeled as a supersonic inflow boundary, but to allow the exit of the reflected and transmitted waves later in the simulation, the boundary is changed to a non-reflecting characteristic outflow boundary later in the simulation. This prohibits the non-physical reflection of waves from the boundary, which could corrupt the mixing-layer growth at late times.

The development of the RMI is highly sensitive to the initial structure of the interface separating the light (air) and heavy (SF_6) species.³⁰ In the current study, the interface is formed by specifying the SF_6 mass fraction, Y_{SF_6} , with an initial hyperbolic tangent profile²² centered at $x = 0.0$ m and a characteristic thickness of δ given by

$$Y_{\text{SF}_6}(x, y, z; 0) = \frac{1}{2} - \frac{1}{2} \tanh\left(\frac{x - \eta_I(y, z)}{\delta}\right), \quad (15)$$

where $\eta_I(y, z)$ is the interface perturbation. Following previous numerical simulations,^{28–30} an “egg-carton” sinusoidal perturbation for $\eta_I(y, z)$ is used to model the wire-meshed membrane separating the air and SF_6 gases in the experiments and is described by the expression

$$\eta_I(y, z) = a_0 |\sin(k_0 y) \sin(k_0 z)| + a_1 \cos(k_1 y) \cos(k_1 z) + a_2 \Psi(y, z), \quad (16)$$

where the first term represents the small-scale perturbations resulting from the wire-mesh, and the second term represents the scales associated with the transverse dimensions of the shock tube. The last term includes random perturbations, which are used to account for small-scale irregularities and to break the symmetry of the initial conditions and accelerate the transition of the RMI to nonlinear growth. The values of the coefficients used in the current study are $a_0 = a_1 = 1.25 \times 10^{-3}$ m and $a_2 = 2.5 \times 10^{-4}$ m with the random initial small-scale perturbations, $\Psi(y, z)$, prescribed by an adapted von Karman power spectrum,³⁰

$$E_\Psi(k) = k^{-2} \left[\frac{kL}{\sqrt{(kL)^2 + B}} \right]^4, \quad (17)$$

where $L = 0.95$ cm, $B = 5\sqrt{2}$, and $k = \sqrt{k_y^2 + k_z^2}$, where $k_y = 2\pi/L_y$ and $k_z = 2\pi/L_z$. The random fluctuations, $\Psi(y, z)$, were normalized such that they have a root-mean-square amplitude of one with the amplitude is set by a_2 . These values as well as the simulation configuration parameters are summarized in Table II.

Figure 2(a) shows the time evolution of the mixing length, $\eta(t)$, compared to the experimental growth-rate data for the two re-shock configurations defined in Table I. In practice, there are many ways to define the width of the mixing zone. In this study, an integral definition is adopted where

TABLE II. Summary of the simulation configurations used in the re-shock validation experiment (VS) and the multi-mode (MM) and single-mode (SM) numerical simulations. The function \mathcal{U}_r represents a uniform random variable chosen on the interval $[0,1]$, $k_0 = 2\pi/L_y$, and Δx is the grid resolution used for each case. All dimensional values are given in units of centimeters.

Case name	$\eta_I(y, z)$	$\Psi(y, z)$	a_0	a_1	a_2	$k_0\eta_0$	L_y, L_z	L_p	L_s	Δx
VS	Eq. (16)	Eq. (17)	0.25	0.125	0.125	0.00926	27.0	...	5.0	0.105
MM	Eq. (16)	Eq. (17)	0.25	0.125	0.125	0.0185	13.5	65.0	5.0	0.105
SM	Eq. (19)	...	0.25	0.0	0.0	0.0185	13.5	65.0	5.0	0.105
SMR	Eq. (19)	\mathcal{U}_r	0.25	0.0	0.2	0.0185	13.5	65.0	5.0	0.105
SMN	Eq. (19)	...	2.5	0.0	0.0	0.185	13.5	65.0	5.0	0.105

the mixing length is given by

$$\eta(t) = 4 \int_{-0.2}^{L_x} \langle Y_{SF_6} \rangle (1.0 - \langle Y_{SF_6} \rangle) dx. \quad (18)$$

The quantity $\langle \cdot \rangle$ represents a volumetric average in the transverse directions over the distances L_y and L_z , and is a function of only the time, t , and x , the longitudinal direction.

For a single-mode initial perturbation, the mixing length growth is approximately linear following the theoretical estimation given by Richtmyer's impulsive model,³ $\dot{\eta} = v_0 = k_0\eta_0 A^+ \Delta V$. In this equation, η_0 is the initial amplitude [= a_0], A^+ is the post-shock Atwood number [= $(\rho_{SF_6} - \rho_{Air})/(\rho_{SF_6} + \rho_{Air})$], and ΔV is the velocity jump at the contact discontinuity. The initial perturbation is given by

$$\eta_I(y, z) = \frac{a_0}{2} (\sin(k_0 y) + \sin(k_0 z)) + a_2 \Psi(y, z), \quad (19)$$

with the values of a_0 and a_2 given in Table II and the configuration summarized in Table III. The evolution of the normalized mixing length for the single-mode RMI is shown in Fig. 2(b). Even under these conditions, however, the RMI transitions to nonlinearity and is more appropriately described by the model of Sadot *et al.*⁸ also shown in Fig. 2(b).

For case VS0-VI at $t = 3.46$ ms, re-shock occurs. This results in a compression of the mixing zone, noticeable by the reduction in the mixing length, followed by a subsequent increase in the

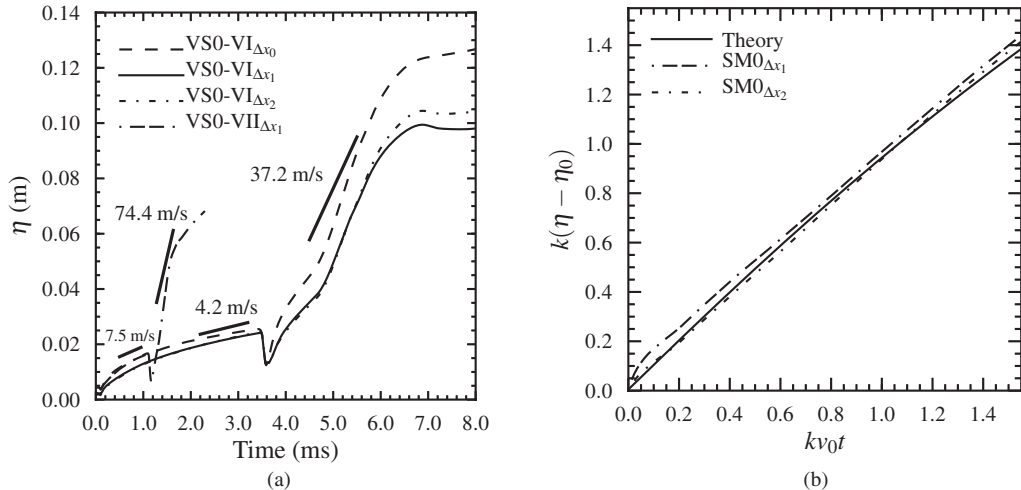


FIG. 2. (a) Evolution of the mixing layer $\eta(t)$ at three different grid resolutions ($\Delta x_0 = 0.21$ cm, $\Delta x_1 = 0.105$ cm, $\Delta x_2 = 0.07$ cm) with comparison to the experimental measurements summarized in Table I. (b) Time history of the normalized mixing length in single-mode RMI at the same grid resolutions (Δx_1 , Δx_2) with a comparison to the nonlinear theory of Sadot *et al.*⁸

TABLE III. Summary of the multi-phase initial conditions used in the numerical simulations. Simulations are referred to by the case name (i.e., SM, MM, etc.) defined in Table II and the case number defined below. For reference, this table additionally provides the RMI growth-rate data for the SM cases.

Case no.	α_0	r_p (μm)	N_0	\mathcal{P}	SM			
					St	ΔV (m/s)	A^+	A_m^+
0	0.0	147.9	0.781	...
1	2.0×10^{-5}	30	2 094 876	3	1.11	146.4	0.725	0.689
2	2.0×10^{-5}	60	261 859	1	3.21	146.5	0.725	0.689
3	2.0×10^{-5}	120	32 732	1	9.98	146.3	0.725	0.689
4	4.0×10^{-5}	5	904 986 837	1300	0.09	135.7	0.709	0.641
5	4.0×10^{-5}	10	113 123 354	170	0.23	137.6	0.717	0.649
6	4.0×10^{-5}	30	4 189 753	6	1.11	142.7	0.724	0.656
7	4.0×10^{-5}	60	523 719	1	3.22	145.5	0.725	0.657
8	4.0×10^{-5}	120	65 464	1	9.98	146.2	0.725	0.657
9	1.0×10^{-4}	30	10 474 384	15	1.11	142.2	0.719	0.572
10	1.0×10^{-4}	60	1 309 298	2	3.21	142.7	0.724	0.576
11	1.0×10^{-4}	120	163 662	1	9.98	143.7	0.724	0.576
12	2.0×10^{-4}	30	20 948 769	30	1.11	141.6	0.716	0.470
13	2.0×10^{-4}	60	2 618 596	4	3.21	142.5	0.720	0.475
14	2.0×10^{-4}	120	327 324	1	9.98	142.9	0.724	0.478

mixing length as the reflected shock further amplifies the perturbations in developing mixing zone. This tends to hasten the production of small-scale structures prompting the development of an inertial sub-range.^{20,23}

The results in Fig. 2 are given for three different grid resolutions: $\Delta x_0 = 0.21$ cm, $\Delta x_1 = 0.105$ cm, and $\Delta x_2 = 0.07$ cm. For the two highest resolutions, the RMI growth-rates are indistinguishable with only small differences in the final saturated mixing length and thus serving as a reasonable demonstration of grid convergence. A grid resolution of $\Delta x = \Delta x_1 = 0.105$ cm, which was used in previous studies,²⁹ is chosen for the rest of the studies resulting in a computational grid of $780 \times 256 \times 256$. The numerical results show good agreement to the experimental measurements of the RMI growth-rates before and after re-shock, and in the case of the single-mode simulations, to the analytical models of the RMI growth-rate prior to re-shock. These results lend confidence to the numerical methodology, simulation configuration, and initialization used in this study. As a final note, it is emphasized that the comparison between the experimental data and the computational predictions are of the RMI growth-rates only. In the experiments, the initial perturbation amplitudes develop at a much smaller scale. After re-shock, the mixing lengths are more comparable. The experimental mixing length at 6.25 ms is 10.2 cm (as taken from Hill *et al.*²⁹), whereas the numerical prediction is approximately 9.7 cm at that time.

B. Multi-phase simulations

For the two-phase simulations, a uniform region of spherical particles with a radius of r_p spanning the cross-sectional area of $L_y \times L_z$ and the length L_p is superimposed onto the single-mode and multi-mode configurations discussed in Sec. III A and shown schematically in Fig. 1. From theoretical analysis,^{37,38} two parameters are used to characterize the dynamics of the RMI in a dilute gas-particle mixture: the mass loading (f) and the Stokes number (St). The mass loading is defined as the ratio of the particle mass per unit volume to the gas density ($f = mn_0/\rho$, where n_0 is the number of particles per unit volume, m is the particle mass, and ρ is the fluid density). From this, a multi-phase Atwood number can be defined as³⁷

$$A_m = \frac{\rho_2(1 + f_2) - \rho_1(1 + f_1)}{\rho_2(1 + f_2) + \rho_1(1 + f_1)}, \quad (20)$$

where the subscripts 1 and 2 refer, respectively, to the light (air) and the heavy (SF_6) gases separated by the contact discontinuity. If no particles are present ($f_1 = f_2 = 0$), as in case SM0, then A_m reduces to A . Also, note that for $A > 0$ and uniform particle loading across the contact discontinuity, A_m is always less than A . By linearizing the dilute gas-particle equations, it is possible to derive a multi-phase impulsive theory,³⁷ which results in the following linear equation for the mixing length as a function of time:

$$\eta(t) = \eta_0(1.0 + k_0 A_m \Delta V t) = \eta_0 + v_{0,m} t. \quad (21)$$

The result is that A_m simply replaces A where the use of A_m accounts for the reduction in the effective impulse strength resulting from the particle mass loading of the flow. This theory, however, is derived in the limit of vanishing Stokes number, and thus is only applicable for $\text{St} \ll 1.0$ flows. The Stokes number is computed as $\tau_p/\tau_{RMI} = kA\Delta V\tau_p$, where the time-scale of the particles is $\tau_p = (1/4)\pi r_p \rho_p C_D \mu$. For the SM cases, τ_{RMI} is approximately 2.4 ms. In this study, the particles are chosen to have the properties of steel, such that $\rho_p = 7800 \text{ kg/m}^3$. Therefore, given the same gas-phase conditions, St is a strong function of the particle radius.

Using these multi-phase parameters, A_m and St , a parameter study is conducted to study the RMI in a dilute gas-particle mixture. The gas-phase reference conditions ($M_s = 1.5$, $p_0 = 23 \text{ kPa}$, $T_0 = 298.15 \text{ K}$) of case VS0-VI from Table I are kept constant (for reasons explained in Sec. III A), while the size (r_p) and the number of particles (N_0) within the domain are varied independently. The multi-phase conditions discussed in this study are summarized in Table III. The values of r_p and N_0 considered in this study are limited by the dilute assumption, i.e., dispersed-phase volume fractions, α , less than 1%. While the simulations presented here are only a portion of the possible conditions, additional simulations indicate that the conclusions drawn from the data reported here apply over a much larger range within the limits of the numerical formulation. Furthermore, as will be discussed in more detail later, the particle cloud compresses throughout the simulation which limits the initial value of α_0 . Henceforth, these numerical experiments are referred to by the case name (i.e., SM, MM, etc.) defined in Table II and the case number (i.e., 0, 1, 2, etc.) defined in Table III. The former defines the initial configuration and perturbation interface, while the latter defines multi-phase parameters. For example, case MM0 refers to a multi-mode, single-phase simulation.

Also given in Table III is the number of particles per parcel, \mathcal{P} , used in each case as well as the initial volume fraction α_0 , which is defined as the ratio of the total volume occupied by the particles, $V_p = N_0(4/3)\pi r_p^3$, to the volume $V = L_y L_z L_p$, where L_p is the distance from the end-wall in the x -direction occupied by the particles (see Fig. 1). In this study, $L_p = 65.0 \text{ cm}$ is kept constant.

IV. RESULTS AND DISCUSSION

There are noticeable differences in the time evolution of the RMI in multi-phase flows. Figure 3 shows the time history of the mixing length, $\eta(t)$, and mixing fraction, $\Theta(t)$, of two representative multi-phase cases, MM12 and MM14, compared to results from the single-phase simulation MM0. The molecular mixing fraction, Θ , is defined as

$$\Theta(t) = \frac{\int \langle Y_{\text{SF}_6} Y_{\text{air}} \rangle dx}{\int \langle Y_{\text{SF}_6} \rangle \langle Y_{\text{air}} \rangle dx}. \quad (22)$$

It is a more useful description of how well-mixed the two species are in the mixing zone since the span-wise averaged mass fraction carries no distinction between regions that are completely mixed and those regions that are unmixed, but contain equal portions of species. Thus, Θ quantifies the relative amount of molecularly mixed fluid within the mixing layer, such that $\Theta = 1.0$ would mean that the entrained fluids were completely mixed within each transverse plane.

For $\alpha_0 > 1.0 \times 10^{-4}$, there is a noticeable increase in the growth-rate of the multi-phase RMI before re-shock as well as a corresponding decrease in the molecular mixing fraction meaning that the rate of entrainment is increased. A comparison of the mass fraction contours colored by the x -velocity at $t = 3.0 \text{ ms}$ in Fig. 4 shows that the presence of particles in flow effectively increases the size and distortion of the mixing interface, while decreasing its convective velocity. The location

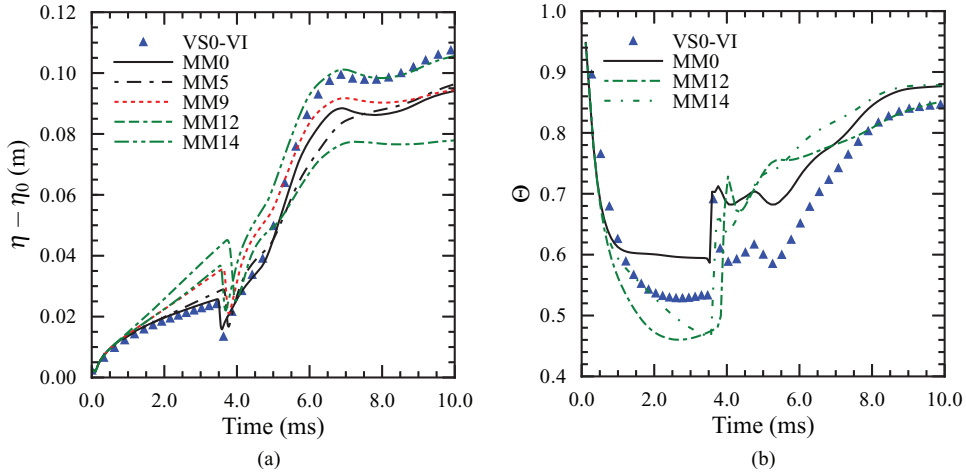


FIG. 3. Time evolution of (a) the mixing layer width, $\eta(t)$, and (b) the mixing fraction, $\Theta(t)$, for the multi-mode RMI in a dilute gas-particle mixture compared to the single-phase results of VS0-VI and MM0.

of the mixing zone can be identified by using a threshold value of the species mass fraction. Thus, the left (spike) and right (bubble) interfaces are defined by $x_{\eta,L} = x|_{Y_{SF_6}=0.01}$ and $x_{\eta,R} = x|_{Y_{SF_6}=0.99}$. Further, the particle cloud is defined between x_p , the position of the leftmost particle, and the end-wall at 0.62 m.

The x - t diagram, shown in Fig. 5(a), shows the location of the shock in relation to the mixing zone and the particle cloud. For small St, the particle cloud is significantly compressed and interacts with the mixing zone after re-shock. The compression of the particle cloud is further indicated by the ratio of the volume fraction to the initial volume fraction, α/α_0 . Thus for low St, the mass loading increases throughout the simulation. Note that the volume fraction still remains within dilute limit. This results in a reduction in the mixing zone length at late-times; however, the molecular mixing fraction for all cases asymptote to values between 0.84 and 0.88.

A. Initial growth-rate

RMI develops as a result of vorticity deposited along the interface by the production of baroclinic torque. This process can be investigated using the compressible vorticity transport equation, given by Eq. (23), which is derived by taking the curl of the momentum conservation equation. The tensor form of this equation is given as

$$\begin{aligned} \frac{D\omega_i}{Dt} &= \omega_j \frac{\partial u_i}{\partial x_j} - \omega_i \frac{\partial u_j}{\partial x_j} + \epsilon_{ijk} \frac{\partial}{\partial x_j} \left(\frac{1}{\rho} \frac{\partial \tau_{km}}{\partial x_m} \right) + \frac{1}{\rho^2} \epsilon_{ijk} \frac{\partial \rho}{\partial x_j} \frac{\partial p}{\partial x_k} + \epsilon_{ijk} \frac{\partial}{\partial x_j} \left(\frac{\dot{F}_{p,k}}{\rho} \right) \\ &= \Omega_i^s + \Omega_i^d + \Gamma_i + \beta_i + \Pi_i. \end{aligned} \quad (23)$$

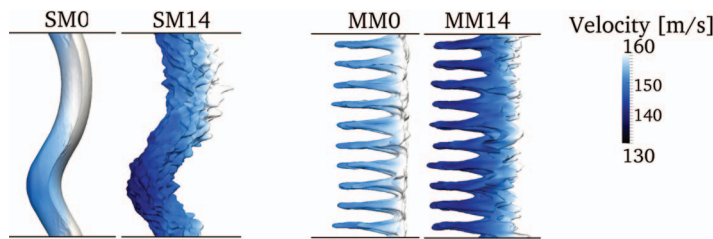


FIG. 4. Contours of the species mass fraction, $Y_{SF_6} = Y_{Air} = 0.5$ for the single-phase cases SM0 and MM0 compared to representative multi-phase cases SM14 and MM14 colored by the velocity in the x -direction.

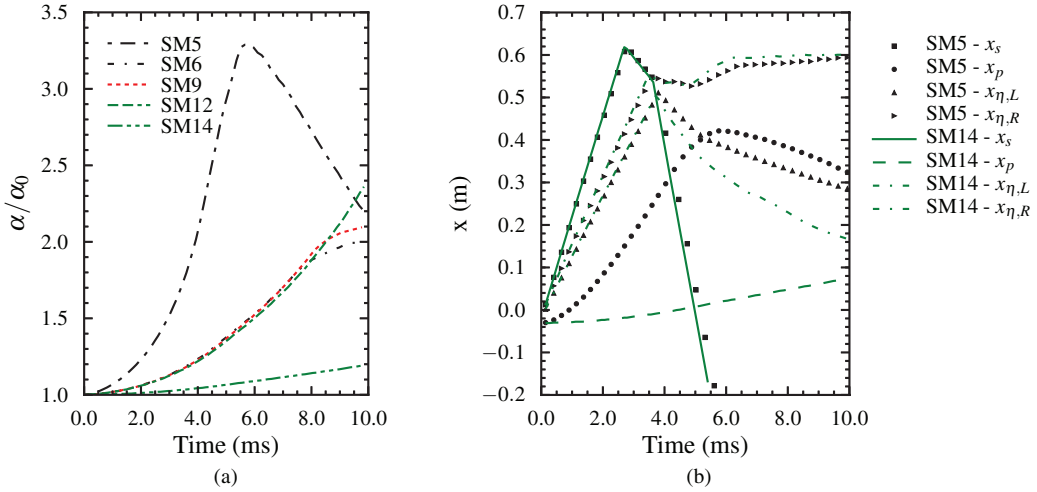


FIG. 5. (a) Time evolution of the ratio of the particle cloud volume fraction, α , to the initial volume fraction, α_0 . (b) x - t diagram of the time history of the shock location, x_s , the left interface of the particle cloud, x_p , and the left (spike) and right (bubble) interfaces of the mixing zone, $x_{\eta,L}$ and $x_{\eta,R}$, respectively.

The first two terms in this equation, Ω_i^s and Ω_i^d , represent the transport of vorticity through vortex stretching and dilatation. The third term, Γ_i , represents the production of vorticity by viscous stresses, while the fourth term, β_i , represents the production/destruction of vorticity by baroclinic torque. In addition to these terms, an additional vorticity production occurs in multi-phase flows resulting from the inter-phase momentum coupling term, $\dot{F}_{p,k}$, which is represented by the term, Π_i . The viscous contribution to vorticity dissipation is ignored here.

For $St < 1$, cases SM4 and SM5, Fig. 6(a) shows that the width of the mixing-layer is reduced by approximately 11%. This reduction is predicted by the linear impulsive model of Ukai *et al.*,³⁷ given by Eq. (21), where $\dot{\eta}_{\text{num}}/\dot{\eta}_{\text{model}} = 0.96$. For the cases where $St > 1$, however, the mixing-layer growth rate increases with the increase proportional to the mass loading (larger r_p and larger α_0). For cases SM12 and SM14, there is a 7.3% and 10.8% increase, respectively, while for cases SM9 and SM11, there is only a 3.0% and 5.7% increase, respectively. To ensure that this observation is a direct result of the gas-particle interaction, a case without particles, but with a random multi-mode initialization, case SMR0 (not shown), is also simulated and shows no observable change in the mixing layer from case SM0. Therefore, the increase in the multi-phase RMI mixing length is a result of the continued presence of the particles within the flow. A possible explanation for this is the presence of an additional vorticity production term in Eq. (23), which is non-zero as a result of the differential gas-particle velocities. Figure 6(b) shows the time evolution of the magnitude of the vorticity production contributions from the baroclinic torque, $|\beta_i(t)|$, and the interphase particle term, $|\Pi_i(t)|$, volume averaged over the mixing layer, defined as extending between $x_{\eta,L}$ and $x_{\eta,R}$ in the longitudinal direction and L_y and L_z in the transverse directions. For simulations where the particle vorticity production is much less than the vorticity production by baroclinic torque ($|\beta_i(t)| \gg |\Pi_i(t)|$), there is a correspondingly little or no increase in the mixing-layer growth rate. However, when the two terms are of similar magnitude, the mixing-layer growth-rate increases as a result of this additional vorticity production. For example, the magnitude of the span-wise volume averaged vorticity, $|\omega_i(t)|$, at $t = 2.5$ ms for case SM14 is 38.7 s^{-2} compared to 20.6 s^{-2} for case SM0.

By increasing $k_0\eta_0$, the initial misalignment of the pressure and the density at the interface increases the baroclinic torque production and therefore, the relative difference between $|\Pi_i(t)|$ and $|\beta_i(t)|$, is altered. Though not shown here, this trend is observed by comparing the deviations of cases SMN12-14 and SM12-14 from the single-phase cases SMN0 and SM0, respectively. The mixing zone width at $t = 3.0$ ms for case SMN12 is slightly reduced by 1.78% compared to case SMN0 ($\eta_{\text{SMN12}} = 0.143$, $\eta_{\text{SMN0}} = 0.145$), and for case SMN14, a small increase of 2.2% is observed. These

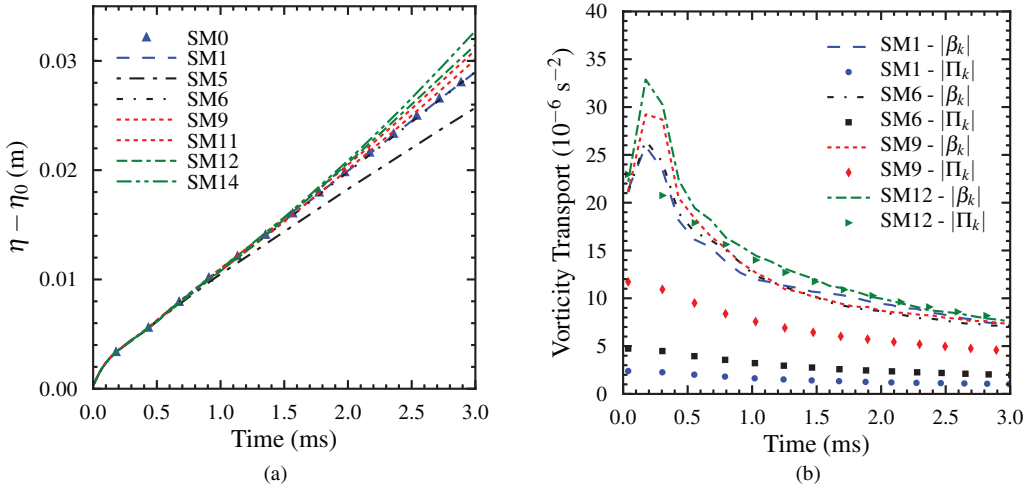


FIG. 6. (a) Evolution of the mixing layer width, $\eta(t)$, at different α_0 and St. (b) The vorticity transport budget during the initial growth of the RMI for cases with the same r_p where $|\Pi_k(t)|$ and $|\beta_k(t)|$ are the magnitude of the vorticity production due to the particle acceleration term and the baroclinic torque volume-averaged over the mixing zone.

deviations from the single-phase results are much less than those observed for SM12 and SM14 shown in Fig. 6(a), with case SM12 actually showing reduction in η instead of an increase.

Also, it is interesting to note that from comparison of cases MM12-14 and SM12-14 between Figs. 3(a) and 6(a), the increase in the width of the mixing layer is much larger for the multi-mode initializations than the single-mode initializations. Physically, this results from an increase in the inter-phase coupling within the mixing layer for the multi-mode initializations, and is ultimately observed in the vorticity transport budget. It should be further noted that in the multi-mode RMI, the width of the mixing layer is larger for case MM12 than case MM14. This is a reversal in the trend observed in single-mode RMI, which can be explained by the differences in time-history of vorticity magnitude. For case MM12, at $t = 2.5$ ms, $|\omega_i|$ is 35.5 s^{-2} compared to a value of 25.5 s^{-2} for case MM14, where for the single-mode cases SM12 and SM14 at $t = 2.5$ ms, $|\omega_i|$ is 38.9 s^{-2} and 42.1 s^{-2} , respectively.

In summary, for $\text{St} \ll 1$, the assumption of gas-particle equilibrium is more accurate, and the two-phase linear impulse model² and multi-phase buoyancy-drag model³⁸ match the trends observed in the current three-dimensional numerical simulations. For $\text{St} > 1$, however, the assumptions made in these models are less accurate since the nonlinear two-phase coupling terms are significant.

B. Re-shock

After the initial shock refraction, the transmitted wave continues to propagate through the two-phase medium. The presence of the particles reduces the speed of the shock wave, thus the time for the wave to reach the end wall and reflect is increased. For instance, the shock wave takes 2.64 ms to travel the length of the domain in case SM0, while it takes 2.81 ms in case SM5. In general, the dynamics of the shock, particle cloud and mixing zone is summarized in x - t diagram in Fig. 5(a). At re-shock the reflected wave compresses the flow further and refracts through the developing mixing-zone. As a result of the particle drag, the time at which re-shock is delayed as observed in Fig. 7(a). This analysis, however, is complicated by the time-dependence of the mass loading. For a given initial volume fraction, simulations with a smaller St (smaller r_p) show that the effective volume fraction increases in the domain (see Fig. 5(b)) as the particle cloud compresses due to the presence of the end-wall. Thus, the total drag is more significant for flows of the same α_0 but smaller St. For example, the mixing layer width just begins to compress at $t_r = 3.73$ ms for case SM12 and at $t_r = 3.51$ ms for case SM14, a 6% change, while between cases SM5 and SM8 there is only a 4.5% change ($t_r = 3.61$ ms and $t_r = 3.45$ ms, respectively).

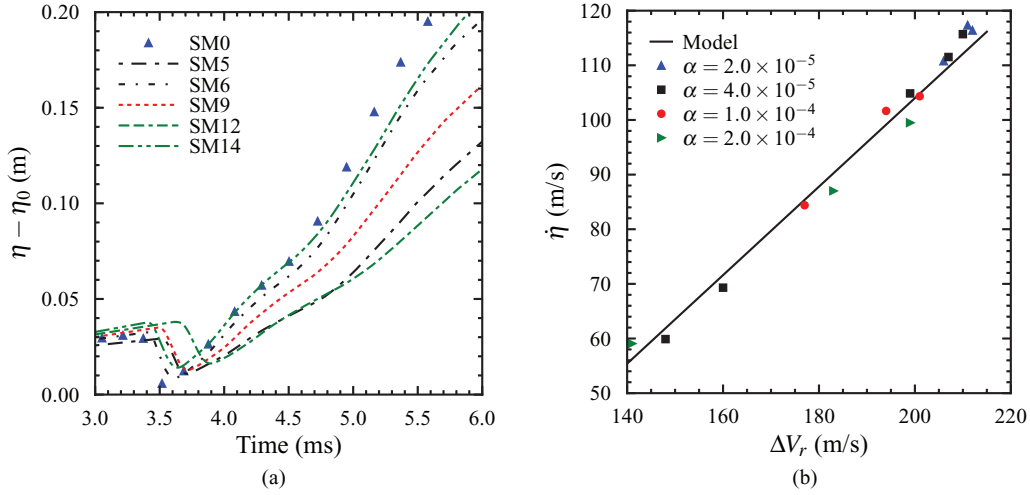


FIG. 7. (a) Time evolution of the mixing-layer growth, $\eta(t)$, after re-shock. (b) Relationship between the velocity jump, ΔV_r , at re-shock and the re-shocked RMI growth-rate, $\dot{\eta}_r$, compared to the model given by Eq. (25).

The correlation between the velocity jump across the contact at re-shock and the re-shocked RMI growth-rate is shown in Fig. 7(b) with the data summarized in Table IV. As observed in Fig. 7(b), there is a clear linear relationship between ΔV_r and $\dot{\eta}_r$. This follows the trends observed in the single-phase re-shock experiments²⁵ and corresponds to the analytical model derived by Mikaelian²⁶ given by the correlation

$$\dot{\eta}_r = C A_r^+ \Delta V_r, \quad (24)$$

where C is an empirical constant determined by Mikaelian²⁶ to be 0.28, ΔV_r is the jump in velocity across the contact at re-shock, and A_r^+ is the post re-shock Atwood number. Thornber *et al.*³³ have modified this relationship to account for differences in the initial conditions which are manifested through the changes in the molecular mixing fraction at the time of re-shock. The time evolution of $\Theta(t)$ shown in Fig. 9 indicates that the molecular mixing fraction prior to re-shock is a function of the initial St, where the molecular mixing fraction at re-shock, Θ_r , is larger for smaller St. Given this dependence, a semi-analytical model for the re-shocked RMI growth rate can be adapted for dilute

TABLE IV. Summary of the re-shocked RMI growth-rate data with the numerically computed value of the linear coefficient, $C_{r, num}$.

Case	A_r^+	$A_{m,r}^+$	Θ_r	ΔV_r (m/s)	$\dot{\eta}_r$ (m/s)	$C_{r, num}$
SM1	0.779	0.739	0.304	206.0	110.8	0.872
SM2	0.771	0.741	0.288	211.0	117.3	0.889
SM3	0.771	0.741	0.297	212.0	116.4	0.883
SM4	0.739	0.610	0.439	148.0	59.9	0.886
SM5	0.743	0.640	0.408	160.0	69.3	0.880
SM6	0.768	0.704	0.283	199.0	104.9	0.884
SM7	0.769	0.711	0.286	207.0	111.5	0.896
SM8	0.770	0.712	0.292	210.0	115.7	0.920
SM9	0.755	0.614	0.350	177.0	84.4	0.963
SM10	0.761	0.631	0.293	194.0	101.7	0.987
SM11	0.770	0.643	0.280	201.0	104.3	0.952
SM12	0.754	0.556	0.416	141.0	59.1	0.986
SM13	0.756	0.581	0.322	183.0	87.0	0.994
SM14	0.766	0.599	0.294	199.0	99.5	0.993

gas-particle mixtures and is given by

$$\dot{\eta}_r = C_r \sqrt{1 - \Theta_r} A_{m,r}^+ \Delta V_r, \quad (25)$$

where similar to the multi-phase impulsive model, Eq. (21), the post re-shock multi-phase Atwood number, $A_{m,r}^+$, replaces A_r^+ . The value of C_r is determined to be approximately 0.895. Table IV gives the numerically calculated values of the constant C_r . This model is then used to predict the re-shocked RMI growth rate of the multi-mode cases MM12-14. The agreement is within 10% of the numerically predicted values further indicating that both $A_{m,r}^+$ and Θ_r are able to capture the dependence of the re-shocked growth-rate on the initial mass loading and the particle radius. The constant, however, seems to be weakly dependent on the initial volume fraction.

C. Late-time mixing

After re-shock, the growth of the mixing zone further accelerates, and as the bubble structures merge and the anisotropy decreases, the dominate wave number shifts to lower wavelengths while increasingly smaller scales are created through vortex stretching. Previous experimental measurements and computational predictions²⁹ show that at late times the re-shocked mixing zone closely approximates decaying isotropic inertial range turbulence. In the multi-mode simulations conducted here, a similar trend is observed; the fluctuating energy spectrum at $t = 8.0$ ms is shown in Fig. 8 for cases MM0, MM12, and MM14. For the same volume fraction, higher mass loadings result in more energetic large-scale fluctuations. The total turbulent kinetic energy, $TKE = \int E(k)dk$ is approximately 51 m/s for MM14 and only 18.25 m/s at $t = 8$ ms, where $E(k)$ is the fluctuating specific kinetic energy. At $t = 10$ ms, the TKE decays to 21 m/s and 7.5 m/s, respectively. Likewise the turbulent energy dissipation rate, $\epsilon = \int 2\nu k^2 E(k)dk$, is much larger for case MM14 than MM12. These conditions are borne out of the differences in the asymptotic widths of the mixing zone ($\eta_{MM0} \approx 9.5$ cm, $\eta_{MM12} = 7.9$ cm and $\eta_{MM14} = 10.5$ cm), which were a result of the variance in the re-shock time and growth-rate. The late-time mixing fraction (see Fig. 3(b)), however, is roughly equivalent for all cases simulated in this study, and varies only between 0.84 and 0.88, a further indication that mixing zone has reached a state of decaying self-similar turbulence.

For the single-mode initializations, the width of the mixing zone does not saturate, which is evident by Fig. 9(a), during the time period simulated in this study. As a result, the scales of the flow at the same time ($t = 8$ ms) are much larger and more anisotropic as compared to the multi-mode cases. This results in a wide-range of molecular mixing fractions as observed in Fig. 9(b) compared to those in Fig. 3(b). Initially, Θ is close to one since the mixing layer is only a small diffuse layer and decreases as the instability develops, and the “bubble” and “spike” structures entrain the two pure fluids. At higher volume fractions and for cases with smaller particle radius, the pre re-shock mixing

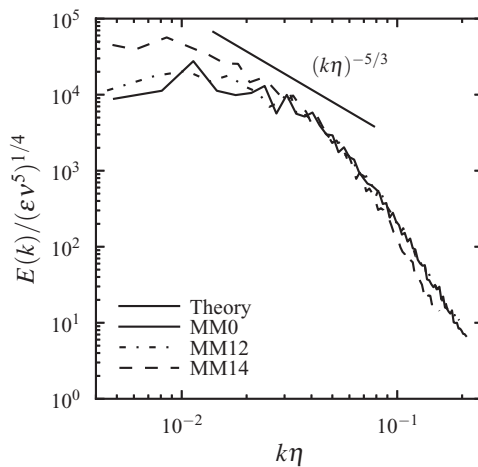


FIG. 8. Normalized spectra of the turbulent kinetic energy (TKE) for the multi-mode cases MM0, MM12, and MM14 at time $t = 8$ ms.

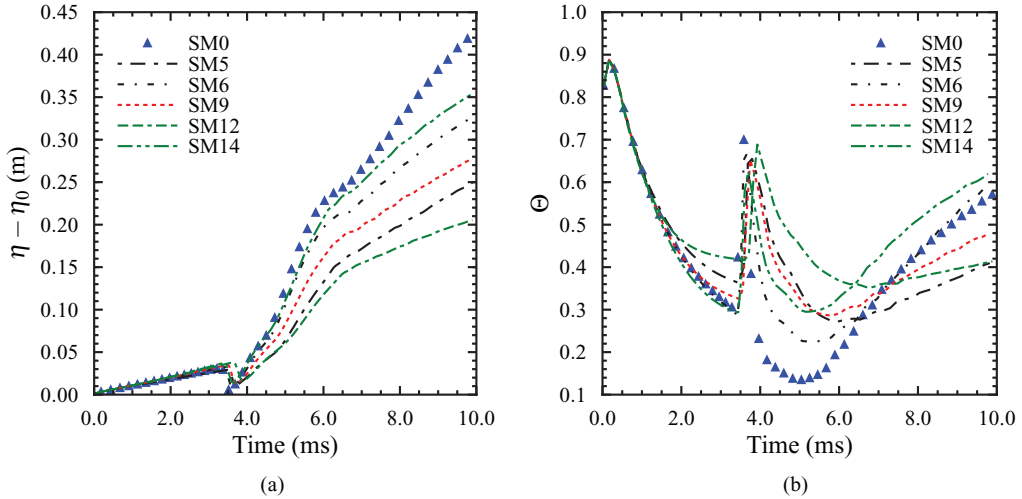


FIG. 9. Time evolution of (a) the mixing length, $\eta(t)$, and (b) the molecular mixing fraction, $\Theta(t)$ for the dilute gas-particle single-mode cases compared to the single-phase results, SM0.

layer is more well-mixed. This is a result of the increased vorticity production by the presence of the particles (see Fig. 6(b)). The re-shock then compresses the mixing layer and enhances the level of mixing such that after re-shock, the molecular mixing fraction first reaches a minimum and then increases indicating that mixing within the layer is occurring at a faster rate than the entrainment of the pure fluids. This minimum is larger for higher mass loadings. Interestingly, the initial mixing enhancement of case SM14 does not result in higher levels of mixing at late-times. Figure 10 shows contours of the species mass fraction at $Y_{SF_6} = Y_{Air} = 0.5$ and the particle cloud colored by the magnitude of the particle velocity for cases SM0, SM5, SM9, and SM14. There is a noticeable difference in the structure of the mixing zones between cases SM0 and SM14. For cases SM5 and SM9, which have intermediate Stokes numbers, the mixing zone is moving in the opposite direction of the particle cloud. This motion is apparent from the x - t diagram in Fig. 5(a), which shows that even for $St < 1.0$ the trailing edge of the particle cloud lags the mixing zone. This opposed fluid-particle motion when combined with an increase in the volume fraction from the compression of the particle cloud results in an increase in the drag on the flow and causes a reduction in the mixing length. This suggests that in certain two-phase flows the mixing efficiency of the RMI-induced mixing zone at late times can either be enhanced or inhibited with the determination largely dependent on the

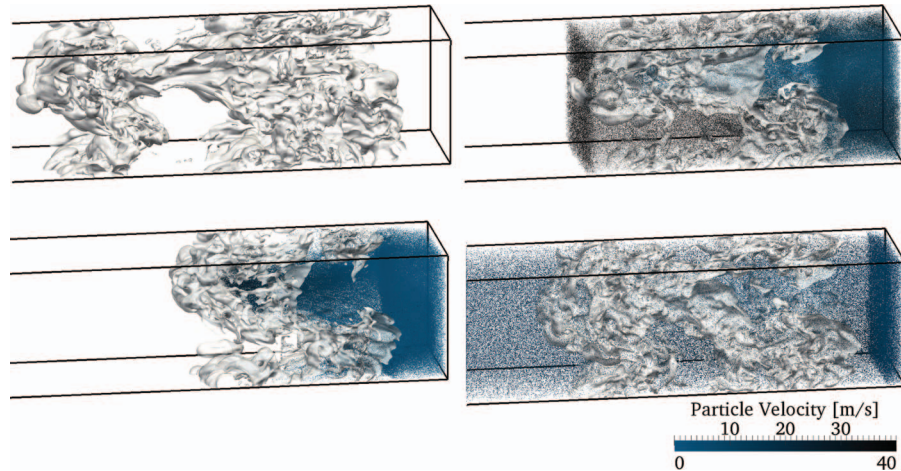


FIG. 10. Contours of the species mass fraction at $Y_{SF_6} = Y_{Air} = 0.5$ and particle locations colored by the magnitude of the particle velocity for cases SM0 (top left), SM5 (bottom left), SM9 (top right), and SM14 (bottom right).

impulse of the re-shock event and the Stokes number. In the case of no re-shock, however, higher mass loadings seem to indicate an enhancement in the mixing.

V. CONCLUSIONS

Using detailed three-dimensional numerical simulations, RMI in dilute gas-particle mixtures is investigated both before and after re-shock for a variety of initialization conditions. Single-phase simulations of re-shocked RMI show good agreement to experimental and theoretical results giving confidence to the numerical methodology and serving as a baseline for comparison to the multi-phase results. Two parameters are used to characterize the dynamics of the two-phase RMI, the mass loading and the Stokes number, which are varied by changing the initial particle volume fraction and the particle radius for both single-mode and multi-mode initializations. At $St < 1$, there is a reduction in the initial growth-rate of the RMI, but with increases in St and mass loading, there is an observable increase in the width of the mixing layer, as much as 43% in the range of conditions investigated. This increase is attributed to the additional vorticity production due to the presence of particles and inter-phase momentum coupling—a nonlinear effect not observable in the prior simplified analytical models of two-phase RMI. In addition, re-shock RMI is investigated, and it is observed that the growth-rate of the RMI after re-shock is impeded by the presence of a denser particle cloud in the case of lower Stokes number subsequently affecting the width of the mixing zone at late-times. For the multi-mode initializations, the mixing-zone saturates and closely approximates a decaying self-similar turbulent mixing layer. The particle cloud, however, only weakly affects the decay rate of the turbulent mixing layer. Most importantly, the re-shocked RMI growth rate is shown to be linearly correlated to the velocity jump at re-shock, which is reduced for smaller Stokes numbers. A new growth-rate correlation for the re-shocked RMI growth rate is introduced that is dependent on the molecular mixing fraction and the multi-phase Atwood number at re-shock resulting in a growth-rate constant of approximately 0.895. This constant, however, is a weak function of the initial volume fraction. In the future, the effect of the location particle cloud relative to the initial contact discontinuity and the re-shock distance should be investigated.

ACKNOWLEDGMENTS

This work is supported by the Defense Threat Reduction Agency (Dr. S. Peiris, Program Manager). The computational resources were provided by DoD HPC Centers at the Air Force Research Laboratory, the Engineer Research and Development Center, and the Navy DoD Supercomputing Resource Center.

- ¹ M. Brouillette, “The Richtmyer-Meshkov instability,” *Annu. Rev. Fluid Mech.* **34**, 445 (2002).
- ² S. Ukai, K. Balakrishnan, and S. Menon, “Growth rate predictions of single- and multi-mode Richtmyer-Meshkov instability with reshock,” *Shock Waves* **21**, 533 (2011).
- ³ R. D. Richtmyer, “Taylor instability in shock acceleration of compressible fluids,” *Commun. Pure Appl. Math.* **13**, 297 (1960).
- ⁴ M. Jones and J. Jacobs, “A membraneless experiment for the study of Richtmyer-Meshkov instability of a shock-accelerated gas interface,” *Phys. Fluids* **9**, 3078 (1997).
- ⁵ R. L. Holmes, G. Dimonte, B. Fryxell, M. L. Gittings, J. W. Grove, M. Schneider, D. H. Sharp, A. L. Velikovich, R. P. Weaver, and Q. Zhang, “Richtmyer-Meshkov instability growth: experiment, simulation and theory,” *J. Fluid Mech.* **389**, 55 (1999).
- ⁶ P. R. Chapman and J. W. Jacobs, “Experiments on the three-dimensional incompressible Richtmyer-Meshkov instability,” *Phys. Fluids* **18**, 074101 (2006).
- ⁷ H. Hecht, U. Alon, and D. Shvarts, “Potential flow models of Rayleigh-Taylor and Richtmyer-Meshkov bubble fronts,” *Phys. Fluids* **6**, 4019 (1994).
- ⁸ O. Sadot, L. Erez, U. Alon, D. Oron, and L. Levin, “Study of nonlinear evolution of single-mode and two-bubble interaction under Richtmyer-Meshkov instability,” *Phys. Rev. Lett.* **80**, 1654 (1998).
- ⁹ Q. Zhang and S.-I. Sohn, “Nonlinear theory of unstable fluid mixing drive by shock wave,” *Phys. Fluids* **9**, 1106 (1997).
- ¹⁰ P. G. Saffman and D. I. Meiron, “Kinetic energy generated by the incompressible Richtmyer-Meshkov instability in a continuous stratified fluid,” *Phys. Fluids A* **1**, 1767 (1989).
- ¹¹ M. Brouillette and B. Sturtevant, “Experiments on the Richtmyer-Meshkov instability: single-scale perturbations on a continuous interface,” *J. Fluid Mech.* **263**, 271 (1994).
- ¹² G. Dimonte, C. E. Frerking, and M. Schneider, “Richtmyer-Meshkov instability in the turbulent regime,” *Phys. Rev. Lett.* **74**, 4855 (1995).

¹³ B. Thornber, D. Drikakis, D. L. Youngs, and R. J. R. Williams, "The influence of initial conditions on turbulent mixing due to Richtmyer-Meshkov instability," *J. Fluid Mech.* **654**, 99 (2010).

¹⁴ G. Dimonte and M. Schneider, "Turbulent Richtmyer-Meshkov instability experiments with strong radiatively driven shocks," *Phys. Plasmas* **4**, 4347 (1997).

¹⁵ G. Dimonte and M. Schneider, "Density ratio dependence of Rayleigh-Taylor mixing for sustained and impulsive acceleration histories," *Phys. Fluids* **12**, 304 (2000).

¹⁶ J. K. Prasad, A. Rasheed, S. Kumar, and B. Sturtevant, "The late-time development of the Richtmyer-Meshkov instability," *Phys. Fluids* **12**, 2108 (2000).

¹⁷ D. Oron, L. Arazi, D. Kartoon, A. Rikanati, U. Alon, and D. Shvarts, "Dimensionality dependence of the Rayleigh-Taylor and Richtmyer-Meshkov instability late-time scaling laws," *Phys. Plasmas* **8**, 2883 (2001).

¹⁸ O. Sadot, L. Erez, D. Oron, G. Erez, G. Ben-Dor, U. Alon, L. A. Levin, and D. Shvarts, "Studies on the nonlinear evolution of the Richtmyer-Meshkov instability," *Astrophys. J. Suppl. Ser.* **127**, 469 (2000).

¹⁹ J. Ramshaw, "Simple model for linear and nonlinear mixing at unstable fluid interfaces with variable accelerations," *Phys. Rev. E* **58**, 5834 (1998).

²⁰ M. Lombardini, D. I. Pullin, and D. I. Meiron, "Transition to turbulence in shock-driven mixing: a Mach number study," *J. Fluid Mech.* **690**, 203 (2012).

²¹ G. C. Orlicz, B. J. Balakumar, C. D. Tomkins, and K. P. Prestridge, "A Mach number study of the Richtmyer-Meshkov instability in a varicose, heavy-gas curtain," *Phys. Fluids* **21**, 064102 (2009).

²² M. Lombardini, D. J. Hill, D. I. Pullin, and D. I. Meiron, "Atwood ratio dependence of Richtmyer-Meshkov flows under reshock conditions using large-eddy simulations," *J. Fluid Mech.* **670**, 439 (2011).

²³ B. J. Balakumar, G. C. Orlicz, J. R. Ristorcelli, S. Balasubramanian, K. P. Prestridge, and C. D. Tomkins, "Turbulent mixing in a Richtmyer-Meshkov fluid layer after reshock: velocity and density statistics," *J. Fluid Mech.* **696**, 67 (2012).

²⁴ E. Leinov, G. Malamud, Y. Elbaz, L. A. Levin, G. Ben-Dor, D. Shvarts, and O. Sadot, "Experimental and numerical investigation of the Richtmyer-Meshkov instability under re-shock conditions," *J. Fluid Mech.* **626**, 449 (2009).

²⁵ M. Vetter and B. Sturtevant, "Experiments on the Richtmyer-Meshkov instability of an air/SF₆ interface," *Shock Waves* **4**, 247 (1995).

²⁶ K. O. Mikaelian, "Turbulent mixing generated by Rayleigh-Taylor and Richtmyer-Meshkov instabilities," *Physica D* **36**, 343 (1989).

²⁷ A. A. Charakhch'yan, "Reshocking at the non-linear stage of Richtmyer-Meshkov instability," *Plasma Phys. Control. Fusion* **43**, 1169 (2001).

²⁸ R. H. Cohen, W. P. Dannevick, A. M. Dimits, D. E. Eliason, A. A. Mirin, and Y. Zhou, "Three-dimensional simulation of a Richtmyer-Meshkov instability with a two-scale initial perturbation," *Phys. Fluids* **14**, 3692 (2002).

²⁹ D. J. Hill, C. Pantano, and D. I. Pullin, "Large-eddy simulation and multiscale modelling of a Richtmyer-Meshkov instability with reshock," *J. Fluid Mech.* **557**, 29 (2006).

³⁰ O. Schilling and M. Latini, "High-order WENO simulations of three-dimensional reshocked Richtmyer-Meshkov instability to late times: dynamics, dependence of initial conditions, and comparisons to experimental data," *Acta Math. Sci.* **30**, 595 (2010).

³¹ L. Houas and I. Chemouni, "Experimental investigation of the Richtmyer-Meshkov instability in shock tube," *Phys. Fluids* **8**, 614 (1996).

³² A. A. Gowardhan and F. F. Grinstein, "Numerical simulation of Richtmyer-Meshkov instabilities in shocked gas curtains," *J. Turbul.* **12**, N43 (2011).

³³ B. Thornber, D. Drikakis, D. L. Youngs, and R. J. R. Williams, "Growth of a Richtmyer-Meshkov turbulent layer after reshock," *Phys. Fluids* **23**, 095107 (2011).

³⁴ K. O. Mikaelian, "Analytic approach to nonlinear Rayleigh-Taylor and Richtmyer-Meshkov instabilities," *Phys. Rev. Lett.* **80**, 508 (1998).

³⁵ K. Balakrishnan and S. Menon, "On turbulent chemical explosions into dilute aluminum particle clouds," *Combust. Theory Model.* **14**, 583 (2010).

³⁶ P. K. Shukla, "A survey of dusty plasma physics," *Phys. Plasmas* **8**, 1791 (2001).

³⁷ S. Ulkai, K. Balakrishnan, and S. Menon, "On Richtmyer-Meshkov instability in dilute gas-particle mixtures," *Phys. Fluids* **22**, 104103 (2010).

³⁸ K. Balakrishnan and S. Menon, "A multi-phase buoyancy-drag model for the study of Rayleigh-Taylor and Richtmyer-Meshkov instabilities in dusty gases," *Laser Part. Beams* **29**, 201 (2011).

³⁹ Y. Srebro, Y. Elbaz, O. Sadot, L. Arazi, and D. Shvarts, "A general buoyancy-drag model for the evolution of the Rayleigh-Taylor and Richtmyer-Meshkov instabilities," *Laser Part. Beams* **21**, 347 (2003).

⁴⁰ F. Genin and S. Menon, "Studies of shock/turbulence shear layer interaction using large-eddy simulation," *Comput. Fluids* **39**, 800 (2010).

⁴¹ J. C. Schulz, K. C. Gottiparthi, and S. Menon, "Ionization in gaseous detonation waves," *Shock Waves* **22**, 579 (2012).

⁴² D. M. Snider, "An incompressible three-dimensional multiphase particle-in-cell model for dense particle flows," *J. Comput. Phys.* **170**, 523 (2001).

⁴³ K. C. Gottiparthi and S. Menon, "A study of interaction of clouds of inert particles with detonation in gases," *Combust. Sci. Technol.* **184**, 406 (2012).

⁴⁴ S. Srinivasan, A. Smith, and S. Menon, "Accuracy, reliability and performance of spray combustion models in large-eddy simulations," in *Quality and Reliability of Large-Eddy Simulations II* (Springer, 2011), pp. 211–220.

⁴⁵ V. Boiko, V. Kiselev, S. Keselev, A. Papyrin, S. Poplavsky, and V. Fomin, "Shock wave interaction with a cloud of particles," *Shock Waves* **7**, 275 (1997).

⁴⁶ R. Drake, "Discussion on the paper entitled 'Forced convection heat transfer from an isothermal sphere to water' by G. C. Violet and G. Leppert," *ASME J. Heat Transfer* **83**, 170 (1961).



Simulations of heterogeneous detonations and post-detonation turbulent mixing and afterburning

Kalyana Chakravarthi Gottiparthi and Suresh Menon

Citation: [AIP Conf. Proc. 1426](#), 1639 (2012); doi: 10.1063/1.3686600

View online: <http://dx.doi.org/10.1063/1.3686600>

View Table of Contents: <http://proceedings.aip.org/dbt/dbt.jsp?KEY=APCPCS&Volume=1426&Issue=1>

Published by the [American Institute of Physics](#).

Additional information on AIP Conf. Proc.

Journal Homepage: <http://proceedings.aip.org/>

Journal Information: http://proceedings.aip.org/about/about_the_proceedings

Top downloads: http://proceedings.aip.org/dbt/most_downloaded.jsp?KEY=APCPCS

Information for Authors: http://proceedings.aip.org/authors/information_for_authors

ADVERTISEMENT

An advertisement for AIP Advances. On the left, the AIP Advances logo is displayed, featuring the text 'AIP Advances' in a stylized blue and green font, with several orange spheres of varying sizes trailing off to the right. Below this, a green button with the text 'Submit Now' in white is visible. On the right, a green rectangular area contains text about the journal's features: 'Explore AIP's new open-access journal', 'Article-level metrics now available', and 'Join the conversation! Rate & comment on articles'.

SIMULATIONS OF HETEROGENEOUS DETONATIONS AND POST-DETONATION TURBULENT MIXING AND AFTERBURNING

Kalyana C. Gottiparthi* and Suresh Menon*

*School of Aerospace Engineering, Georgia Institute of Technology, Atlanta, GA 30332

Abstract. We conduct three-dimensional numerical simulations of the propagation of blast waves resulting from detonation of a nitromethane charge of radius 5.9 cm loaded with aluminum particles and analyze the afterburn process as well as the generation of multiple scales of mixing in the post detonation flow field. In the current study, the particle combustion is observed to be dependent on particle dispersal and mixing of gases in the flow where particle dispersal spreads aluminum within the flow and mixing provides the necessary oxidizer. Thus, $5 \mu\text{m}$ aluminum particles are burnt more effectively in comparison to $10 \mu\text{m}$ particles for a fixed initial mass of particles. Also, for a fixed initial particle size, increase in the initial mass of aluminum particles resulted in greater mixing.

Keywords: Detonation, Blast Wave, Afterburn

PACS: *43.28.Mw, 47.40.Rs, 47.27.wj

INTRODUCTION

Augmentation of impulsive loading is known to occur when solid metal particles are added to an explosive charge, termed heterogeneous explosive, due to the momentum and energy delivered by the particles. When such a charge is detonated, the high-pressure combustion products rapidly expand to drive a blast wave which attenuates due to the effects of spreading [1]. At the same time the metal particles pick up momentum from the gas due to drag, penetrate the contact surface and generate perturbations which grow into hydrodynamic instabilities. These instabilities which are initially Rayleigh-Taylor (RT) [2] in nature are essentially three-dimensional and give rise to mixing of the hot detonation products and the shock-compressed air. Also, as the primary blast wave is driven outward, the flow is over-expanded by the inward moving rarefaction wave, and a secondary-shock is generated. The interaction of the hydrodynamic structures and the secondary-shock results in Richtmyer-Meshkov (RM) instability [3] leading to superior mixing due to vorticity generation by baroclinic effects. Although experi-

mental studies provide evidence of hydrodynamic instabilities in heterogeneous explosions [4], due to the destructive nature of the flow, measurements to characterize the mixing in these explosions may never be possible. Thus, numerical simulations can play a vital role in exploring the details of the mixing and the flow physics, especially in the post-detonation flow.

If the initial charge contains reactive metal particles, the afterburn can provide a significant contribution to the total impulsive loading of the charge [1]. This afterburn is dependent on magnitude of mixing which in turn depends on instability generation. Although previous investigations explored post-detonation flow instabilities due to homogeneous and heterogeneous explosives with inert solid particles [1, 5], the afterburn and mixing in the post-detonation flow of a heterogeneous explosives with reactive solid particles are yet to be explored. Thus, in this paper, we use numerical simulations to study the instability generation and combustion of metal particles ensuing from detonation of a heterogeneous nitromethane charge with aluminum particles. The effects of particle size and the mass loading (η), defined as ratio of mass of particles to mass of the gas

in the initial charge, on the particle dispersal, mixing and afterburn are also investigated.

NUMERICAL METHOD

Following past numerical studies [1, 5], an Eulerian-Lagrangian formulation is used in the current study to perform three-dimensional simulations of heterogeneous blast waves. The compressible, unsteady, multi-species, multiphase Navier-Stokes equations for reacting gas flow are used to solve for the gas phase whereas Lagrangian tracking approach is used to solve for the position, the mass, the velocity and the temperature of the solid particles. Noble-Abel equation of state is used here for thermodynamic closure [6]. For brevity, the full set of equations, described elsewhere [1], are not presented here. The reaction rates for the problem in the present paper are expected to be very fast, and so, infinite rate chemistry is used to simplify the combustion model following previous studies [1, 7]. The flow is assumed to comprise of 9 species (H_2O , H_2 , CO , N_2 , O_2 , Al , CO_2 , Al_2O_3 and Al/O) and a five step chemistry employed here is obtained from the six step chemistry presented in [1].

The momentum and energy transfer between the two phases is evaluated using empirical expressions for drag coefficient (C_D) and Nusselt number (Nu) [8]. Following past studies [8, 9], evaporation law specified as, $\frac{dr_p}{dt} = -\frac{r_p}{t_b} (1 + 0.276(Re)^{0.5})$, is used, where r_p denotes the particle radius, Re , the particle Reynolds number, and t_b , the burning time. The burn time data from [9] is used here and the ignition temperature of the aluminum particles is assumed to be 1000 K [8].

The governing equations for the gas phase are solved using MUSCL shock-capturing scheme with HLLC/E Riemann solver [1], and a predictor-corrector scheme for time accuracy. The scheme is second order accurate in both space and time. A 4th order Runge-Kutta scheme is used to solve the solid phase governing equations. Detailed validation of this simulation strategy and numerical approach for shock-turbulence interaction [10], blast waves [1, 5] and detonations [11] has been reported elsewhere.

Three-dimensional sector, with 45° in azimuthal directions, and spherical grids are used in the current study [1] with resolutions $1000 \times 60 \times 60$ and $1000 \times 200 \times 200$, respectively. These resolutions

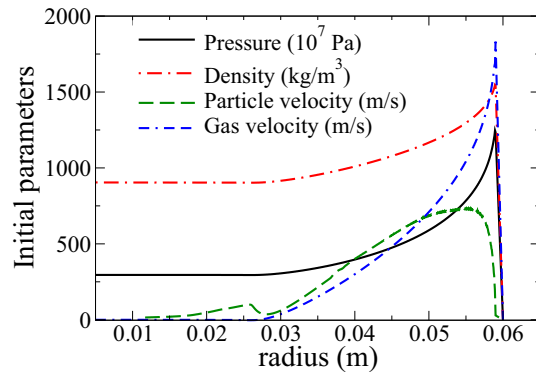


FIGURE 1. Initial detonation profile for heterogeneous nitromethane charge with aluminum particles.

TABLE 1. Initial radius of particles (r_{p0}), mass loading and number of particles tracked in each case. Particles are tracked by tracking parcels [1], group of particles. Here, each parcel contains 50 particles.

Case	η	r_{p0} (μm)	Number of parcels
1	1.0	10.0	86881
2	2.0	10.0	173762
3	1.0	5.0	695048

are chosen based on extensive resolution studies performed earlier [1]. The maximum extent in radial direction in both grid configurations is 2.4 m. The initial detonation and particle profiles, shown in Fig. 1, are computed from a 1D simulation based on the Gas-Interpolated-solid Stewart-Prasad-Asay (GISPA) method [12]. Aluminum particles are placed uniformly within the initial charge radius which is 5.9 cm. As indicated in Table 1, η and r_{p0} are varied and the resulting post-detonation flow is studied in each case.

RESULTS AND DISCUSSION

The detonation of a homogeneous explosive charge results in four critical phases of post-detonation flow which can be summarized as (i) blast wave phase, (ii) implosion phase, (iii) re-shock phase and (iv) asymptotic mixing phase [8]. During the blast wave phase, the initial perturbations at the contact surface of the hot detonation products and the ambient air generate RT instabilities. These

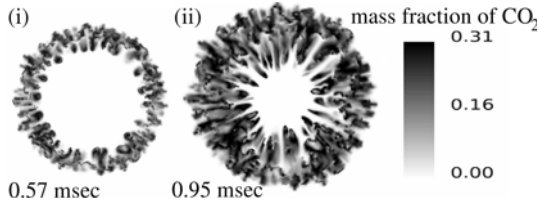


FIGURE 2. Formation of CO_2 due to afterburn in the post-detonation flow of a homogeneous nitromethane charge during (i) blast wave and (ii) implosion phases.

perturbations are considered to occur due to the imperfections in the charge or due to the small scale disturbances arising from molecular scales. In the current study, the perturbations at the contact surface are initialized stochastically based on Gaussian distribution. The mixing of the detonation products with air causes afterburn of CO to generate CO_2 . In Fig. 2, the mass fraction of CO_2 is presented to show the mixing layer generated in blast wave and implosion phases. Figure 2 also shows the formation of ‘finger-like’ projections or spikes due to the expansion of gases towards the center during the implosion phase.

Although simulations performed using spherical grids provide flow features in all directions in great detail, as shown in Fig. 2, these simulations are computationally expensive to perform parametric studies. Thus, we employed sector grids to analyze the effects of η and r_{p_0} on the post-detonation flow. The degree of mixedness obtained using spherical and sector grids is almost identical as shown in Fig. 3 which supports the sector grid configuration employed in the rest of this paper. Here, the degree of mixedness (DM), based on previous studies [8], is defined as $DM = \left[\frac{\int Y_{CO}(Y_{N_2} - Y'_{N_2})dV}{\int dV} \right] / \left[\left(\frac{\int Y_{CO}dV}{\int dV} \right) \left(\frac{\int (Y_{N_2} - Y'_{N_2})dV}{\int dV} \right) \right]$, where Y_{CO} and Y'_{N_2} are, respectively, the instantaneous mass fractions of CO and N_2 and Y'_{N_2} is the mass fraction of N_2 in the detonation products.

When a heterogeneous charge explodes the solid particles present within the charge are driven out and as these particles disperse outward they perturb the contact surface between the detonation products and ambient air. Thus, increase in the number of particles results in increased perturbations and hence increase in mixing. Thus, in Cases 2 and 3, due to increased mixing, as a result of more number of particles in

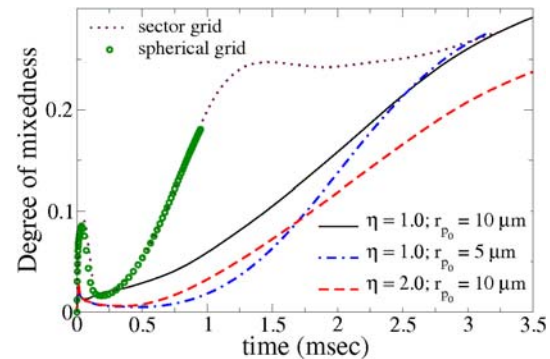


FIGURE 3. Variation of degree of mixedness with time. Dots and circles (sector and spherical grids) indicate cases with homogeneous explosive.

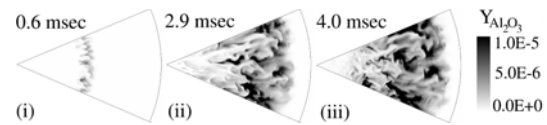


FIGURE 4. Formation of Al_2O_3 due to the combustion of Al in the post-detonation flow of a heterogeneous nitromethane charge (Case 1) during (i) blast wave, (ii) implosion, and (iii) re-shock phases.

comparison to Case 1, CO is converted to CO_2 and DM , in Fig. 3, decreases initially till time (t) = 0.5 ms. However, in Case 3, the $5\mu m$ particles burn quickly in comparison to $10\mu m$ particles. The Al combustion consumes O_2 needed for CO_2 production and thus DM in Case 3 increases above the values of DM for Cases 1 and 2 at t = 2.5 ms and 1.75 ms, respectively. In Case 2, the value of DM remains lower than that of Case 1 because of greater mixing and same burn rate for Al . Thus, for a fixed η , DM increased with decrease in r_{p_0} after the implosion phase and for a fixed initial r_{p_0} , DM decreased with increase in η .

As the blast wave is driven outwards, the initial mixing of aluminum particles with air and detonation products results in particle burning and increase in the mass fraction of Al_2O_3 ($Y_{Al_2O_3}$). This is followed by the implosion phase in which the particles are drawn towards the center along with the gases and hence the particle burning is enhanced. As the secondary-shock is formed after the implosion phase, the re-shock drives the particles outwards and the particle burning continues in the mixing layer.

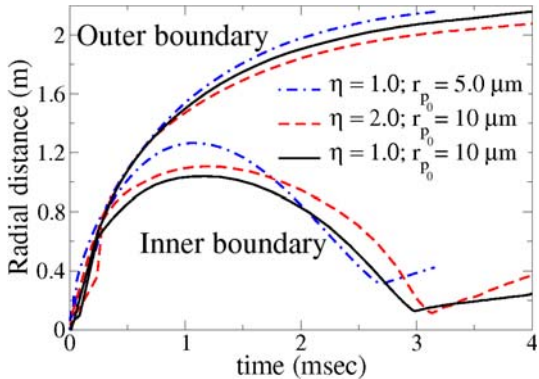


FIGURE 5. Variation of the inner and the outer boundaries of Al combustion with time. Here, the inner most and the outer most radial locations where the mass fraction of Al_2O_3 is atleast 5% of maximum mass fraction of Al_2O_3 is defined as the inner and the outer boundary, respectively.

These phases are shown in Fig. 4. Figure 5 shows the effect of particle dispersion, which determines Al availability, and mixing, which determines the amount of oxidizer (O_2 for ‘aerobic’, and H_2O and CO_2 for ‘anaerobic’ reactions) available, on the particle combustion. In Case 3, even though mixing is greater than Case 1 due to larger number of particles, the burning rate is high and thus the outer boundary overtakes the outer boundary of Case 1. Also, $5\text{ }\mu\text{m}$ particles are entrained and dragged towards center easily in comparison to $10\text{ }\mu\text{m}$ particles. Hence, the inner boundary in Case 3 is drawn below the inner boundary of Cases 1 and 2 during the implosion phase. Again during the re-shock phase, as $5\text{ }\mu\text{m}$ particles have relatively less inertia, the inner boundary overtakes the inner boundaries of Cases 1 and 2. In Case 2, the burn rate of particles is same as in Case 1. Hence higher mixing results in both the inner and outer boundaries of Case 2 to be within the inner and outer boundaries of Case 1. Thus, burn rate and mixing which directly depend on η and r_{p0} determine the afterburn and particle combustion.

CONCLUSIONS

Three-dimensional numerical simulations of blast wave propagation ensuing from detonation of a heterogeneous nitromethane charge of 5.9 cm radius with aluminum particles are presented. Both homogeneous and heterogeneous explosions generated hy-

drodynamic instabilities (RT and RM) which resulted in mixing of detonation products and ambient air and enhanced the afterburn. The simulations suggest that the combustion of Al is controlled by the particle dispersion and mixing of gases. In each case, mixing controls the amount of oxidizer available for different species to react and the net effect determines the extent of afterburn (Al or CO).

ACKNOWLEDGMENTS

This work is supported by the Defense Threat Reduction Agency (Dr. S. Peiris, Program Manager). The computational resources were provided by DoD HPC centers at AFRL and ERDC.

REFERENCES

1. Balakrishnan, K. and Menon, S., *Combust. Sci. Technol.*, **182**, 186–214 (2010).
2. Taylor, G. I., *Proc. R. Soc. London. A*, **201**, 192–196 (1950).
3. Richtmyer, R. D., *Commun. Pure Appl. Math.*, **13**, 297–319 (1960).
4. Frost, D. L., Zarei, Z. and Zhang, F., “Instability of Combustion Products Interface from Detonation of Heterogeneous Explosives,” in *20th International Colloquium on the Dynamics of Explosions and Reactive Systems*, Montreal, Canada, 2005.
5. Balakrishnan, K., Nance, D. V. and Menon, S., *Shock Waves*, **20**, 217–239 (2010).
6. Johnston, I. A., The Noble-Abel equation of state: Thermodynamic derivations for ballistics modelling, Tech. Rep. DSTO-TN-0670, Defence Science and Technology Organization (2005).
7. Kuhl, A. L., Ferguson, R. E. and Oppenheim, A. K., *Prog. Astronaut. Aeronaut.*, **173**, 251–261 (1997).
8. Balakrishnan, K. and Menon, S., *Combust. Theory Modell.*, **14**, 583–617 (2010).
9. Tanguay, V., Goroshin, S., Higgins, A. J. and Zhang, F., *Combust. Sci. Technol.*, **181**, 670–693 (2009).
10. Génin, F. and Menon, S., *Comput. Fluids*, **39**, 800–819 (2010).
11. Gottiparthi, K. C. Génin, F., Srinivasan, S. and Menon, S., *47th AIAA Aerospace Sciences Meeting* Orlando, Florida, 2009-0437 (2009).
12. Xu, S., Aslam, T. and Stewart, D. S., *Combust. Theory Modell.*, **1**, 113–142 (1997).

On the neutralization of bacterial spores in post-detonation flows

K. C. Gottiparthi · J. C. Schulz · S. Menon

Received: 4 August 2013 / Revised: 11 March 2014 / Accepted: 21 March 2014 / Published online: 9 April 2014
© Springer-Verlag Berlin Heidelberg 2014

Abstract In multiple operational scenarios, explosive charges are used to neutralize confined or unconfined stores of bacterial spores. The spore destruction is achieved by post-detonation combustion and mixing of hot detonation product gases with the ambient flow and spore clouds. In this work, blast wave interaction with bacterial spore clouds and the effect of post-detonation combustion on spore neutralization are investigated using numerical simulations. Spherical explosive charges (radius, $R_C = 5.9$ cm) comprising of nitromethane are modeled in the vicinity of a spore cloud, and the spore kill in the post-detonation flow is quantified. The effect of the mass of the spores and the initial distance, d^0 , of the spore cloud from the explosive charge on the percentage of spores neutralized is investigated. When the spores are initially placed within a distance of $3.0R_C$, within 0.1 ms after detonation of the charge, all the spores are neutralized by the blast wave and the hot detonation product gases. In contrast, almost all the spores survived the explosion when d^0 is greater than $8.0R_C$. The percentage of intact spores varied from 0 to 100 for $3.0R_C < d^0 < 8.0R_C$ with spore neutralization dependent on time spent by the spores in the post-detonation mixing/combustion zone.

Keywords Detonation · Blast wave · Bacterial spores

1 Introduction

Spores produced by certain bacteria are known to pose severe threats to human health and safety [1]. Neutralization of these biological agents has been a vital component of many threat reduction scenarios. In real life conditions, one of the operational strategies is to use explosive charges to destroy spores in both confined and unconfined environments. Past experimental investigations suggest that the spore neutralization can be achieved by heating and chemical corrosion [2]. Detonation of explosive charges produces a high temperature gaseous environment along with possible corrosive detonation product gases, both of which can be effectively used in multiple bio-agent defeat scenarios. However, there have been no reported studies in the open literature on the effects of explosive charges on spores. Such studies are essential and would enable the development of novel methods of spore neutralization.

Investigation of spore neutralization by explosive charges using experimental methods is challenging, and in some cases not feasible due to the destructive nature of the flow. When experimental investigations are not viable, numerical simulations have been successfully employed to analyze the post-detonation flow dynamics [3, 4]. With the aid of the computational studies, the main stages of blast wave propagation and post-detonation combustion have been investigated in both confined and unconfined environments [3–5]. In particular, when a spherical or a cylindrical explosive charge is detonated in an unconfined domain, an outward propagating blast wave is produced, which is followed by a contact surface separating the shock compressed air and the detonation product gases. As the blast wave and the contact surface move outward, a rarefaction wave propagates inwards, overexpands and produces a secondary shock. Meanwhile, the initial imperfections on the charge surface perturb the

Communicated by F. Zhang.

K. C. Gottiparthi · J. C. Schulz · S. Menon (✉)
School of Aerospace Engineering, Georgia Institute of Technology,
Atlanta, GA 30332-0150, USA
e-mail: suresh.menon@ae.gatech.edu

K. C. Gottiparthi
e-mail: kalyan.gottiparthi@gatech.edu

contact surface resulting in the growth of the Rayleigh–Taylor instability (RTI) and the generation of a mixing zone. The secondary shock, after being initially swept outwards, propagates inwards (implosion) and explodes outwards after reflection from the origin. The outward propagating secondary shock interacts with the hydrodynamic structures in the mixing zone and results in the Richtmyer–Meshkov instability (RMI) [5]. The vorticity production in the mixing zone due to RTI and RMI sustains the mixing in the post-detonation flow [6]. With the primary focus on the dispersion and the heating of bacterial spores by detonated explosive charges, this chronology of blast wave propagation and instability generation are modeled and presented in the current article following the procedure described by Balakrishnan et al. [3].

Bacteria are known to form spores that can survive harsh conditions, such as high temperatures, high pressures, and toxic chemical environments [7]. To address the challenges involved in spore destruction, many experimental and numerical studies in the past focused on the methods of spore kill and the effectiveness of these methods. Thermal inactivation of spores has been investigated in the past by exposing spores to temperatures in the range of 90–200 °C for several seconds [1]. However, explosive charges are known to produce conditions with gas temperatures in the order of 10^3 – 10^4 K. Also, most of the blast and post-detonation combustion events occur in the time span of few microseconds to few milliseconds. Therefore, it is not possible to accurately assess the spore kill rate by explosives based on the experiments, which are performed at different time scales and temperature ranges.

Recently, investigations on the interaction of spores with shock waves have been performed to estimate spore kill due to shock induced acceleration [8] and shock heated gas [9]. Sislian and co-workers used an impactor to study the spore break up by aerodynamic shocks and provided the critical acceleration (3.9 – 16×10^9 m/s²) needed for bacterial spore destruction [8]. Spore breakdown in a post-shock heated gas investigated by McCartt et al. [9] provides the percentage of spores intact after heating at different post-shock temperatures. These studies were aimed to understand spore kill in conditions analogous to conditions in post-detonation flows. However, explosive charges not only produce strong blast waves but also high temperature reacting regions, which can cause both thermal and mechanical spore rupture. Also, the hydrodynamic instabilities (RMI/RTI) in the post-detonation region can disperse spores and affect their survival. Thus, it is essential to consider the combined effect of dispersion, heating and mechanical impact to provide critical conditions for spore kill useful in operational conditions. In this article, these aspects are investigated using three-dimensional numerical simulations of interaction of spore clouds with post-detonation flow ensuing from explosive charges. Here,

we define a spore cloud as a cluster of spores, which are organized to occupy a specified initial volume, and has a specified initial concentration and distribution. The motion and the temperature of the spores are evaluated using the Lagrangian tracking method, which can characterize the particle dispersion accurately in complex flows [10]. Past results suggest that the strength of the blast wave is reduced as it propagates outwards. Thus, the effect of the initial distance of the spore cloud from the explosive charge on spore kill is investigated in detail. However, before analyzing the interaction of the spore cloud with the post-detonation flow, a spore aerosol model is developed based on past experiments [9] and is evaluated in a shock tube configuration. The shock tube simulations are used to validate the spore aerosol model and quantify the uncertainties in the critical parameters, such as the aerosol size distribution and the spore neutralization temperature. The validated model is employed to study spore neutralization by explosive charges.

This article is organized in the following manner. The governing equations and the numerical method used to model the spore dispersion and the post-detonation flow are presented in Sect. 2. In Sect. 3, spore destruction in post-shock flow and post-detonation flow is discussed, and the percentage of damaged spores for different initial configurations is presented. Also, the effect of varying modeling parameters such as the density, the heat conductivity and the size of spore aerosol droplet is analyzed in this section. Finally, conclusions from the current work and possible future investigations are summarized in Sect. 4.

2 Formulation

2.1 Gas phase

The unsteady, compressible, reacting, multi-species Navier–Stokes equations employed in the current work to perform numerical simulations are [11]:

$$\begin{aligned} \frac{\partial}{\partial t} \begin{bmatrix} \rho \\ \rho u_i \\ \rho E \\ \rho Y_k \end{bmatrix} + \frac{\partial}{\partial x_j} \begin{bmatrix} \rho u_j \\ \rho u_i u_j + p \delta_{ij} - \tau_{ij} \\ (\rho E + p) u_j - u_i \tau_{ji} + q_j \\ \rho Y_k (u_j + V_{j,k}) \end{bmatrix} \\ = \begin{bmatrix} 0 \\ 0 \\ 0 \\ \dot{\omega}_k \end{bmatrix} + \begin{bmatrix} \dot{\rho}_p, \\ \dot{F}_{p,i}, \\ \dot{Q}_p + \dot{W}_p, \\ \dot{S}_{p,k}, \end{bmatrix} \end{aligned} \quad (1)$$

where ρ denotes the density, p is the pressure, u_i is the i -th component of velocity, E is the specific total energy given by the sum of the internal (e) and the kinetic energy, $e + \frac{1}{2} u_i u_i$, Y_k is the mass fraction of the k -th species, and $\dot{\omega}_k$ represents the chemical production of the k -th species. The species index

k varies from 1 to N_s with N_s being the total number of chemical species considered. Also, the stress tensor, the heat flux in the j -direction and the j -component diffusion velocity are denoted by τ_{ij} , q_j , and $V_{j,k}$, respectively, and are given by

$$\tau_{ij} = \mu \left(\frac{\partial u_i}{\partial x_j} + \frac{\partial u_j}{\partial x_i} \right) + \delta_{ij} \lambda \frac{\partial u_l}{\partial x_l}, \quad (2)$$

$$q_j = -\kappa \frac{\partial T}{\partial x_j} + \rho \sum_{k=1}^{N_s} h_k Y_k V_{j,k}, \quad (3)$$

$$V_{j,k} = -\frac{D_k}{Y_k} \frac{W_k}{\bar{W}} \left(\frac{\partial X_k}{\partial x_j} \right), \quad (4)$$

where μ is the viscosity of the gas phase obtained from Sutherland's law, δ_{ij} is the Kronecker delta function, $\lambda (= -2/3\mu)$ is the bulk viscosity, T is the gas phase temperature and κ is the thermal conductivity of the gas phase. Also, h_k is the specific enthalpy, X_k is the mole fraction, and W_k is the molecular weight of the k -th species. \bar{W} is the mixture average molecular weight and D_k is the diffusion coefficient of the k -th species obtained from the assumption that the Schmidt number has a value of unity. The inter-phase interaction terms, $\dot{\rho}_p$, $\dot{F}_{p,i}$, \dot{Q}_p , \dot{W}_p and $\dot{S}_{p,k}$, are evaluated using Lagrangian tracking and are provided elsewhere [11]. Following past studies [3, 6], the assumption that the combustion process in the post-detonation regime is mixing controlled rather than chemically controlled is employed to determine the chemical source term, $\dot{\omega}_k$. At each time step, the concentrations of fuel (CO and H₂) and oxygen are compared within a computational cell to determine if the mixture is fuel lean or fuel rich. If the mixture is fuel lean, all the fuel is instantaneously consumed, and the amount of oxygen required for combustion is determined based on the following reactions



On the other hand, if the mixture is fuel rich, all the oxygen is consumed, and the amount of fuel needed for combustion is determined based on the stoichiometry. Finally, to relate the thermodynamic variables in the high temperature and the high pressure blast/post-detonation environment, the Jones–Wilkins–Lee (JWL) equation of state [3, 12] is used and is given as

$$p = A \exp\left(\frac{-R_1 \rho_0}{\rho}\right) + B \exp\left(\frac{-R_2 \rho_0}{\rho}\right) + \omega \rho C_v T, \quad (6)$$

where A , B , R_1 , R_2 , ρ_0 and ω are explosive-dependent constants and are documented elsewhere [12].

2.2 Dispersed phase

The governing equations to compute the particle velocity vector ($u_{p,i}$), the particle position vector ($x_{p,i}$), the particle

temperature (T_p) and the particle mass (m_p) employing the Lagrangian approach are [6]:

$$\frac{dx_{p,i}}{dt} = u_{p,i}, \quad (7)$$

$$m_p \frac{du_{p,i}}{dt} = \frac{\pi}{2} r_p^2 C_D \rho |u_i - u_{p,i}| (u_i - u_{p,i}) - \frac{4}{3} \pi r_p^3 \frac{\partial p}{\partial x_i} - \frac{4}{3} \pi r_p^3 C_A \left[\frac{\partial p}{\partial x_i} + \frac{d(\rho u_{p,i})}{dt} \right], \quad (8)$$

$$m_p C_p \frac{dT_p}{dt} = 2\pi r_p \kappa N u (T - T_p) - \dot{m}_p L_v, \quad (9)$$

$$\frac{dm_p}{dt} = -\dot{m}_p, \quad (10)$$

where r_p is the particle radius, L_v is the latent heat of vaporization, $C_A = 0.5$ is the added-mass coefficient [13] and C_p is the specific heat of the particle. Note that, in (8), the acceleration of the particle is computed based on the contributions from the quasi-steady drag, the pressure gradient and the added mass effect. The role of these terms in spore neutralization is discussed in the results presented here. The contribution of the Basset force, the buoyancy and the lift to the particle acceleration are small in comparison to the terms included in (8) [10] and hence are not considered here. The drag coefficient, C_D , used here, expressed in terms of the particle Reynolds number ($Re_p = 2r_p|u_{p,i} - u_i|/\rho/\mu$) and the particle Mach number ($M_p = |u_{p,i} - u_i|/a_s$) is [10, 14]

$$C_D = \left[0.38 + \frac{24}{Re_p} + \frac{4}{Re_p^{0.5}} \right] \left[1 + \exp\left(\frac{-0.43}{M_p^{4.467}}\right) \right], \quad (11)$$

where a_s is the speed of sound in the gas. In all the cases presented here, the flow is dilute, i.e., the volume occupied by the spore aerosol is less than one percent of the total volume available. Hence, the inter-particle interaction has been neglected.

2.3 Spore aerosol modeling

In the current study, droplets of a spore-laden aqueous solution are introduced into the domain of interest, i.e., the reshock zone of the shock tube or in the vicinity of a detonated explosive charge. The spores are considered to be of the *Bacillus* species. Although most spores of this species are elliptical, in the current work, they are assumed to be spherical with radius, $r_s = 0.4 \mu\text{m}$ [15]. The spore aerosol considered has a particular droplet size distribution and a specific concentration of spores in the initial solution. Also, a specific initial concentration of spores in the domain is chosen. These parameters are set based on the past experimental studies [16], so that the current results can be compared with the results available in the literature.

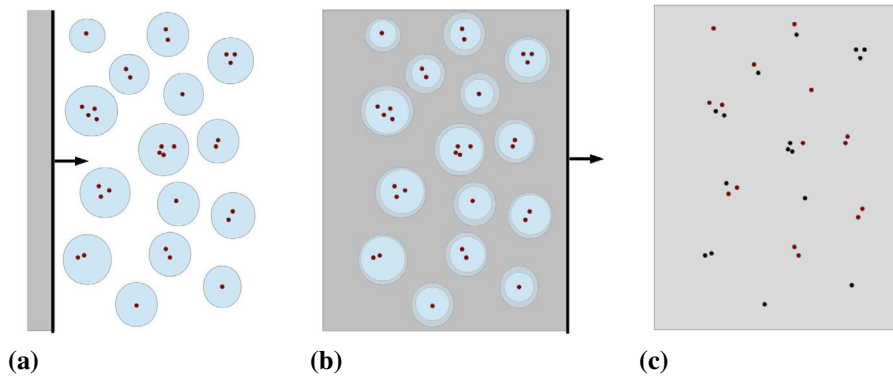


Fig. 1 Schematic of spore aerosol interaction with shock/blast wave and subsequent spore kill modeled in the current study. The arrows indicate the direction of motion and vertical line in **a**, and **b** indicates shock/blast wave. The blue circles indicate aerosol droplets, and the dotted circles indicate the mixture of evaporated water and ambi-

ent gases. The post-shock/post-blast wave region is shown in grey. Black dots indicate damaged spores, and red dots indicate intact spores. **a** Pre-shock spore-laden aerosol, **b** droplet evaporation in post-shock zone, **c** exposed spore heating

When the spore aerosol interacts with the hot gases in either a post-shock or a post-detonation flow, the water enveloping the spores evaporates and exposes the spores to the heat. Based on the aerosol droplet radius, there could be multiple spores in a given droplet. These spores, after the evaporation of water, can stay clustered or disperse. As the temperature of the spores increases, based on the quantity of heat received by each spore, the spore kill can occur due to heating or mechanical rupture. These processes are illustrated in Fig. 1. When the spore-laden aerosol is nebulized, the droplets of aerosol are distributed in the domain of interest with each droplet having an initial radius, r_p^0 . In general, r_p^0 can be specified based on a distribution function. However, as the exact distribution of the droplet size is not known, r_p^0 (microns), based on a Gaussian distribution, is specified as

$$r_p^0 = \min(\chi, \mu_\chi), \quad (12)$$

where χ is a Gaussian random variable with mean μ_χ and standard deviation σ_χ . As the values of μ_χ and σ_χ are not available, a range of values are used initially for the shock tube simulations and the values which provide good agreement with experimental results are then used in cases with explosive charges. Also, the initial atomization is assumed to reduce all droplets to a size μ_χ . Further, the number of spores per droplet (n_s^p) is set based on the concentration of the spores in the initial aqueous solution. In the current study, for an initial spore concentration of 10^{10} spores/ml, n_s^p varies from 1 to 5 [16]. Also, the concentration of the spores in the domain, χ_s^0 , is varied from 10 to 10^6 spores/cm³.

Due to the heat transfer to the droplets in the post-shock region, the water encapsulating the spores evaporates and this rate of mass transfer is given as [17]

$$\dot{m}_p = 2\pi\rho D r_p Sh \ln(1 + B_M), \quad (13)$$

where D is the diffusivity of the gas. The expressions for the Nusselt number (Nu), the Sherwood number (Sh) and the Spalding mass transfer number (B_M) for droplets are available elsewhere [17]. After the water evaporates, no mass transfer is considered from individual spores or spore clusters. Hence, these expressions for \dot{m}_p and Nu are used until the radius of the droplet reduces to the effective radius of the spore cluster present inside the droplet, i.e., $r_p > r_s^c$. Here, the effective radius of the spore cluster is determined as

$$r_s^c = r_s \left(\frac{n_s^p}{f_p} \right)^{1/3}, \quad (14)$$

where f_p is the packing fraction and is taken to be 1 when $n_s^p = 1$ and 0.74 otherwise, i.e., close packing assumption. The expression for Nu used when $r_p \leq r_s^c$ is provided elsewhere [10].

Once the spores are exposed to a high-temperature gaseous environment, the temperature of the spores increases to a critical value (T_C). Past calculations of thermo-structural response of individual spores show that this critical temperature should result in the spore membrane rupture and/or heating of the spore core leading to spore kill [18]. Experimental studies suggest that the loss of spore viability and structural damage occurs at gas temperatures of about 750K and above [19]. However, for the cases considered here, the exact quantity of heat needed to kill a spore or to reach T_C is not available. Hence, T_C is assumed as a variable parameter and a range of values are used in each case to obtain the percentage of spores killed. In cases presented here, any spore whose temperature exceeds T_C is assumed to be neutralized. Note that the loss of viability can occur before the spore is damaged [19]. Hence, in the current studies, the spores that are not intact are considered to have lost their viability and are neutralized. The sensitivity of spore kill to T_C is ana-

lyzed, and the intact spore percentages are compared with shock tube experimental results such that this criteria can be used with confidence in cases with explosive charges.

2.4 Numerical method and initial setup

The governing equations for the gas phase are solved using a finite-volume formulation in which a higher-order flux difference splitting method is used to capture shocks and discontinuities. Monotone Upstream-centered Schemes for Conservation Laws (MUSCL) reconstruction along with Monotonized Central limiter is used in the flux-difference splitting method. An approximate hybrid Riemann solver, which employs the Harten–Lax–van Leer with contact (HLLC) method everywhere, except in the shock capturing region, is used to solve for the fluxes at the cell interface. In the directions transverse to the shock, Harten–Lax–van Leer–Einfeldt (HLLE) Riemann solver is used. The scheme is second order accurate in both space and time. This approach has already been validated to simulate shock-turbulence interaction [20], detonations [10, 21], blast wave propagation [3] and post-detonation combustion [6, 22]. A fourth-order Runge–Kutta scheme is used to solve the dispersed phase governing equations [6, 10].

2.4.1 Shock tube setup

A shock tube of length 2.6 m is considered in the current work to investigate the spore neutralization by shock waves. Initial pressure in the driver section is varied to obtain the desired shock Mach number (M_s). The shock tube is closed at both ends. Thus, the normal shock propagates from one end of the tube to the other end and reflects back. The lengths of driven and driver sections are chosen such that constant post-reshock properties are obtained for a given residence time. The residence time (t_r) considered in the current work, following experimental investigations [19], is ~ 2.5 ms. M_s is varied from 1.5 to 2.1 such that the post-reshock temperature (T_5) varies from 600 to 1,100 K. The spore-laden aerosol is introduced at the end of the shock tube away from the driver section. Note that, in all cases investigated here, the flow properties in post-reshock regime, $R5$, remain almost constant for the residence time considered. This is demonstrated for $M_s = 1.7$ in Fig. 2. The initial length (L^0) of the shock tube occupied by the aerosol and the number of droplets in the aerosol (n_p) are varied such that the initial concentration of the spores (χ_s^0) in the shock tube is of the desired value. The values of L^0 , μ_χ , σ_χ , n_p , total number of spores considered (n_s^t) and χ_s^0 for each case are provided in Table 1.

The shock tube domain is discretized using a uniform mesh. The dimensions of the cross section and the width of each computational cell (Δ) used here are provided in

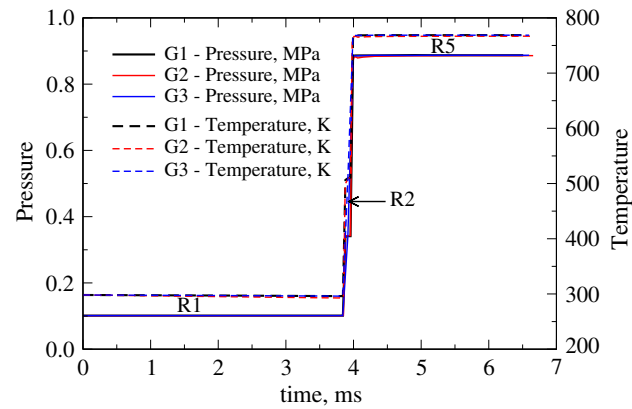


Fig. 2 Variation of temperature and pressure in the shock tube at the location where spores are released for $M_s = 1.7$. Region R1 indicates the pre-shock condition, R2 indicates the post-shock condition and R5 indicates the post-reshock condition. The details of the grids G1, G2 and G3 are provided in Table 2

Table 1 Parameters used to specify the initial conditions of the dispersed phase in the shock tube (ST) studies

Case	n_p	μ_χ	σ_χ	n_s^t	L^0 (cm)	$\chi_s^0 (\times 10^6 \text{ cm}^3)$
ST1	2,500	5.0	0.5	2,500	5.0	0.185
ST2	2,500	5.0	0.5	9,070	5.0	0.670
ST3	4,000	5.0	0.5	14,504	5.0	1.000
ST4	4,000	5.0	0.5	14,504	5.0	1.000
ST5	4,000	5.0	0.6	14,504	5.0	1.000
ST6	4,000	5.0	0.7	14,504	5.0	1.000
ST7	4,000	5.0	0.4	14,504	5.0	1.000
ST8	4,000	5.0	0.5	14,504	10.0	0.500
ST9	4,000	5.2	0.5	14,504	5.0	1.000
ST10	4,000	4.8	0.5	14,504	5.0	1.000

Table 2 Shock tube cross sections and grid resolution used in the current studies

Case	Dimensions	Cross section (mm)	$\Delta (\mu\text{m})$
G1	1D	0.52×0.52	520.0
G2	3D	1.56×1.56	520.0
G3	1D	1.04×1.04	1,040.0

Table 2. In all Cases G1–G3, the flow properties are almost identical as shown in Fig. 2. Thus, for the rest of the studies presented here, the grid setup as in Case G1 is used. As the focus of the current studies is the neutralization of spores in unconfined post-detonation flows, only the particle dispersion effects away from the wall boundaries are considered, and all the walls of the shock tube are assumed to be slip walls.

2.4.2 Setup for simulations with explosive charges

To carry out studies in the post-detonation flow, the initial detonated explosive charge is modeled using the Gas-Interpolated-Solid Stewart-Prasad-Assay (GISPA) method [3, 23]. A homogeneous spherical nitromethane charge of diameter 11.8 cm is considered in the current investigations. The detonation energy and the initial density of the nitromethane charge are 4.35 MJ/kg and 1,128.0 kg/m³, respectively [3]. Note that, in the post-detonation flow analysis, all the temporal and spatial scales provided correspond to this detonation energy, initial charge density and initial charge volume. The initial profiles of the pressure, the temperature, the density and the velocity for this charge are available elsewhere [3]. The detonated charge is initialized in an unconfined domain, which is modeled by a three-dimensional spherical sector (2.4 m × 45° × 45°). A structured mesh (1,000 × 60 × 60) is used to resolve the domain. The justification for the domain configuration, the resolution used and the boundary conditions are provided elsewhere [3, 22]. The initial composition of the product gases in the charge is specified based on the chemical reaction: CH₃NO₂ (nitromethane) → 0.5 N₂ + CO + H₂O + 0.5H₂. The ambient gas is specified to be air at 1.01325 MPa and 300 K. The spore-laden aerosol is initially distributed in the ambient flow at a specific radial distance, d^0 , away from the initial charge. The thickness (L^0) of the aerosol cloud is specified based on the initial concentration (χ_s^0) and the total number of spores in the cloud (n_s^t). These parameters for each case investigated are presented in Table 3.

3 Results and discussion

3.1 Spore neutralization in shock tube

The shock tube studies are set to compare with the available experimental results and used to analyze the significance of the modeling parameters discussed in the previous section. The intact spore ratio (I_s) = (100.0 × n_s^t) / n_s^i , where n_s^i is number of intact spores after time $t = t_r$, in each case is evaluated and the role of each modeling parameter is discussed. Note that the value of I_s ranges from 0 to 100, i.e., complete neutralization to no neutralization.

3.1.1 Sensitivity analysis

A normal shock of Mach number, M_s , is simulated in a shock tube closed at both ends and filled with argon to study the spore-laden aerosol neutralization in post-shock flow. Here, the shock wave is allowed to reflect from the closed end to produce a reflected shock and a post-reshock flow with a temperature (T_5 ~ 600–1,200 K) considerably higher than

Table 3 Parameters used to specify the initial conditions of the dispersed phase in the simulation with explosive charges

Case	n_p	n_s^t	L^0 (mm)	χ_s^0 (×10 ³ /cm ³)	d^0 (cm)
NM0C1	4,000	14,504	3.0	0.545	12.0
NM1C1	4,000	14,504	3.0	0.138	24.0
NM2C1	4,000	14,504	3.0	0.035	48.0
NM3C1	4,000	14,504	3.0	0.009	96.0
NM4C1	4,000	14,504	3.0	0.015	72.0
NM5C1	4,000	14,504	3.0	0.244	18.0
NM6C1	4,000	14,504	3.0	0.180	21.0
NM7C1	4,000	14,504	3.0	0.218	19.0
NM8C1	4,000	14,504	3.0	0.062	36.0
NM0C2	8,000	29,008	3.0	1.090	12.0
NM1C2	8,000	28,828	3.0	0.276	24.0
NM2C2	8,000	28,828	3.0	0.070	48.0
NM4C2	8,000	29,171	3.0	0.031	72.0
NM5C2	8,000	29,346	3.0	0.494	18.0
NM6C2	8,000	29,008	3.0	0.360	21.0
NM8C2	8,000	29,008	3.0	0.124	36.0
NM0C4	32,000	116,032	3.0	4.360	12.0
NM0C6	128,000	464,128	3.0	17.440	12.0
NM1C4	32,000	116,032	3.0	0.552	24.0
NM1D2	4,000	14,504	6.0	0.068	24.0
NM1D3	8,000	29,008	12.0	0.068	24.0

the post-shock (T_2 ~ 440–650 K) temperature. Initially, the spore-laden aerosol droplets are distributed uniformly over L^0 and span the entire cross section of the shock tube. As the aerosol droplets interact with the shock heated gas, the water surrounding the spores evaporates resulting in a reduction in the droplet radius and an increase in the droplet temperature. As M_s is increased, the rate of change in the average droplet size and the average droplet temperature increases due to the increase in the post-shock/post-reshock gas temperature (see Fig. 3). Here, the average quantities are the average values evaluated over all the droplets. Note that for $M_s = 1.6$, even after 7 ms, the average droplet temperature is about 400 K. Thus, I_s is nearly 100 for $M_s = 1.6$. Similarly, for $M_s = 2.0$, the average droplet temperature is about 1,100 K after 6.5 ms and I_s is nearly 0.

One of the important criteria determining the survival of spore is T_C . Values of T_C in the range 650–690 K show a negligible change (about 0.2) in I_s , as shown in Fig. 4, computed for T_5 ranging from 650 to 1,100 K. Thus, in all the current studies, $T_C = 670$ K is used to determine the number of intact spores at any given time. The significance of the acceleration due to the pressure gradient (PG) and the added-mass (AM) effect on the intact spore percentages for different T_5 is investigated by considering simulations with individual acceleration terms. Figure 5 shows that the difference in the predicted values of the number of intact spores

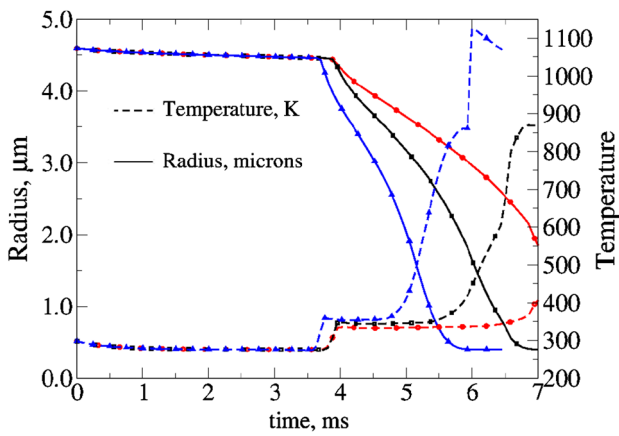


Fig. 3 Variation of average particle radius and average particle temperature with time for $M_s = 1.6$ (red, dots), 1.8 (black, squares) and 2.0 (blue, triangles). Initial conditions correspond to Case ST4

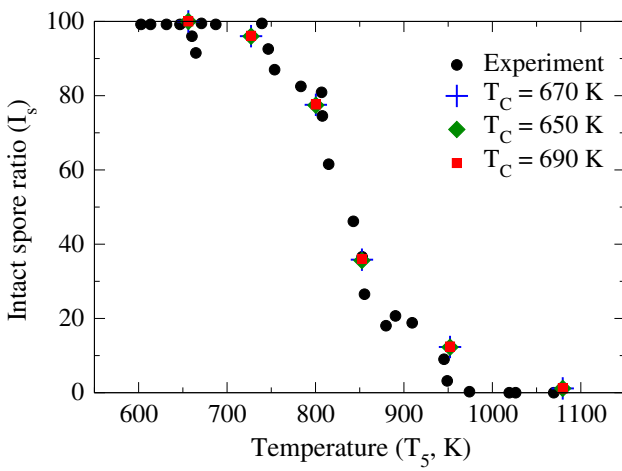


Fig. 4 Percentage of spores left intact for different post-reshock temperatures (T_5) for different spore neutralization temperatures, T_C . Results from experiments [19] are shown for comparision

is negligible and the calculations with only the quasi-steady drag, the dominant acceleration term, provide results with good accuracy. Thus, for all other studies reported here on, the acceleration due to PG and AM effects are neglected.

The spore density (ρ_s) and heat capacity (C_s) are varied as shown in Table 4. These values are considered based on the values provided by earlier investigations [18]. Change in both ρ_s and C_s results in a negligible change in I_s , as shown in Fig. 6, and hence the values in Case ST4 are used in all the cases with post-detonation flows. The effect of the spore-aerosol modeling parameters is investigated by varying χ^0 , μ_χ and σ_χ as shown in Table 1. The maximum change in I_s , in comparison to Case ST4, is 10.0 when σ_χ is varied from 0.4 to 0.7 for $\mu_\chi = 5.0$. Also, when μ_χ is varied from 4.8 to 5.2, the maximum change in I_s , compared to Case ST4, is 30.0. Both, μ_χ and σ_χ determine the range and the maximum size of the droplets in the aerosol. With an increase in the droplet

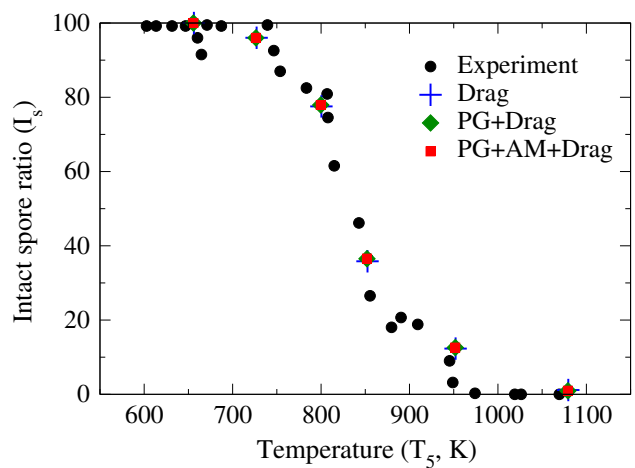


Fig. 5 Percentage of spores left intact for different post-reshock temperatures (T_5) for different particle acceleration terms considered. Here, PG indicates the pressure gradient term, and AM indicates the added-mass effect. The residence time of spores in reshock zone is nearly 2.5 ms. Results from experiments [19] are shown for comparision

Table 4 Spore density (ρ_s) and heat capacity (C_s) used in the current studies

Case	ρ_s (kg/m ³)	C_s (J/kg/K)
ST1-10	1,000.0	4,180.0
ST11	1,300.0	4,180.0
ST12	1,000.0	2,500.0
ST13	1,300.0	2,500.0

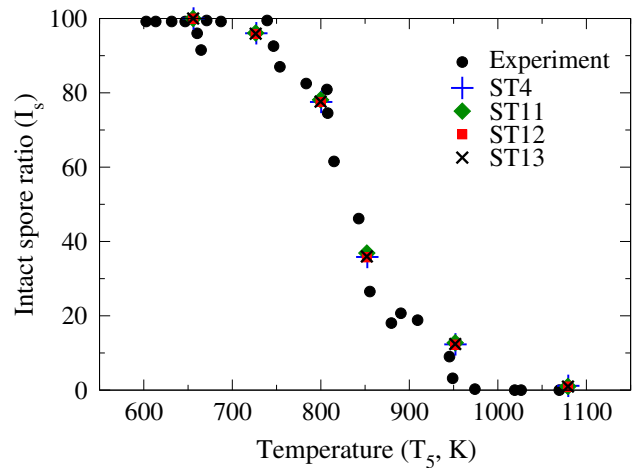


Fig. 6 Percentage of spores left intact for different post-reshock temperatures (T_5) for different physical properties (shown in Table 4) of spores. Results from experiments [19] are shown for comparision

size, the time required to evaporate the water encapsulating the spores increases. Thus, the time needed to expose the spores increases with an increase in the droplet size. Hence, the dependence of I_s on μ_χ and σ_χ is significant with $\mu_\chi = 5.0$ and $\sigma_\chi = 0.5$ showing a good agreement with the experimental values. Hence, these values of μ_χ and σ_χ are used

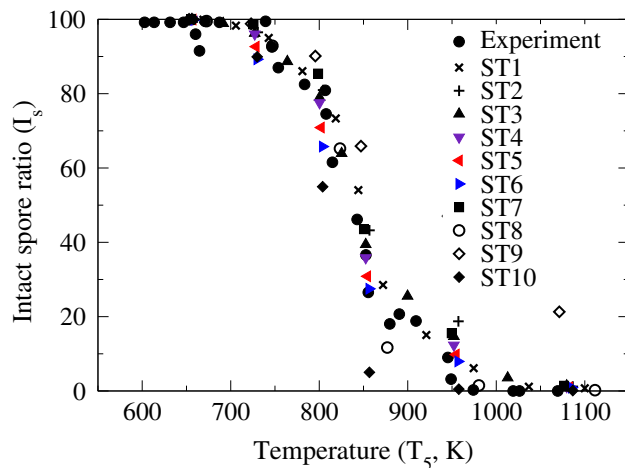


Fig. 7 Percentage of spores left intact for different post-reshock temperatures (T_5) for cases shown in Table 1. The residence time of spores in reshock zone is nearly 2.5 ms. Results from experiments [19] are shown for comparison

for all cases investigated in post-detonation flows. When all the water evaporates, the spores in a given droplet remain clustered or disperse. The spores are allowed to remain clustered in Case ST3 and are dispersed in Case ST4 to evaluate the differences in the number of intact spores. Between Case ST3 and Case ST4, the maximum difference in I_s is 4.4 (at $M_s = 1.9$) with the average difference in $I_s = 1.31$ (over all M_s). Since the average difference is not significant, for studies in post-detonation flows, the spores are assumed to be dispersed.

To summarize, the standard deviation and the mean of the initial droplet size are important parameters determining the time required to neutralize the spores, whereas the parameters such as ρ_s , C_s , T_C , L^0 and n_s^p have a negligible effect on I_s . The sensitivity analysis indicates that the number of intact spores for different post-shock conditions agree reasonably with the experimental results (see Fig. 7) over a wide range of parameters as shown in Table 5. Especially, the values for the representative case, Case ST4, are in good agreement,

and hence, the set of spore-aerosol parameters used in this case are used for all the cases investigated in post-detonation flows.

3.2 Spore neutralization by explosive charges

Spore neutralization in post-detonation flow is investigated by varying the initial distance of the spore cloud, d^0 , the initial spore cloud concentration, χ_s^0 , and the initial spore cloud width in the radial direction, L^0 , as shown in Table 3. Here, a spore cloud is a cluster of spore-laden aerosol droplets uniformly distributed in the azimuthal and the zenith directions and placed at radial distance d^0 from the center of the explosive charge.

3.2.1 Effect of initial spore concentration and initial spore cloud width

When the explosive charge is detonated in the vicinity of the spore cloud, the blast wave from the explosion propagates outwards from the charge and a post-detonation flow comprising of hot detonation product gases is generated. The events in this post-detonation flow can be categorized into four phases: (a) primary phase, (b) implosion phase, (c) reshock phase and (d) asymptotic phase (see Fig. 8). Initially, during the primary phase, the detonation product gases propagate outward along with the primary shock (PS) and engulf the spore aerosol cloud. The aerosol droplets are heated by the resulting high-temperature gaseous environment, and the evaporation of the water encapsulating the spores is initiated. During this phase, a secondary shock (SS) is formed due to the over expansion of the local flow by the inward moving rarefaction. The aerosol cloud, overtaken by the contact surface between detonation product gases and the ambient air, perturbs the contact surface and results in the formation of RTI [6] and the mixing/combustion zone. The afterburn of CO and H₂ further increases the temperature of the mixing zone.

Table 5 Modeling parameters affecting the intact spore ratio

Parameter	Definition	Range	ΔI_s^E	ΔI_s^N
T_C	Critical spore temperature (K)	650–690	3.5	0.2
C_s	Heat capacity of spore (J/kg/K)	2,500.0–4180.0	3.7	0.2
ρ_s	Density of spore (kg/m ³)	1,000.0–1,300.0	3.7	1.0
μ_χ	Mean spore aerosol droplet radius (μm)	4.8–5.2	21.0	30.0
σ_χ	Standard deviation of aerosol droplet radius	0.4–0.7	9.0	10.0
χ_s^0	Initial concentration of spores in the domain ($10^6/\text{cm}^3$)	0.185–1.0	6.0	2.0
L^0	Initial spore cloud length (cm)	5.0–10.0	6.0	2.0
n_s^p	Spores per aerosol droplet	1–5	5.0	1.0

Experimental results [19] (ΔI_s^E) and Case ST4 (ΔI_s^N) are used as a reference to compute the maximum difference in I_s over all M_s for each parameter

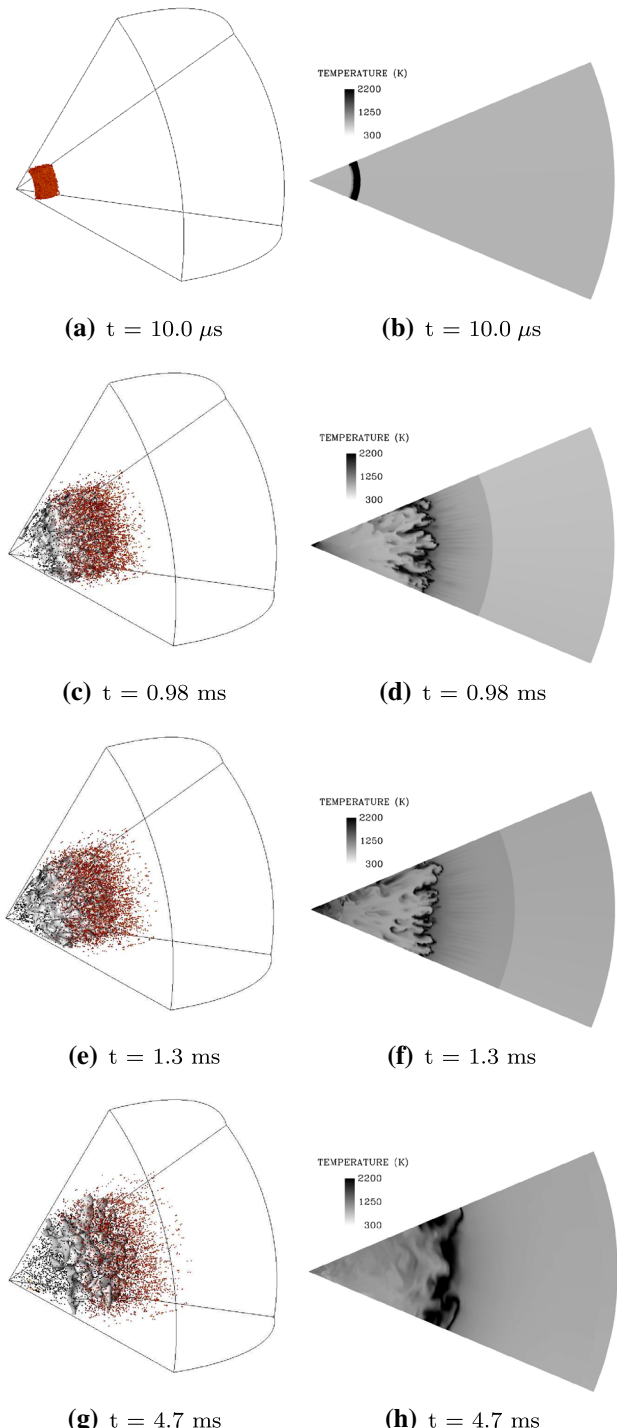


Fig. 8 Position of the damaged (black) and the intact (red) spores in the post-detonation flow for Case NM1C2. The mixing zone is indicated by iso-surface of N_2 ($Y_{N_2} = 0.5$). **a, b** Correspond to the primary phase; **c, d** correspond to the implosion phase; **e, f** correspond to the reshock phase; and **g, h** correspond to the asymptotic phase

At $t \sim 0.4$ ms, the secondary shock starts propagating inwards, as shown in Fig. 9, as the core pressure is reduced by the rarefaction. This initiates the implosion phase, where the aerosol cloud is dragged towards the origin along with the

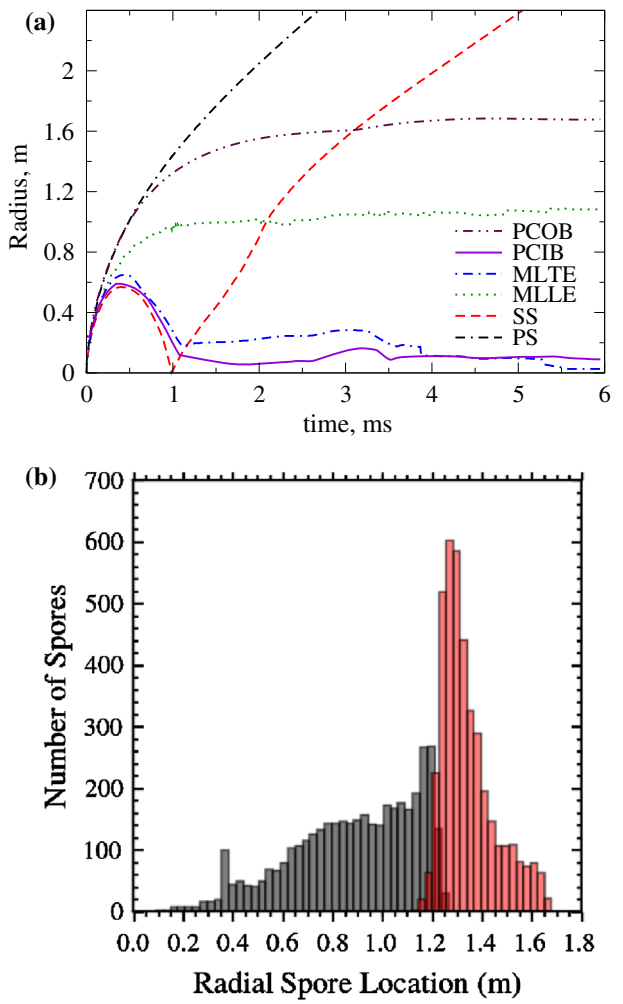


Fig. 9 **a** Position of the primary shock (PS), the secondary shock (SS), the leading and the trailing end of the mixing layer (MLLE and MLTE), the inner and the outer boundaries of the particle cloud (PCIB and PCOB) at different time for Case NM1C2. **b** Histograms showing the distribution of the intact (red) and the damaged (black) spores based on their radial location at $t = 6$ ms. The radial positions are obtained by averaging the quantities in the azimuthal and the zenith directions

mixing layer. However, the aerosol droplets, which acquired sufficient momentum due to the interaction with the outward propagating gases, remain outside the mixing zone and continue propagating outward. This motion of the leading edge of the mixing layer (MLLE), the trailing edge of the mixing layer (MLTE), the inner boundary of the spore cloud (PCIB) and the outer boundary of the spore cloud (PCOB) are shown in Fig. 9. Here, the radial location of the mixing layer boundaries is calculated as $r_{MLTE} = r|_{Y_{CO}=0.9Y_{CO}^i}$ and $r_{MLLE} = r|_{Y_{CO}=0.1Y_{CO}^i}$, where Y_{CO}^i is the initial mass fraction of CO in the detonation product gases. Also, the inner and the outer spore cloud boundaries are evaluated as the minimum and the maximum of the radial location of all the spores, respectively.

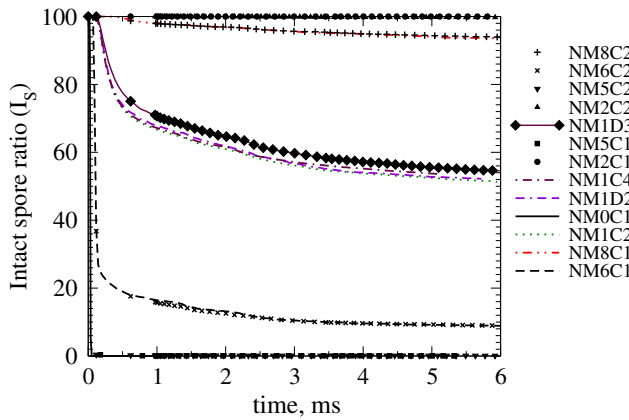


Fig. 10 Variation of percentage of spores left intact with time for cases shown in Table 3

After propagating towards the origin, at $t \sim 1.0$ ms, the secondary shock reflects back from the origin and interacts with the flow structures. This phase, termed as the reshock phase, gives rise to further mixing due to RMI [6]. The aerosol droplets, dragged towards the origin in the implosion phase, are pushed into the high-temperature mixing zone. Also, the outward propagating secondary shock further drags the aerosol droplets, dispersed beyond the mixing zone, outward. The mixing zone, after interaction with the secondary shock in the reshock phase, settles into an asymptotic mixing phase, where the combustion is sustained by the continuous mixing of the detonation product gases and the ambient air. In all the phases of the post-detonation flow, the spores are exposed to the hot gases. However, the spores in the aerosol droplets with relatively higher water content take considerable time to get exposed. The neutralization of the spores in these droplets is facilitated by the asymptotic phase, where sustained mixing enables relatively longer residence time in the hot gases. Further, during the asymptotic phase, as the aerosol outside the mixing zone moves outwards, spores outside the mixing zone escape and remain intact. After 5.5 ms, most of the spores within the mixing zone are neutralized and the number of intact spores reaches an asymptotic value as shown in Fig. 10.

When the initial concentration of the spore cloud is increased from 0.276 to $0.552 \times 10^3/\text{cm}^3$ (Cases NM1C2 and NM1C4), I_s increases from 52.3 to 53.6 at $t = 6$ ms. This negligible change is attributed to the difference in the number of spores that escape the mixing zone and the neutralization. Variation of χ_s^0 in other cases, shown in Table 3, also shows a negligible change in I_s (see Fig. 10). Similarly, changing L^0 from 3.0 to 12.0 mm results in a nominal increase in I_s from 52.3 to 54.6 (Cases NM1C2 and NM1D3). Here, again, the change in the number of intact spores is attributed to the change in the number of spores dispersed away from the mixing zone. Thus, when χ_s^0 and L^0 are varied for a fixed d^0 , the variation in I_s is not significant. This is expected because of the dilute nature of the spore-laden flow considered here.

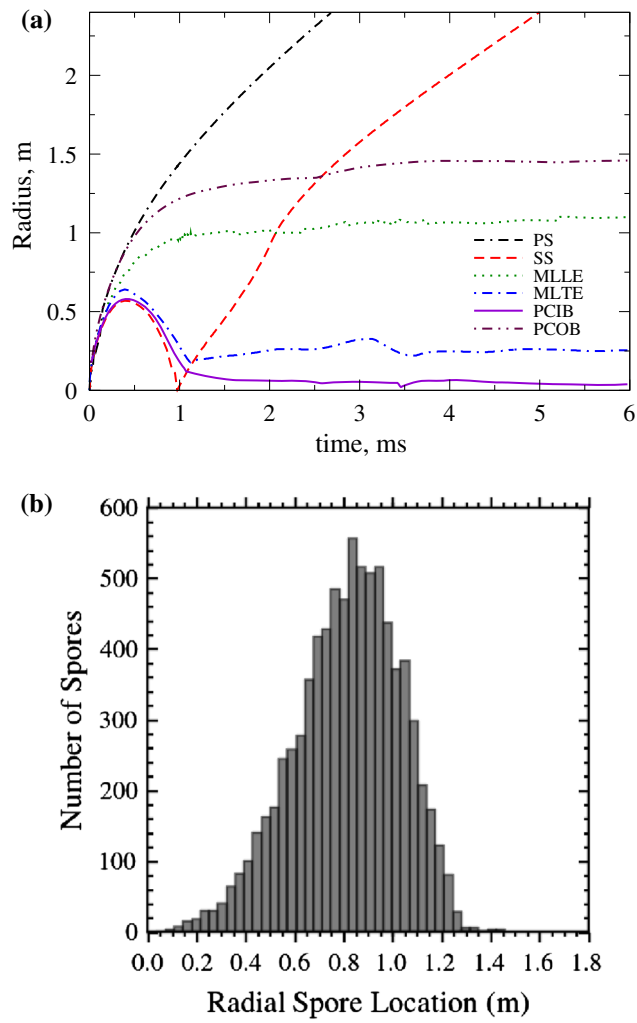


Fig. 11 **a** Position of the primary shock (PS), the secondary shock (SS), the leading and the trailing end of mixing layer (MLLE and MLTE), the inner and the outer boundaries of the particle cloud (PCIB and PCOB) at different time for Case NM5C2. **b** Histogram showing the distribution of the spores based on their radial location at $t = 6$ ms. The radial positions are obtained by averaging the quantities in the azimuthal and the zenith directions

3.2.2 Effect of initial distance from the charge

When the initial radial location of the spore-laden aerosol cloud, d^0 , is varied from 12 to 98.0 cm, I_s changes from 0.0 to 100.0. Here, the post-detonation flow can be divided into three distinct regions based on the number of spores neutralized. These regions are (1) ISR1 ($d^0 \leq 3.0R_C$), (2) ISR2 ($3.0R_C < d^0 < 8.0R_C$) and (3) ISR3 ($d^0 \geq 8.0R_C$). In ISR1, the aerosol is initially located near the explosive charge, and most of the spores are neutralized in the primary phase after the initial engulfment. The droplets are not scattered away from the mixing zone and remain within the mixing layer boundaries as shown in Fig. 11. This enables maximum heat exposure and almost complete spore neutralization. Thus in ISR1, $I_s \sim 0.0$.

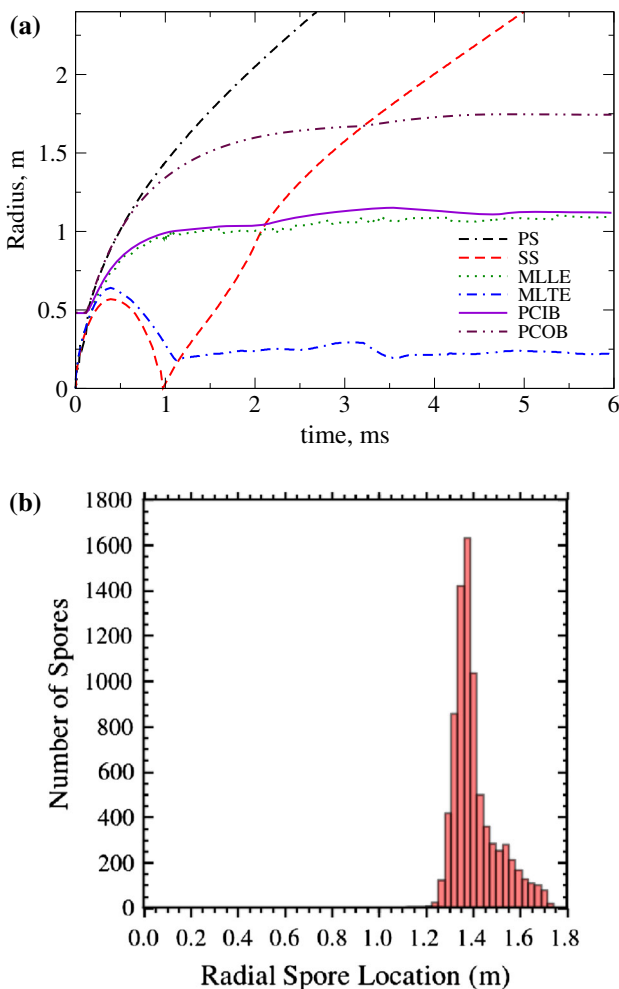


Fig. 12 **a** Position of the primary shock (PS), the secondary shock (SS), the leading and the trailing end of mixing layer (MLLE and MLTE), the inner and the outer boundaries of the particle cloud (PCIB and PCOB) at different time for Case NM2C2. **b** Histogram showing the distribution of the spores based on their radial location at $t = 6$ ms. The radial positions are obtained by averaging the quantities in the azimuthal and the zenith directions

In ISR2, the spores are partially located within the mixing zone (see Fig. 9). The spore neutralization occurs over the primary, the implosion, the reshock and the asymptotic phases. Within this region, as d^0 is increased from $3.0R_C$ to $8.0R_C$, the proportion of spores neutralized in the primary phase decreases from 100.0 to $\sim 0.0\%$. Thus, the role of the mixing zone in spore neutralization increases. When $d^0 \geq 8.0R_C$, i.e., in ISR3, the aerosol is dispersed beyond the mixing zone by $t \sim 0.2$ ms as shown in Fig. 12. The temperature in the post-PS and post-SS flow is relatively low in comparison to the temperature within the mixing zone and sufficient heat is not transferred to the aerosol. Thus, $I_s \sim 100.0$ in ISR3.

In summary, the initial concentration of the aerosol and the initial width of the spore cloud have a negligible effect on the spore survival. Since the cases considered here fall in the

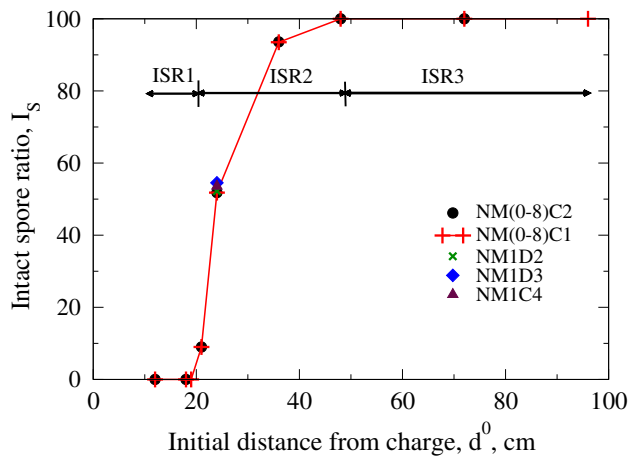


Fig. 13 Percentage of spores left intact for different initial distance from the charge (d^0) for cases shown in Table 3. The intact spore regions (ISR1, ISR2 and ISR3), based on d^0 , are also labeled

dilute regime of two-phase flows, this is expected. However, depending on the aerosol droplet dispersal within and beyond the mixing/combustion zone in the post-detonation flow, a change in the initial radial distance from the charge affects the spore survival. Three regions, ISR1, ISR2 and ISR3 are defined, shown in Fig. 13, which provide a continuous change in I_s from 0 to 100 as d^0 is increased from 12 to 96.0 cm ($\sim 2.0R_C$ to $\sim 16.0R_C$).

4 Conclusions

Bacterial spore neutralization in post-shock and post-detonation flows is investigated numerically. The key components of the interaction of a spore-laden aerosol with shock/blast waves are simulated by accounting for the heat and the mass transfer between the phases. The spore-laden aerosol is modeled based on parameters such as the concentration of spores and the aerosol droplet size distribution so that the results can be compared with the available experimental results. The intact spore percentages obtained in the shock tube studies agree well with the experiments over a wide range of modeling parameters. These investigations provide sufficient confidence to employ the spore-laden aerosol model to study spore neutralization in post-detonation flows of explosive charges.

In post-detonation flows, the initial concentration of the spores is shown to have a negligible effect on the overall spore survival. However, the initial distance from the explosive charge has a substantial effect on the intact spore ratio. When the spore cloud is placed within a distance of $3R_C$, nearly all the spores are damaged in about 0.2 ms. When spores are placed at distances of $8R_C$ and above, $I_s \sim 100.0$ as all the aerosol droplets are found to be scattered beyond the mixing zone before complete evaporation occurs. In the case

with the initial radial distance from the charge between $3R_C$ and $8R_C$, I_s varies from ~ 0.0 to ~ 100.0 . In these cases, a portion of spores is always found within the mixing/combustion zone. Thus, three regions of spore neutralization are simulated in the post-detonation flow based on initial distance from the explosive charge. The investigations presented here are in the dilute regime, and hence, changes in the spore concentration produce little effect on I_s . Future investigations will focus on the neutralization of dense spore clouds, where the initial spore concentrations may have significant effects. Also, since the spore survival is dependent on the temperature in the post-detonation flow, investigations with different explosive charge strengths, along with the appropriate scaling analysis, will be reported in future.

Acknowledgments This work is supported by the Defense Threat Reduction Agency (Dr. S. Peiris, Program Manager). The computational resources are provided by DoD HPC Centers at the US Air Force Research Laboratory DoD Supercomputing Resource Center and Engineer Research and Development Center.

References

- Whitney, E.A.S., Beatty, M.E., Taylor Jr. T.H., Weyant, R., Sobel, J., Arduino, M.J., Ashford, D.A.: Inactivation of *Bacillus anthracis* spores. *Emerg. Infect. Dis.* **9** (2003)
- Setlow, P.: Spores of *Bacillus subtilis*: their resistance to and killing by radiation, heat and chemicals. *J. Appl. Microbiol.* **101**, 514–525 (2006)
- Balakrishnan, K., Genin, F., Nance, D.V., Menon, S.: Numerical study of blast characteristics from detonation of homogeneous explosives. *Shock Waves* **20**, 147–162 (2010)
- Kuhl, A.L., Bell, J.B., Beckner, V.E., Reichenbach, H.: Gasdynamic model of turbulent combustion in TNT explosions. *Proc. Combust. Inst.* **33**, 2177–2185 (2011)
- Fedina, E., Fureby, C.: Investigating ground effects on mixing and afterburning during a TNT explosion. *Shock Waves* **23**, 251–261 (2013)
- Balakrishnan, K., Menon, S.: On turbulent chemical explosions into dilute aluminum particle clouds. *Combust. Theor. Model.* **14**, 583–617 (2010)
- Nicholson, W.L., Munakata, N., Horneck, G., Melosh, H.J., Stelow, P.: Resistance of *Bacillus* endospores to extreme terrestrial and extraterrestrial environments. *Microbiol. Mol. Biol. Rev.* **64**, 548–572 (2000)
- Sislian, P.R., Rau, J., Zhang, X., Pham, D., Li, M., Madler, L., Christofides, P.D.: Bacterial aerosol neutralization by aerodynamic shocks using an impactor system: experimental results for *B. atrophaeus* spores. *Chem. Eng. Sci.* **65**, 4803–4815 (2010)
- McCartt, A.D., Gates, S., Lappas, P., Jeffries, J.B., Hanson, R.K.: In situ optical measurements of bacterial endospore breakdown in a shock tube. *Appl. Phys. B* **106**, 769–774 (2012)
- Gottiparthi, K.C., Menon, S.: A study of interaction of clouds of inert particles with detonation in gases. *Combust. Sci. Technol.* **184**, 406–433 (2012)
- Balakrishnan, K., Menon, S.: On the role of ambient reactive particles in the mixing and afterburn behind explosive blast waves. *Combust. Sci. Technol.* **182**, 186–214 (2010)
- Zukas, J.A., Walters, W.P.: Explosive Effects and Applications. Springer, New York (1997)
- Crowe, C.T., Sommerfeld, M., Tsuji, Y.: Multiphase Flows with Droplets and Particles. CRC Press, Boca Raton (1998)
- Boiko, V.M., Kiselev, V.P., Keselev, S.P., Papyrin, A.P., Poplavsky, S.V., Fomin, V.M.: Shock wave interaction with a cloud of particles. *Shock Waves* **7**, 275–285 (1997)
- Carrera, M., Zandomeni, R.O., Fitzgibbon, J., Sagripanti, J.L.: Difference between the spore sizes of *Bacillus anthracis* and other *Bacillus* species. *J. Appl. Microbiol.* **102**, 303–312 (2007)
- Gates, S.D., McCartt, A.D., Lappas, P., Jeffries, J.B., Hanson, R.K., Hokama, L.A., Mortelmans, K.E.: *Bacillus* endospore resistance to gas dynamic heating. *J. Appl. Microbiol.* **109**, 1591–1598 (2010)
- Abramzon, B., Sirignano, W.A.: Droplet vaporization model for spray combustion calculations. *Int. J. Heat Mass Transf.* **32**, 1605–1618 (1989)
- Kumar, R., Saurav, S., Titov, E.V., Levin, D.A., Long, R.F., Neely, W.C., Setlow, P.: Thermo-structural studies of spores subjected to high temperature gas environments. *Int. J. Heat Mass Transf.* **54**, 755–765 (2011)
- Gates, S.D., McCartt, A.D., Jeffries, J.B., Hanson, R.K., Hokama, L.A., Mortelmans, K.E.: Extension of *Bacillus* endospore gas dynamic heating studies to multiple species and test conditions. *J. Appl. Microbiol.* **111**, 925–931 (2011)
- Génin, F., Menon, S.: Studies of shock/turbulence shear layer interaction using large-eddy simulation. *Comput. Fluids* **39**, 800–819 (2010)
- Schulz, J., Gottiparthi, K.C., Menon, S.: Ionization in gaseous detonation waves. *Shock Waves* **22**, 579–590 (2012)
- Gottiparthi, K.C., Menon, S.: Simulations of heterogeneous detonations and post-detonation turbulent mixing and afterburning. *AIP Conf. Proc.* **1426**, 1639–1642 (2012)
- Xu, S., Aslam, T., Stewart, D.S.: High resolution numerical simulation of ideal and non-ideal compressible reacting flows with embedded internal boundaries. *Combust. Theor. Model.* **1**, 113–142 (1997)

Bibliography

- [1] S. Menon. Acoustic-vortex-flame interactions in gas turbine combustors. *Progress in Astronautics and Aeronautics*, 210:277–314, 2005.
- [2] K. C. Gottiparthi and S. Menon. A study of interaction of clouds of inert particles with detonation in gases. *Combustion Science and Technology*, 184(3):406–433, 2012.
- [3] F. Génin and S. Menon. Studies of shock / turbulent shear layer interaction using large-eddy simulation. *Computers & Fluids*, 39:800–819, 2010.
- [4] K. Balakrishnan, S. Ukai, and S. Menon. Clustering and combustion of dilute aluminum particle clouds in a post-detonation flow field. *Proc. Combust. Inst.*, 33:2255–2263, 2011.
- [5] J. C. Schulz, K. C. Gottiparthi, and S. Menon. Richtmyer-Meshkov instability in dilute gas-particle mixtures with re-shock. *Physics of Fluids*, 25(114105), 2013.
- [6] S. Menon and N. Patel. Subgrid modeling for simulation of spray combustion in large-scale combustors. *AIAA Journal*, 44:709–723, 2006.
- [7] W. W. Kim and S. Menon. A new in-compressible solver for large- eddy simulations. *International Journal for Numerical Methods in Fluid Mechanics*, 31:983–1017, 1999.
- [8] W. W. Kim and S. Menon. Numerical modeling of turbulent premixed flames in the thin-reaction-zones regime. *Combustion Science and Technology*, 160:119–150, 2000.
- [9] K. Balakrishnan, D. V. Nance, and S. Menon. Simulation of impulse effects from explosive charges containing metal particles. *Shock Waves*, 20:217–239, 2010.
- [10] K. C. Gottiparthi and S. Menon. Study of deflagration-to-detonation transition in gas-particle mixtures. *AIAA Paper 2010-0801*, 2011.
- [11] K. C. Gottiparthi, J. C. Schulz, and S. Menon. Multi-scale simulation of deflagration-to-detonation transition in turbulent dense two-phase reactive mixtures. *DoD High Performance Computing Modernization Program Contributions to Mission Success*, 2013.
- [12] K. C. Gottiparthi and S. Menon. Flame acceleration and transition to detonation in gas-particle mixtures. *Proceedings of the European Combustion Meeting*, 2013.
- [13] K. C. Gottiparthi and S. Menon. Multi-scale simulation of deflagration-to-detonation transition in turbulent dense two-phase reactive mixtures. *DoD High Performance Computing Modernization Program Contributions to Mission Success*, 2014.

- [14] K. C. Gottiparthi and S. Menon. Simulations of heterogeneous detonations and post detonation turbulent mixing and afterburning. *AIP Conference Proceedings*, 1426:1639–1642, 2012.
- [15] K. C. Gottiparthi, J. C. Schulz, and S. Menon. On the neutralization of bacterial spores in post-detonation flows. *Shock Waves*, 24:455–466, 2014.
- [16] M. Cowperthwaite. Significance of some equations of state obtained from shock-wave data. *American Journal of Physics*, 34:1025–1030, 1966.
- [17] J. A. Zukas and W. P. Walters. *Explosive Effects and Applications*. Springer, New York, 1998.
- [18] D. M. Snider. An incompressible three-dimensional multiphase particle-in-cell model for dense particle flows. *Journal of Computational Physics*, 170:523–549, 2001.
- [19] N. A. Patankar and D. D. Joseph. Modeling and numerical simulation of particulate flows by the eulerian-lagrangian approach. *International Journal of Multiphase Flow*, 27:1659–1684, 2001.
- [20] F. Zhang, K. Gerrard, and R. C. Ripley. Reaction mechanism of aluminum-particle-air detonation. *Journal of Propulsion and Power*, 25(4):845–858, 2009.
- [21] S. D. Gates, A. D. McCartt, J. B. Jeffries, R. K. Hanson, L. A. Hokama, and K. E. Mortelmans. Extension of *Bacillus* endospore gas dynamic heating studies to multiple species and test conditions. *Journal of Applied Microbiology*, 111:925–931, 2011.

DISTRIBUTION LIST
DTRA-TR-15-88

DEPARTMENT OF DEFENSE

DEFENSE TECHNICAL
INFORMATION CENTER
8725 JOHN J. KINGMAN ROAD,
SUITE 0944
FT. BELVOIR, VA 22060-6201
ATTN: DTIC/OCA

**DEPARTMENT OF DEFENSE
CONTRACTORS**

QUANTERION SOLUTIONS, INC.
1680 TEXAS STREET, SE
KIRTLAND AFB, NM 87117-5669
ATTN: DTRIAC